



POLITECNICO
MILANO 1863

SCUOLA DI INGEGNERIA INDUSTRIALE
E DELL'INFORMAZIONE

Dynamic Simulation, Flight Control and Guidance Synthesis for Fixed Wing UAV Swarms

TESI DI LAUREA MAGISTRALE IN
AERONAUTICAL ENGINEERING - INGEGNERIA AERONAUTICA

Author: **Marco Tomasoni**

Student ID: 969266

Advisor: Prof. Carlo E. D. Riboldi

Academic Year: 2022-2023

Abstract

Autonomous unmanned flight based on fixed-wing aircraft offers a practical and cost-effective solution for transportation missions to remote or underserved areas, particularly when payload capacity and range are critical factors. In such contexts, the use of UAV swarms presents an attractive approach to leverage payload capabilities. Additionally, within the military domain, deploying swarms of smaller aircraft could enhance logistic modularity, reducing the risk of losing the entire mission's cargo or weaponry when traversing hostile territories.

This thesis comprehensively addresses various aspects of fixed-wing UAV swarm flight, encompassing 6-degree-of-freedom flight dynamics modeling, aircraft stabilization through Linear Quadratic Regulator approach, path tracking for autonomous guidance, intra-swarm formation control, overall performance evaluation, and disturbance management. One of the notable features of this research is the implementation of several guidance algorithms designed to serve different purposes of a typical reconnaissance mission. These algorithms are tailored to ensure effective navigation, target identification, and data collection, enhancing the swarm's capability to perform complex reconnaissance tasks.

Concerning swarm management, the research is grounded in predefined hierarchical structures based on the leader-follower paradigm, and simulates swarm dynamics, accounting for the complete nonlinear motion of each involved UAV.

A distributed coordination law is chosen and synthesized based on different available strategies for information conveyance, such as relative position/velocity versus absolute position/velocity, among others. The swarm assembly commences with a simple two-element formation and gradually scales up in complexity by incorporating additional elements in a comprehensive complete reconnaissance mission simulation.

The methodologies and case studies presented in this work exemplify the design and coordination of a UAV swarm, facilitated by robust control techniques, and rigorously demonstrated within a comprehensive nonlinear simulation environment.

Examples based on the actual aerodynamic and inertial characteristics of an existing military UAV are presented, shedding light on both the potential benefits and challenges associated with its integration into a swarm.

Keywords: fixed-wing UAVs, formation flight, swarm coordination, stabilization control, guidance control, flight simulation.

Abstract in lingua italiana

Il volo autonomo senza pilota basato su velivoli ad ala fissa offre una soluzione pratica ed economica per missioni di trasporto in destinazioni remote o sottoservite, in particolare quando la capacità di carico e l'autonomia risultano essere fattori critici. In contesti simili, l'impiego di sciame di UAV rappresenta un approccio interessante per aumentare la capacità di carico. Inoltre, nel contesto militare, il dispiegamento di sciame di velivoli di ridotte dimensioni potrebbe migliorare la modularità logistica, riducendo il rischio di perdere l'intero carico di missione o armamenti durante l'attraversamento di territori ostili.

Questa tesi affronta in modo completo vari aspetti del volo di uno sciame di UAVs ad ala fissa, tra cui la modellazione della dinamica di volo a 6 gradi di libertà, la stabilizzazione dei velivoli mediante l'approccio LQR, il tracciamento di percorsi predefiniti per la guida autonoma, il coordinamento della formazione, la valutazione delle prestazioni complessive e la gestione delle perturbazioni.

Una delle caratteristiche più rilevanti di questa ricerca è l'implementazione di diversi algoritmi di guida progettati per servire scopi diversi di una tipica missione di ricognizione. Questi algoritmi sono progettati in modo da garantire una navigazione efficace, l'identificazione dei bersagli e la raccolta di dati, migliorando così la capacità dello sciame nell'eseguire compiti complessi di ricognizione.

Per quanto riguarda la gestione dello sciame, la ricerca si basa su strutture gerarchiche predefinite basate sul paradigma del leader-gregario e simula la dinamica dello sciame, tenendo conto del moto non lineare di ciascun UAV coinvolto.

Una legge di coordinamento distribuita viene scelta e sintetizzata in base a diverse strategie disponibili per la trasmissione delle informazioni, come posizione/velocità relative rispetto a posizione/velocità assolute, tra le altre. L'assemblaggio dello sciame inizia con una formazione di due elementi, scalando gradualmente in complessità andando a incorporare ulteriori elementi in una simulazione completa di una missione di ricognizione.

Le metodologie e i casi studio presentati in questo lavoro illustrano la progettazione e il coordinamento di uno sciame di UAV, facilitato da comprovate tecniche di controllo e dimostrato in modo rigoroso all'interno di un completo ambiente di simulazione non

lineare.

Gli esempi presentati, sono basati sulle reali caratteristiche aerodinamiche e inerziali di un UAV militare esistente, mettendo in luce sia i potenziali vantaggi che le sfide legate alla sua integrazione all'interno di uno sciame.

Parole chiave: UAVs ad ala fissa, coordinazione di sciame, controllo di stabilizzazione, controllo di guida, simulazione di volo

Contents

Abstract	i
Abstract in lingua italiana	iii
Contents	v
Introduction	1
1 Fixed-wing UAV Modeling	13
1.1 Coordinate Frames	13
1.1.1 Local Horizon Frame \mathcal{F}^h	15
1.1.2 Body Frame \mathcal{F}^B	17
1.1.3 Stability and Wind frames, \mathcal{F}^S and \mathcal{F}^W	18
1.1.4 Change of Reference	19
1.1.5 Wind triangle	21
1.2 Kinematics	23
1.3 Rigid Body Dynamics	26
1.3.1 Inertia Tensor	27
1.3.2 Aerodynamic Forcing Terms	28
1.3.3 Propulsive Forcing Terms	31
1.3.4 Gravitational Forcing Term	32
1.4 Scalar Equations of Motion	32
1.5 Testbed Aircraft	33
1.5.1 General Characteristics	35
1.5.2 Dimension Specification	35
1.5.3 Stability and Control Derivatives	37
1.5.4 Actuators	38
2 Stability Augmentation System (SAS)	39

2.1	Linear Dynamic Model	39
2.1.1	Trim Point Solution	39
2.1.2	Linearized System Derivation	41
2.2	Eigenanalysis	46
2.3	Controller Design	52
2.3.1	Linear Quadratic Regulator (LQR)	54
2.3.2	LQR with Output Feedback	55
2.3.3	Controller Implementation	57
2.4	Simulation and Results	59
2.4.1	Free Response Testing	59
2.4.2	Forced Response Testing	64
3	Single-Aircraft Guidance Algorithms	67
3.1	Beam Tracking	67
3.1.1	Longitudinal Beam Tracking	68
3.1.2	Lateral-directional Beam Tracking	71
3.1.3	Trajectory Blending	73
3.2	Circular Trajectory Tracking	76
3.2.1	Orbit path definition	77
3.2.2	Vector Field Generation	77
3.3	Rendezvous Guidance	80
3.3.1	Circling Over a Fixed Target	81
3.3.2	Leader Chasing	84
3.4	Simulations and Results	86
3.4.1	Beam Tracking Testing	87
3.4.2	Circular Trajectory Tracking Testing	97
3.4.3	Rendezvous Testing	100
4	Formation Modeling and Control	105
4.1	Wake Interference Modeling	106
4.1.1	Vortex Lattice Method	108
4.1.2	Tandem Wing Analysis	110
4.2	Formation Control Mode Synthesis	115
4.2.1	Flying Over Target: GM vs FCM	118
4.3	Simulations and Results	118
4.3.1	Two-aircraft Formation: Single Leg Trajectory Path	119
4.3.2	Three-aircraft Formation: Hexagonal Pattern	121
4.3.3	Three Aircraft Formation: Triangular Path	122

4.3.4	Formation Testing in windy condition	124
5	Mission Simulation	131
5.1	Phase 1: Rendezvous	135
5.2	Phase 2: Waypoint Navigation	138
5.3	Phase 3: Target 1 Overflight	140
5.3.1	Alternative Scenario: Leader's GM Failure Over Target	142
5.4	Phase 4: Target 2 Overflight	143
5.5	Phase 5: Disengagement and Formation Splitting	146
6	Conclusions and Outlook	149
	Bibliography	153
A	Appendix A	157
B	Appendix B	159
C	Appendix C	161
D	Appendix D	163
	List of Figures	165
	List of Tables	171
	List of Symbols	173
	Acknowledgements	177

Introduction

Unmanned Aerial Vehicles (UAVs) have revolutionized military and civilian operations by offering unprecedented flexibility, especially concerning deployment and recovery, cost-effectiveness, and reduced risk to human personnel. .

In recent years, the emergence of fixed-wing UAV swarms has captured the attention of defense and aerospace industries worldwide. These swarms, composed of numerous small, low-cost, and coordinated autonomous aircraft, hold the potential to disrupt conventional warfare paradigms and redefine the landscape of modern air operations concerning potential applications of UAV swarms beyond military domains, including search and rescue, surveillance, agriculture, and environmental monitoring.

Autonomous unmanned flight based on fixed-wing aircraft constitutes a practical and economical solution also for transport missions toward remote destinations or disadvantaged communities, for which payload and range represent interesting figures of merit. In those scenarios, the employment of UAV swarms appears as a promising way to pursue a scale effect on payload. Considering the military market, the deployment of smaller aircraft swarms may enable logistic modularity, mitigating the risk of losing the entire mission cargo or war-load by flying over hostile areas. As we delve into this compelling area of research, a comprehensive assessment of the background surrounding fixed-wing UAV swarms is needed.

The concept of UAV swarming dates back to the early 2000s, with initial research conducted primarily in the defense sector. As advancements in artificial intelligence, sensor technology, and communication systems accelerated, the viability and potential of fixed-wing UAV swarms have grown exponentially. These swarms, capable of executing complex collaborative tasks, present a disruptive and cost-efficient alternative to traditional military aircraft, challenging the dominance of expensive and complex aircraft acquisition programs.

In the early stages, UAV swarms demonstrated simple formations and limited autonomy, but with the advancement of computing power and artificial intelligence, researchers began developing more sophisticated swarm coordination algorithms. These improvements enabled UAV swarms to perform complex tasks, adapt to changing conditions, and collab-

orate efficiently. A key milestone in the development of UAV swarms was the improvement of communication protocols, allowing for reliable and rapid data exchange among individual UAVs. This decentralization of operations made swarms more resilient, flexible, and scalable.

Recent research efforts have further enriched UAV swarm capabilities, incorporating advanced mission planning algorithms and swarm behavior simulations to improve coordination and decision-making processes. Inspired by collective behaviors observed in nature, researchers have also explored the use of swarm intelligence, leading to the development of adaptive and self-organizing swarming behaviors.

Despite significant progress, challenges remain.

Looking ahead, fixed-wing UAV swarms are expected to play a substantial role in various applications, thanks to their potential to transform aerial operations, enhance efficiency, and reduce costs. Their versatility has garnered interest from defense agencies, commercial enterprises, and research institutions worldwide, promising a future of unmanned systems capable of tackling diverse challenges with exceptional capability.



Figure 1: fixed-wing UAVs swarm for military surveillance.

Coordinating multiple UAVs in a swarm enables enhanced mission capabilities, improved efficiency, and resilience. However, achieving seamless coordination and cohesion within a swarm demands the implementation of sophisticated control strategies. The first and most immediate classification of such control strategies can be made according to how information from the environment is managed and how communications are conveyed.

Centralized Control Strategies:

Centralized control involves a hierarchical approach where a single central controller,

often referred to as the "master" or "leader," governs the behavior of all individual UAVs within the swarm. The central controller collects data from all UAVs, processes the information, and issues directives to guide the swarm's collective behavior. This approach offers precise and coordinated decision-making, making it suitable for missions with well-defined objectives and dynamic environments.

Advantages:

- **Efficient decision-making:** Centralized control allows for globally optimized decisions, ensuring that the swarm operates as a single, cohesive unit, avoiding conflicts and redundancies in actions.
- **Complex mission handling:** In scenarios requiring sophisticated coordination, such as large-scale surveillance or target tracking, centralized control can efficiently manage the collective efforts of the swarm.

Challenges:

- **Single point of failure:** The central controller represents a potential single point of failure, as the entire swarm's functionality heavily relies on its uninterrupted operation. Malfunctions or communication breakdowns with the central controller can severely impact the swarm's performance.
- **Scalability limitations:** As the swarm size increases, the computational burden on the central controller grows exponentially, potentially leading to delays in decision-making and communication.

. Distributed Control Strategies:

Distributed control, in contrast, adopts a decentralized approach, where each UAV acts as an autonomous agent making decisions based on local information and interactions with nearby neighbors. The absence of a central controller promotes swarm intelligence, enabling self-organization and emergent behaviors to achieve the collective objective.

Advantages:

- **Robustness and fault tolerance:** Distributed control enhances the swarm's resilience, as the loss of individual UAVs has minimal impact on the overall system's functionality. The swarm can adapt and reorganize itself in response to changes in the environment or the loss of some members.
- **Scalability and flexibility:** As new UAVs join the swarm, the distributed control system can easily incorporate them without overburdening any central entity, allowing for seamless scalability.

Challenges:

- Limited global optimization: Decentralized control might struggle to achieve globally optimized solutions, especially in complex missions requiring precise coordination and collaboration among multiple UAVs.
- Communication overhead: Distributed control necessitates frequent communication among UAVs to exchange information and reach consensus, which can lead to increased communication overhead and potential network congestion.

The choice between these approaches depends on the specific mission requirements, environmental conditions, and desired levels of coordination and scalability. As research and technological advancements progress, striking a balance between centralized and distributed elements might pave the way for hybrid control strategies, combining the best of both worlds to unlock the full potential of fixed-wing UAV swarms in various real-world applications.

Literature Review

The new frontier in this field of application is certainly represented by rotary-wing UAVs, which are a rather flexible alternative especially because of hovering capability, and lighter-than-air platforms [1]. However, fixed-wing aircraft still represent arguably the best solution in terms of mission range, fuel consumption, and payload [2].

While, on the one hand, the literature reports extensive documentation on the dynamics and control of fixed-wing UAVs, based on both classical and modern control techniques for stabilization and guidance [3–9], the same cannot be said for the dynamic characterization and control of a cooperating formation.

The problem of fixed-wing UAVs swarms synthesis is often approached in the literature from the perspective of mission management, with a focus on swarm coordination and communication logic, more than on rigorous dynamic modeling and on the accurate physical description of the problem [10–14]. Actually, aircraft dynamics is typically modeled in 2D by associating each element in the swarm with three states (two displacements and one rotation within the longitudinal plane), sometimes neglecting state and control input constraints, mainly related to the aircraft's minimum airspeed for sustained flight (stall) and more generally, to aerodynamic effects. Moreover, a significant portion of the literature on this subject is rooted in multi-agent interacting systems, which have long been explored in the field of robotics. As scalability stands as the primary performance metric that research in this domain focuses on, the evident complexity of the scenario

necessitates heightened attention toward devising control strategies for the synthesis and management of the entire system, often simplifying the dynamics of individual agents. In [11], the scalability issue is addressed by clustering UAVs into distinct and non-overlapping groups, each led by a designated leader (group-based hierarchical architecture). Coordinated centralized path following is implemented for group leaders to manage inter-group coordination, while follower UAVs exploit a distributed leader-following formation control law to maintain alignment with their direct leaders.

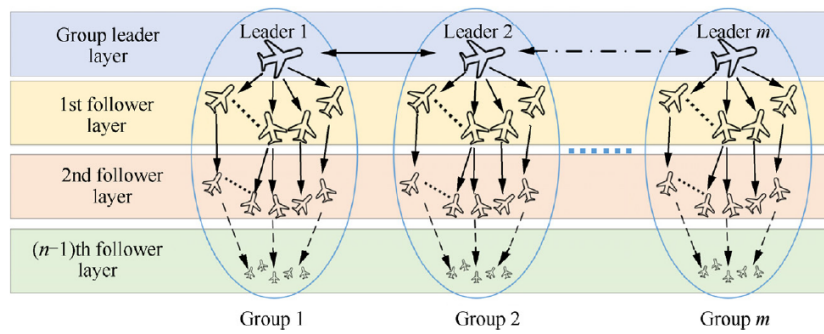


Figure 2: Group-based hierarchical model proposed by [11].

When expanding the swarm's size and, consequently, the degrees of freedom of the entire system, it becomes necessary to introduce certain simplifications:

- Each element of the swarm is treated as a material point, devoid of mass and inertial properties.
- Many of the swarm's operations are assumed to be carried out at a constant altitude, thereby enabling the modeling of flight dynamics solely within the horizontal plane of the local horizon frame.
- The swarm's performance is primarily constrained by the minimum and maximum airspeeds attainable by each individual agent, as well as a restriction on the heading rate, which is associated with the maximum bank angle imposed and theorized for each aircraft. However, it is essential to note that these limitations do not consider the dynamics of the actuators, and consequently, they do not account for the actuators' ability to precisely follow the commanded input issued by the control system.

In the same conceptual framework, studies focus on the implementation of distributed control networks aimed at specific mission tasks, such as cluster rejoining, route-based formation switching, and obstacle avoidance along the path [12], or the utilization of

Model Predictive Control (MPC) to optimize the formation's trajectory at each time step while considering constraints on speed, angular rates, and command saturation [15]. These studies aim to enhance the capabilities of UAV swarms and other multi-agent systems by tailoring the control strategies to specific mission objectives, unlocking the potential for more complex and sophisticated missions, while drastically reducing the problem degrees of freedom considering two-dimension dynamics.

Indeed, some studies address the modeling of flight in close formation. In references [16] and [17, 18], the dynamics of the 6-degree-of-freedom (6-DOF) aircraft are modeled by linearizing the equations of motion and decoupling longitudinal and lateral-directional dynamics. Subsequently, an inner control loop is constructed based on this linearized model to stabilize the aircraft, while an outer loop functions as an autopilot for guiding and maintaining the formation. The inner loop, often referred to as the attitude control loop, focuses on stabilizing the aircraft by regulating its orientation, while the outer loop, known as the position control loop, is responsible for guiding the aircraft and maintaining the desired formation. This well-established and thoroughly validated approach proves particularly effective when operating in the vicinity of the specific trim condition upon which the linearized model was developed. As a result, the control system also performs optimally in such conditions. However, it is essential to be mindful of potential challenges when operating outside this specific region, as the dynamics may deviate significantly from the linear model, necessitating adaptations or more sophisticated control strategies. This gap in documented research motivates this thesis work, which is focused on analyzing the problem of UAV swarm formation flight without simplifying aircraft dynamics, and putting in place control strategies applicable in the field, taking into account the non-linearities inherent to the problem at hand.

SILCROAD Environment

The current study relies on a non-linear simulation framework developed employing an object-oriented library in `Matlab (R2022b)`[®], called `SILCROAD` (*Simulation Library for Craft Object Advanced Dynamics*), and developed at the Department of Aerospace Science and Technology, Politecnico di Milano.

The core of this object-oriented programming library revolves around the superclass "Craft." Through a series of abstract properties and methods, this superclass proficiently prescribes the dynamics of a generalized flying vehicle, thereby simulating its behavior within the simulation environment. The employment of this sophisticated library fosters a remarkable versatility, empowering the user to tailor the simulation environment according to their specific needs. Furthermore, the implementation of design patterns and best

practices in the library’s architecture fosters reusability, maintainability, and scalability. This leads to enhanced code comprehension, facilitating the collaborative development of complex simulation scenarios. The implemented high-fidelity non-linear dynamics approach further enhances the model’s precision by considering the nonlinear relationships governing the flying craft motion. This sophisticated technique enables the simulation to capture intricate nonlinear phenomena that might arise during flight, such as aerodynamic stall, inertia coupling, and various other complex interactions that significantly impact the air vehicle’s behavior. Within the library, specific tools are embedded for the linearization of the dynamic model, serving purposes such as eigenanalysis and general stability analysis. Additionally, dedicated tools are provided for control system design.

Let’s delve deeper into the structure of the library and review the methods and properties of the *Craft* superclass.

Properties	Description	Dimension
m	Mass	1x1
J_P	Body inertia components	3x3
r_{CG}	Body components of center of gravity	3x1
Vol	Volume (for buoyancy computations)	1x1
r_{CB}	Body components of center of buoyancy	3x1
$x_{P_{GND}}$	Position of generic point P in GND ref.- GND comp.	3x1
v_P	Velocity of generic point P in GND ref. - BODY comp.	3x1
ω_B	Body Rotational rates in GND ref. - BODY comp.	3x1
e_{321}	Attitude angles ϕ, θ, ψ of body reference wrt.GND	3x1
Wind	Wind - BODY comp.	3x1
PSD	Previous step derivatives	12x1
PSC	Previous step command	4x1

Table 1: *Craft* superclass properties.

In addition to the properties, which represent the characteristics or data describing the object’s state as listed in Table 1, the main methods are listed in the table below (Table 2). These methods encompass the operations that the object can execute, defining the object’s behavior and its interactions with other objects or the external environment, manipulating the object’s properties, or yielding results based on them.

Methods	Description
GravityAtAltitude(Obj);	Gravity acceleration at altitude
AtmosphereAtAltitude(Obj);	Atmosphere at altitude
GravityForce(Obj);	Gravity force - BODY comps.
GravityMomentP(Obj);	Gravity moment wrt. P- BODY comps.
BuoyancyForce(Obj);	Buoyancy force - BODY comps.
BuoyancyMomentP(Obj);	Buoyancy moment wrt. P - BODY comps.
AeroForce(Obj);	Aerodynamic force -BODY comps.
AeroMomentP(Obj);	Aerodynamic moment wrt. P - BODY comps.
ThrustForce(Obj);	Aerodynamic force -BODY comps.
ThrustMomentP(Obj);	Aerodynamic moment wrt. P - BODY comps.
xP(Obj);	Position of ref. point P wrt. GND ref.- BODY comp
vPGND(Obj);	Velocity of ref. point P wrt. GND ref. - GND comp.
omegaBGND(Obj);	Rotational rate of body B wrt. GND ref.- GND comp.
aP(Obj);	Acceleration of point P wrt. body ref.- BODY comp.
aPWrtGround(Obj);	Acceleration of point P wrt. GND ref.- BODY comp.
aPGND(Obj);	Acceleration of point P wrt. BODY ref. - GND comp.
aPWrtGroundGND(Obj);	Acceleration of point P wrt. GND ref.- GND comp.
omegadotB(Obj);	Rotational acceleration of body - BODY comp.
omegadotBGND(Obj);	Rotational acceleration of body - GND comp.
Airspeed(Obj);	Airspeed in BODY components
AirspeedGND(Obj);	Airspeed in GND components, from wind and motion
Alpha(Obj);	Angle of attack
Beta(Obj);	Sideslip angle
Alphadot(Obj);	Derivative of angle of attack
Betadot(Obj);	Derivative of sideslip angle
Gamma(Obj);	Climb angle
Chi(Obj);	Course angle
RotationGroundToBody(Obj);	Rotation matrix from ground to body reference
GeneralizedRate(Obj);	Time derivatives of craft state
TrimProblemWrapper(Obj);	To be called by trim solver of any subclass
ChangeInertiaRefP(Obj,rRef);	Change object inertia property wrt. new ref. point

Table 2: *Craft* superclass methods.

Within the *Craft* parent class, subclasses are defined to provide a more specific object's definition. Each subclass, characterized by its own properties and methods, can still make use of all the aforementioned properties and methods inherited from the superclass *Craft*. For the purposes of this work, it is necessary to assemble a formation of fixed-wing UAVs objects, defined through the *Airplane* subclass. The instantiation of the *Airplane* object occurs through the definition of a data structure, in this case called *AircraftData*, which contains all the geometric, aerodynamic, and propulsive properties of the aircraft, as well as the current state of commands. These data are directly managed by the *Airplane* subclass, as reported in Figure 3. Additionally, other data, such as inertial properties, flight dynamic states, and inertial position, are managed by the *Craft* parent class.

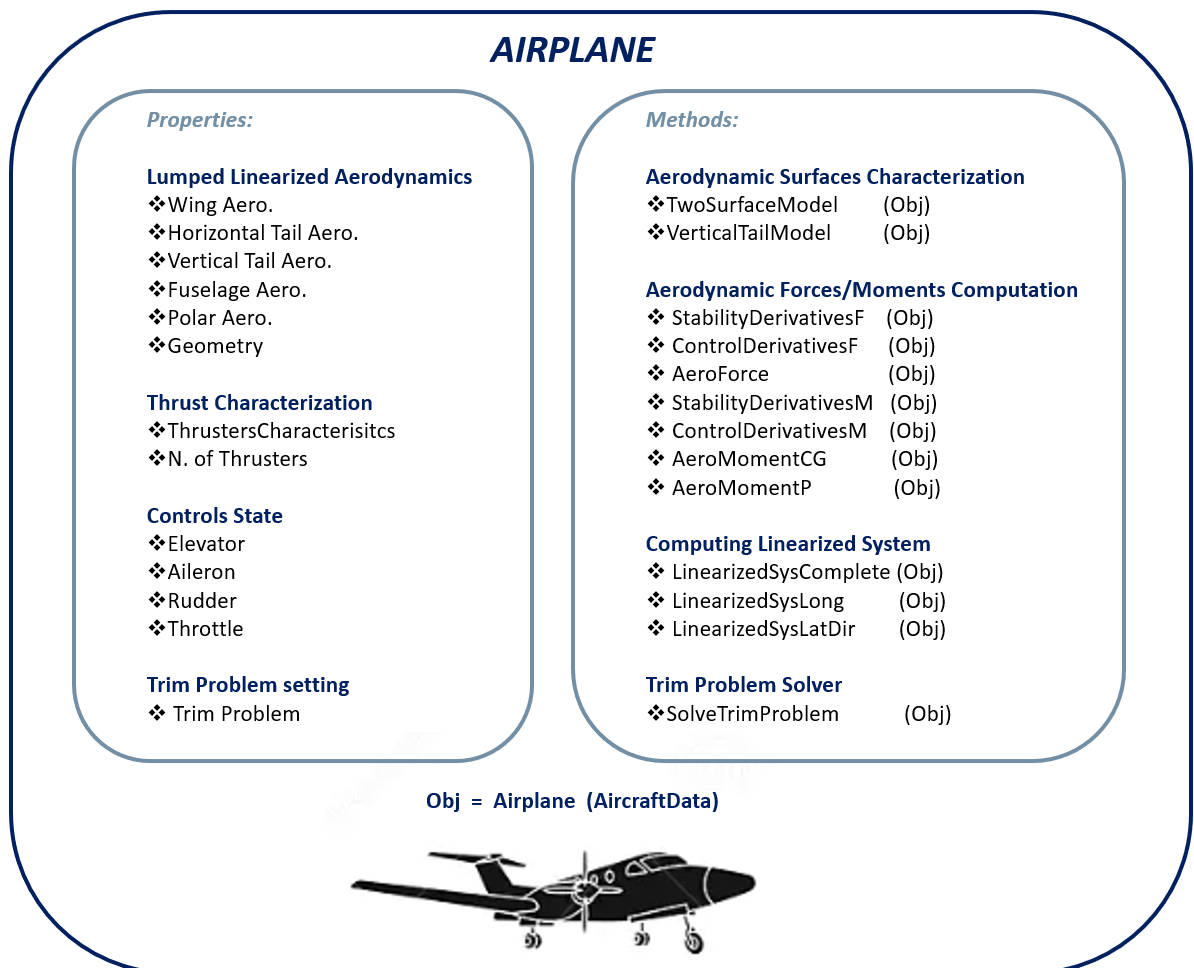


Figure 3: Airplane Object definition.

A clearer and more comprehensive explanation of how the simulation is initialized and handled is outlined Appendix A.

In conclusion, this environment provides enhanced flexibility for adding or removing units from the formation, with each unit having its own control system, and being implemented as a separate object within the inter-agent simulation environment. As a result, this approach significantly streamlines and expedites the simulation environment generation process, by circumventing the inherent rigidity of simulation programs such as SIMULINK (R2022b)[®]. Connecting the multitude of states and inputs originating from each formation component in SIMULINK (R2022b)[®] would require a substantial effort, which is alleviated by the proposed approach.

Thesis Description and Outline

In this thesis, the focus lies on fixed-wing UAVs swarms, aiming to overcome the dynamics modeling simplifications commonly found in the literature. Rather than relying on complex control strategies, the objective is to implement a comprehensive non-linear modeling of the aircraft. Furthermore, control laws for stabilization, guidance, and formation control will be applied. These control laws will be explored and tested within the non-linear context, making them applicable to real-world scenarios.

By adopting this approach, the aim is to avoid designing control systems from scratch in a linearized framework, which might not ensure optimal performance outside of specific design conditions.

The outcomes of this thesis will demonstrate the practical feasibility and benefits of applying established, reliable, and straightforward control strategies to improve the overall effectiveness and coordination of fixed-wing UAVs swarms.

Another fundamental aspect pertains to the validation of the SILCROAD tool as a dynamic simulation environment. This tool is adept at orchestrating the interactive co-simulation of multiple aircraft, thus facilitating the exploration of control and coordination techniques for swarm scalability. Additionally, it allows for the artificial adaptation to real-world operational challenges, enabling a comprehensive assessment of the applicability of swarm systems in practical scenarios.

The document will be organized as follow:

- **Chapter 1:** this chapter will focus on the dynamic modeling of the 6-degree-of-freedom (6DOF) aircraft using non-linear equations of motion. It will delve into the mathematical representation of the aircraft's dynamics, considering its complex interactions and movements in a non-linear framework. The chapter will provide a detailed analysis of the equations and the underlying principles governing the aircraft's

motion. Subsequently, a brief description of the testbed aircraft will be presented. It will include an overview of the aircraft's geometric configuration and performance specifications. The characteristics of the testbed aircraft will be outlined, providing essential background information for further analysis and experimentation in the subsequent sections of the document.

- **Chapter 2:** this chapter, will encompass a detailed discussion of the stabilization system using optimal control (LQR - Linear Quadratic Regulator). The theoretical background of LQR will be presented, followed by its application to the dynamic model of the 6 D.O.F. aircraft. The chapter will elaborate on the design process and the selection of relevant control parameters for an effective stabilization system, which is tested, at the end, for different flight conditions.
- **Chapter 3:** the synthesis of three different guidance algorithms will be discussed, targeting different phases of a reconnaissance mission: **beam-tracking** control to pursue waypoints navigation, **circular trajectory tracking** for loitering phases, and a specific procedure for **rendezvous** and formation rejoining, along with their integration into the overall Automatic Flight Control System of the aircraft. The chapter will include illustrations and examples to demonstrate the system's performance in various flight scenarios.
- **Chapter 4:** this chapter on formation flight control will delve into the design and implementation of a control system that enables multiple aircraft to fly in a coordinated formation. Theoretical frameworks for maintaining desired formations will be explored, along with practical considerations for real-world applications. Additionally, the chapter will include a specialized section devoted to studying the aerodynamic interaction between adjacent components within the formation. This section will focus on understanding how the separation between two aircraft impacts their aerodynamic forces and moments.

In the final section, the focus is on addressing the disturbance rejection problem in the context of formation flight. The scenario envisions an instance where a wind stream tube affects the formation's path, and the investigation centers around how the formation can respond to maintain its proximity to the desired trajectory. The intent, is to enhance the formation flight control system's resilience and adaptability in the face of external disturbances.

- **Chapter 5:** after the prior assembling of the various AFCS modes, for individual aircraft and verifying the feasibility of automatic formation flight, in this final chapter, a ground reconnaissance mission will be simulated utilizing a 9 UAVs swarm.

The objective is to assess the applicability and reliability of the proposed systems control logic in coordinating a swarm deployed within a real or realistically simulated operational scenario.

- **Chapter 6:** the conclusions drawn from this study are summarized briefly in this section. Additionally, will be outlined potential future outlooks for enhancing the themes explored and expanding the scope of research.

1 | Fixed-wing UAV Modeling

Through this chapter, the theoretical background of fixed-wing aircraft dynamics will be defined. Starting with the definition of the main reference frames and the rotation formalism that allows the transition from one reference frame to another. Then, we will proceed to define the kinematics and the dynamics formulation of the 6-DOF (degrees of freedom) aircraft coming to write the nonlinear equations system describing the aircraft motion. Finally, a brief overview of the aerodynamic and propulsive forces modeling will be discussed. Afterward, a dedicated section will provide a concise description of the selected testbed aircraft, including dimensional specifications and performance aspects.

1.1. Coordinate Frames

When dealing with different reference systems, it is essential to establish fundamental rules that define the transition from one system to another.

Taking the example of Figure 1.1, the generic vector \mathbf{p} can be expressed in both reference frames \mathcal{F}^0 , defined by a set of mutually orthogonal basis vectors $\mathbf{i}^0, \mathbf{j}^0, \mathbf{k}^0$, and in the reference frame \mathcal{F}^1 , accordingly defined by the unit vectors set $\mathbf{i}^1, \mathbf{j}^1, \mathbf{k}^1$.

The transition of \mathbf{p} components in reference frame \mathcal{F}^1 , while having prior knowledge of its components in \mathcal{F}^0 , occurs through the application of a rotation matrix \mathcal{R}_0^1 . According to this notation, the rotation matrix \mathcal{R}_0^1 facilitates the seamless transformation of vector coordinates from \mathcal{F}^0 to \mathcal{F}^1 , and its representation doesn't change regardless whether it is measured in reference \mathcal{F}^0 or \mathcal{F}^1 . The operation is formalized through the following equation:

$$\mathbf{p}^1 = \mathcal{R}_0^1 \mathbf{p}^0 . \quad (1.1)$$

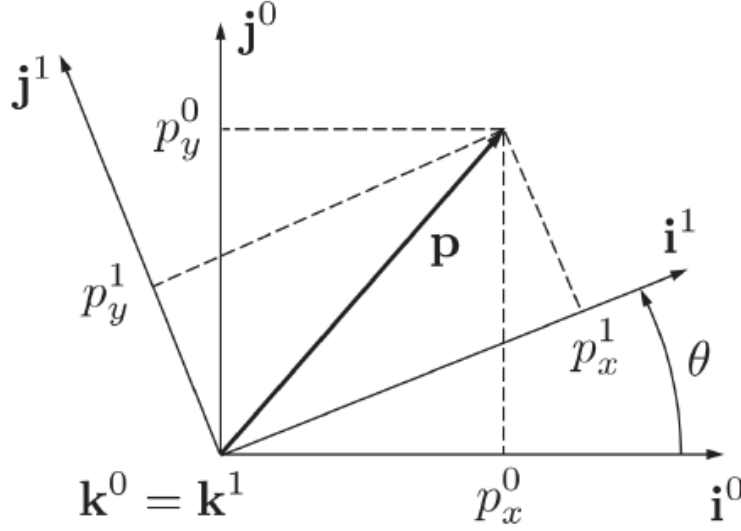


Figure 1.1: Rotation about \mathbf{k} (\mathbf{k} axis point outwards).

For a right-handed rotation around \mathbf{k}^0 of θ , the rotation matrix takes this form.

$$\mathcal{R}_0^1 = \begin{bmatrix} \cos \theta & \sin \theta & 0 \\ -\sin \theta & \cos \theta & 0 \\ 0 & 0 & 1 \end{bmatrix}. \quad (1.2)$$

Proceeding with the same conceptual methodology, a rotation of the same amount around \mathbf{j}^0 would have been performed with the rotation matrix

$$\mathcal{R}_0^1 = \begin{bmatrix} \cos \theta & 0 & -\sin \theta \\ 0 & 1 & 0 \\ \sin \theta & 0 & \cos \theta \end{bmatrix}, \quad (1.3)$$

and a rotation about \mathbf{i}^0 would be

$$\mathcal{R}_0^1 = \begin{bmatrix} 1 & 0 & 0 \\ 0 & \cos \theta & \sin \theta \\ 0 & -\sin \theta & \cos \theta \end{bmatrix}. \quad (1.4)$$

.

The matrices obtained in this way are also referred to as direction cosine matrices since each component represents the cosine of the angle included between the corresponding basis vectors of the two frames. The rotation Matrix \mathcal{R}_0^1 possesses the following properties:

- Orthogonality: The rotation matrix is orthogonal, meaning its columns (and rows) are orthonormal vectors. This property ensures that the length of each column vector is 1 (unit vectors), and any two distinct column vectors are mutually orthogonal (perpendicular) to each other.
- Determinant equal to 1: The determinant of the rotation matrix is equal to 1. This property ensures that the rotation preserves the orientation of vectors and does not involve any reflection or mirroring: $\det(\mathcal{R}_0^1) = 1$.
- Inverse: The rotation matrix is invertible. This property allows us to easily transform vectors back to the original reference frame: $(\mathcal{R}_0^1)^{-1} = (\mathcal{R}_0^1)^T = \mathcal{R}_0^1$.
- Composition: When performing multiple rotations, the result can be obtained by multiplying the individual rotation matrices in the reverse order: $\mathcal{R}_1^2 \mathcal{R}_0^1 = \mathcal{R}_0^2$.
- Preservation of dot products: The dot product of two vectors is preserved under rotation: $\mathbf{u} \cdot \mathbf{v} = \mathcal{R}_0^1(\mathbf{u}) \cdot \mathcal{R}_0^1(\mathbf{v})$.

1.1.1. Local Horizon Frame \mathcal{F}^h

The Local Horizon Frame has its origin at **CG** point on the aircraft and features orthogonal axes ($\mathbf{x}^h, \mathbf{y}^h, \mathbf{z}^h$) such that the $\mathbf{x}^h \mathbf{y}^h$ -plane is tangent to the Earth's surface, and the \mathbf{z}^h -axis points downward, aligning with the direction of gravity acceleration as reported in Figure 1.2. Under appropriate assumptions, is treated as an inertial reference frame, therefore, also reported as \mathcal{F}^I . The unit vectors in this frame are denoted as $\mathbf{e}_x^h, \mathbf{e}_y^h, \mathbf{e}_z^h$. Typically, the $\mathbf{x}^h - \mathbf{y}^h$ axes are aligned in the North-East direction, hence the usual name NED frame (*North-East-Down*).

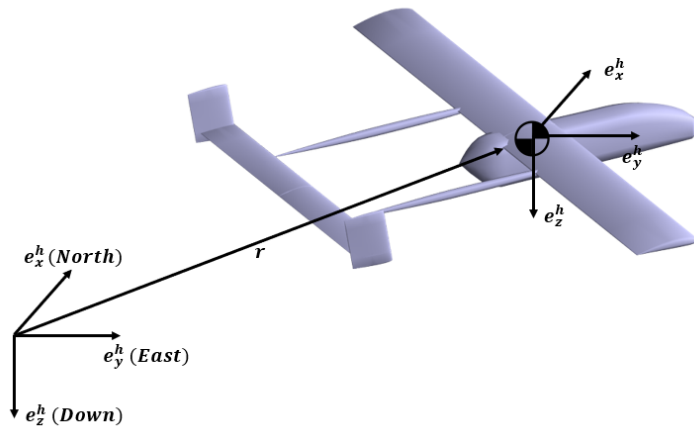


Figure 1.2: The LocalHorizon Frame \mathcal{F}^h

The Local Horizon Frame allows for formalizing various kinematic quantities relevant to describing the aircraft's motion and characterizing its performance. Among these are:

- **Flight Altitude:** is the vertical distance between the aircraft and the Earth's surface. Formally, the flight altitude h is defined as the projection of the position vector \mathbf{r} onto the vertical axis \mathbf{e}_z^h of the Local Horizon Frame. Mathematically, it can be expressed as:

$$h = -\mathbf{e}_z^h \cdot \mathbf{r} . \quad (1.5)$$

- **Vertical and horizontal velocity:** respectively defined as the projection of the flight velocity \mathbf{V} onto the vertical axis and the horizontal plane. Vertical velocity is also referred as *Rate of climb* (R/C).

$$V_v = -\mathbf{e}_z^h \cdot \mathbf{V} , \quad (1.6)$$

$$V_h = \|\mathbf{V} + V_v \mathbf{e}_z^h\| . \quad (1.7)$$

- **Trajectory angles:** *flight path angle* γ defined as the angle between the airspeed vector \mathbf{V} and the horizontal plane $\mathbf{x}^h \mathbf{y}^h$, and *track angle* χ , defined as the angle included between the projection of airspeed vector \mathbf{V} onto the horizontal plane $\mathbf{x}^h \mathbf{y}^h$ and the \mathbf{x}^h axis.

$$\gamma = -\arcsin \frac{\mathbf{e}_z^h \cdot \mathbf{V}}{V} , \quad (1.8)$$

$$\chi = \arctan \frac{\mathbf{e}_y^h \cdot \mathbf{V}}{\mathbf{e}_x^h \cdot \mathbf{V}} . \quad (1.9)$$

From equation 1.8 is possible to re-formulate vertical and horizontal velocity expressions as:

$$V_v = V \sin(\gamma) , \quad (1.10)$$

$$V_h = V \cos(\gamma) . \quad (1.11)$$

while from equation 1.9, the aircraft velocity along \mathbf{e}_x^h and \mathbf{e}_y^h axes can be expressed as:

$$V_x = V_h \cos(\chi) , \quad (1.12)$$

$$V_y = V_h \sin(\chi) . \quad (1.13)$$

Through the trajectory angles, it is possible to express the flight velocity in components

within the local horizon reference frame as follows:

$$\mathbf{V} = V(\cos \chi \cos \gamma \mathbf{e}_x^h + \sin \chi \cos \gamma \mathbf{e}_y^h - \sin \gamma \mathbf{e}_z^h). \quad (1.14)$$

This is simply equivalent to adopting spherical coordinates rather than Cartesian coordinates for describing the scalar components of vector \mathbf{V} , where V is the radius of the sphere, χ is the longitude angle and γ is the latitude.

1.1.2. Body Frame \mathcal{F}^b

The body frame is a reference frame integral to the aircraft and therefore movable with respect to the inertial system. This frame is commonly adopted for expressing the aircraft equations of motion, and it's particularly convenient as all inertial properties are constant if measured about this reference. It originates at **CG** point on the aircraft and features $(\mathbf{x}^b, \mathbf{y}^b, \mathbf{z}^b)$ orthonormal axes such that the $\mathbf{x}^b\mathbf{z}^b$ plane coincides with the aircraft symmetry plane, the \mathbf{x}^b -axis coincides with the longitudinal fuselage axis, and the \mathbf{y}^b -axis directed toward the right wing. The \mathbf{z}^b -axis, to complete the orthonormal triad, is directed outward the lower portion of the fuselage.

Analogous to what has been seen for trajectory angles, it is possible to further characterize the orientation of flight speed through aerodynamics angles:

- **angle of attack, AoA**, α : the angle included between the airspeed projection onto the aircraft symmetry plane and the \mathbf{x}^b -axis.

$$\alpha = \arctan \frac{\mathbf{e}_z^b \cdot \mathbf{V}}{\mathbf{e}_x^b \cdot \mathbf{V}}. \quad (1.15)$$

- **angle of sideslip, SSA**, β : the angle included between airspeed direction and aircraft symmetry plane $\mathbf{x}^b\mathbf{z}^b$

$$\beta = \arcsin \frac{\mathbf{e}_y^b \cdot \mathbf{V}}{V}. \quad (1.16)$$

Through the aerodynamic angles, it is possible to express the airspeed in components within the body reference frame as follows:

$$\mathbf{V} = V(\cos \alpha \cos \beta \mathbf{e}_x^b + \sin \beta \mathbf{e}_y^b + \sin \alpha \cos \beta \mathbf{e}_z^b). \quad (1.17)$$

A comprehensive representation of aerodynamics angles is reported in Figure 1.3.

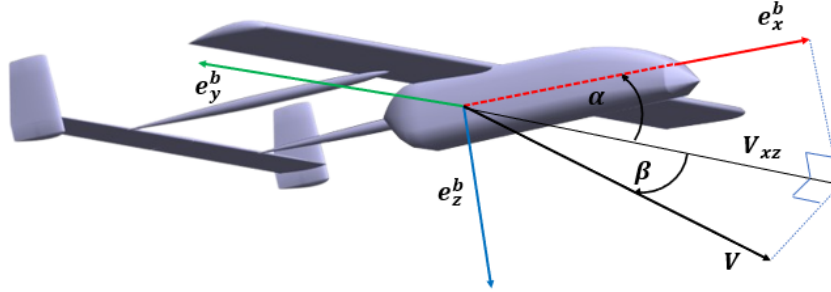


Figure 1.3: α and β definition on body-frame \mathcal{F}^B

1.1.3. Stability and Wind frames, \mathcal{F}^S and \mathcal{F}^W

We must introduce the stability and wind coordinate systems to establish a comprehensive framework for analyzing aerodynamic forces and moments.

To properly incorporate the concept of angle of attack, we introduce the stability frame as a left-handed rotation about the \mathbf{y}^b -axis by the angle α from the body frame \mathcal{F}^B . The choice of a left-handed rotation arises from the convention that the angle of attack should be positive when transitioning from the stability frame to the body frame.

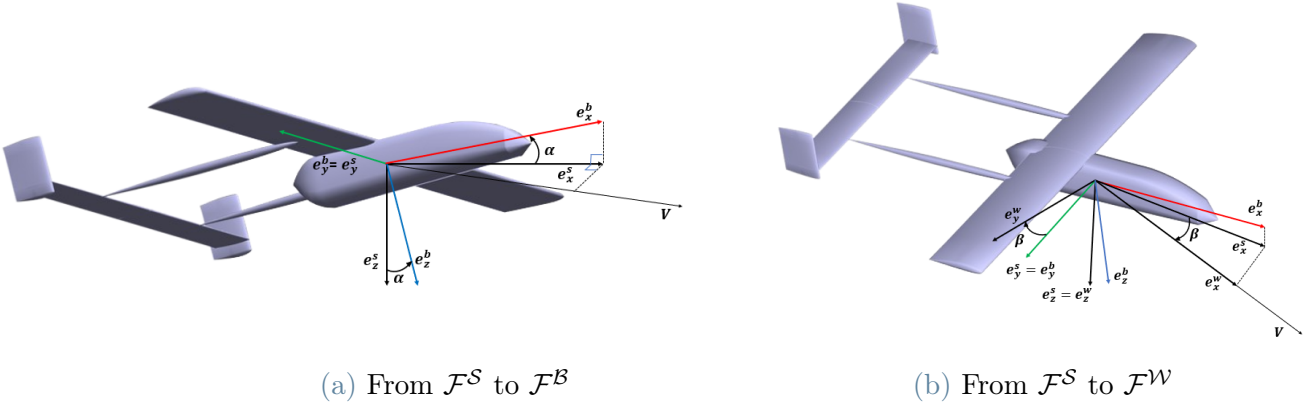
\mathcal{F}^S feature a \mathbf{x}^s -axis that lay on the airspeed projection onto the aircraft plane of symmetry, while \mathbf{y}^s -axis coincides with the \mathbf{y}^b -axis; the \mathbf{z}^s -axis is defined consequently to complete the orthonormal triad (Figure 1.4a).

With the stability frame in place, we can effectively determine the stability and control derivatives, which are crucial parameters for understanding the aircraft's response to various flight conditions and control inputs.

Similarly, we can define the Wind Reference Frame as a coordinate system generated by rotating about the \mathbf{z}^s -axis by an angle β . This reference frame is especially useful when the airspeed does not lies in the aircraft's plane of symmetry. Even in this case, the wind-frame has its origin in \mathbf{CG} , featuring $(\mathbf{x}^w, \mathbf{y}^w, \mathbf{z}^w)$ orthonormal axes such that \mathbf{x}^w points toward the relative airspeed vector, \mathbf{z}^w -axis is overlapped to \mathbf{z}^s -axis, and \mathbf{y}^w is defined to complete the orthonormal triad (Figure 1.4b).

The definition of airspeed vector within the wind frame, turns out to be quite simple.

$$\mathbf{V} = V \mathbf{e}_x^w . \quad (1.18)$$

Figure 1.4: Representation of stability and wind frame, \mathcal{F}^S and \mathcal{F}^W

1.1.4. Change of Reference

Inertial system to body-axes system.

Describing the orientation of an aircraft in space, known as its attitude, involves various possible approaches. One widely used method in flight mechanics is based on Euler angles. Euler angles consist of a set of three angles, referred to as *azimuth* ψ , *elevation* θ and *rotation* ϕ , defined by a sequence of partial planar rotations transitioning from \mathcal{F}^I inertial reference to the body reference frame \mathcal{F}^B , in the following order:

1. rotation about \mathbf{e}_z^i , third axis of inertial reference, by an angle $\psi \in [-\pi, \pi)$.
2. rotation about second axis of the intermediate triad, by an angle $\theta \in [-\pi/2, \pi/2)$.
3. rotation about \mathbf{e}_x^b , first axis of the arrival triad, by an angle $\phi \in [-\pi, \pi)$.

We can formalize these three partial rotations using Equation (1.1). The first rotation, by means of rotation matrix $\mathcal{R}_I^{n_1}(\psi)$, brings vector \mathbf{p} into the coordinate description of reference triad \mathcal{F}^{n_1} , which first axis $\mathbf{e}_x^{n_1}$ points outward the airframe nose.

$$\mathbf{p}^{n_1} = \mathcal{R}_I^{n_1}(\psi)\mathbf{p}^I. \quad (1.19)$$

The second partial rotation about $\mathbf{e}_y^{n_1}$ by the elevation angle θ , define a new intermediate coordinate system \mathcal{F}^{n_2} . In this case $\mathbf{e}_x^{n_2}$ point outward the aircraft nose, while $\mathbf{e}_z^{n_2}$ point outward the fuselage lower portion.

$$\mathbf{p}^{n_2} = \mathcal{R}_{n_1}^{n_2}(\theta)\mathbf{p}^{n_1}. \quad (1.20)$$

The final rotation, is performed about $\mathbf{e}_x^{n_2}$ by the rotation angle ϕ , reaching the arrival reference frame \mathcal{F}^b

$$\mathbf{p}^{\mathcal{B}} = \mathcal{R}_{n_2}^{\mathcal{B}}(\phi)\mathbf{p}^{n_2} . \quad (1.21)$$

Exploiting the composition property of rotation matrices, the overall coordinate transformation can be expressed by Equation (1.22).

$$\mathcal{R}_{\mathcal{I}}^{\mathcal{B}}(\phi, \theta, \psi) = \mathcal{R}_{n_2}^{\mathcal{B}}(\phi)\mathcal{R}_{n_1}^{n_2}(\theta)\mathcal{R}_{\mathcal{I}}^{n_1}(\psi) = \begin{bmatrix} c_\theta c_\psi & c_\theta s_\psi & -s_\theta \\ s_\psi s_\theta c_\psi - c_\phi s_\psi & s_\phi s_\theta s_\psi + c_\phi c_\psi & s_\phi c_\theta \\ c_\phi s_\theta c_\psi + s_\phi s_\psi & c_\psi s_\theta s_\psi - s_\psi c_\psi & c_\phi c_\theta \end{bmatrix} . \quad (1.22)$$

having placed for the sake of brevity $c_\psi := \cos \psi$, $s_\psi := \sin \psi$ and similarly for θ, ϕ . The matrix obtained represents the direction cosine matrix for the transformation from coordinates expressed in $\mathcal{F}^{\mathcal{I}}$ to coordinates in $\mathcal{F}^{\mathcal{B}}$. It can be interpreted as a matrix with columns containing the scalar components of the unit vectors of the $\mathcal{F}^{\mathcal{I}}$ frame expressed in the $\mathcal{F}^{\mathcal{B}}$ reference frame or with rows containing the scalar components of the unit vectors of the $\mathcal{F}^{\mathcal{B}}$ expressed in components of $\mathcal{F}^{\mathcal{I}}$ reference frame.

The sequential rotations are visually represented in Figure 1.5.

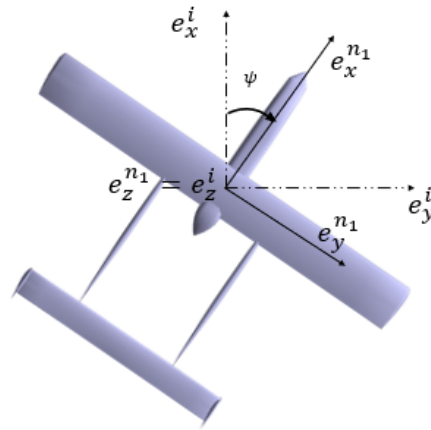
Body-axes system to wind-axes system.

To characterize the orientation of the aerodynamic reference frame \mathcal{F}^w relative to the body reference frame $\mathcal{F}^{\mathcal{B}}$, a sequence of partial Eulerian rotations is also considered. However, in this case, only two rotations are sufficient, as the \mathbf{z}^w -axis is, by definition, confined to the $\mathbf{x}^b \mathbf{z}^b$ plane of symmetry, reducing the number of independent parameters needed to define the rotation. These angles are α and β , and the sequence of rotations is defined by:

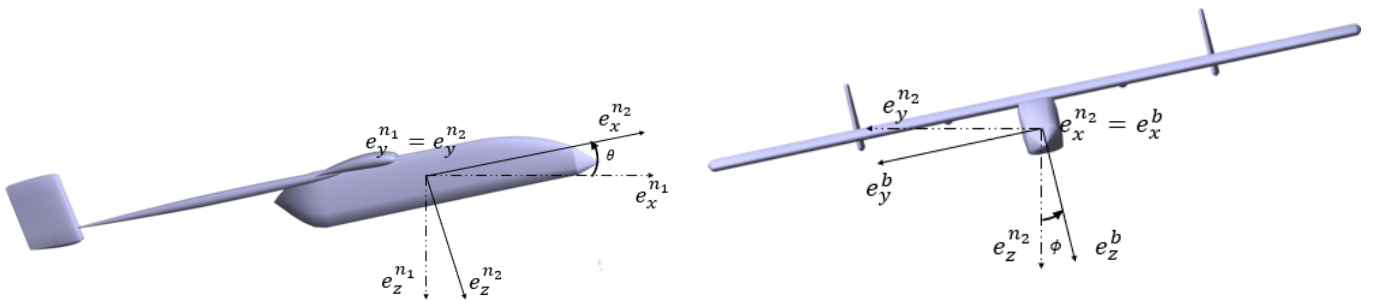
1. rotation about \mathbf{e}_y^b , second axis of body reference, by an angle $(-\alpha)$, with $\alpha \in [-\pi, \pi)$.
2. rotation about \mathbf{e}_z^w , third axis of the arrival triad, by an angle $\beta \in [-\pi/2, \pi/2)$.

This set of sequential rotations could be also interpreted as a first coordinate transformation from $\mathcal{F}^{\mathcal{B}}$ to $\mathcal{F}^{\mathcal{S}}$, with a rotation matrix $\mathcal{R}_{\mathcal{B}}^{\mathcal{S}}(\alpha)$, and a second transformation from $\mathcal{F}^{\mathcal{S}}$ to \mathcal{F}^w with rotation matrix $\mathcal{R}_{\mathcal{S}}^w(\beta)$. Formally:

$$\mathcal{R}_{\mathcal{B}}^w(\alpha, \beta) = \mathcal{R}_{\mathcal{S}}^w(\beta)\mathcal{R}_{\mathcal{B}}^{\mathcal{S}}(\alpha) = \begin{bmatrix} \cos \beta \cos \alpha & \sin \beta & \cos \beta \sin \alpha \\ -\sin \beta \cos \alpha & \cos \beta & -\sin \beta \sin \alpha \\ -\sin \alpha & 0 & \cos \alpha \end{bmatrix} . \quad (1.23)$$



(a) From \mathcal{F}^I to \mathcal{F}^{n_1}



(b) From \mathcal{F}^{n_1} to \mathcal{F}^{n_2}

(c) From \mathcal{F}^{n_2} to \mathcal{F}^B

Figure 1.5: Sequential rotation from \mathcal{F}^I to \mathcal{F}^B

The matrix obtained represents the direction cosine matrix for the transformation from coordinates expressed in \mathcal{F}^B to coordinates in \mathcal{F}^W . It can be interpreted as a matrix with columns containing the scalar components of the unit vectors of the \mathcal{F}^B frame expressed in the \mathcal{F}^W reference frame or with rows containing the scalar components of the unit vectors of the \mathcal{F}^W expressed in components of \mathcal{F}^B reference frame.

1.1.5. Wind triangle

When considering small to medium-scale UAVs, it becomes evident that wind significantly impacts their airspeed. Given that aerodynamic forces and moments inherently rely on

airspeed, the presence of wind becomes a crucial factor that demands careful consideration in flight dynamic modeling. The definitions of various flight mechanics quantities, as discussed earlier, serve as valuable tools in establishing the interrelations between essential vectors, such as the airspeed vector \mathbf{V} , the wind speed \mathbf{V}_w , and the ground speed \mathbf{V}_G . These vectors are related by the equation:

$$\mathbf{V} = \mathbf{V}_G - \mathbf{V}_w . \quad (1.24)$$

By means of the rotations governing the transition between the considered reference frames, we can express the following relationships:

$$\mathbf{V}_G^{\mathcal{B}} = \mathbf{v}_{CG/\mathcal{I}}^{\mathcal{B}} = \begin{bmatrix} U \\ V \\ W \end{bmatrix} = \mathcal{R}_{\mathcal{I}}^{\mathcal{B}}(\phi, \theta, \psi) \begin{bmatrix} V_N \\ V_E \\ V_D \end{bmatrix} . \quad (1.25)$$

In Equation (1.25), the notation $\mathbf{v}_{CG/\mathcal{I}}^{\mathcal{B}}$, is used to point out the ground speed as the aircraft center of gravity velocity with respect to the inertial system, expressed in body-axes components.

The same reasoning applies to the definition of wind components in body axes.

$$\mathbf{V}_w^{\mathcal{B}} = \mathbf{v}_{w/\mathcal{I}}^{\mathcal{B}} = \begin{bmatrix} U_w \\ V_w \\ W_w \end{bmatrix} = \mathcal{R}_{\mathcal{I}}^{\mathcal{B}}(\phi, \theta, \psi) \begin{bmatrix} V_{wN} \\ V_{wE} \\ V_{wD} \end{bmatrix} , \quad (1.26)$$

with *Inertial system to body-axes* rotation applied to the wind vector measured in ground components.

Recalling Equation (1.24) and Equation (1.18), we can state that, the airspeed vector \mathbf{V} , expressed in body components is:

$$\mathbf{V}^{\mathcal{B}} = \begin{bmatrix} U - U_w \\ V - V_w \\ W - W_w \end{bmatrix} = \begin{bmatrix} U_r \\ V_r \\ W_r \end{bmatrix} = \mathcal{R}_{\mathcal{W}}^{\mathcal{B}}(\alpha, \beta) \begin{bmatrix} V \\ 0 \\ 0 \end{bmatrix} = V \begin{bmatrix} \cos \alpha \cos \beta \\ \sin \beta \\ \sin \alpha \cos \beta \end{bmatrix} . \quad (1.27)$$

Equation (1.27) allows us to formalize how $\mathbf{v}_{CG/\mathcal{I}}^{\mathcal{B}}$ is equivalent to airspeed only in the case of still air, while more generally the modulus of airspeed expressed in body components is described by:

$$\mathbf{V}^{\mathcal{B}} = \sqrt{U_r^2 + V_r^2 + W_r^2} , \quad (1.28)$$

and, solving for α and β , we have:

$$\alpha = \tan^{-1} \left(\frac{W_r}{U_r} \right), \quad \beta = \sin^{-1} \left(\frac{V_r}{\sqrt{U_r^2 + V_r^2 + W_r^2}} \right), \quad (1.29)$$

which recall exactly the aerodynamic angles definitions provided in Section 1.1.2. Figure 1.6 relates flight mechanics quantities discussed so far in the context of a flight condition under wind disturbance.

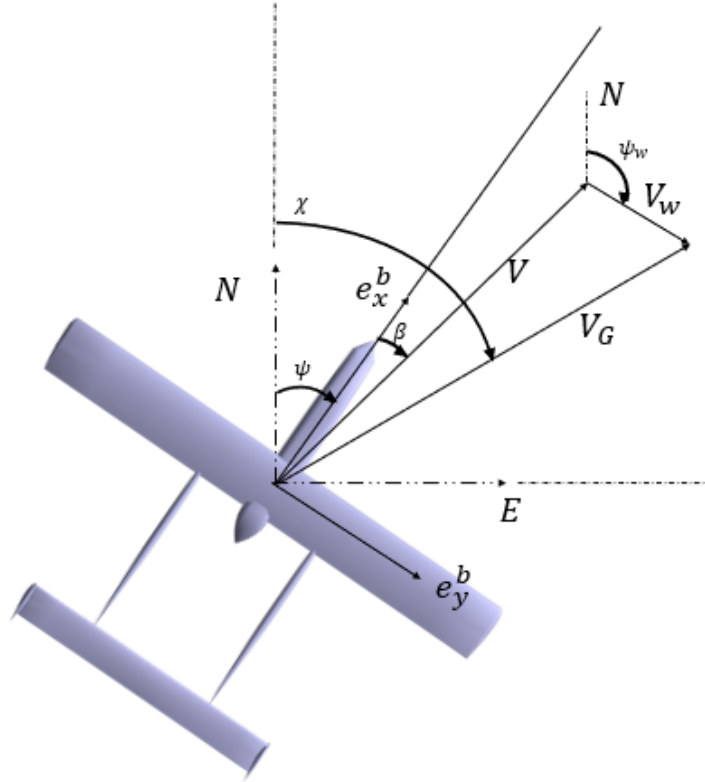


Figure 1.6: The wind triangle

1.2. Kinematics

The three-dimensionality of the problem necessitates defining velocities at every point on the aircraft using the concept of rigid body motion.

$$\mathbf{V}_Q = \mathbf{V}_P + \boldsymbol{\omega} \times (\mathbf{Q} - \mathbf{P}). \quad (1.30)$$

In the case of rigid body motion, two vector quantities (or six scalar quantities in space) are considered. These are the linear velocity of a point \mathbf{P} , such as the one at the origin of

the mobile frame, and the angular velocity ω , which is a vector enabling the expression of the derivatives of the mobile frame unit vectors according to Poisson's formulas:

$$\dot{e}_x^b = \omega \times e_x^b, \quad (1.31)$$

$$\dot{e}_y^b = \omega \times e_y^b, \quad (1.32)$$

$$\dot{e}_z^b = \omega \times e_z^b. \quad (1.33)$$

Given Equation (1.30), also known as the rule of velocity transport, it is possible to characterize the airspeed about any generic point \mathbf{Q} fixed on the aircraft as a function of the translational velocity, typically referred to the origin of the moving frame with respect to the inertial system, and a rotational velocity ω . The airspeed vector and all the associated characteristics previously described conveniently referred to a significant material point, which is the aircraft's center of gravity \mathbf{CG} .

The scalar components of the angular velocity ω , measured in body-axes system are referred to as (p, q, r) namely *roll rate*, *pitch rate*, *yaw rate*:

$$\omega_{\mathcal{B}/\mathcal{I}}^{\mathcal{B}} = \begin{bmatrix} p \\ q \\ r \end{bmatrix} = \omega \cdot \begin{bmatrix} e_x^b \\ e_y^b \\ e_z^b \end{bmatrix}. \quad (1.34)$$

Also in this case, the notation $\omega_{\mathcal{B}/\mathcal{I}}^{\mathcal{B}}$, stands for defining the rotational velocity vector of the body triad with respect to the inertial reference, measured in the body reference.

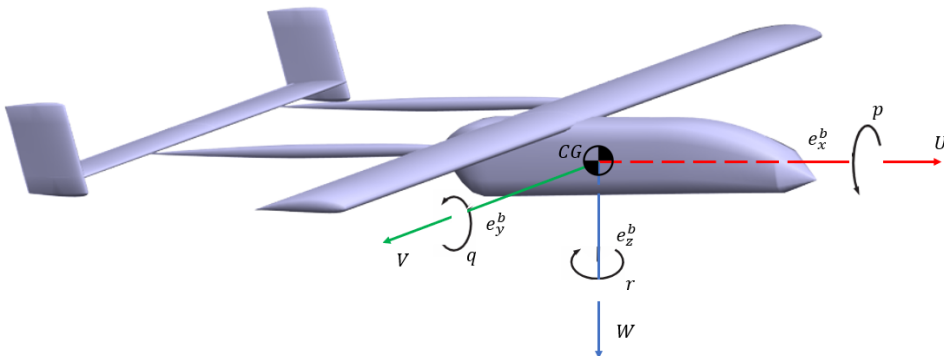


Figure 1.7: Body-axes components of translational and angular velocities.

As the angular velocity is related to the derivatives of the mobile frame unit vectors, we can express its components in the body frame using direction cosines and their derivatives.

Consequently, we can utilize expressions involving the Cardan angles (ϕ, θ, ψ) . Given the definition of Cardan angles and the additivity of angular velocities from partial motions, we can assume that the aircraft's angular velocity is composed of the following rotational motions:

1. Azimuthal rotation with intensity $\dot{\psi}$ around z^i -axis.
2. Elevation motion with intensity $\dot{\theta}$ around y^{n_1} -axis, second axis of intermediate triad.
3. Rotation motion with intensity $\dot{\phi}$ around x^b .

Therefore:

$$\omega = \dot{\phi}\mathbf{e}_x^b + \dot{\theta}\mathbf{e}_y^{n_1} + \dot{\psi}\mathbf{e}_z^i. \quad (1.35)$$

To determine the components in \mathcal{F}^B , we need to express the unit vectors of inertial triad and intermediate triad, in body components:

$$\mathbf{e}_z^i = -\sin\theta\mathbf{e}_x^b + \cos\theta\sin\phi\mathbf{e}_y^b + \cos\theta\cos\phi\mathbf{e}_z^b \quad (1.36)$$

$$\mathbf{e}_y^{n_1} = \cos\phi\mathbf{e}_y^b - \sin\phi\mathbf{e}_z^b, \quad (1.37)$$

which results in the following:

$$\begin{aligned} \omega &= \dot{\phi}\mathbf{e}_x^b + \dot{\theta}(c_\phi\mathbf{e}_y^b - s_\phi\mathbf{e}_z^b) + \dot{\psi}(-s_\theta\mathbf{e}_x^b + c_\theta s_\phi\mathbf{e}_y^b + c_\theta c_\phi\mathbf{e}_z^b) \\ &= (\dot{\phi} - \dot{\psi}s_\theta)\mathbf{e}_x^b + (\dot{\psi}c_\theta s_\phi + \dot{\theta}c_\phi)\mathbf{e}_y^b + (\dot{\psi}c_\theta c_\phi - \dot{\theta}s_\phi)\mathbf{e}_z^b, \end{aligned} \quad (1.38)$$

from which we immediately derive the expressions for the roll pitch and yaw rates:

$$\begin{aligned} p &= \dot{\phi} - \dot{\psi}\sin\theta, \\ q &= \dot{\psi}\cos\theta\sin\phi + \dot{\theta}\cos\phi, \\ r &= \dot{\psi}\cos\theta\cos\phi - \dot{\theta}\sin\phi. \end{aligned} \quad (1.39)$$

in matrix form, highlighting the sequential rotation through the rotation matrices:

$$\begin{bmatrix} p \\ q \\ r \end{bmatrix} = \begin{bmatrix} \dot{\phi} \\ 0 \\ 0 \end{bmatrix} + \mathcal{R}_{n_2}^B(\phi) \begin{bmatrix} 0 \\ \dot{\theta} \\ 0 \end{bmatrix} + \mathcal{R}_{n_2}^B(\phi)\mathcal{R}_{n_1}^{n_2}(\theta) \begin{bmatrix} 0 \\ 0 \\ \dot{\psi} \end{bmatrix}, \quad (1.40)$$

which gives:

$$\begin{bmatrix} p \\ q \\ r \end{bmatrix} = \begin{bmatrix} 1 & 0 & -\sin\theta \\ 0 & \cos\phi & \sin\phi\cos\theta \\ 0 & -\sin\phi & \cos\phi\cos\theta \end{bmatrix} \begin{bmatrix} \dot{\phi} \\ \dot{\theta} \\ \dot{\psi} \end{bmatrix}. \quad (1.41)$$

Even though $(\dot{\phi}, \dot{\theta}, \dot{\psi})$ are not mutually orthogonal, the matrix that relates the body-axis rates to the rates of Euler angles can still be inverted, allowing us to establish the inverse kinematic relation.

$$\begin{bmatrix} \dot{\phi} \\ \dot{\theta} \\ \dot{\psi} \end{bmatrix} = \begin{bmatrix} 1 & \sin \phi \tan \theta & \cos \phi \tan \theta \\ 0 & \cos \phi & -\sin \phi \\ 0 & \sin \phi / \cos \theta & \cos \phi / \cos \theta \end{bmatrix} \begin{bmatrix} p \\ q \\ r \end{bmatrix}. \quad (1.42)$$

Equation (1.42) reveals a significant aspect of the Euler angles representation of the attitude, highlighting a mathematical singularity occurring when $\theta = \pi/2$. In this scenario, the yaw angle ψ is undefined, leading to what is commonly known as gimbal lock. This situation can cause challenges in accurately representing the orientation of the aircraft, particularly when rotations are close to the singularity. However, for the considered case scenario encountering gimbal lock is improbable since, under normal flight conditions, the pitch angle θ is usually small. This inherent constraint helps ensure that the UAV's orientation remains well-defined, allowing for stable and predictable behavior during flight operations.

1.3. Rigid Body Dynamics

The dynamics equations that will be briefly discussed in this section, represent the dynamic equilibrium of translation and rotation around the aircraft center of gravity, with respect to inertial frame \mathcal{F}^I . We resume the kinematic quantities required to describe the aircraft's rigid body motion, namely \mathbf{v}_{CG} describing the CG position rate of change in \mathcal{F}^I , and $\boldsymbol{\omega}_{B/I}$ as the angular velocity of body triad also referred to \mathcal{F}^I , collecting them within a single vector.

$$\mathbf{w}_{CG} = \{\mathbf{v}_{CG}, \boldsymbol{\omega}_{B/I}\}^T. \quad (1.43)$$

The dynamic equilibrium can be expressed by means of the generalized balance equation:

$$\mathbf{M}_{CG} \dot{\mathbf{w}}_{CG} + \mathbf{w}_{CG} \times \mathbf{M}_{CG} \mathbf{w}_{CG} = \mathbf{r}_{CG}, \quad (1.44)$$

where, in Equation (1.44), \mathbf{M}_{CG} , represent the generalized inertia matrix wrapping inside the static moment tensor \mathbf{S}_{CG} , and the inertia tensor \mathbf{J}_{CG} with respect to point \mathbf{CG} , thus yielding:

$$\mathbf{M}_{CG} = \begin{bmatrix} m\mathbf{I} & \mathbf{S}_{CG} \\ \mathbf{S}_{CG} & \mathbf{J}_{CG} \end{bmatrix}. \quad (1.45)$$

The term $\mathbf{w}_{CG} \times$ represents the generalized velocity vector with the southwest cross product operator applied. This operator rearranges the subvectors \mathbf{v}_{CG} and $\boldsymbol{\omega}_{B/I}$ in a [6x6] dimension matrix, filling it with their skew forms, i.e. $\mathbf{v}_{CG \times}$ and $\boldsymbol{\omega}_{B/I \times}$ as the [3x3] anti-symmetric matrices composed with respective subvectors components. More explicitly:

$$\mathbf{w}_{CG} \times = \begin{bmatrix} \boldsymbol{\omega}_{B/I \times} & 0_{[3 \times 3]} \\ \mathbf{v}_{CG} & \boldsymbol{\omega}_{B/I \times} \end{bmatrix} \quad (1.46)$$

The right-hand side term r_{CG} represent the generalized forcing term collecting together aerodynamic, propulsive, and gravitational forces and moments, formally:

$$\mathbf{r}_{CG} = \left\{ \begin{array}{c} f_a + f_p + f_g \\ m_{a_{CG}} + m_{p_{CG}} + m_{g_{CG}} \end{array} \right\} . \quad (1.47)$$

Adopting the CG as reference point for \mathcal{F}^B allows some simplifications to be applied to the equations 1.44, such as the cancellation of static moments and gravitational force moment, enabling the possibility to easily decouple the generalized balance equation, resulting in two equivalent vector equations:

$$m (\dot{\mathbf{v}}_{CG} + \boldsymbol{\omega}_{B/I} \times \mathbf{v}_{CG}) = f_a + f_p + f_g , \quad (1.48)$$

$$\mathbf{J}_{CG} \dot{\boldsymbol{\omega}}_{B/I} + \boldsymbol{\omega}_{B/I} \times \mathbf{J}_{CG} \boldsymbol{\omega}_{B/I} = m_{a_{CG}} + m_{p_{CG}} . \quad (1.49)$$

1.3.1. Inertia Tensor

To exploit the inertial symmetry properties of the aircraft, we carry the generalized equation into the body reference frame. At this point, the inertia tensor is expressed in the following form:

$$\mathbf{J}_{CG}^B = \begin{bmatrix} J_{xx} & 0 & -J_{xz} \\ 0 & J_{yy} & 0 \\ -J_{xz} & 0 & J_{zz} \end{bmatrix} , \quad (1.50)$$

where $J_{xx} = \int_{V_B} \delta m (y_b^2 + z_b^2)$ represent the inertia with respect to longitudinal axis, $J_{yy} = \int_{V_B} \delta m (x_b^2 + z_b^2)$ similar to the latter but referred to pitch axis, and $J_{zz} = \int_{V_B} \delta m (x_b^2 + y_b^2)$, inertial term referred to yaw axis, typically rather small. $J_{xz} = \int_{V_B} \delta m (x_b z_b)$ provide a measure of the aircraft symmetry in planes spanned by $x^b y^b$ and $z^b y^b$, while since aircraft are commonly symmetric about the plane spanned by x^b and z^b , we let $J_{yz} = J_{xy} = 0$

1.3.2. Aerodynamic Forcing Terms

In its standard configuration, the aircraft is controlled by deflecting movable surfaces. These adjustments alter the flow field around the vehicle, giving rise to aerodynamic forces that in turn modify its orientation. The aileron deflection δ_a govern the roll rate p , the elevator deflection δ_e manages the pitch rate q , and the rudder deflection δ_r , controls the yaw rate r , according to the convention reported in Figure 1.8.

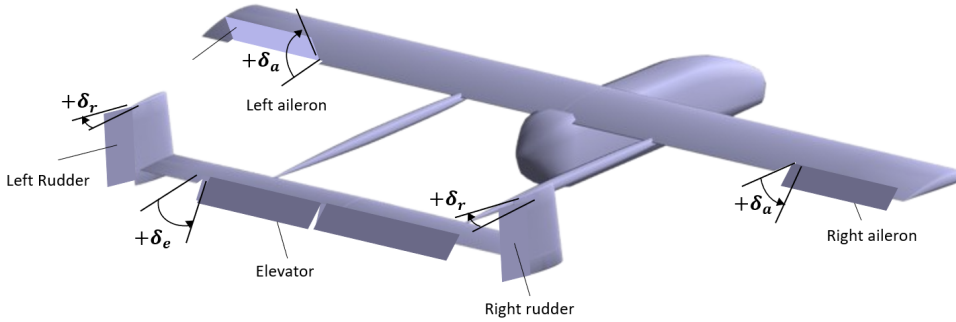


Figure 1.8: Aerodynamic control surfaces deflections.

Let us now enter a more in-depth description of aerodynamic forces and moments, distinguishing for convenience between those acting in the longitudinal plane and those acting in the lateral-directional plane, and recalling the general model description adopted for each aerodynamic forcing term, which is expressed through a linear breakdown with respect to generalized state \mathbf{w}_{CG} , aerodynamic controls, and the non-dimensional parameters Mach and Reynolds.

Longitudinal aerodynamics The forces and moment acting on the plane spanned by x^b and z^b are: *Lift*, *Drag* and *Pitch moment*; their definitions are respectively:

$$L = \frac{1}{2}\rho V^2 S C_L(\alpha, \dot{\alpha}, q, \delta_e, Ma, Re) , \quad (1.51)$$

$$D = \frac{1}{2}\rho V^2 S C_D(\alpha, \dot{\alpha}, q, \delta_e, Ma, Re) , \quad (1.52)$$

$$\mathcal{M} = \frac{1}{2}\rho V^3 S c C_M(\alpha, \dot{\alpha}, q, \delta_e, Ma, Re) , \quad (1.53)$$

where ρ is the local air density, V is the airspeed, c is the wing mean-chord, S is the wing planform surface C_L, C_D, C_M represent non-dimensional forces and moment coefficients which depend on the angle of attack α , and its derivative $\dot{\alpha}$, on pitch rate q and on elevator control deflection δ_e . For the restricted flight regimes in terms of speed and altitude to which the aircraft will be subjected, it is deemed an acceptable approximation to neglect

the dependence on the Mach Ma and Reynolds Re dimensionless parameters.

The explicit dependency can be approximated with a first-order Taylor series expansion:

$$C_L(\alpha, \dot{\alpha}, q, \delta_e) = \left[C_{L_0} + \frac{\partial C_L}{\partial \alpha} \alpha + \frac{\partial C_L}{\partial \dot{\alpha}} \dot{\alpha} + \frac{\partial C_L}{\partial q} q + \frac{\partial C_L}{\partial \delta_e} \delta_e \right]. \quad (1.54)$$

In the aforementioned expression, it is noteworthy to underscore that despite variables α and $\dot{\alpha}$ may not be explicitly encompassed within the vector of generalized states, their interrelation with said vector is established through body-axis velocity components. In particular, reference is made to Equation (1.29) regarding α , while $\dot{\alpha}$ is computed as follows:

$$\dot{\alpha} = \frac{\dot{W}U - \dot{U}W}{U^2 + W^2}. \quad (1.55)$$

Equation (1.54) can be restated in a more compact form, and concurrently normalizing the third and fourth terms, such that:

$$\hat{\alpha} = \frac{\dot{\alpha}c}{2U}, \quad \hat{q} = \frac{qc}{2U}. \quad (1.56)$$

At this point, Equation (1.54) now becomes:

$$C_L(\alpha, \hat{\alpha}, \hat{q}, \delta_e) = \left[C_{L_0} + C_{L_\alpha} \alpha + C_{L_{\hat{\alpha}}} \hat{\alpha} + C_{L_{\hat{q}}} \hat{q} + C_{L_{\delta_e}} \delta_e \right]. \quad (1.57)$$

The Equation (1.57) embodies the linear decomposition of the lift coefficient, where the influence of current states is weighted by stability derivatives, defined within the stability axes system, and the contribution of aerodynamic control state, proportionately influenced by its corresponding control derivative, also defined in the stability axes \mathcal{F}^S .

Contextually, drag force and pitching moment coefficients are expressed as follows:

$$C_D(\alpha, \hat{\alpha}, \hat{q}, \delta_e) = \left[C_{D_0} + C_{D_\alpha} \alpha + C_{D_{\hat{\alpha}}} \hat{\alpha} + C_{D_{\hat{q}}} \hat{q} + C_{D_{\delta_e}} \delta_e \right], \quad (1.58)$$

$$C_M(\alpha, \hat{\alpha}, \hat{q}, \delta_e) = \left[C_{M_0} + C_{M_\alpha} \alpha + C_{M_{\hat{\alpha}}} \hat{\alpha} + C_{M_{\hat{q}}} \hat{q} + C_{M_{\delta_e}} \delta_e \right]. \quad (1.59)$$

We have thus derived the formulation of the forces and moment, defined in stability axes, acting within the aircraft's symmetry plane. While the pitching moment, defined around the y^s axis, which aligns with the y^b axis, requires no transformation, lift and drag forces must be brought onto the body reference frame:

$$\begin{bmatrix} X \\ 0 \\ Z \end{bmatrix} = \mathcal{R}_S^B(\alpha) \begin{bmatrix} -D \\ 0 \\ -L \end{bmatrix}. \quad (1.60)$$

The negative sign is explained by the conventional definition of lift and drag forces, which are inverted with respect to x^s and z^s axes for a positive angle of attack.

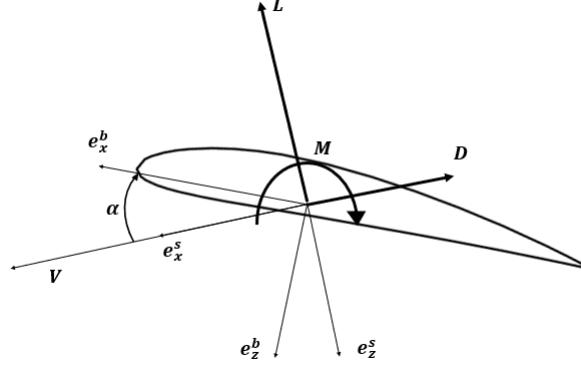


Figure 1.9: Lift and drag forces direction for a positive α .

Lateral-directional aerodynamics Similarly, for the lateral-directional case we define: the side force Y , and the roll and yaw moments, respectively \mathcal{L} , and \mathcal{N} . These terms are mainly influenced by β , and its derivative $\dot{\beta}$, p , r , δ_a and δ_r . The analytic expression for $\dot{\beta}$ is here provided:

$$\dot{\beta} = \frac{1}{\sqrt{1 - \left(\frac{V}{U^2 + V^2 + W^2}\right)^2}} \left(\dot{V} (U^2 + V^2 + W^2) \right) - 2 \frac{(U\dot{U} + V\dot{V} + W\dot{W})}{(U^2 + V^2 + W^2)^2} . \quad (1.61)$$

The forcing terms for lateral-directional aerodynamics are summarized in following equations:

$$Y = \frac{1}{2} \rho V^2 S C_Y \left(\beta, \dot{\beta}, p, r, \delta_a, \delta_r, Ma, Re \right) , \quad (1.62)$$

$$\mathcal{L} = \frac{1}{2} \rho V^3 S b C_{\mathcal{L}} \left(\beta, \dot{\beta}, p, r, \delta_a, \delta_r, Ma, Re \right) , \quad (1.63)$$

$$\mathcal{N} = \frac{1}{2} \rho V^3 S b C_{\mathcal{N}} \left(\beta, \dot{\beta}, p, r, \delta_a, \delta_r, Ma, Re \right) . \quad (1.64)$$

For the same reasons provided before, it is possible to neglect the dependence on Ma and Re . Additionally, also in this case, it is affordable to normalize the non-dimensional coefficients expression with respect $\dot{\beta}$, p and r , scaling them by wing span b , such that:

$$\hat{\beta} = \frac{\dot{\beta} b}{2U^2}, \quad \hat{p} = \frac{pb}{2U^2}, \quad \hat{r} = \frac{rb}{2U^2} . \quad (1.65)$$

The first-order Tylor series for non-dimensional coefficients C_Y, C_l and C_N are:

$$\begin{aligned} C_Y \left(\beta, \hat{\beta}, \hat{p}, \hat{r}, \delta_a, \delta_r \right) &= \left[C_{Y_0} + C_{Y_\beta} \beta + C_{Y_{\hat{\beta}}} \hat{\beta} + C_{Y_{\hat{p}}} \hat{p} + C_{Y_{\hat{r}}} \hat{r} + C_{Y_{\delta_a}} \delta_a + C_{Y_{\delta_r}} \delta_r \right] \\ C_L \left(\beta, \hat{\beta}, \hat{p}, \hat{r}, \delta_a, \delta_r \right) &= \left[C_{L_0} + C_{L_\beta} \beta + C_{L_{\hat{\beta}}} \hat{\beta} + C_{L_{\hat{p}}} \hat{p} + C_{L_{\hat{r}}} \hat{r} + C_{L_{\delta_a}} \delta_a + C_{L_{\delta_r}} \delta_r \right] \\ C_N \left(\beta, \hat{\beta}, \hat{p}, \hat{r}, \delta_a, \delta_r \right) &= \left[C_{N_0} + C_{N_\beta} \beta + C_{N_{\hat{\beta}}} \hat{\beta} + C_{N_{\hat{p}}} \hat{p} + C_{N_{\hat{r}}} \hat{r} + C_{N_{\delta_a}} \delta_a + C_{N_{\delta_r}} \delta_r \right] . \end{aligned}$$

Within previous expressions, current states and controls are proportionally weighted with their respective stability and control derivatives.

1.3.3. Propulsive Forcing Terms

The management of propulsive forcing terms has been meticulously devised to ensure an accurate representation of propulsion-related forces and moments at any designated measurement point. This approach takes into account factors such as the number of thrusters, their responsiveness concerning flight speed and air density, as well as their spatial configuration and alignment relative to the body reference frame.

The general expression for Thrusters forces and moments is given in Equation (1.67).

$$f_p^{\mathcal{B}} = f^p(\delta_t, \sigma_i, \gamma_i) = \sum_{i=1}^{N_t} T_i \left[\cos \sigma_i \cos \gamma_i, \sin \sigma_i, \cos \sigma_i \sin \gamma_i \right]^T, \quad (1.66)$$

$$m_{pCG}^{\mathcal{B}} = m^p(\delta_t, \sigma_i, \gamma_i, \mathbf{r}_{TP}^{\mathcal{B}}) = \sum_{i=1}^{N_t} T_i \left(\mathbf{r}_{TP}^{\mathcal{B}} \times \left[\cos \sigma_i \cos \gamma_i, \sin \sigma_i, \cos \sigma_i \sin \gamma_i \right]^T \right) \quad (1.67)$$

Here, $\mathbf{r}_{TP}^{\mathcal{B}}$ represents the positional vector originating from the center of gravity \mathbf{CG} and extending towards the point of application of thrust force T_i exerted by the i -th thruster. The angle σ_i gauges the misalignment between the aircraft's vertical plane of symmetry and the thrust line of the i -th thruster. Meanwhile, the angle γ_i defines the angle included between the projection of the i -th thruster thrust line onto the vertical plane of symmetry and the x^b -axis.

Thrust intensity T_i , is expressed as a function of throttle setting δ_t as follows:

$$T_i = \tilde{T}_i K(\delta_t) \delta_t, \quad (1.68)$$

where \tilde{T}_i is the nominal thrust intensity of i -th thruster, measured at sea level. The throttle setting δ_t operates by modulating the nominal value by means of the shaping function $K(\delta_t)$. This function is designed to replicate potential efficiency variations associated with different operational regimes (e.g. airspeed and altitude) or nonlinear characteristics

specific to the particular thruster technology in use. Moreover, the permissible range of δ_t values can differ based on the employed thruster technology. For instance, in the case of a piston engine, this control could be constrained to positive values only, ranging from 0% to 100%. However, for electric motors, the range might extend to include negative values, thereby enabling a reversal thrust force. This feature leverages a well-established advantage associated with these types of thrusters compared to conventional piston-powered alternatives.

1.3.4. Gravitational Forcing Term

The gravity forcing term is simply defined as function of mass m and aircraft attitude angles $\{\phi, \theta, \psi\}$. The effect is described as a force acting in the z^i -axis direction at the aircraft's center of gravity.

$$f_g^{\mathcal{B}} = f_g^{\mathcal{B}}(m, \phi, \theta, \psi) = \mathcal{R}_{\mathcal{I}}^{\mathcal{B}}(\phi, \theta, \psi) \begin{bmatrix} 0 \\ 0 \\ mg \end{bmatrix} . \quad (1.69)$$

1.4. Scalar Equations of Motion

Referring back to equations Equation (1.48) and 1.49, and having explicitly accounted for the forcing terms expressed in the body reference frame, we can now proceed to write the balance equations in scalar form. Therefore, we derive three equations for translational motion (moment balance) and an additional three equations for rotational motion (moment of momentum balance). To enhance notational simplicity, propulsive forces are collected within vector \mathbf{T} , whereas, associated moments are collected within vector $\mathbf{\Gamma}$.

$$m \left(\dot{U} + (Wq - Vr) \right) = X - mg \sin \theta + T_x , \quad (1.70a)$$

$$m \left(\dot{V} + (Ur - Wp) \right) = Y + mg \cos \theta \sin \phi + T_y , \quad (1.70b)$$

$$m \left(\dot{W} + (Vp - Uq) \right) = Z + mg \cos \theta \cos \phi + T_z . \quad (1.70c)$$

$$J_x \dot{p} - J_{xz} (\dot{r} - pq) + (J_z - J_y) rq = \mathcal{L} + \Gamma_x , \quad (1.71a)$$

$$J_y \dot{q} - J_{xz} (r^2 - p^2) + (J_x - J_z) pr = \mathcal{M} + \Gamma_y , \quad (1.71b)$$

$$J_z \dot{r} - J_{xz} (\dot{p} - qr) + (J_y - J_x) pq = \mathcal{N} + \Gamma_z . \quad (1.71c)$$

We have thereby obtained six scalar equations involving nine unknowns $\{U, V, W, p, q, r, \phi, \theta, \psi\}$. Consequently, it is essential to incorporate an additional set of three equations to achieve

the matching condition. These equations, by referring to Equation (1.42), will encompass the kinematic relationships that link the Euler angles derivatives with the body angular rates $\{p, q, r\}$ t, which, written out explicitly in scalar form give:

$$\dot{\phi} = p + \sin \phi \tan \theta q + \cos \phi \tan \theta r , \quad (1.72a)$$

$$\dot{\theta} = \cos \phi q - \sin \phi r , \quad (1.72b)$$

$$\dot{\psi} = \sin \phi \sec \theta q + \cos \phi \sec \theta r . \quad (1.72c)$$

Lastly, by employing rotation matrix $\mathcal{R}_{\mathcal{I}}^{\mathcal{B}^T}(\phi, \theta, \psi)$ it is affordable to incorporate an additional set of three interdependent equations aimed at determining the rate of change of the aircraft's inertial position for navigation purposes.

$$\dot{P}_N = c_\theta c_\psi U + (s_\psi s_\theta c_\psi - c_\phi s_\psi) V + (c_\phi s_\theta c_\psi + s_\phi s_\psi) W , \quad (1.73a)$$

$$\dot{P}_E = c_\theta s_\psi U + (s_\phi s_\theta s_\psi + c_\phi c_\psi) V + (c_\psi s_\theta s_\psi - s_\phi c_\psi) W , \quad (1.73b)$$

$$\dot{P}_D = -s_\theta U + s_\phi c_\theta V + c_\phi c_\theta W . \quad (1.73c)$$

The set of 12 equations presented in this section is encompassed within the *GeneralizedRate* subroutine. In this subroutine, these equations are built up based on flight condition data, aircraft current state, and control inputs, to determine the aerodynamic and propulsive forces and moments. Within a broader function designed as an interface to manage aircraft-utilizable data and to impose specific control law, the *GeneralizedRate* subroutine is fed to "ode45" for integration.

1.5. Testbed Aircraft

In the present research, the testbed considered as a constituting unit within the swarm has been selected as a small reconnaissance drone, the AAI RQ-2 Pioneer (see Figure 1.10), featuring a compact size, good maneuverability, and a conventional configuration, easy to capture with good accuracy without deploying highly sophisticated aerodynamic models. The AAI RQ-2 Pioneer, developed by AAI Corporation (now Textron Systems), emerged as a pivotal platform in the evolution of UAVs. Initially introduced in the 1980s, the RQ-2 Pioneer was designed as a surveillance and reconnaissance vehicle for the United States Navy. Its innovative features, such as a modular payload bay, autonomous flight capabilities, and real-time data transmission, set the stage for subsequent UAV advancements.

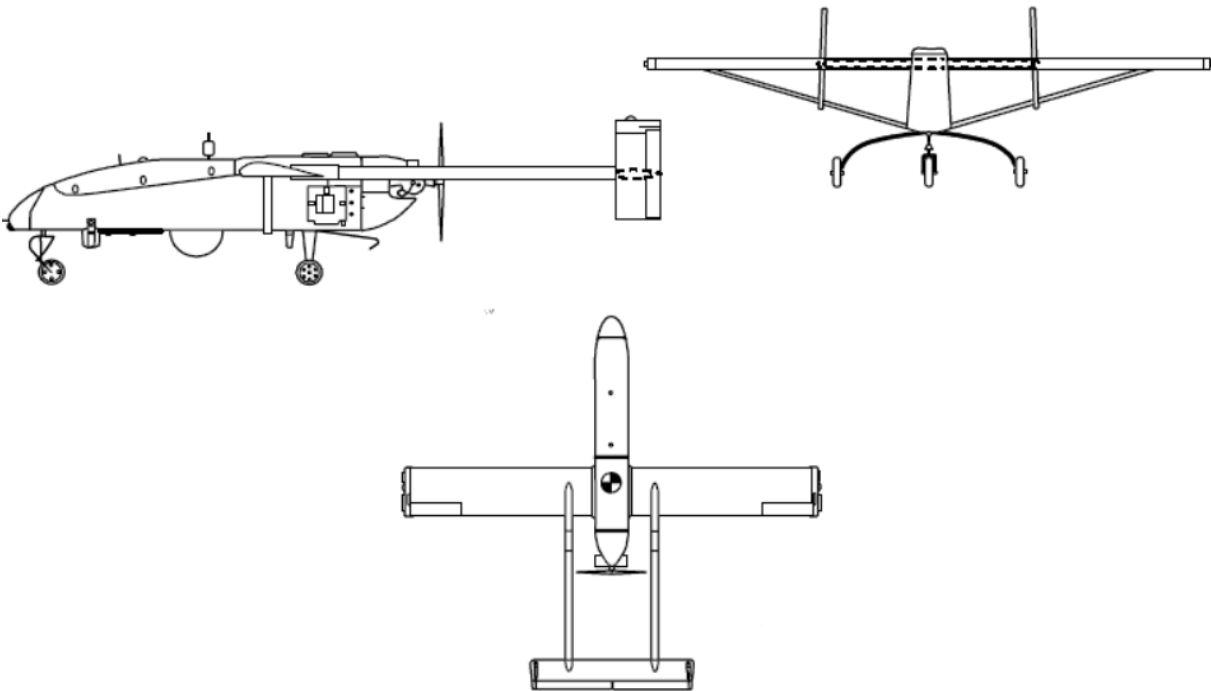


Figure 1.10: AAI RQ-2 Pioneer 2D views.

Several factors contribute to the selection of the AAI RQ-2 Pioneer as the testbed for studying UAV swarms:

- **Historical Significance:** The RQ-2 Pioneer played a pivotal role in shaping the UAV landscape, making it an apt choice for historical context and comparative analysis against modern UAVs.
- **Platform Capabilities:** The modular design and autonomous flight capabilities of the Pioneer facilitate the integration of modern control algorithms and swarm communication protocols, enabling comprehensive swarm behavior studies.
- **Accessible Data:** With a wealth of historical data available, it is feasible to conduct retrospective analyses and draw insights to inform swarm deployment strategies and decision-making processes.
- **Avionics and system simplicity:** Pioneer's relatively simpler avionics and control systems offer an advantageous platform for implementing experimental swarm algorithms, allowing to focus on the nuances of swarm behavior without excessive complexity.
- **Technology Transition:** Exploring swarm behavior on a platform like the Pioneer can bridge the gap between legacy UAV technology and cutting-edge swarm

research, potentially leading to practical applications in various sectors.

1.5.1. General Characteristics

In order to comprehensively understand the technical attributes of the AAI RQ-2 Pioneer Unmanned Aerial Vehicle (UAV), a detailed overview of its essential specifications is provided in Table 1.1.

Specification	Value
Wingspan	5.79 m (19 ft)
Length	5.13 m (16 ft 10 in)
Height	1.12 m (3 ft 8 in)
Empty Weight	170 kg (375 lb)
MTOW	260 kg (573 lb)
Fuel Capacity	80 liters (21 gallons)
Engine	One two-stroke piston engine
Engine Power Output	35-40 hp (26-29 kW)
Maximum Speed	220 km/h (137 mph)
Cruising Speed	130-160 km/h (80-100 mph)
Endurance	Up to 5 hours
Range	250-300 km (155-186 miles)
Service Ceiling	3,000 m (9,800 ft)
Absolute Ceiling	5,000 m (16,400 ft)
Payload Capacity	Varies with mission
Control System	Manual remote control
Launch and Recovery Method	Catapult launch, net-based recovery
Communication	Line-of-Sight (LOS) radio communication

Table 1.1: General Characteristics of the AAI RQ-2 Pioneer UAV.

1.5.2. Dimension Specification

Moving forward, a more specific examination of the geometric specifics of the aircraft is undertaken. It's important to note that all aircraft-related information has been extrapolated from [19], which stems from a comprehensive wind tunnel characterization study. These gathered insights are compiled in the ensuing table (Table 1.2). All characteristic distances are measured from the nose of the aircraft.

Inertia	
m	205 kg
J_{xx}	47.23 kg m ² (1121 lbs ft ²)
J_{yy}	90.95 kg m ² (2158 lbs ft ²)
J_{zz}	111.47 kg m ² (2645 lbs ft ²)
J_{xz}	-6.65 kg m ² (-157.8 lbs ft ²)
J_{xy}, J_{yz}	0 kg m ² (0 lbs ft ²)

(a) Inertia properties

Fuselage	
Width	0.32 m (1.05 ft)
Length	2.48 m (8.13 ft)
Height	0.43 m (1.41 ft)
Length FWD Cone	0.93 m (3.05 ft)
Distance AFT Cone	2.14 m (7.02 ft)
Length AFT Cone	0.37 m (1.21 ft)

(b) Fuselage properties

Wing	
Area	2.82 m ² (30.42 ft ²)
Span	5.15 m (16.9 ft)
Aspect Ratio	9.36
Chord	0.54 m (1.80 ft)
x_{AC}	1.63 m (5.34 ft)
z_{AC}	0.34 m (1.11 ft)
Airfoil	NACA 4415
Incidence	2.0 deg
Aileron Deflection	± 20.0 deg

(c) Wing properties

Horizontal Tail	
Area	0.56 m ² (6.07 ft ²)
Span	1.85 m (6.07 ft)
Aspect Ratio	6.07
Chord	0.30 m (1.00 ft)
x_{AC}	4.01 m (13.16 ft)
z_{AC}	0.31 m (1.02 ft)
Airfoil	NACA 0012
Incidence	-3 deg
Elevator Deflection	± 20.0 deg

(d) Horizontal tail properties

Vertical Tail	
Area	0.20 m ² (2.17 ft ²)
Span	0.66 m (2.17 ft)
Aspect Ratio	2.17
Chord	0.30 (1ft)
x_{AC}	4.05 m (13.29 ft)
z_{AC}	0.5 m (1.64 ft)
Airfoil	NACA 0012
Rudder Deflection	± 20.0 deg

(e) Vertical tail properties

Table 1.2: AAI RQ-2 Pioneer Inertial and geometric specifics.

1.5.3. Stability and Control Derivatives

While a dedicated subroutine exists within the `SILCROAD` library for stability and control derivatives computation by means of empirical formulas [20], to mitigate potential calculation uncertainties arising from geometric parameter inaccuracies, this subroutine has been replaced with look-up tables compiled through experimentally collected data from [19]. A list of stability and control derivatives considered for stability analysis purposes is presented in Table 1.3. All listed parameters are referred to CG location at $x_{CG} = 1.96$ m, $z_{CG} = 0.34$ m from the aircraft nose (33% of MAC on thrust line).

C_{L0}	$C_{L\alpha}$	$C_{L\hat{\alpha}}$	$C_{L\hat{q}}$	$C_{L\delta_e}$	$C_{L\delta_t}$
0.385	4.78	2.42	8.05	0.40	0.0
C_{D0}	$C_{D\alpha}$	$C_{D\hat{\alpha}}^*$	$C_{D\hat{q}}^*$	$C_{D\delta_e}$	$C_{D\delta_t}$
0.060	0.43	0.0	0.0	0.018	-1
C_{M0}	$C_{M\alpha}$	$C_{M\hat{\alpha}}$	$C_{M\hat{q}}$	$C_{M\delta_e}$	$C_{M\delta_t}$
0.194	-2.12	-11.0	-36.6	-1.76	0.0

(a) Longitudinal stability and control derivatives

$C_{Y\beta}$	$C_{Y\hat{\beta}}^*$	$C_{Y\hat{p}}^*$	$C_{Y\hat{r}}^*$	$C_{Y\delta_a}$	$C_{Y\delta_r}$
-0.819	0.003	-0.062	0.663	0.0	0.191
$C_{\mathcal{L}\beta}$	$C_{\mathcal{L}\hat{\beta}}^*$	$C_{\mathcal{L}\hat{p}}$	$C_{\mathcal{L}\hat{r}}$	$C_{\mathcal{L}\delta_a}$	$C_{\mathcal{L}\delta_r}$
-0.023	0.0014	-0.450	0.265	0.161	-0.0023
$C_{\mathcal{N}\beta}$	$C_{\mathcal{N}\hat{\beta}}^*$	$C_{\mathcal{N}\hat{p}}$	$C_{\mathcal{N}\hat{r}}$	$C_{\mathcal{N}\delta_a}$	$C_{\mathcal{N}\delta_r}$
0.109	-0.0057	-0.110	-0.200	-0.020	-0.092

(b) Lateral-directional stability and control derivatives

Table 1.3: Stability and control derivatives

For certain values among those listed in the table, marked with *, direct validation through existing literature was unattainable. Consequently, reliance was placed on empirical calculations executed within the library's dedicated subroutine based on Roskam's empirical methods. All the gathered data has been compiled into the designated fields of the *Airplane* subclass for object instantiation. Consequently, all results provided by the

Craft/Airplane methods are based on the data listed so far.

1.5.4. Actuators

The dynamic model of the actuators installed on board the aircraft, both for control surfaces and throttle, has been initially approximated using first-order transfer functions (see Table 1.4). This approach aims to capture the fundamental characteristics of the response to control inputs provided by the control system, including time constant, time delays, and damping factors, while still maintaining computational efficiency.

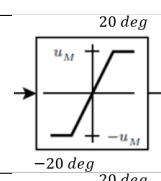
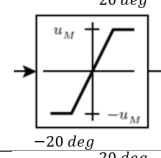
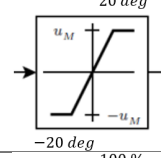
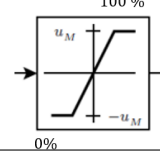
Control	Saturation	Transfer Function
Elevator		$H(s)_{\delta_e/\delta_e^*} = \frac{1}{0.1s+1}$
Aileron		$H(s)_{\delta_a/\delta_a^*} = \frac{1}{0.1s+1}$
Rudder		$H(s)_{\delta_r/\delta_r^*} = \frac{1}{0.1s+1}$
Throttle		$H(s)_{\delta_t/\delta_t^*} = \frac{1}{1.5s+1}$

Table 1.4: Actuators dynamics models

The time constants were selected based on literature [21]. For small-sized aircraft, plausible time constant values might typically fall within the following ranges:

Control Surface Actuators: - Elevator, Aileron, Rudder: Time constant (τ) in the range of 0.05 s to 0.2 s.

Piston Engine Control: - Throttle Control: Time constant (τ) in the range of 1.0 s to 2.5 s. A value of $\tau = 0.1$ s was chosen for the control surface actuators, while for regulating the engine power output, a reasonable value of $\tau = 1.5$ s was adopted.

2 | Stability Augmentation System (SAS)

In this document section, a description of the stability augmentation system, geared towards flying qualities enhancement, will be provided. Starting from aircraft stability analysis, with prior aircraft dynamic model linearization, passing through the description of the LQR (*Linear Quadratic Regulator*) controller design procedure up to the nonlinear implementation within the simulation framework. To achieve this objective, illustrative cases will undergo scrutiny, wherein a comparative analysis will be conducted between outcomes derived from the linearized model and those originating from the fully nonlinear one.

2.1. Linear Dynamic Model

2.1.1. Trim Point Solution

In the realm of dynamic systems analysis, a pivotal concept revolves around the linearization of models in the vicinity of trim solutions. Trim solutions represent equilibrium points where the system's forces and moments are balanced, yielding steady-state flight. By linearizing the system around such equilibria, a simplified representation emerges, enabling the application of stability analysis and linear control theory. This approach proves particularly valuable for understanding the system's behavior in the proximity of its operational states, under these formalized assumptions:

- $\mathbf{w}_{CG}^B = \bar{\mathbf{w}}_{CG}^B$ constant $\Rightarrow \dot{\mathbf{w}}_{CG}^B = 0$.
- $\boldsymbol{\delta} = \{\delta_e, \delta_a, \delta_r, \delta_t\} = \bar{\boldsymbol{\delta}}$ constant.

Therefore, by substituting the trim solution into the generalized balance equation we obtain:

$$\bar{\mathbf{w}}_{CG}^{\mathcal{B}} \times \mathbf{M}_{CG}^{\mathcal{B}} \bar{\mathbf{w}}_{CG}^{\mathcal{B}} = \left\{ \begin{array}{l} f_a^{\mathcal{B}}(0, \bar{\mathbf{w}}_{CG}^{\mathcal{B}}, \bar{\boldsymbol{\delta}}) + mg \begin{Bmatrix} -\sin \theta \\ \sin \phi \cos \theta \\ \cos \phi \cos \theta \end{Bmatrix} \\ m_a^{\mathcal{B}}(0, \bar{\mathbf{w}}_{CG}^{\mathcal{B}}, \bar{\boldsymbol{\delta}}) \end{array} \right\}. \quad (2.1)$$

Having to satisfy equilibrium, even the body-axis components of the gravitational force must remain constant. Consequently, it follows that:

- $\theta, \phi = \bar{\theta}, \bar{\phi} \Rightarrow \dot{\theta}, \dot{\phi} = 0$

No conditions are imposed on ψ ; therefore, the $\dot{\psi}$ component of aircraft rotational rate in $\mathcal{F}^{\mathcal{I}}$ remains, leading to assert that the aircraft rotational rate in trimmed condition will have a non-null inertial component aligned with gravity. Furthermore, it is known that:

$$\omega_{\mathcal{B}/\mathcal{I}}^{\mathcal{B}} = \mathcal{R}_{\mathcal{I}}^{\mathcal{B}}(\phi, \theta, \psi) \omega_{\mathcal{B}/\mathcal{I}}^{\mathcal{I}} = \mathcal{R}_{\mathcal{I}}^{\mathcal{B}}(\phi, \theta, \psi) \begin{bmatrix} 0 \\ 0 \\ \dot{\psi} \end{bmatrix}. \quad (2.2)$$

However, the generalized state vector is set to remain constant, with $\omega_{\mathcal{B}/\mathcal{I}}^{\mathcal{B}} = \bar{\omega}_{\mathcal{B}/\mathcal{I}}^{\mathcal{B}}$ constant, leading to a further condition for trim point definition, which is :

- $\dot{\psi} = \bar{\dot{\psi}}$ constant

Under these assumptions, the overarching result of the trim condition takes the form of a helical trajectory aligning its axis parallel to gravity. Among distinct subcases, for the purpose of dynamic system linearization, a wings-level steady-state flight condition will be considered, wherein:

- $\bar{\dot{\psi}} = 0$, and $\bar{U}, \bar{V}, \bar{W}$ are configured to maintain a horizontal trajectory within $\mathcal{F}^{\mathcal{I}}$.

more specifically, taking also into account aerodynamic angles definitions, the considered steady-state flight condition is defined by subsequent assumptions:

- $\beta, \phi, \dot{\phi}, \dot{\psi}, p, q, r = 0$
- $\alpha = \alpha_0, \theta = \theta_0$
- $v_{CG}^{\mathcal{B}} = [U_0, 0, 0]^{\mathbf{T}}$.

2.1.2. Linearized System Derivation

Dealing with linearized dynamic systems involves working with the perturbed form of the dynamics equations. The system behaves linearly in the close vicinity of the reference condition, wherein the variables at play are expressed through a first-order truncated Taylor expansion:

$$\begin{aligned} \mathbf{w}_{CG} &= \mathbf{w}_{CG_0} + \Delta \mathbf{w}_{CG} , \\ \dot{\mathbf{w}}_{CG} &= \dot{\mathbf{w}}_{CG_0} + \Delta \dot{\mathbf{w}}_{CG} , \\ r_{CG} &= \underbrace{r_{CG_0}}_{\text{reference value}} + \underbrace{\Delta r_{CG}}_{\text{perturbation}} , \end{aligned}$$

yielding:

$$\mathbf{M}_{CG} \Delta \dot{\mathbf{w}}_{CG} + \mathbf{w}_{CG_0} \times \mathbf{M}_{CG} \Delta \mathbf{w}_{CG} + \Delta \mathbf{w}_{CG} \times \mathbf{M}_{CG} \mathbf{w}_{CG_0} = \Delta r_{CG} . \quad (2.3)$$

The perturbed form stated in Equation (2.3) refers to Equation (1.44), stripped of the reference solution, matching, in this case, the trim point solution. The variables at play thus represent variations in the aircraft's states and control inputs around the trim condition. Let's denote as x and δ the states vector and the input vector respectively, such that :

$$x = \{u, \Delta\beta, \Delta\alpha, \Delta p, \Delta q, \Delta r, \Delta\phi, \Delta\theta, \Delta\psi\} \quad (2.4)$$

$$\delta = \{\Delta\delta_e, \Delta\delta_a, \Delta\delta_r, \Delta\delta_t\} , \quad (2.5)$$

where $u = \frac{\Delta U}{U_0}$, and $\Delta\beta \simeq \frac{\Delta V}{U_0}$, $\Delta\alpha \simeq \frac{\Delta W}{U_0}$, considering $U_0 \gg V_0, W_0$.

In common practice, under the aforementioned assumptions of symmetrical flight within the vertical plane and considering an aircraft with a standard configuration, linearization can be conducted without sacrificing generality, by separating the longitudinal dynamics from the lateral-directional dynamics. However, a deliberate decision has been made to derive the complete linearized system, this is due to the fact that, without prior knowledge of the aircraft's dynamic behavior, the aim is to verify the absence of any unusual couplings between longitudinal and lateral-directional dynamics associated with specific geometric characteristics of the aircraft and thus, inherently linked to the collected stability and control derivatives. With regard to that, complete decoupling is expected, even though we are aware that, in the nonlinear realm, minimal coupling arises due to the intrinsically interconnected nature of the equations of motion. Furthermore, this approach has been chosen to achieve a more generally accurate model that ensures proper representation without being specific to the aforementioned reference condition.

Lastly, for the purposes of optimal control, as will be detailed subsequently, considering

the aircraft's motion across all three axes simultaneously proves advantageous. Although it might seem counterintuitive, a complete linearized system can simplify the optimal controller design process. This could streamline the practical implementation of optimal control and ensure more natural and seamless control responses.

The objective is to arrive at the formulation of the complete linearized dynamic system in the form of a first-order differential equation:

$$\mathbf{M} \dot{x} + \mathbf{K} x = \mathbf{F} \delta . \quad (2.6)$$

Since the complete linearized system entails a certain level of complexity in notation, with matrices \mathbf{M} and \mathbf{K} both of size [9x9], and control sensitivity matrix \mathbf{F} of dimension [9x4], smaller submatrices will be defined and subsequently assembled to construct the complete matrices.

Within the matrices, stability and control derivatives appears as defined in the \mathcal{F}^B reference frame. These parameters, which are obtained through a conversion system [22], reflect a measure of the direct sensitivity of body-axis forces and moments with respect to the states and control inputs.

$$M_{11} = \begin{bmatrix} m_1 - c_1 C_{X_{\dot{u}}} & -b_1 C_{X_{\dot{\beta}}} & -c_1 C_{X_{\dot{\alpha}}} \\ c_1 C_{Y_{\dot{u}}} & m_1 - b_1 C_{Y_{\dot{\beta}}} & -c_1 C_{Y_{\dot{\alpha}}} \\ -c_1 C_{Z_{\dot{u}}} & -b_1 C_{Z_{\dot{\beta}}} & m_1 - c_1 C_{Z_{\dot{\alpha}}} \end{bmatrix}$$

$$M_{12} = \mathbf{0}_{3 \times 3}, \quad M_{13} = \mathbf{0}_{3 \times 3}$$

$$M_{21} = \begin{bmatrix} -c_1 C_{\mathcal{L}_{\dot{u}}} & -b_1 C_{\mathcal{L}_{\dot{\beta}}} & -c_1 C_{\mathcal{L}_{\dot{\alpha}}} \\ -c_1 C_{\mathcal{M}_{\dot{u}}} & -b_1 C_{\mathcal{M}_{\dot{\beta}}} & -c_1 C_{\mathcal{M}_{\dot{\alpha}}} \\ -c_1 C_{\mathcal{N}_{\dot{u}}} & -b_1 C_{\mathcal{N}_{\dot{\beta}}} & -c_1 C_{\mathcal{L}_{\dot{\alpha}}} \end{bmatrix}, \quad M_{22} = \begin{bmatrix} J_{x1} & 0 & -J_{xz1} \\ 0 & J_{y1} & 0 \\ -J_{xz1} & 0 & J_{z1} \end{bmatrix}$$

$$M_{23} = \mathbf{0}_{3 \times 3}, \quad M_{31} = \mathbf{0}_{3 \times 3}, \quad M_{32} = \mathbf{0}_{3 \times 3}, \quad M_{33} = \mathbf{I}_{3 \times 3}$$

$$\mathbf{M}_{9 \times 9} = \begin{bmatrix} M_{11} & M_{12} & M_{13} \\ M_{21} & M_{22} & M_{23} \\ M_{31} & M_{32} & M_{33} \end{bmatrix} \quad (2.7)$$

The assembled matrix \mathbf{M} represents the generalized mass matrix, containing the elements that, in Equation (2.6), will contribute to weighting the terms of the scaled linear accelerations vector $\{\dot{u} = \frac{\Delta\dot{U}}{U_0}, \Delta\dot{\beta} \simeq \frac{\Delta\dot{V}}{U_0}, \Delta\dot{\alpha} \simeq \frac{\Delta\dot{W}}{U_0}\}$, the dimensional angular acceleration vector $\{\Delta\dot{p}, \Delta\dot{q}, \Delta\dot{r}\}$, and the Δ -attitude rates of change vector $\{\Delta\dot{\phi}, \Delta\dot{\theta}, \Delta\dot{\psi}\}$.

Let's move forward with \mathbf{K} matrix build-up.

$$K_{11a} = \begin{bmatrix} -C_{X_u} - 2C_{X_0} & -m_1 r_0 - C_{X_\beta} & m_1 q_0 - C_{X_\alpha} \\ m_1 r_0 - C_{Y_u} - 2C_{Y_0} & -C_{Y_\beta} & -m_1 p_0 - C_{Y_\alpha} \\ -m_1 q_0 - C_{Z_u} - 2C_{Z_0} & m_1 p_0 - C_{Z_\beta} & -C_{Z_\alpha} \end{bmatrix}$$

$$K_{11b} = \frac{1}{\frac{1}{2}\rho U_0^2 S} \begin{bmatrix} -T_{x_u} U_0 & 0 & 0 \\ -T_{y_u} U_0 & 0 & 0 \\ -T_{z_u} U_0 & 0 & 0 \end{bmatrix}$$

$$K_{12} = \begin{bmatrix} -b_1 C_{X_{\dot{p}}} & m_1 \frac{W}{U_0} - c_1 C_{X_{\dot{q}}} & -m_1 \frac{V}{U_0} - b_1 C_{X_{\dot{r}}} \\ -m_1 \frac{W}{U_0} - b_1 C_{Y_{\dot{p}}} & -c_1 C_{Y_{\dot{q}}} & m_1 - b_1 C_{Y_{\dot{r}}} \\ m_1 \frac{V}{U_0} - b_1 C_{Z_{\dot{p}}} & -m_1 - c_1 C_{Z_{\dot{q}}} & -b_1 C_{Z_{\dot{r}}} \end{bmatrix}$$

$$K_{13} = \frac{-mg}{\frac{1}{2}\rho U_0^2 S} \begin{bmatrix} 0 & -\cos \theta_0 & 0 \\ \cos \theta_0 \cos \phi_0 & -\sin \theta_0 \sin \phi_0 & 0 \\ -\cos \theta_0 \sin \phi_0 & -\sin \theta_0 \cos \phi_0 & 0 \end{bmatrix}$$

with $K_{11} = K_{11a} + K_{11b}$. The aforementioned set of submatrices will compose the uppermost three rows of the generalized stiffness matrix and conveys how aerodynamic, propulsive, and gravitational forces distribution is affected by aircraft's states perturbation. The terms $\frac{1}{\frac{1}{2}\rho U_0^2 S} T_{i_u} U_0$ within submatrix K_{11b} express the thrust force sensitivity with respect to airspeed, computed along each of the three body axes, expressed in non-dimensional form. The sensitivity parameter T_u is computed within a dedicated subroutine that evaluates the incremental thrust ratio concerning variations in airspeed. The algorithm establishes lower and upper bounds, set at ± 5 m/s from the reference airspeed. By averaging the thrust changes across these two intervals, a comprehensive representation of the thrust's responsiveness to changes in airspeed is obtained.

$$K_{21a} = \begin{bmatrix} -C_{\mathcal{L}_u} - 2C_{\mathcal{L}_0} & -C_{\mathcal{L}_\beta} & -C_{\mathcal{L}_\alpha} \\ -C_{\mathcal{M}_u} - 2C_{\mathcal{M}_0} & -C_{\mathcal{M}_\beta} & C_{\mathcal{M}_\alpha} \\ -C_{\mathcal{N}_u} - 2C_{\mathcal{N}_0} & -C_{\mathcal{N}_\beta} & C_{\mathcal{N}_\alpha} \end{bmatrix}$$

$$K_{21b} = \frac{1}{\frac{1}{2}\rho U_0^2 S} \begin{bmatrix} -\frac{\Gamma_{xu}}{b} U_0 & 0 & 0 \\ -\frac{\Gamma_{yu}}{c} U_0 & 0 & 0 \\ -\frac{\Gamma_{zu}}{b} U_0 & 0 & 0 \end{bmatrix}$$

$$K_{22a} = \begin{bmatrix} -J_{xz1}q_0 - b_1 C_{\mathcal{L}_{\hat{p}}} & -J_{y2}r_0 - c_1 C_{\mathcal{L}_{\hat{q}}} & J_{z1}q_0 - b_1 C_{\mathcal{L}_{\hat{r}}} \\ J_{x2}r_0 + J_{xz2}p_0 - b_1 C_{\mathcal{M}_{\hat{p}}} & -c_1 C_{\mathcal{M}_{\hat{q}}} & -J_{xz2}r_0 - J_{z2}r_0 - J_{z2}p_0 - b_1 C_{\mathcal{M}_{\hat{r}}} \\ -J_{x1}q_0 - b_1 C_{\mathcal{N}_{\hat{p}}} & J_{y2}p_0 - c_1 C_{\mathcal{N}_{\hat{q}}} & J_{xz1}q_0 - b_1 C_{\mathcal{N}_{\hat{r}}} \end{bmatrix}$$

$$K_{22b} = \begin{bmatrix} 0 & -J_{xz1}p_0 + J_{z1}r_0 & -J_{y2}q_0 \\ J_{xz2}p_0 - J_{z2}r_0 & 0 & p_0 J_{x2} - J_{xz2}r_0 \\ J_{y2}q_0 & -p_0 J_{xz1} + J_{xz1}r_0 & 0 \end{bmatrix}$$

$$K_{23} = \mathbf{0}_{3 \times 3}$$

with $K_{21} = K_{21a} + K_{21b}$, and $K_{22} = K_{22a} + K_{22b}$. The submatrices array just provided constitutes the central sub-block of size [3x9] within the stiffness matrix, and it describes how aerodynamic and propulsive moments distribution is influenced by aircraft's states perturbation. Similar reasoning as before applies to $\frac{1}{\frac{1}{2}\rho U_0^2 S} \frac{\Gamma_{iu}}{[b;c;b]} U_0$ terms, pertaining thrust-induced moments sensitivity with respect to airspeed, in non-dimensional form.

$$K_{31} = \mathbf{0}_{3 \times 3}$$

$$K_{32} = - \begin{bmatrix} 1 & \tan \theta_0 \sin \phi_0 & \tan \theta_0 \cos \phi_0 \\ 0 & \cos \phi_0 & -\sin \phi_0 \\ 0 & \sin \phi_0 / \cos \theta_0 & \cos \phi_0 / \cos \theta_0 \end{bmatrix}$$

$$K_{33} = - \begin{bmatrix} \tan \theta_0 (\cos \phi_0 q_0 - \sin \phi_0 r_0) & (\tan^2 \theta_0 + 1) (\sin \phi_0 q_0 + \cos \phi_0 r_0) & 0 \\ -\sin \phi_0 q_0 - \cos \phi_0 r_0 & 0 & 0 \\ \cos \phi_0 / \cos \theta_0 q_0 - \sin \phi_0 / \cos \theta_0 r_0 & 2 \sin \theta_0 (q_0 \sin \phi_0 + r_0 \cos \phi_0) / \cos \theta_0^3 & 0 \end{bmatrix}$$

The last three submatrices stem from the linearized form of the kinematic relationship

expressed in Equation (1.42), which can be restated as follow:

$$\dot{e}_{321} = \mathbf{S}_{321}^{\mathcal{B}^{-1}} \omega_{\mathcal{B}/\mathcal{I}}^{\mathcal{B}} \quad (2.8)$$

wherein $\mathbf{S}_{321}^{\mathcal{B}^{-1}}$ enable to derive Euler angles derivatives (\dot{e}_{321}), starting from body-axes measured angular rates. It is the inverse (not the transpose), of direct kinematic relationship passing from Euler angles derivatives to body-axes measured angular rates, appearing in Equation (1.41). Contextually, the corresponding linearized form of Equation (2.8) comes as:

$$\Delta \dot{e}_{321} = \mathbf{S}_{321_0}^{\mathcal{B}^{-1}} \Delta \omega_{\mathcal{B}/\mathcal{I}}^{\mathcal{B}} + \Delta \mathbf{S}_{321}^{\mathcal{B}^{-1}} \omega_{\mathcal{B}/\mathcal{I}_0}^{\mathcal{B}} \quad (2.9)$$

Therefore, K_{31} is a null submatrix, as there exists no direct kinematic relationship between translational velocities and Euler angles. Moreover, referring to Equation (2.9), K_{32} aligns with $\mathbf{S}_{321_0}^{\mathcal{B}^{-1}}$, and K_{33} is derived from $\Delta \mathbf{S}_{321}^{\mathcal{B}^{-1}}$, rearranged to express $\Delta \dot{e}_{321}$ in terms of Euler angles rather than reference roll, pitch, and yaw rates.

The overall stiffness matrix is assembled as follows:

$$\mathbf{K}_{9 \times 9} = \begin{bmatrix} K_{11} & K_{12} & K_{13} \\ K_{21} & K_{22} & K_{23} \\ K_{31} & K_{32} & K_{33} \end{bmatrix} \quad (2.10)$$

We then proceed with \mathbf{F} matrix assembly.

$$F_{11} = \begin{bmatrix} C_{X\delta_e} & C_{X\delta_a} & C_{X\delta_r} \\ C_{Y\delta_e} & C_{Y\delta_a} & C_{Y\delta_r} \\ C_{Z\delta_e} & C_{Z\delta_a} & C_{Z\delta_r} \end{bmatrix}, \quad F_{12} = \frac{1}{\frac{1}{2}\rho U_0^2 S} \begin{bmatrix} T_{x\delta_t} & T_{y\delta_t} & T_{z\delta_t} \end{bmatrix}^T$$

$$F_{21} = \begin{bmatrix} C_{\mathcal{L}\delta_e} & C_{\mathcal{L}\delta_a} & C_{\mathcal{L}\delta_r} \\ C_{\mathcal{M}\delta_e} & C_{\mathcal{M}\delta_a} & C_{\mathcal{M}\delta_r} \\ C_{\mathcal{N}\delta_e} & C_{\mathcal{N}\delta_a} & C_{\mathcal{N}\delta_r} \end{bmatrix}, \quad F_{22} = \frac{1}{\frac{1}{2}\rho U_0^2 S} \begin{bmatrix} \frac{\Gamma_{x\delta_t}}{b} & \frac{\Gamma_{y\delta_t}}{c} & \frac{\Gamma_{z\delta_t}}{b} \end{bmatrix}^T$$

with F_{11} and F_{21} representing the sensitivity of aerodynamic forces and moments with respect to control surfaces inputs, whereas, F_{12} and F_{22} collect the thrust-induced forces and moments sensitivity parameters, in non-dimensional form, as a function of throttle control input. The overall control sensitivity matrix is assembled as follows:

$$\mathbf{F} = \begin{bmatrix} F_{11} & F_{12} \\ F_{21} & F_{22} \\ \mathbf{0}_{3 \times 3} & \mathbf{0}_{3 \times 3} \end{bmatrix} \quad (2.11)$$

All featured scaled geometric and inertial parameters are hereafter reported:

$$\begin{aligned}
 m_1 &= \frac{m}{\frac{1}{2}\rho U_0^2 S} & J_{x1} &= \frac{J_{xx}}{\frac{1}{2}\rho U_0^2 S b} & J_{x2} &= \frac{J_{xx}}{\frac{1}{2}\rho U_0^2 S c} & J_{xz1} &= \frac{J_{xz}}{\frac{1}{2}\rho U_0^2 S b} \\
 c_1 &= \frac{c}{2U_0} & J_{y1} &= \frac{J_{yy}}{\frac{1}{2}\rho U_0^2 S c} & J_{y2} &= \frac{J_{yy}}{\frac{1}{2}\rho U_0^2 S b} & J_{xz2} &= \frac{J_{xz}}{\frac{1}{2}\rho U_0^2 S c} \\
 b_1 &= \frac{b}{2U_0} & J_{z1} &= \frac{J_{zz}}{\frac{1}{2}\rho U_0^2 S b} & J_{z2} &= \frac{J_{zz}}{\frac{1}{2}\rho U_0^2 S c} & &
 \end{aligned}$$

It is now possible to derive the state space model as follows:

$$\begin{cases} \dot{x} = (-\mathbf{M}^{-1}\mathbf{K}) x + (\mathbf{M}^{-1}\mathbf{F}) \delta = \mathbf{A} x + \mathbf{B} u & (2.12a) \\ y = \mathbf{C} x + \mathbf{D} u = \mathbf{I}_{9 \times 9} x + \mathbf{0}_{9 \times 4} u & (2.12b) \end{cases}$$

By leveraging the state space model, it is then feasible to perform the system stability analysis. This entails examining the eigenvalues spectrum of the state matrix A , and subsequently, applying suitable control strategies. Moreover, it facilitates the execution of time-marching simulations, which are totally descriptive of the aircraft's states time evolution caused by equilibrium perturbation.

2.2. Eigenanalysis

The system has been linearized around a particular trim condition that accurately reflects a substantial portion of the aircraft's operational conditions.

Trim condition: $V_{GND} = 140$ km/h, $H = 300$ m						
α_0	U_0	W_0	q_0	θ_0	δ_{e_0}	δ_{t_0}
4.83 deg	38.7 m/s	3.27 m/s	0.0 deg	4.83 deg	0.49 deg	43 %

Table 2.1: Trim output at $V = 140$ km/h, $H = 300$ m.

The eigenanalysis yielded a set of nine eigenvalues, including three complex conjugate pairs and three real eigenvalues, collectively capturing the distinctive essence of the aircraft's dynamics in terms of modes natural frequencies and damping ratios. Illustrated in Figure 2.1 and 2.2, the pole distribution of the linearized open-loop system is reported. The blue markers denote eigenvalues of longitudinal dynamics, encompassing two complex conjugate pairs associated with the short-period and phugoid modes. The red markers correspond to eigenvalues governing lateral-directional dynamics. Specifically, they encompass one complex conjugate pair responsible for the oscillatory dutch roll mode, as well as two real eigenvalues governing roll subsidence and spiral modes, complemented by

one zero root which corresponds to the neutrally stable behavior with regard to aircraft's directional motion.

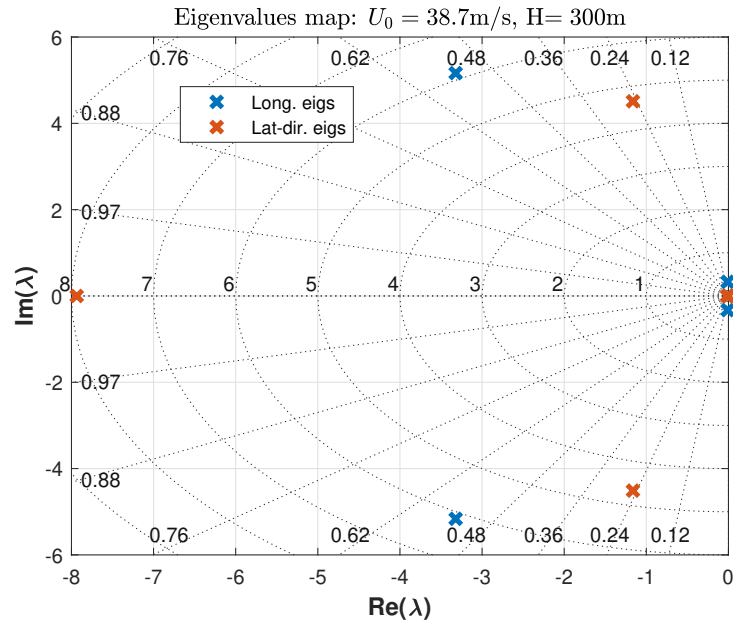


Figure 2.1: Complete system eigenvalues map. Blue: longitudinal eigenvalues. Red: lateral-directional eigenvalues.

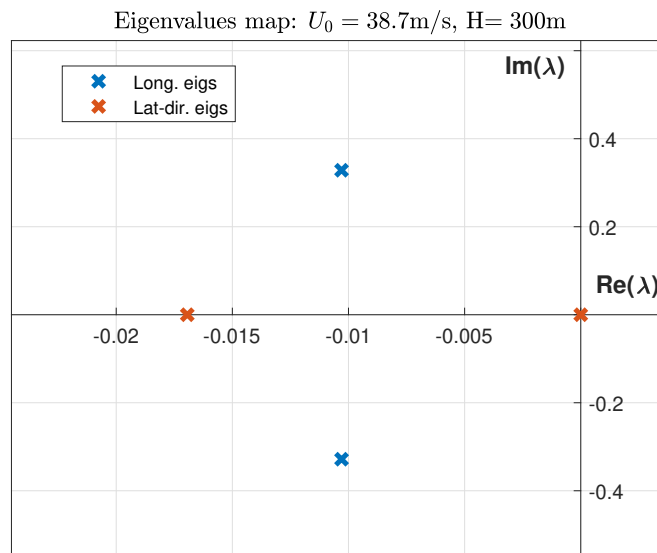


Figure 2.2: Complete system eigenvalues map. Origin close-up

All the poles of the system are distributed in the stability region, thus ensuring that the

aircraft can cope with the equilibrium state's perturbations by asymptotically reducing their intensity. The modes characterization in terms of natural frequency and damping ratio is reported in Table 2.2 and 2.3.

Short-period	
ω_n	6.14 rad/s
ξ	0.54

(a) Short-period

Phugoid	
ω_n	0.33 rad/s
ξ	0.03

(b) Phugoid

Table 2.2: Longitudinal modes characteristics

Roll-subsidence	
ω_n	7.9 rad/s
ξ	1

(a) Roll-subsidence

Spiral	
ω_n	0.01 rad/s
ξ	1

(b) Spiral

Dutch-roll	
ω_n	4.66 rad/s
ξ	0.25

(c) Dutch-roll

Table 2.3: Lateral-directional modes characteristics

For a thorough evaluation of the aircraft's flight characteristics, it is advisable to reference the military certification (MIL-F-87-85C), which establishes the flying qualities requirements for various aircraft classes, operational categories, and levels of adequacy. The aircraft classification, according to the military certification taxonomy, is documented in Table 2.4. The set of requirements for the specific classification has been summarized in

AAI RQ-2 Pioneer classification	
Class I	Small, light airplanes, including light observation craft
Category A	Non-terminal flight phases that require rapid maneuvering, precision tracking, or precise flight path control
Level I	Flying qualities adequate for the mission flight phase.

Table 2.4: AAI RQ-2 Pioneer flying qualities classification

Table 2.5. Within the table, the specifications regarding flying qualities are expressed in terms of minimum and/or maximum damping ratios ξ , minimum natural frequencies ω_n , maximum time constant τ for the Roll mode, and the doubling time T_2 for the Spiral mode, for which instability is permissible as long as the aircraft response doubles its amplitude within a time interval equal to T_2 .

MIL-F-87-85C requirements		
Phugoid	ξ_{min}	0.04
Short-period	ξ_{min}	0.35
	ξ_{max}	1.30
	$\omega_{n_{max}}$	8.70 rad/s
Dutch-roll	$\omega_{n_{min}}$	1 rad/s
	$\xi\omega_{n_{min}}$	0.35 rad/s
	ξ_{max}	0.19
Roll-subsidence	τ_{max}	1 s
Spiral	T_2	12 s

Table 2.5: MIL-F-87-85C requirements for *Class I* aircraft, *Category A* flight phase, *Level I* adequacy.

An immediate visualization of the system's compliance to requirements is depicted in Figure 2.3 and 2.4, where the highlighted complex plane regions correspond to the certification requirements for adequacy levels I, II, and III. Concerning the short-period mode, the system comfortably falls within the prescribed requirements. However, the long-period mode (phugoid) conforms to adequacy level II, signifying a satisfactory level of acceptability while entailing some degradation in mission task effectiveness. All lateral-directional modes, fall within the required specifications.

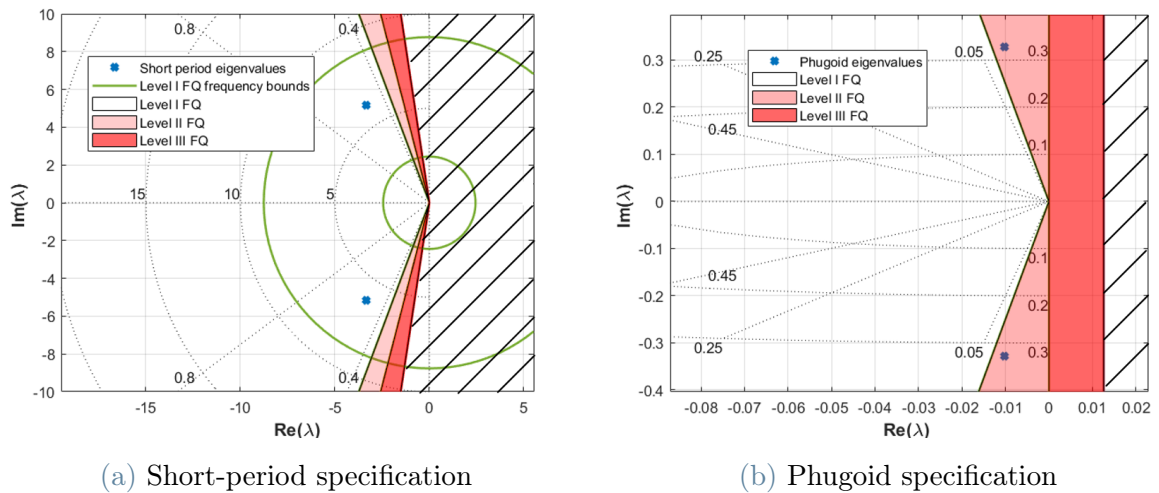


Figure 2.3: Longitudinal modes certification requirements in terms of pole distribution

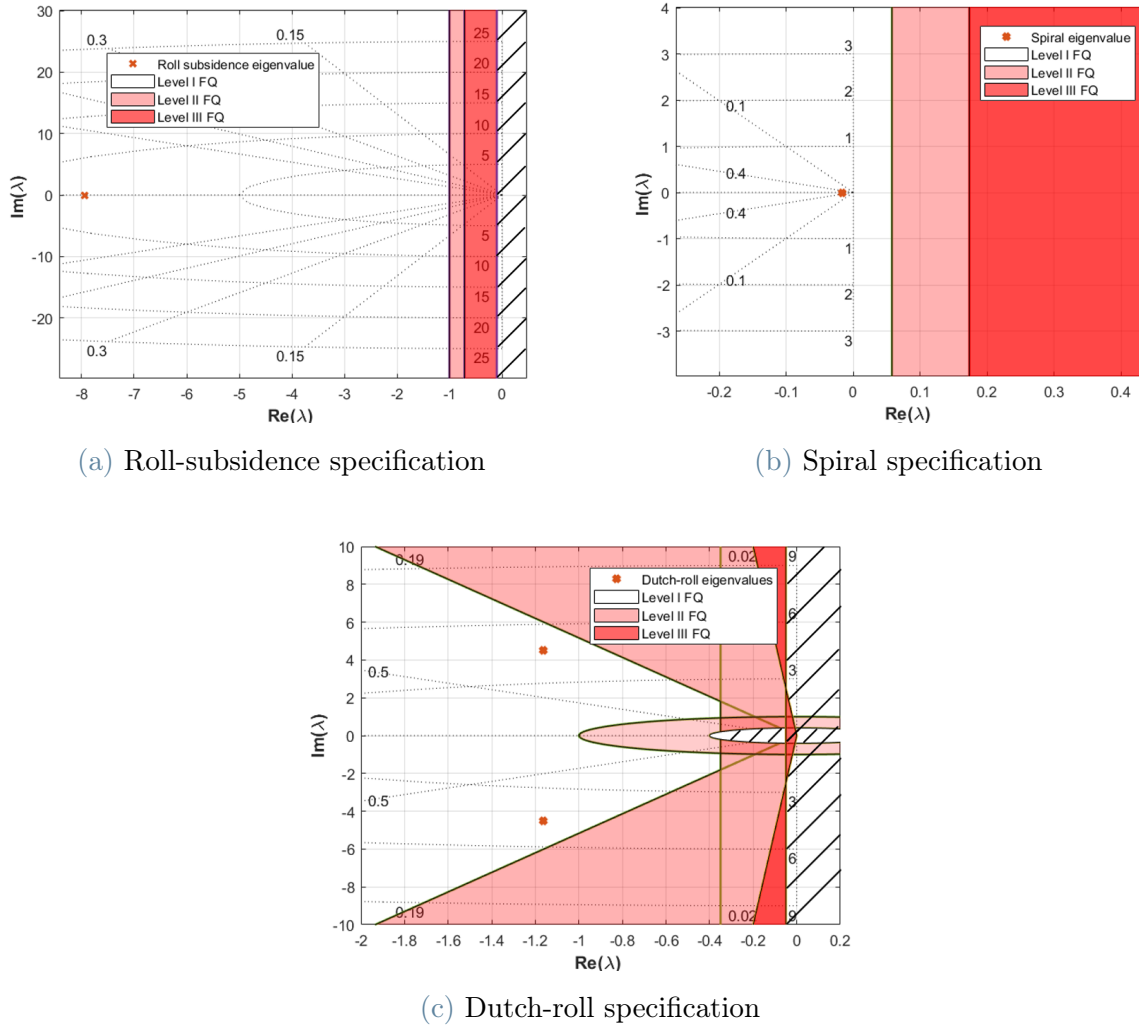


Figure 2.4: Lateral-directional modes certification requirements in terms of pole distribution

Nonetheless, it remains imperative to account for the variability exhibited by the system's poles as operational conditions undergo changes. The subsequent figures intended to illustrate the root loci pertaining to both longitudinal and lateral-directional dynamics, as a function of reference airspeed and altitude. For a better insight into system behavior sensitivity to these parameters, the two effects have been studied independently. Therefore, in Figure 2.5, the root locus generated by a positive variation in altitude is depicted, while maintaining airspeed constant at 39 m/s, equivalent to a ground speed of 140 km/h. Conversely, in the graph presented in Figure 2.6, the root locus resulting from a gradual decrease in airspeed, from 52 m/s to 25 m/s (190 km/h - 90 km/h), is shown while keeping the reference altitude fixed at 300 m. The parameters held constant in both scenarios correspond to typical values of airspeed and altitude relevant to the operational employment of the aircraft.

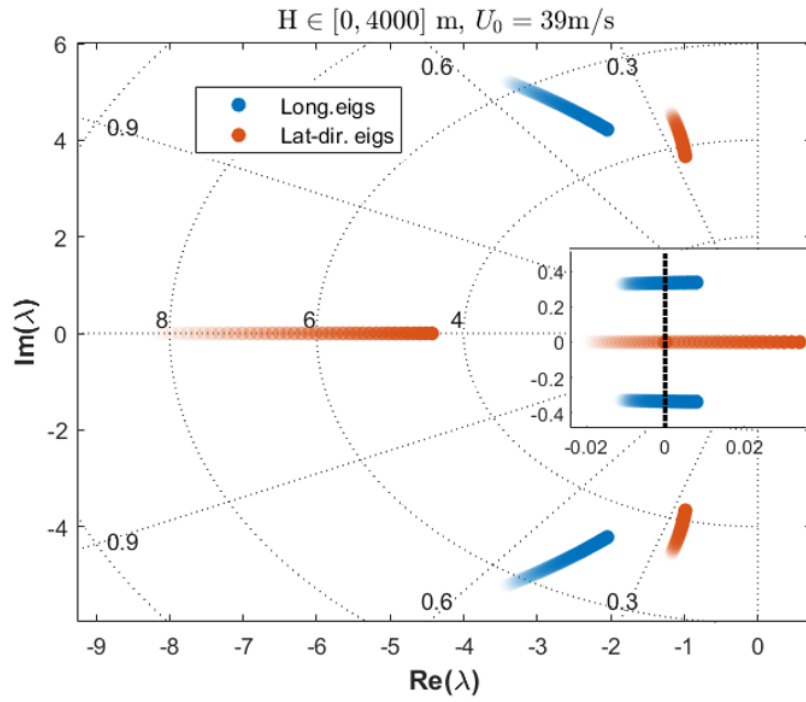


Figure 2.5: Complete system root locus for increasing altitude.

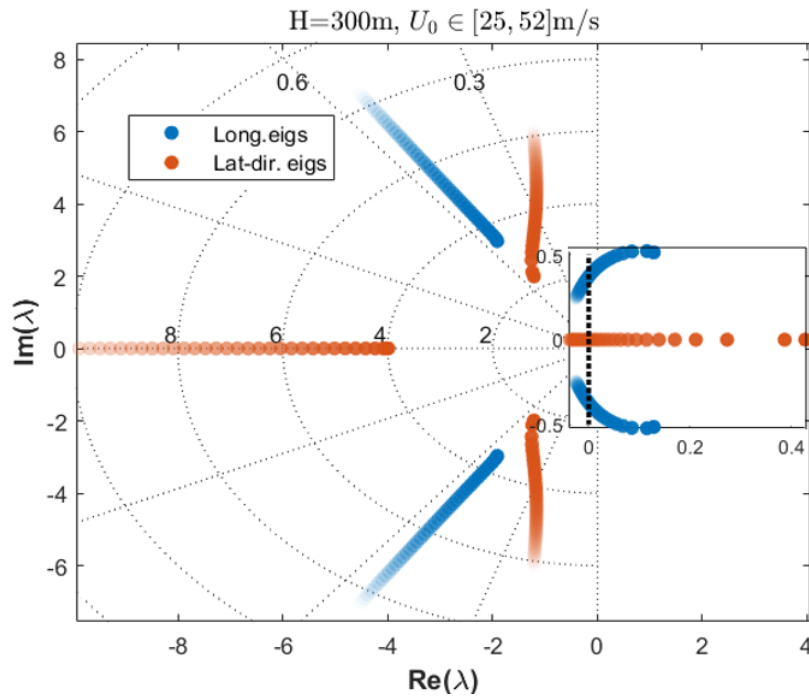


Figure 2.6: Complete system root locus for decreasing airspeed.

In Figure 2.5, when maintaining a constant airspeed, a rise in altitude triggers a gradual shift of the system's poles towards the imaginary axis, thereby modifying and reducing the natural frequency of short-period modes. The shift along the real axis of the pole associated with the roll mode translates into a higher time constant, resulting in a slower aircraft response to disturbances along the roll axis. The effect on phugoid involves a reduction in the damping ratio, while the natural frequency remains nearly unchanged, inducing instability for altitudes exceeding 2000m. Similarly, the spiral mode demonstrates a tendency towards instability at lower altitude levels.

Turning attention to Figure 2.6, a reduction in airspeed induces significant modifications in the dynamic characteristics of the aircraft system. The poles connected with the short-period mode transition closer to the origin, following a constant damping ratio line. Meanwhile, the poles of the Dutch roll mode traverse multiple frequency and damping ratio iso-lines, resulting in highly varying system behavior for the extreme values of airspeed considered. The previously mentioned considerations hold for the remaining modes, where the aircraft becomes less reactive to disturbances along the roll axis (increased roll mode time constant), and instability arises in the phugoid and spiral modes for airspeeds approaching the stall speed.

In conclusion, variations in operational conditions in terms of altitude and airspeed exert a transformative influence on the aircraft's dynamic behavior, degrading its inherent flying qualities and potentially leading to instability. The effect of airspeed variation appears to be predominant. Furthermore, it should be considered that, for the intended application, operating altitudes beyond 1000m are unlikely, effectively reducing the impact of altitude variation. Conversely, it is plausible that within an altitude band spanning from 0 to 1000m, the aircraft would be required to fully exploit the considered airspeed range.

Given the required path-tracking precision for the designated mission objectives and the constraints associated with formation flight, the demand for a stabilization controller becomes mandatory. Such a controller is tasked with ensuring the system's asymptotic stability across all operational flight conditions and the rapid decay of perturbations affecting individual swarm units, accommodating the swarm scalability, by preventing their propagation throughout the entire formation.

2.3. Controller Design

The stability augmentation system (SAS) algorithm proposed herein is based on a model-based approach and optimal control law, specifically the Linear Quadratic Regulator (LQR) technique. This linear control strategy allows to optimally minimize a quadratic cost function. It achieves this goal by employing state feedback, where proportional con-

control gains are calculated based on the aircraft dynamic model, and on user-defined weight matrices that capture the trade-off between state-tracking performance and control effort. In other terms, the controller aims to stabilize the system while achieving a balanced control employment performance.

In contrast to the conventional PID controllers commonly implemented for pitch and yaw-roll dampers, a distinct preference has been shown for employing the LQR approach. This choice stems from a multitude of advantages extending beyond mere performance optimization:

- **Smoother response.** This enhanced response is achieved by factoring in the comprehensive dynamics of the entire system, as the LQR approach adeptly manages states' interdependencies. Notably, empowers the user to engage with the design phase solely by allocating specific weights to states and controls.
- **Multivariable control.** The LQR approach is particularly well-suited for multivariable control, allowing for a coordinated control strategy that inherently contributes to system redundancy, and enhanced sensitivity to variations in the aircraft behavior.
- **Effective non-linear implementation.** A significant aspect of this approach pertains to its suitability for accommodating gain scheduling procedures. This involves the computation of the gain matrix for diverse flight regimes while maintaining consistent weighting factors. This results in a streamlined design process for controller implementation within nonlinear contexts. Additionally, for flight conditions not explicitly sampled during the design phase, the LQR-based system engages in online gain re-tuning by interpolating existing gain values or selecting the most effective pre-computed gain matrix.

Before proceeding, a clarification is necessary. The aircraft Flight Control System (FCS) is intended to encompass an internal control loop dedicated to aircraft stabilization (SAS), and an external loop constituting the autopilot. As expounded upon in the forthcoming chapters, the autopilot will be structured to endow each individual aircraft with two distinct modes for autonomous flight: a guidance mode (GM), aimed at executing a pre-defined trajectory tracking, and a formation control mode (FCM), dedicated to ensuring accurate position maintenance within the swarm.

In order to accurately design the inner control loop, the open-loop linearized system as defined by Equation (2.12) has been extended to incorporate the dynamics of actuators and nine low-pass filters, with a time constant $\tau = 0.1s$, which are applied to the nine

canonical states. This augmentation aims to mitigate high-frequency noise and render these measurements suitable for adequate feedback control. Additionally, washout filters on pitch and yaw rate channels have been implemented to ensure sufficient signal bandwidth for the guidance controller to operate. The extended form of state matrix \mathbf{A}_{TOT} and control matrix \mathbf{B}_{TOT} can be formulated as follows:

$$\mathbf{A}_{TOT} = \begin{bmatrix} \hat{\mathbf{A}}_{9 \times 9} & \mathbf{0}_{9 \times 9} & \mathbf{0}_{9 \times 2} & \hat{\mathbf{B}}_{9 \times 4} \\ \text{diag}\left(\frac{1}{\tau_F}\right)_{9 \times 9} & \text{diag}\left(-\frac{1}{\tau_F}\right)_{9 \times 9} & \mathbf{0}_{9 \times 2} & \mathbf{0}_{9 \times 4} \\ \mathbf{0}_{1 \times 9} & \begin{bmatrix} \mathbf{0}_{1 \times 3} & 1 & \mathbf{0}_{1 \times 5} \\ \mathbf{0}_{1 \times 5} & 1 & \mathbf{0}_{1 \times 3} \end{bmatrix} & \begin{bmatrix} -\frac{1}{\tau_{qw}} & 0 \\ 0 & -\frac{1}{\tau_{qw}} \end{bmatrix} & \mathbf{0}_{1 \times 4} \\ \mathbf{0}_{1 \times 9} & & & \mathbf{0}_{1 \times 4} \\ \mathbf{0}_{4 \times 9} & \mathbf{0}_{4 \times 9} & \mathbf{0}_{9 \times 2} & \text{diag}\left(-\frac{1}{\tau_A}\right)_{4 \times 4} \end{bmatrix} \quad (2.13)$$

$$\mathbf{B}_{TOT} = \begin{bmatrix} \mathbf{0}_{9 \times 4} \\ \mathbf{0}_{9 \times 4} \\ \mathbf{0}_{2 \times 4} \\ \text{diag}\left(\frac{1}{\tau_A}\right)_{4 \times 4} \end{bmatrix} \quad (2.14)$$

The augmented state vector encompasses nine canonical states, nine low-pass filtered states, washout filters states, and actuators states.

$$x_{TOT} = \{\hat{x}_{1 \times 9}, x_{F1 \times 9}, x_{qw}, x_{rw}, \Delta\delta_e, \Delta\delta_a, \Delta\delta_r, \Delta\delta_t\} \quad (2.15)$$

While the input vector u_{TOT} collects the input provided by the outer control loop.

$$u_{TOT} = \{\Delta\delta_e^{Pilot}, \Delta\delta_a^{Pilot}, \Delta\delta_r^{Pilot}, \Delta\delta_t^{Pilot}\} \quad (2.16)$$

2.3.1. Linear Quadratic Regulator (LQR)

Starting from the linearized system (Equation (2.12)), the objective is to derive a control law such that:

$$u = u^{Pilot} - \mathbf{K}_{LQR} x \quad (2.17)$$

where u^{Pilot} is the outer loop control input (namely input provided by autopilot) and \mathbf{K}_{LQR} represents the gain matrix, which is determined through the analytical solution of a constrained optimization problem. In this context, the state equation stands as the defining constraint, while the objective function to minimize is a quadratic cost function

formulated as follows:

$$J = \frac{1}{2} \int_{t_0}^{\infty} (x^T \mathbf{Q}x + u^T \mathbf{R}u) dt \quad (2.18)$$

The integrand function is thus composed of two components. The first component takes into account the variations in the system states, suitably weighted through the user-defined matrix \mathbf{Q} . This is done to ensure specific performance criteria. The second component factors in the variations in control inputs, through a user-defined matrix \mathbf{R} , to calibrate the control effort.

The closed-form solution to this minimization problem involves solving the Algebraic Riccati Equation (ARE).

$$0 = \mathbf{A}^T \mathbf{P} + \mathbf{P} \mathbf{A} + \mathbf{Q} - \mathbf{P} \mathbf{B} \mathbf{R}^{-1} \mathbf{B}^T \mathbf{P} \quad (2.19)$$

This equation is solved for an intermediate matrix, denoted as \mathbf{P} , which is a symmetric positive definite matrix. The constituent elements within the \mathbf{P} matrix establish the relationships between the system states and their corresponding relative weight in the overarching cost function and govern how the controller adjusts the control inputs for cost minimization. Once the matrix \mathbf{P} is determined, it becomes feasible to compute the controller gains \mathbf{K}_{LQR} as follows:

$$\mathbf{K}_{LQR} = \mathbf{R}^{-1} \mathbf{B}^T \mathbf{P} \quad (2.20)$$

The attained solution ensures the asymptotic stability of the closed-loop system dynamics, expressed by the following state equation:

$$\dot{x} = (\mathbf{A} - \mathbf{B} \mathbf{K}_{LQR}) x + \mathbf{B} u^{Pilot} \quad (2.21)$$

provided that (\mathbf{A}, \mathbf{B}) exhibit controllability which implies that each state is attained by the control action, and $(\sqrt{\mathbf{Q}}, \mathbf{A})$ demonstrates observability, meaning basically that all states are weighted in the cost function J . These conditions hold true for the considered system across a reasonably broad range of \mathbf{Q} values.

2.3.2. LQR with Output Feedback

The methodology described in subsection 2.3.1 pertains to the domain of Full-State Feedback LQR. This approach is typically applied in scenarios where complete state information is utilized for control purposes, and the states are appropriately weighted through the employment of the gain matrix \mathbf{K}_{LQR} to ascertain the requisite control inputs. However,

adaptation is necessary when only the filtered states are available for feedback.

Consider the subsequent system model:

$$\begin{cases} \dot{x} = \mathbf{A} x + \mathbf{B} u & (2.22a) \\ y = \mathbf{C} x & (2.22b) \end{cases}$$

In this context, $\mathbf{A} := \mathbf{A}_{TOT}$, $\mathbf{B} := \mathbf{B}_{TOT}$, defined in equations (2.13) and (2.14), $x := x_{TOT}$, $u := u_{TOT}$ from equations (2.15) and (2.16), and y signifies the measured output, suitable for feedback control.

The objective here is to derive a control law that takes the form:

$$u = u^{Pilot} - \mathbf{K}_{LQR} y = u^{Pilot} - \mathbf{K}_{LQR} \mathbf{C} x \quad (2.23)$$

Subsequently, the governing equation for the closed-loop system's state becomes:

$$\dot{x} = (\mathbf{A} - \mathbf{B}\mathbf{K}_{LQR}\mathbf{C})x + \mathbf{B} u^{Pilot} = \mathbf{A}_c x + \mathbf{B} u^{Pilot} \quad (2.24)$$

To facilitate the minimization of the cost function as outlined in equation (2.18), incorporating output feedback requires the inclusion of two auxiliary matrices within computational process, namely \mathbf{P} and \mathbf{S} . These matrices are the solutions to the following system of algebraic Lyapunov equations:

$$0 = \mathbf{A}_c^T \mathbf{P} + \mathbf{P} \mathbf{A}_c + \mathbf{C}^T \mathbf{K}_{LQR}^T \mathbf{B} \mathbf{K}_{LQR} \mathbf{C} + \mathbf{Q} \quad (2.25a)$$

$$0 = \mathbf{A}_c \mathbf{S} + \mathbf{S} \mathbf{A}_c^T + \mathbf{X} \quad (2.25b)$$

Here, $\mathbf{X} = x(0)x(0)^T$. The solution for \mathbf{K}_{LQR} matrix is then given as follows:

$$\mathbf{K}_{LQR} = \mathbf{R}^{-1} \mathbf{B}^T \mathbf{P} \mathbf{S} \mathbf{C}^T (\mathbf{C} \mathbf{S} \mathbf{C}^T)^{-1} \quad (2.26)$$

A numerical solution involving the outlined procedure was originally proposed by [23], as documented in [24]. This approach hinges on iteratively refining the \mathbf{K}_{LQR} matrix until a minimum value, as defined with respect to a predetermined tolerance, is attained for J . The latter, as it is possible to demonstrate, can be evaluated through the expression:

$$J = \frac{1}{2} \text{tr}(\mathbf{P}\mathbf{X}) \quad (2.27)$$

Further details regarding the theoretical treatment of LQR with output feedback and proposed numerical solution algorithm are provided in the Appendix B.

2.3.3. Controller Implementation

The implementation process involves selecting appropriate weighting factors for states and controls. Typically, these parameters are chosen through iterative trials until the closed-loop system achieves the desired performance. However, an automated mechanism exists that provides an initial indication of their magnitudes without entirely discarding iterative parameter evaluation. This approach entails weighting each state and control by the inverse of the square of the corresponding desired maximum deviation.

$$\mathbf{Q} = \text{diag} \left\{ \frac{1}{x_{i_{max}}^2} \right\} \quad (2.28)$$

$$\mathbf{R} = \text{diag} \left\{ \frac{1}{u_{i_{max}}^2} \right\} \quad (2.29)$$

In the case under consideration, the \mathbf{Q} matrix selection demands some additional considerations. States that predominantly impact a specific mode are equally weighted in the cost function. Furthermore, with regard to the extended state vector in Equation (2.15), it will be necessary to determine parameters for each state in the system, even though the concern is only on the nine canonical states. Given that the remaining parameters exclusively govern the time evolution of filters and actuator signals, which aren't inherently linked to the aircraft's dynamic characteristics, a reasonable approach involves assigning a zero weighting factor to these states. However, this could potentially lead to observability issues. Consequently, while the actuator states are uniformly assigned a weight of zero, the filtered states are uniformly weighted with a unit factor. The outcome is:

$$\begin{aligned} \mathbf{Q}_{24 \times 24} = \text{diag} \{ & 1, 5, 3, 3, 3, 5, 3, 1, 1 \times 10^{-4}, \dots \\ & 1, 1, 1, 1, 1, 1, 1, 1, 1, 1, \dots \\ & 0, 0, 0, 0 \} \end{aligned} \quad (2.30)$$

The \mathbf{R} matrix is chosen to strongly penalize control inputs. This design ensures that stabilization efforts minimally interfere with commands provided from the external control loop, while still maintaining effective disturbance rejection. No throttle contribution has been considered for stabilization.

$$\mathbf{R}_{3 \times 3} = \text{diag} \{ 200, 200, 200 \} \quad (2.31)$$

Lastly, the \mathbf{C} matrix, as presented in Equation (2.24) and (2.24), to ensure the control action relies exclusively upon the filtered states, is:

$$\mathbf{C}_{9 \times 24} = \begin{bmatrix} \mathbf{0}_{9 \times 9} & , \mathbf{I}_{9 \times 9} & , \begin{bmatrix} \mathbf{0}_{4 \times 2} \\ -\mathbf{I}_{2 \times 2} \\ \mathbf{0}_{3 \times 3} \end{bmatrix} & \mathbf{0}_{9 \times 4} \end{bmatrix} \quad (2.32)$$

Subsequently, by applying the procedure detailed in section 2.3.2 through the algorithm introduced by Moerder & Calise (1985), a numerical solution for the \mathbf{K}_{LQR} matrix is derived. The solution guarantees the asymptotic stability of the closed-loop system, adhering to the specified requirements, while also accounting for delays introduced by filters and actuators. A block diagram for the proposed controller is provided in Figure 2.7.

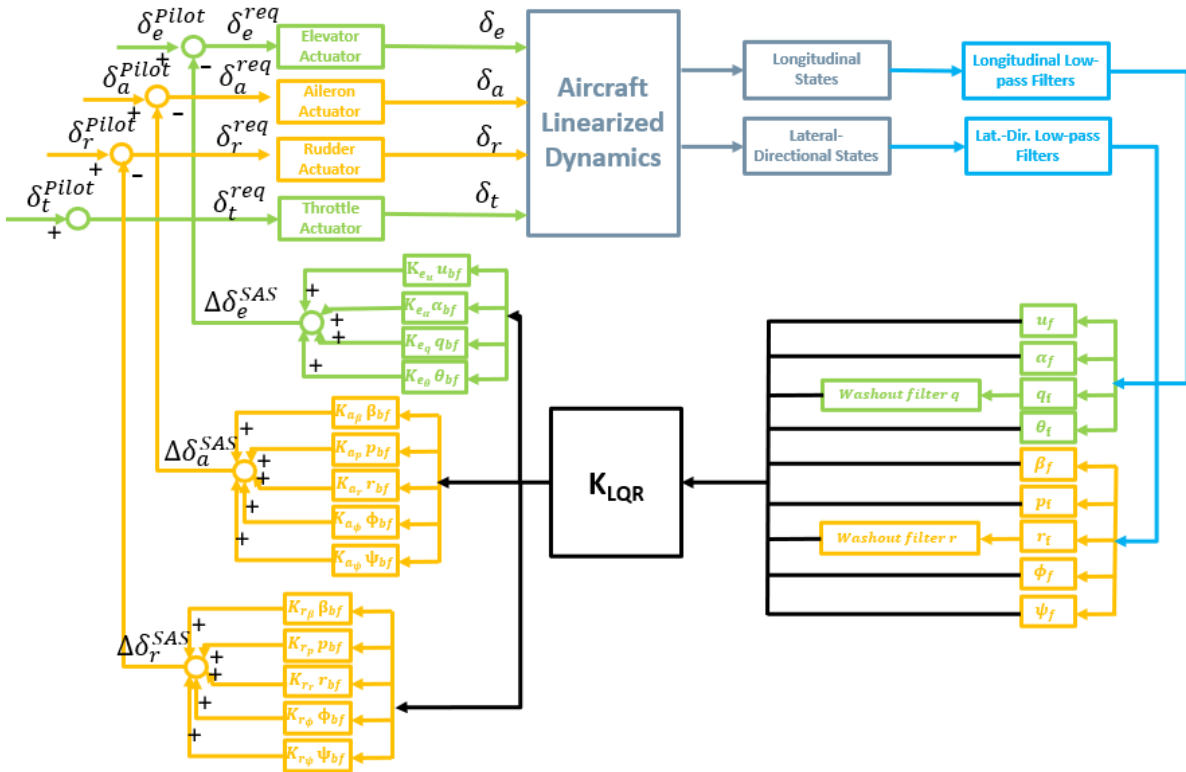


Figure 2.7: Proposed stabilization control. Green: Longitudinal dynamics. Yellow: Lateral-directional dynamics. Cyan: Low-pass filters.

In the LQR gain-tuning process, each row of the gain matrix corresponds to a specific command input. The values in each row, when multiplied by the filtered state vector, contribute to the overall feedback signal applied to the corresponding command. The subscript $(\cdot)_{bf}$ for signals in the feedback branch stands for bandwidth filtered.

2.4. Simulation and Results

The assessment of closed-loop system characteristics goes through the evaluation of pole distribution as illustrated in Figure 2.8 (only the nine canonical states are reported for clarity, omitting filters and actuators poles). The stabilizing effect manifests as a slight increase in both frequency and damping ratio for oscillatory modes, combined with a decreased characteristic response time for roll-subside and spiral. This adaptation ensures a notable separation from the onset of instability of the spiral mode, which, as previously stated for the open-loop system, exhibits a tendency towards instability even for minor variations in operational conditions. Furthermore, the solution ensure the adequacy Level I for phugoid mode.

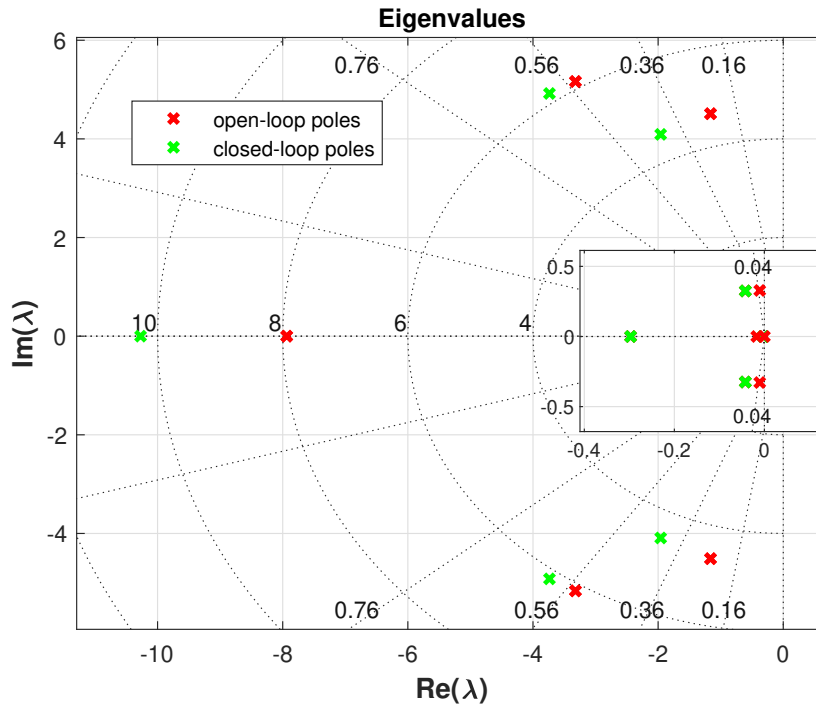


Figure 2.8: Complete system poles distribution. Comparison between open-loop and closed-loop system.

2.4.1. Free Response Testing

This analysis is conducted not only to assess the SAS performance but also to evaluate the affinity between the linear and nonlinear models, thereby verifying the accuracy of the aircraft behavior linear approximation achieved within the close vicinity of a specific trim condition. For accurate comparison, the states derived from the linearized system, which solely represent deviations from the equilibrium state, have been re-scaled and su-

perimposed onto the corresponding state trim solution.

For each of the following cases, a perturbation of 2 m/s in velocity is assumed along each of the three body axes ($\Delta U = \Delta V = \Delta W = 2\text{m/s}$), putting in place a combined set of initial conditions aimed at triggering the aircraft's longitudinal and lateral-directional response simultaneously.

Trim condition 1.

The first condition under examination pertains to the parameter set outlined in Table 2.1: the aircraft is flying wings-leveled at 300 m altitude and 140 km/h ground speed. The perturbed initial condition is defined by:

$$u \simeq 0.05 \text{ m/s}, \quad \Delta\alpha \simeq 3 \text{ deg}, \quad \Delta\beta \simeq 3 \text{ deg}$$

The longitudinal states evolution over a time window of 80 seconds is depicted in Figure 2.9. It can be observed that the two models are sufficiently compatible, although the response of the linear model appears slightly underdamped, particularly with respect to U and θ . However, this effect diminishes with increasing airspeed, as will be seen later. This occurs because, for an equal magnitude of disturbance, lower trim airspeed results in percentage larger deviations in canonical states. This could potentially stray from the assumption of small perturbations, consequently lowering the accuracy of linear approximation. In the closed-loop response, the two models exhibit nearly overlapping behavior. The influence of the SAS is primarily noticeable in the long-period oscillation, which completely dampens within 30 seconds. The progression of the short-period oscillation is challenging to discern, as it is the slow dynamics associated with the phugoid poles that govern the aircraft's behavior around the pitch axis.

The evolution of lateral-directional states (Figure 2.10) becomes apparent over a shortened time frame. In this case, the linear approximation notably captures the aircraft's behavior.

The SAS acts to diminish both the frequency and magnitude of the response oscillations, restoring the states to their trimmed values within 2 seconds.

The control extent is assessable from Figure 2.11, within the first 10 second time window is reported. Each of the four controls remains significantly distant from the saturation bounds thereby ensuring improved aircraft stability with reasonable control effort.

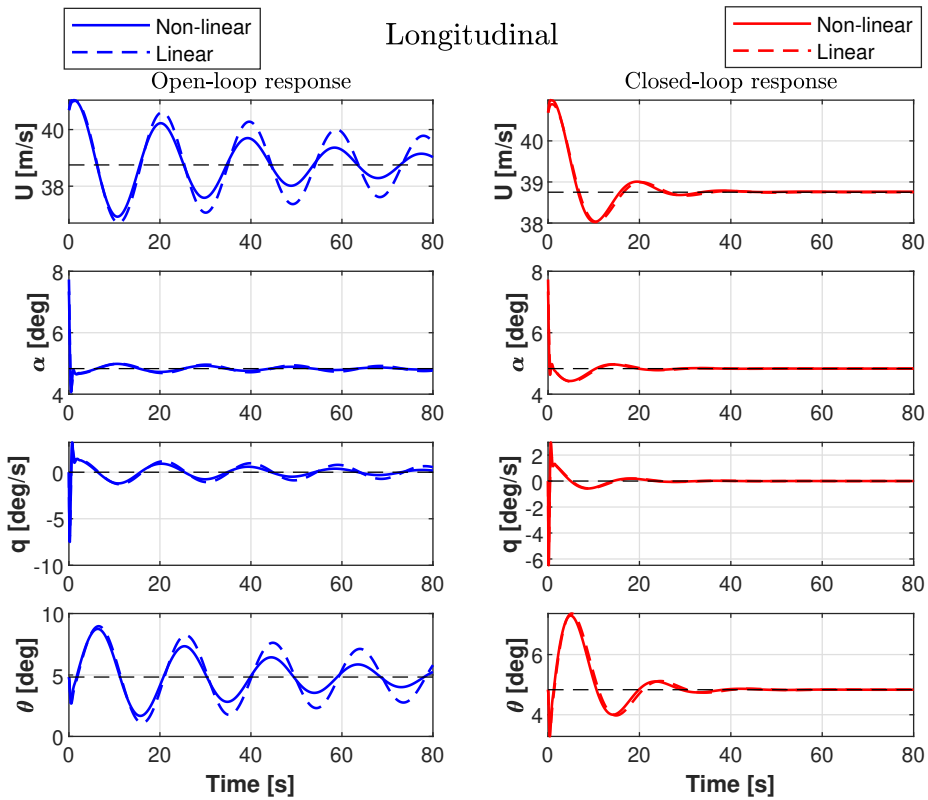


Figure 2.9: Longitudinal states evolution around trim condition 1. Open-loop (left) vs. closed-loop (right). Linear (dotted) vs. non-linear model.

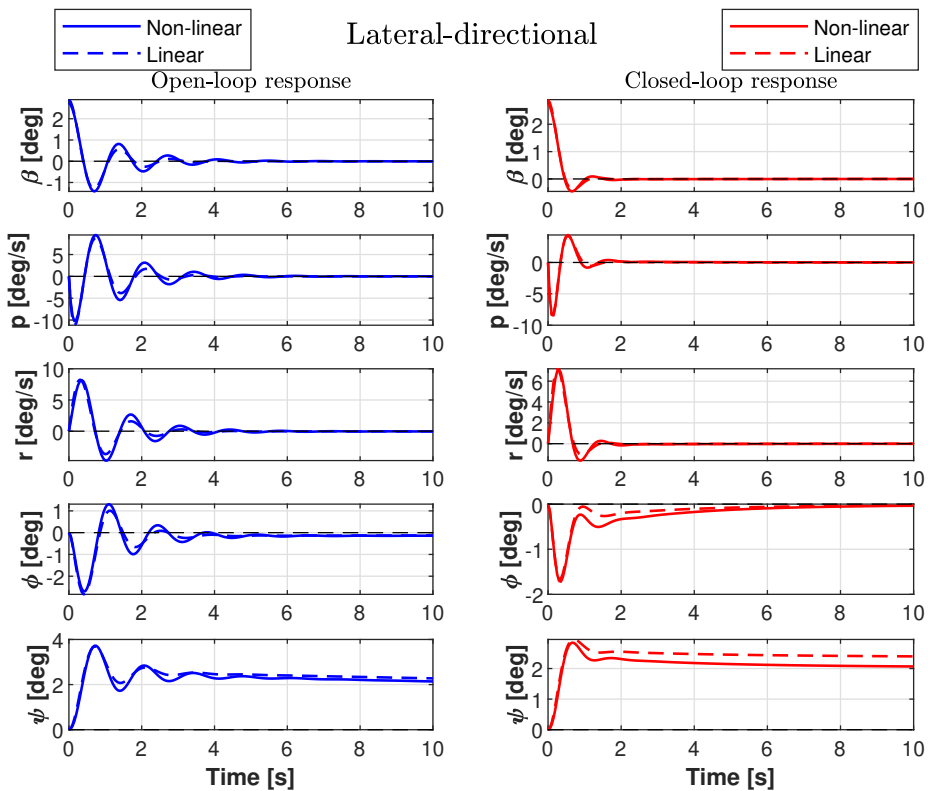


Figure 2.10: Lateral-directional states evolution around trim condition 1. Open-loop (left) vs. closed-loop (right). Linear (dotted) vs. non-linear model.

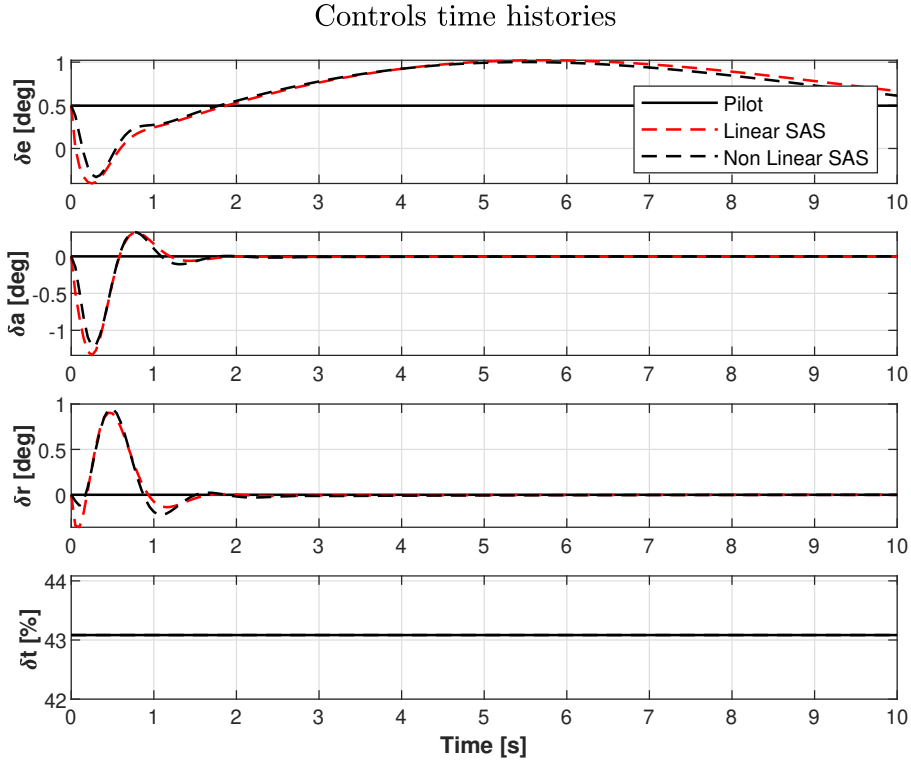


Figure 2.11: SAS control inputs for stabilization around trim condition 1.

Trim condition 2.

It is herein analyzed the case pertaining to trimmed parameters reported in Table 2.6. The increase in altitude above 2000 m and the reduction in ground speed to 120 km/h

Trim condition: $V_{GND} = 120 \text{ km/h}$, $H = 2300 \text{ m}$						
α_0	U_0	W_0	q_0	θ_0	δ_{e_0}	δ_{t_0}
12 deg	32.5 m/s	7.1 m/s	0.0 deg	12.23 deg	-8.42 deg	40 %

Table 2.6: Trim output at $V = 120 \text{ km/h}$, $H = 2300 \text{ m}$.

lead to instability in the phugoid and spiral modes, as observed in Figure 2.12 and 2.13. Although the instability condition renders the linearized model unsuitable for open-loop longitudinal dynamics modeling, the closed-loop system maintains excellent performance by ensuring aircraft stability even at altitude levels far from the standard operating level and at near-stall AOA. The magnitude of the control inputs applied (Figure 2.14) also guarantees a broad maneuvering capability by the outer control loop. The perturbed initial condition is herein:

$$u \simeq 0.06 \text{ m/s}, \quad \Delta\alpha \simeq 3.5 \text{ deg}, \quad \Delta\beta \simeq 3.5 \text{ deg}$$

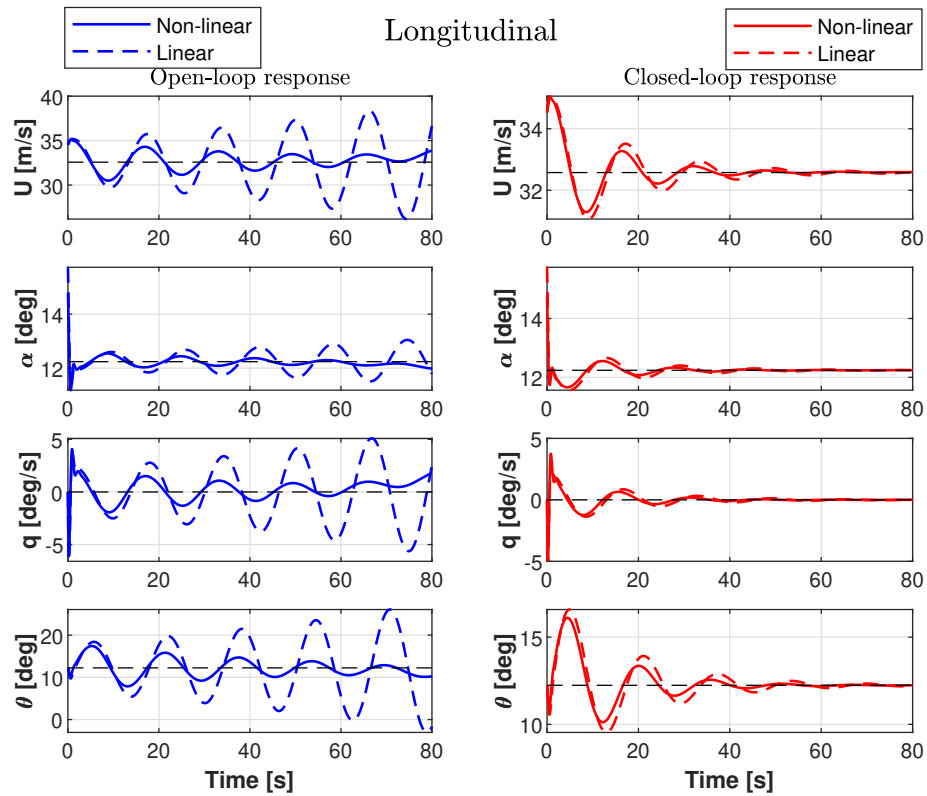


Figure 2.12: Longitudinal states evolution around trim condition 2. Open-loop (left) vs. closed-loop (right). Linear (dotted) vs. non-linear model.

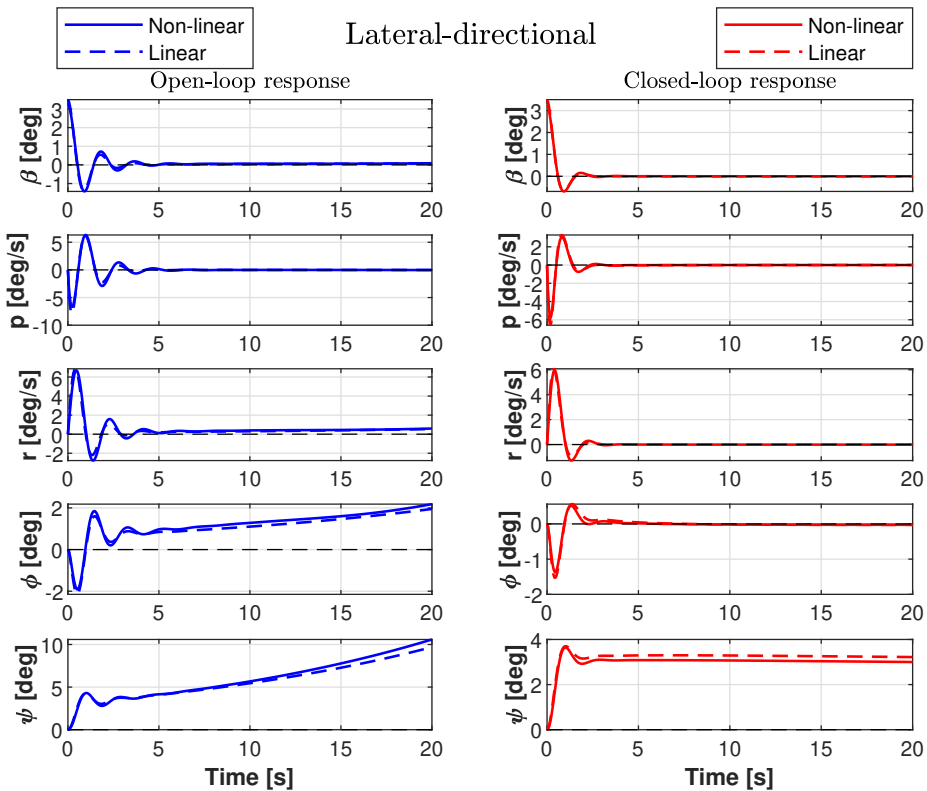


Figure 2.13: Lateral-directional states evolution around trim condition 2. Open-loop (left) vs. closed-loop (right). Linear (dotted) vs. non-linear model.

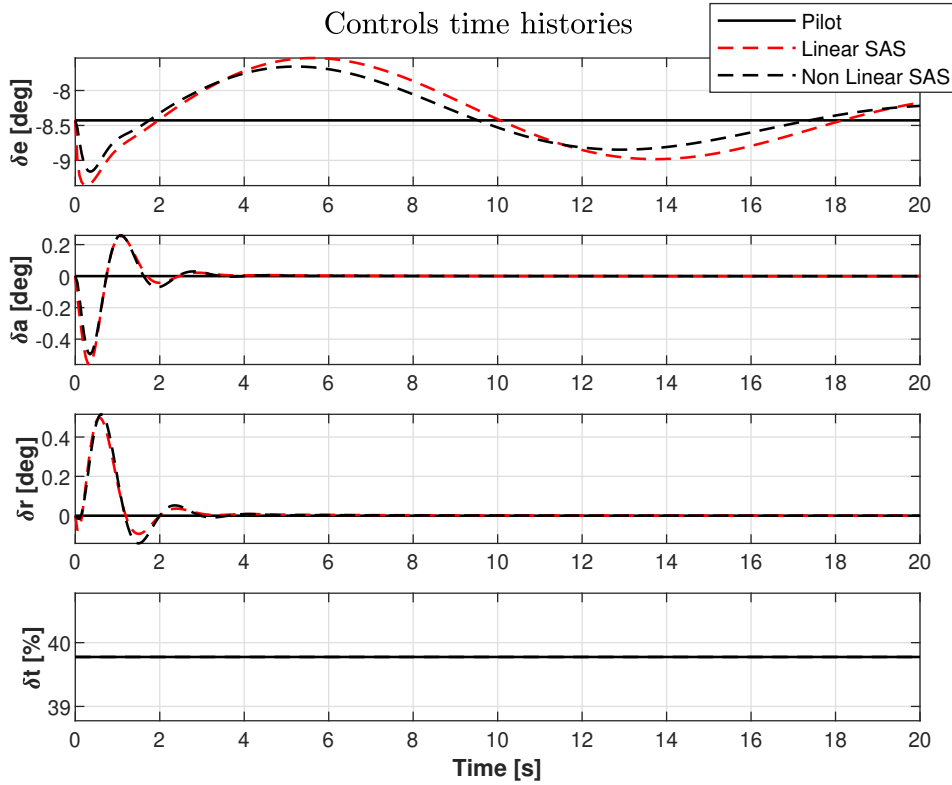


Figure 2.14: SAS control inputs for stabilization around trim condition 2.

2.4.2. Forced Response Testing

The control system is tested also under forced response from an imposed doublet control input on the elevator and aileron. The trimmed condition for this analysis is given by:

Trim condition: $V_{GND} = 180 \text{ km/h}$, $H = 300 \text{ m}$						
α_0	U_0	W_0	q_0	θ_0	δ_{e_0}	δ_{t_0}
0.66 deg	50 m/s	0.58 m/s	0.0 deg	0.66 deg	5.50 deg	58 %

Table 2.7: Trim output at $V = 180 \text{ km/h}$, $H = 300 \text{ m}$.

Analyzing Figure 2.15 and 2.16 for the forced response, the SAS controller operates by dampening the high-frequency oscillations that arise in correspondence to the control input and prevents the triggering of low-frequency oscillations, which can primarily occur around the pitch axis. Overall, the control action doesn't inhibit the commanded input from the autopilot control loop, as evident from Figure 2.17.

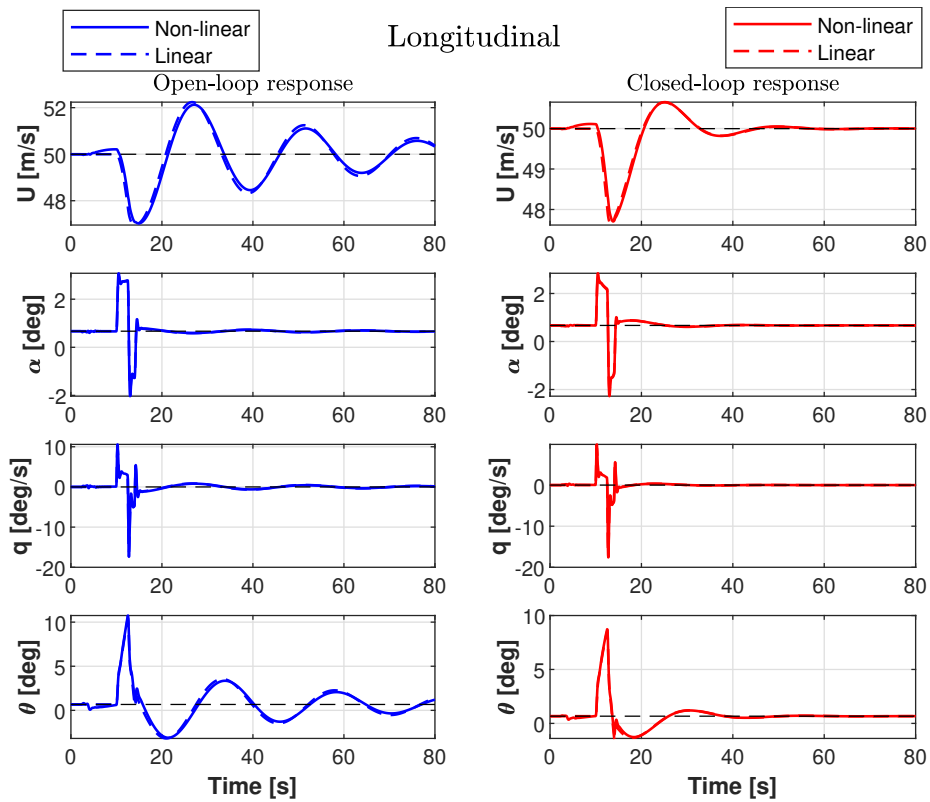


Figure 2.15: Longitudinal states evolution for assigned autopilot inputs. Open-loop (left) vs. closed-loop (right). Linear (dotted) vs. non-linear model.

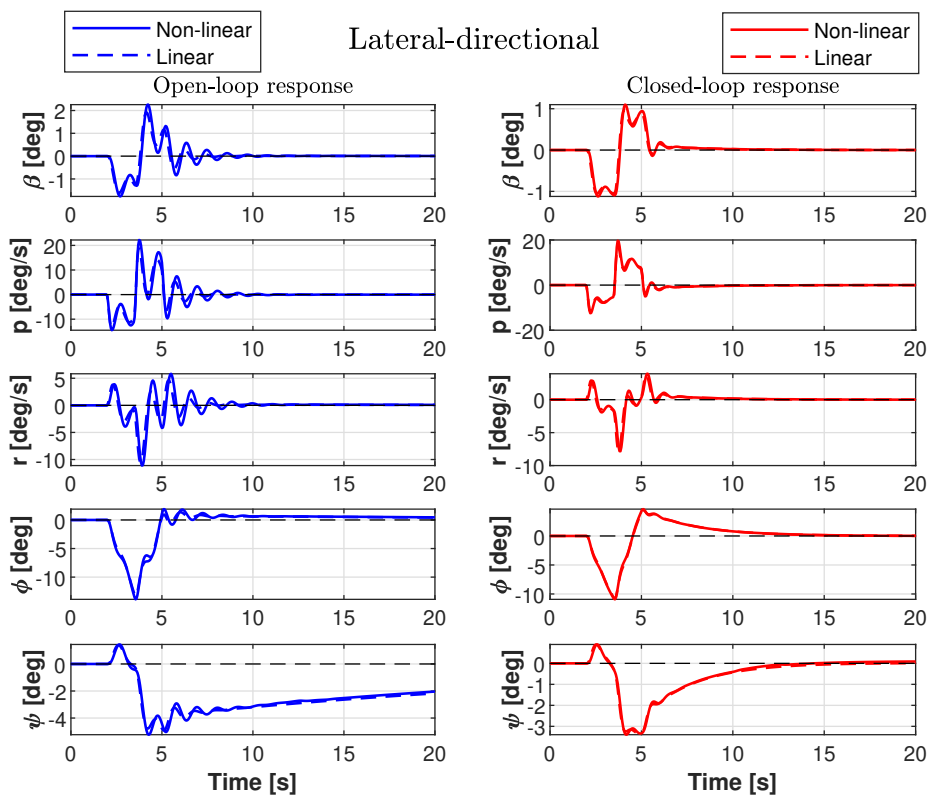


Figure 2.16: Lateral-directional states evolution for assigned autopilot inputs. Open-loop (left) vs. closed-loop (right). Linear (dotted) vs. non-linear model.

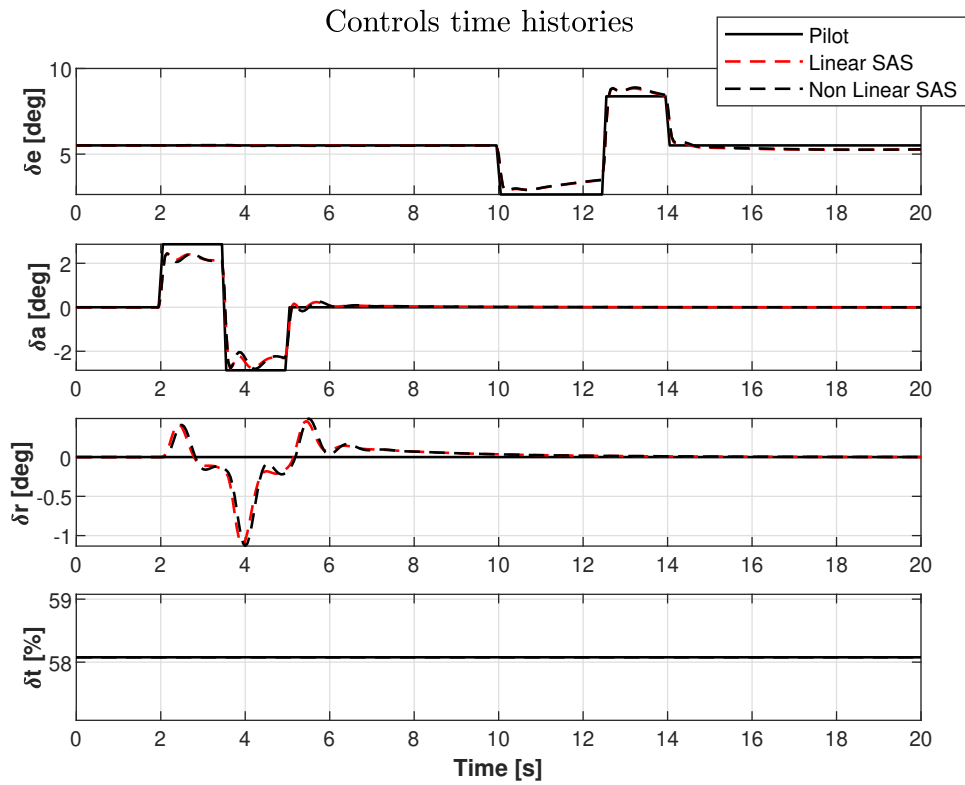


Figure 2.17: Commanded control inputs with SAS enabled.

3 | Single-Aircraft Guidance Algorithms

The synthesis of guidance and navigation algorithms is now under discussion. As briefly mentioned in the previous chapter, each unit within the formation is equipped with an Autonomous Flight Control System (**AFCS**), removing the need for ground station control. Within the AFCS, two aircraft management modes coexist, contingent upon the assigned role (i.e. *Leader* or *Follower*): the Guidance Mode (**GM**) and the Formation Control Mode (**FCM**). The management and interconnection between these two modes will be addressed in the subsequent chapter. At present, it is sufficient to remark that the **GM**-integrated logics to be discussed can be employed by each unit, depending on the mission phase and unit-designated role. Specifically, the following will be analyzed:

- **Beam tracking navigation**, employed during cruise phase or linear ground reconnaissance.
- **Circular trajectory tracking**, availed during loitering or orbital reconnaissance around a fixed target.
- **Rendezvous guidance**, by implementing a specific control to reduce the space and time required for in-flight formation assembly.

3.1. Beam Tracking

Following a pre-assigned set of checkpoints in 3D space, connected by straight legs, is the problem at hand, which is essentially a means to achieve way-point navigation. The purposeful guidance algorithm is inspired by prior work carried out on airship guidance [25, 26]. It essentially relies upon beam tracking logic for both longitudinal and lateral-directional guidance, similar to that used for VOR navigation or ILS systems. This approach encompasses self-contained motion control along longitudinal and horizontal beam planes, defined contingent upon its orientation. This is achieved by introducing a coordinate system fixed on the beam, composed of mutually orthogonal unit vectors,

centered at the departure checkpoint. The coordinate system is defined such that: the unit vector \mathbf{d}_S aligns with the beam and directs towards the destination checkpoint, the unit vector \mathbf{d}_V is orthogonal to \mathbf{d}_S pointing positively upwards, and \mathbf{d}_L completes the triad, indicating rightward direction from above.

A formal definition of the beam-fixed triad with respect to inertial frame \mathcal{F}^I , is herein provided:

$$\mathbf{d}_S = \frac{x_{P_2} - x_{P_1}}{\|x_{P_2} - x_{P_1}\|} \quad (3.1a)$$

$$\mathbf{d}_H = \mathbf{d}_S \cdot \cos \theta_B \quad (3.1b)$$

$$\mathbf{d}_L = \mathbf{i}_3 \times \mathbf{d}_H \quad (3.1c)$$

$$\mathbf{d}_V = \mathbf{d}_L \times \mathbf{d}_S, \quad (3.1d)$$

where: x_{P_1} and x_{P_2} represent the departure and destination checkpoints coordinates respectively, expressed in \mathcal{F}^I , and \mathbf{d}_H is the projection of \mathbf{d}_S on \mathcal{F}^I horizontal plane, through the cosine of the beam elevation angle θ_B .

The core strategy, based on available GPS measurements, is a proportional control logic that aims to minimize the differences between the actual and desired ground speed as well as the vertical and lateral positioning errors with respect to the intended path. Due to the aforementioned distinction between longitudinal and horizontal aircraft motion control, the two control laws will be exposed individually, one at a time.

3.1.1. Longitudinal Beam Tracking

The longitudinal guidance is carried out by the simultaneous employment of throttle and elevator. A primary loop is closed on aircraft ground speed magnitude $|\mathbf{v}_{CG}|$, by adjusting the thrust setting through a proportional control law which aims to reduce the offset from a predefined set-point v_{CG}^* . Introducing the error $e_S = |\mathbf{v}_{CG}| - v_{CG}^*$, the auto-throttle control law writes:

$$\delta_t^{Pilot} = k_p^{e_S} e_S, \quad (3.2)$$

where $k_p^{e_S} < 0$ is selected to amplify the thrust setting when the aircraft's ground speed falls below the desired set-point ($e_S < 0$), and conversely, to reduce it when exceeding the target velocity ($e_S > 0$).

The elevator control is employed for longitudinal precise position tracking by relying on two feedback variables: **vertical displacement error** e_V^{disp} and **vertical velocity error** e_V^{vel} . Indeed, as suggested by [27], it would be impractical to solely rely on position error control. Such an approach would result in a highly reactive control action as the aircraft would lack information on the direction of motion, leading to significant control

inputs even for small position errors. Therefore, the distance between the aircraft CG and the beam is computed in the vertical plane that contains the beam. Geometrically, this can be expressed using the unit vector \mathbf{d}_V as shown in Figure 3.1; \mathbf{d}_V , as mentioned before, is defined to be normal to the straight-line extending from P_1 to P_2 and lies within the vertical plane where the target beam is located. The formal expression for e_V^{disp} is therefore:

$$e_V^{disp} = \mathbf{d}_V \cdot (\mathbf{x}_{CG} - \mathbf{x}_{P_2}) . \quad (3.3)$$

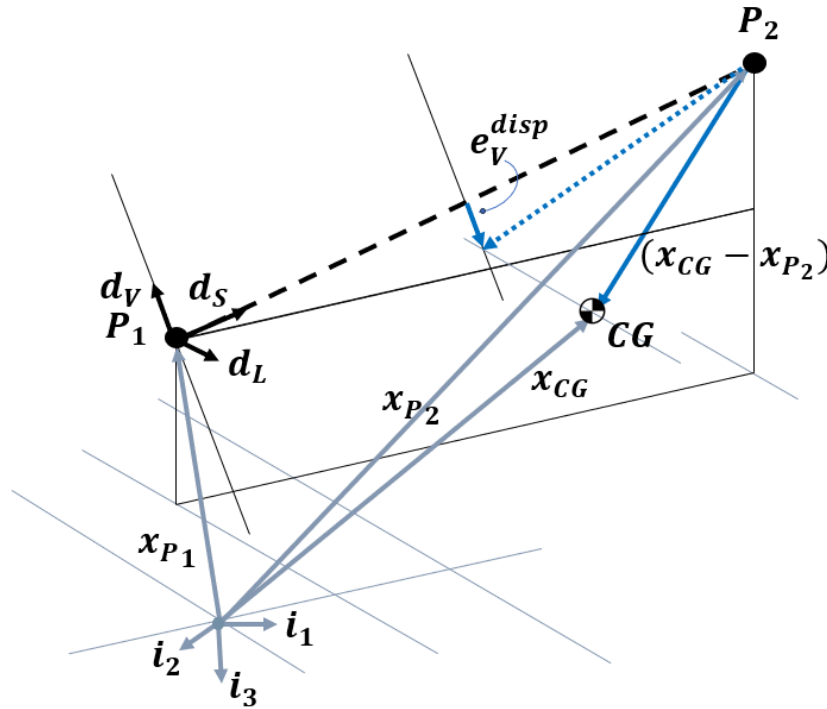


Figure 3.1: Sketch of beam tracking measurement in the longitudinal plane. Definition of e_V^{disp} . Illustration inspired by [25].

The vertical velocity error e_V^{vel} is then computed as the difference between the measured projection of aircraft inertial velocity vector \mathbf{v}_{CG} on \mathbf{d}_V , and a target cross-beam vertical speed v_V^* obtained as a bounded linear function of the cross-beam displacement error e_V^{disp} previously defined.

$$v_V^*(e_V^{disp}) = \begin{cases} v_V^{*,top} , & \text{if } e_V^{disp} < e_V^{disp,bot} \\ \frac{e_V^{disp}}{e_V^{disp,bot}} \cdot v_V^{*,top} , & \text{if } e_V^{disp,bot} \leq e_V^{disp} \leq 0 \\ \frac{e_V^{disp}}{e_V^{disp,top}} \cdot v_V^{*,bot} , & \text{if } 0 \leq e_V^{disp} \leq e_V^{disp,top} \\ v_V^{*,bot} , & \text{if } e_V^{disp} \geq e_V^{disp,top} \end{cases} \quad (3.4)$$

The boundary parameters involved in defining the cross-beam speed can be adjusted as control gains. Specifically, a positive velocity $v_V^{*,top}$, aligned with the \mathbf{d}_V direction, is commanded by the algorithm when reaching the maximum lower deviation limit from the beam, namely $e_V^{disp,bot}$. Conversely, a negative velocity $v_V^{*,bot}$ is commanded upon reaching the upper deviation limit $e_V^{disp,top}$. Finally, a percentage of $v_V^{*,top}$ and $v_V^{*,bot}$ is assigned proportionally to the deviation in cases where the positional error falls within the specified limits. At this juncture, the error e_V^{vel} can be formally defined as:

$$e_V^{vel} = \mathbf{d}_V \cdot \mathbf{v}_{CG} - v_V^*(e_V^{disp}) . \quad (3.5)$$

In order to intuitively capture the measure of $\mathbf{d}_V \cdot \mathbf{v}_{CG}$ term, a geometric sketch is provided in Figure 3.2.

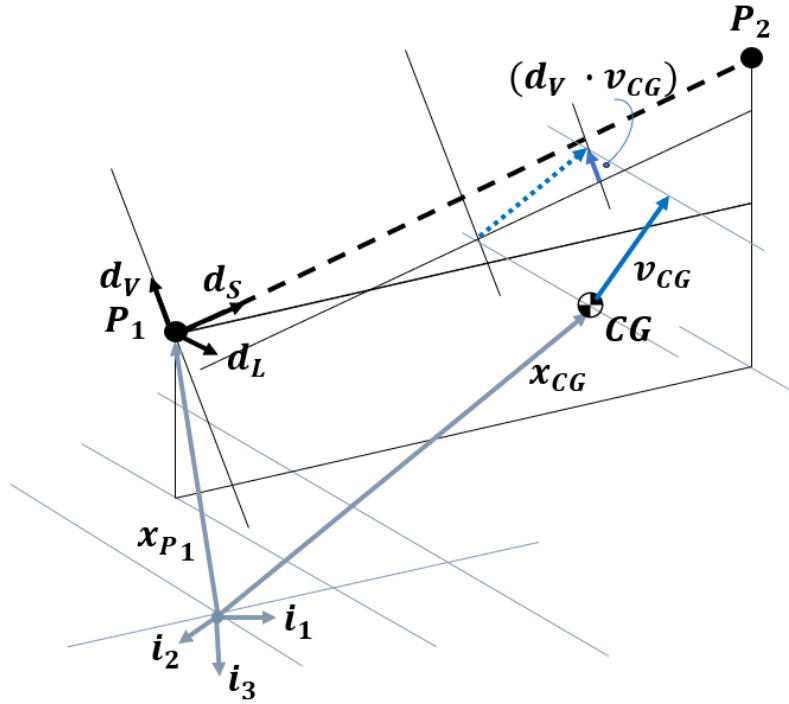


Figure 3.2: Sketch of beam tracking measurement in the longitudinal plane. Definition of $\mathbf{d}_V \cdot \mathbf{v}_{CG}$. Illustration inspired by [25].

Building upon the recently introduced feedback errors, the longitudinal beam-tracking control law for the elevator is assigned:

$$\delta_e^{Pilot} = k_p^{e^{disp}} e_v^{disp} + k_p^{e^{vel}} e_v^{vel} , \quad (3.6)$$

With $k_p^{e^{disp}}$ and $k_p^{e^{vel}}$ to be tuned such that the controller is configured to issue a negative

δ_e^{Pilot} input inducing an upward trajectory curvature when the aircraft is positioned below the beam. Conversely, when the aircraft is positioned above it, the control input is set to a positive δ_e^{Pilot} , directing a trajectory that steers the aircraft down towards the beam. The control action is modulated with fine adjustment of cross-beam speed, in order to approach the correct positioning avoiding abrupt pull-up and push-over maneuvers.

3.1.2. Lateral-directional Beam Tracking

Horizontal guidance is achieved through two cooperative control loops: the first is dedicated to turns coordination, while the second is responsible for actual beam tracking.

Regarding turn coordination, a proportional control law is implemented to generate a rudder deflection that aims to minimize the sideslip angle and bring it closer to zero.

Expressed analytically, the corresponding control law is:

$$\delta_r^{Pilot} = k_p^\beta \beta . \quad (3.7)$$

Conceptually, lateral beam tracking is executed in a akin manner to longitudinal beam tracking. In this case, as well, the control action, assigned to the ailerons, is tailored upon a displacement error, defined as:

$$e_L^{disp} = \mathbf{d}_L \cdot (x_{CG} - x_{P_2}) , \quad (3.8)$$

which represents the projection of CG distance from destination checkpoint P_2 , on the direction encoded by unit vector \mathbf{d}_L . A lateral cross-beam speed error is then measured as the difference between the projection of CG velocity on \mathbf{d}_L , and a lateral rate set-point v_L^* , defined as a bounded linear function of e_L^{disp} :

$$v_L^*(e_L^{disp}) = \begin{cases} v_L^{*,top} , & \text{if } e_L^{disp} < e_L^{disp,bot} \\ \frac{e_L^{disp}}{e_L^{disp,bot}} \cdot v_L^{*,top} , & \text{if } e_L^{disp,bot} \leq e_L^{disp} \leq 0 \\ \frac{e_L^{disp}}{e_L^{disp,top}} \cdot v_L^{*,bot} , & \text{if } 0 \leq e_L^{disp} \leq e_L^{disp,top} \\ v_L^{*,bot} , & \text{if } e_L^{disp} \geq e_L^{disp,top} \end{cases} \quad (3.9)$$

with tunable design parameters $v_L^{*,top}$, $v_L^{*,bot}$, $e_L^{disp,top}$, $e_L^{disp,bot}$, such as, a positive e_L^{disp} arises from flying to the right side of the beam, thus prompting a negative v_L^* adjustment when the maximum deviation $e_L^{disp,top}$ is exceeded, steering the aircraft toward the intended trajectory. Conversely, for a negative e_L^{disp} , the opposite scenario unfolds. A schematic of beam tracking measurements for lateral guidance is provided in Figure 3.3 and 3.4.

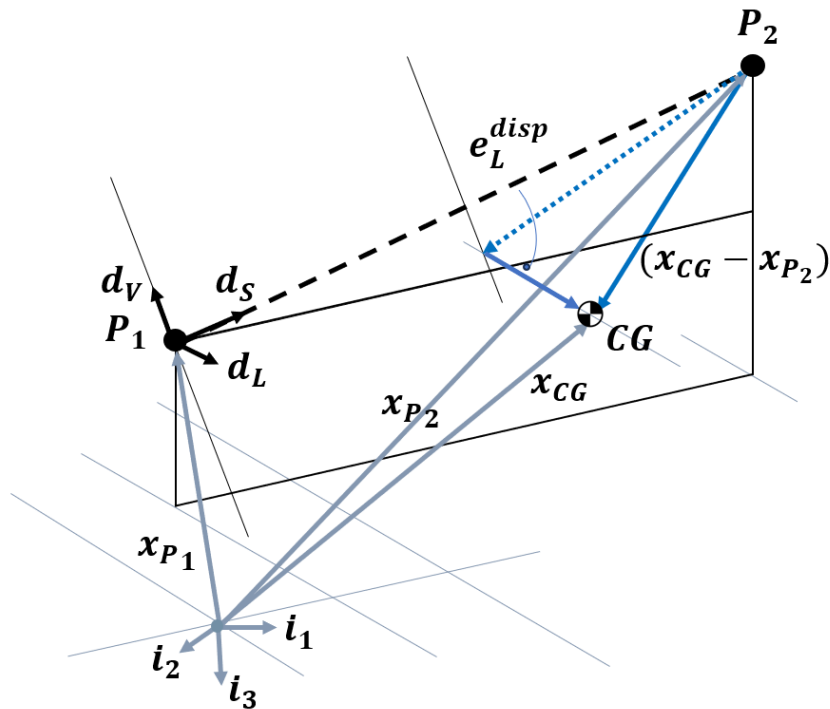


Figure 3.3: Sketch of beam tracking measurement in the beam horizontal plane. Definition of e_L^{disp} . Illustration inspired by [25].

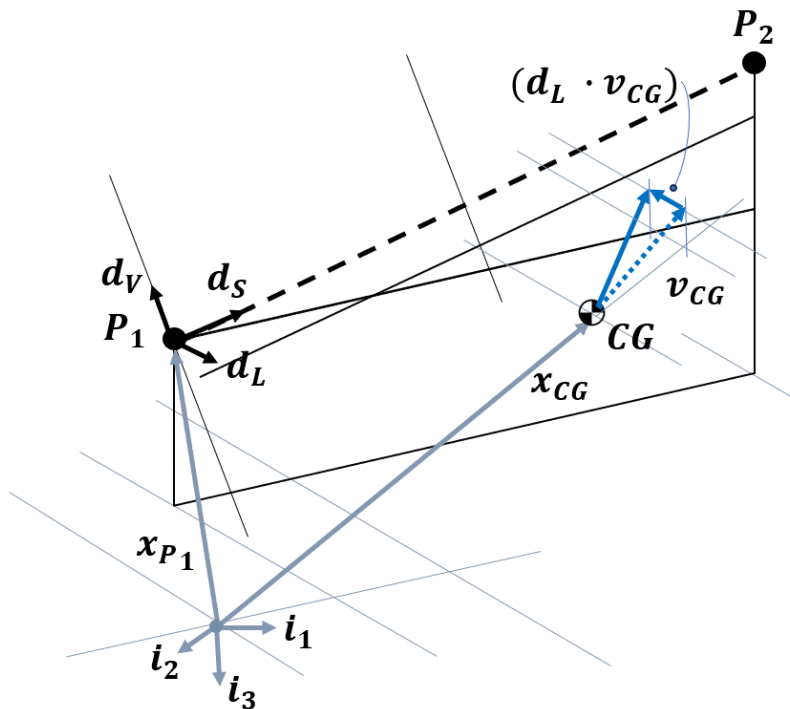


Figure 3.4: Sketch of beam tracking measurement in the beam horizontal plane. Definition of $d_L \cdot v_{CG}$. Illustration inspired by [25].

The analytical expression for e_L^{vel} is then:

$$e_L^{vel} = \mathbf{d}_L \cdot \mathbf{v}_{CG} - v_L^*(e_L^{disp}), \quad (3.10)$$

The control law for lateral beam tracking is derived by merging the two aforementioned feedback errors, resulting in the expression:

$$\delta_a^{Pilot} = k_p^{e_L^{disp}} e_L^{disp} + k_p^{e_L^{vel}} e_L^{vel}. \quad (3.11)$$

3.1.3. Trajectory Blending

During navigation, the aircraft might be assigned a route involving multiple changes in direction, which in turn requires sharp course alterations between successive legs. Engaging the realignment maneuver only after crossing the current waypoint would certainly result in a trajectory overshoot that, at cruising speed, would take the aircraft several hundred meters out of position. To address this issue, an additional variable is incorporated into the controller design, namely, the radius R_p of a proximity sphere centered at the waypoint. When the aircraft enters a position within the spatial confines delineated by the proximity sphere, determined through GPS coordinate comparison, the control system triggers the realignment maneuver, guiding the aircraft toward the subsequent waypoint. An example of waypoint navigation that will be analyzed later in Section 3.4 is depicted in Figure 3.5, where a hexagonal target pattern with multiple staggered checkpoints at different altitudes is assigned.

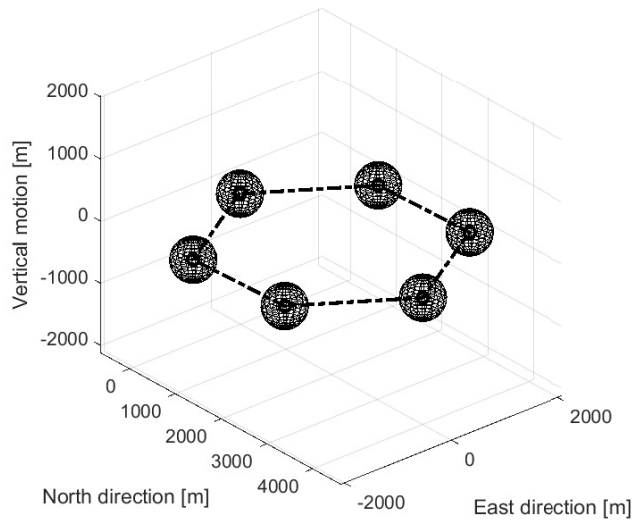


Figure 3.5: Hexagonal pattern target trajectory. Leg length: 2000 m.

The method presented thus far for position control within the context of lateral beam tracking, however, loses effectiveness during abrupt course changes. This is due to the fact that, as soon as the aircraft enters the proximity sphere, the control system instantaneously registers a significant lateral position error. Additionally, it would set the maximum lateral rate value to point the aircraft toward the new leg. The combination of these two errors results in a sharp alteration of the control input, which can lead to unintended oscillations around the target leg or even cause the control input to saturate.

One potential approach could involve reducing the gains $k_p^{eL^{disp}}$ and $k_p^{eL^{vel}}$ within the control law. However, this solution might lead to a decrease in the control system's effectiveness in minimizing lateral position and velocity errors with respect to designated set points. In response, an exploration was conducted to integrate an additional control branch, specifically designed to facilitate trajectory blending.

Conceptually, this involves integrating a course error, such that the control system, by means of a specific proportional gain $k_p^{e\chi}$, aims to minimize the offset between the actual track angle χ (which corresponds to the horizontal azimuth heading ψ in still air) and the designated ground course.

$$e_\chi = \chi^{A/C} - \chi^{track}. \quad (3.12)$$

Exclusive use of this error as the only feedback variable for lateral guidance proves however ineffective. This is because, in order to ensure precise path tracking and rapid response to any disturbances, it is necessary to maintain a fairly high value for $k_p^{e\chi}$, especially compared to $k_p^{eL^{disp}}$ and $k_p^{eL^{vel}}$ (by several orders of magnitude). This approach leads to a situation where, during a change of course along the route, the aircraft quickly aligns itself with the designated course, yet retaining a residual position offset, with respect to the target leg, that remains uncompensated.

To harness both control logics, a concept was conceived to combine them using two variable gains, namely K^{blend} and K^{beam} (one being the reciprocal of the other) as a function of the distance traveled from the departure checkpoint (indeed, it's crucial to underline that every leg is handled as a separate course. Consequently, the destination checkpoint of the current leg transitions into the departure checkpoint for the succeeding leg as soon as the aircraft enters the proximity sphere). This strategy entrusts lateral guidance solely to the course error during maneuvering phases and realignment with the subsequent leg. Meanwhile, once alignment is attained, the control system operates based solely on position and velocity errors, facilitating precise beam-tracking and swift disturbance rejection.

A candidate function suitable for this purpose could be a sigmoid function, which guarantees a smooth transition of gain K^{blend} from 0 to 1 as the aircraft approaches the destination checkpoint shortly before initiating the realignment maneuver. Subsequently, it transitions from 1 to 0 at the outset of the next leg to provide seamless maneuver continuity prior to the activation of the beam tracking control. The analytic expression for the sigmoid function is:

$$K^{blend}(\tilde{d}_{P_1}) = \frac{1}{\left(1 + e^{-p_2(\tilde{d}_{P_1} - L + \varepsilon_2)}\right)} + \left(1 - \frac{1}{\left(1 + e^{-p_1(\tilde{d}_{P_1} - \varepsilon_1)}\right)}\right), \quad (3.13)$$

where \tilde{d}_{P_1} represents the distance covered from the departure checkpoint $\tilde{d}_{P_1} = \|x_{CG} - x_{P_1}\|$, L denotes the length of the current leg, and the parameters p_1 and p_2 are used to regulate the gain's transition rate from 1 to 0 (at the onset of the subsequent leg) and from 0 to 1 (shortly before the realignment maneuver initiation), respectively; ε_1 and ε_2 signify the distances from the starting checkpoint and the destination checkpoint, respectively, at which the transition is intended to achieve the value of 0.5 (mid-transition)

In Figure 3.6, the behavior of K^{blend} is depicted for different values of parameter $p = p_1 = p_2$, along with fixed values for the parameters $\varepsilon_1 = \varepsilon_2 = 400m$. The leg length is $L = 2000m$.

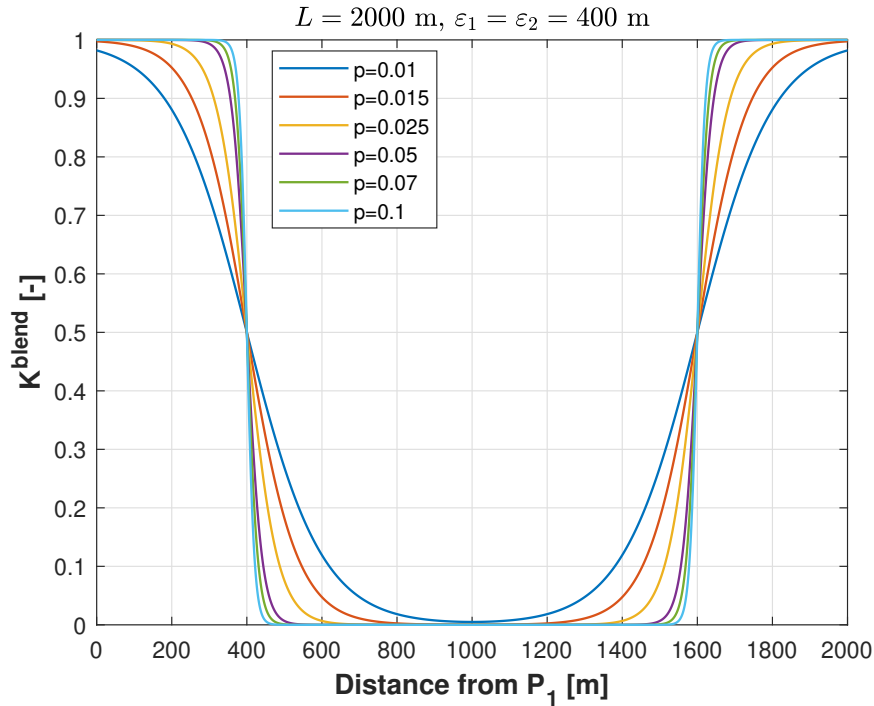


Figure 3.6: K^{blend} behavior for different values of parameter $p = p_1 = p_2$.

Consequently the expression for K^{beam} writes:

$$k^{beam}(\tilde{d}_{P_1}) = \left(1 - K^{blend}(\tilde{d}_{P_1})\right) . \quad (3.14)$$

The lateral guidance control law can be restated by integrating the supplementary control branch for trajectory blending:

$$\delta_a^{Pilot} = K^{beam}(\tilde{d}_{P_1}) \left(k_p^{e_L^{disp}} e_L^{disp} + k_p^{e_L^{vel}} e_L^{vel} \right) + K^{blend}(\tilde{d}_{P_1}) k_p^{e_x} e_x . \quad (3.15)$$

A comprehensive scheme of beam tracking control logic is reported if Figure 3.7.

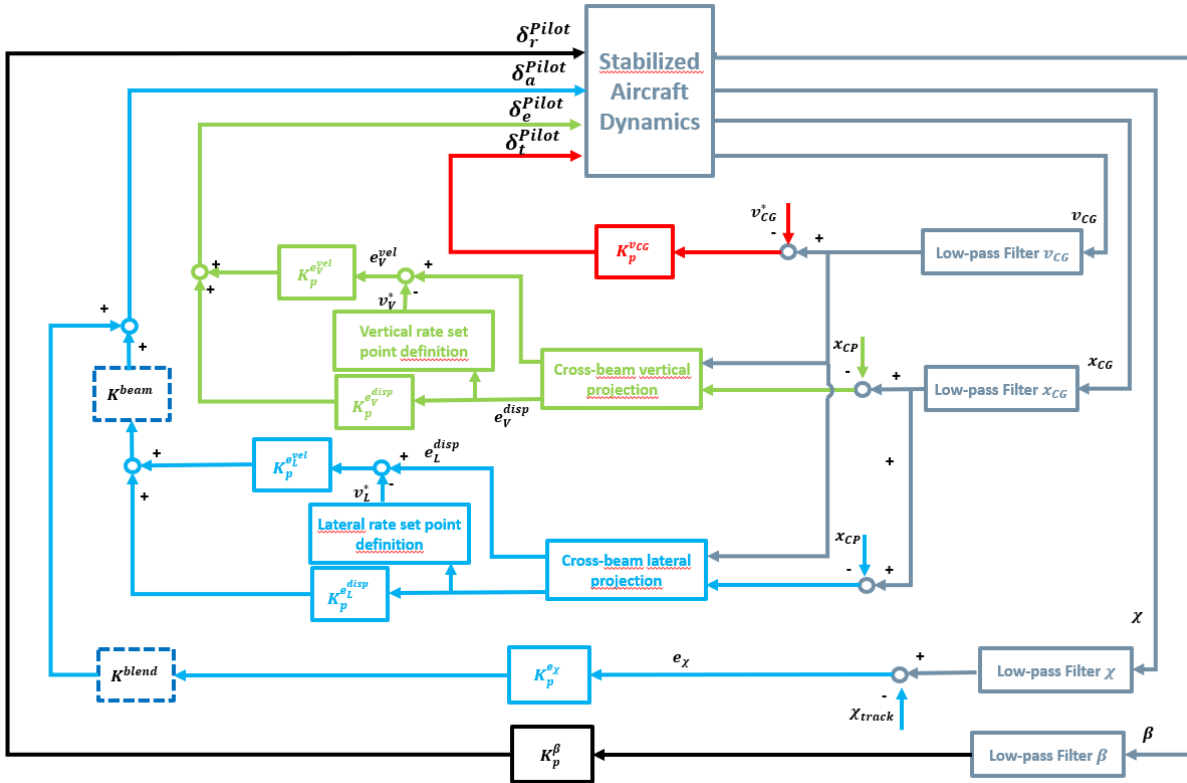


Figure 3.7: Proposed beam tracking control scheme. Red: airspeed tracking. Green: longitudinal beam tracking. Cyan: lateral guidance. Black: turn coordination.

3.2. Circular Trajectory Tracking

For the execution of circular trajectories, inspiration was drawn from several previous works centered around the employment of a vector field-based guidance method ([3, 28]. In contrast to the earlier situation, wherein altitude alterations were attainable via beam tracking, the focus here lies on pursuing a circular trajectory entirely confined within the

horizontal plane of the inertial frame, thus maintaining constant altitude. Furthermore, it's possible to simplify the set of coordinates describing the aircraft's inertial position, namely: $x_{CG} = [x_N; x_E]$, as north and east position's coordinates.

Essentially, the proposed approach aims to asymptotically bring the cross-track error to zero by means of course error e_χ as the only feedback variable for lateral guidance. Consequently, regardless of the UAV's relative position with respect to the required path, the commanded course angle χ_{cmd} must prompt the UAV to move toward the path itself. The ensemble of commanded course angles constitutes what is termed a vector field. This designation is apt as it represents an array of vectors comprising unit course vectors that indicate the desired travel direction.

3.2.1. Orbit path definition

Consider a generic orbit described by following equation:

$$\mathbf{P}_{or}(\mathbf{c}, \rho, \lambda) = \{r \in \mathbb{R}^2 : \mathbf{r} = \mathbf{c} + \lambda\rho [\cos \gamma, \sin \gamma], \lambda \in [0, 2\pi)\} , \quad (3.16)$$

where, \mathbf{c} represents the orbit center, ρ stands for the radius, and γ signifies the phase angle. An additional parameter $\lambda \in \{-1, +1\}$, is introduced to define a counterclockwise/clockwise travel direction.

Upon designating the orbit's radius and center coordinates as $\mathbf{c} = [c_N; c_E]$, it becomes feasible to ascertain the aircraft's polar-coordinate position relative to the orbit. Specifically, $d = \|x_{CG} - \mathbf{c}\|$, as the distance of the aircraft from the orbit center, and the phase angle computed as:

$$\gamma = \arctan \left(\frac{x_E - c_E}{x_N - c_N} \right) . \quad (3.17)$$

3.2.2. Vector Field Generation

Let's define the cross-track error as the distance between the aircraft and the circumference of the orbit, which, in turns, is:

$$\hat{d} = d - \rho. \quad (3.18)$$

Now, it's beneficial to create a suitable function to determine the vector field of unit course vectors based on the cross-track error. This function should operate in such a way that when the cross-track error \hat{d} is large, it guides the aircraft toward the center of the orbit. Conversely, when the aircraft approaches the perimeter of the orbit, the function

should curve the trajectory by $\frac{\pi}{2}$ with respect to the current phase angle (Figure 3.8). This curvature forces the aircraft to follow the tangential direction to the orbit perimeter, according to the orbit travel direction (λ).

Therefore it is possible to express the commanded course angle as:

$$\chi_{cmd} = \gamma + \lambda \left(\frac{\pi}{2} + \tan^{-1}(k_0 \hat{d}) \right), \quad (3.19)$$

with k_0 as a tunable parameter that regulates the transition rate to the orbit path.

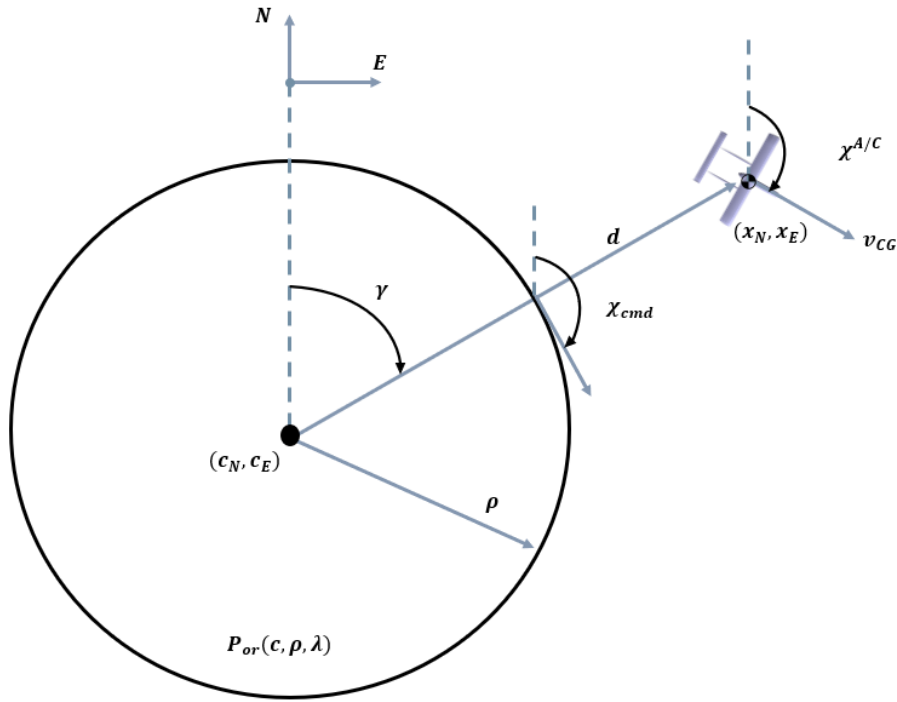


Figure 3.8: Representative sketch for orbit path measurements.

The control structure remains fundamentally consistent with that used for beam tracking (see Figure 3.7). Similarly, the existing control loops for airspeed tracking and turn coordination can be leveraged. The control loop originally employed for longitudinal beam tracking can be adapted for altitude maintenance by choosing checkpoints at the same altitude level. For instance, this could involve selecting a starting point along the orbit's perimeter and the center \mathbf{c} . Lateral guidance is achieved by applying aileron deflections proportionate to the course error $e_\chi = \chi^{A/C} - \chi_{cmd}$, by means of the same gain $k_p^{e_\chi}$ used for trajectory blending:

$$\delta_a^{Pilot} = k_p^{e_\chi} e_\chi. \quad (3.20)$$

An example of a vector field plot for circular trajectory tracking and the effect of k_0

parameter for orbit transition rate adjustment are depicted respectively in Figure 3.9 and Figure 3.10.

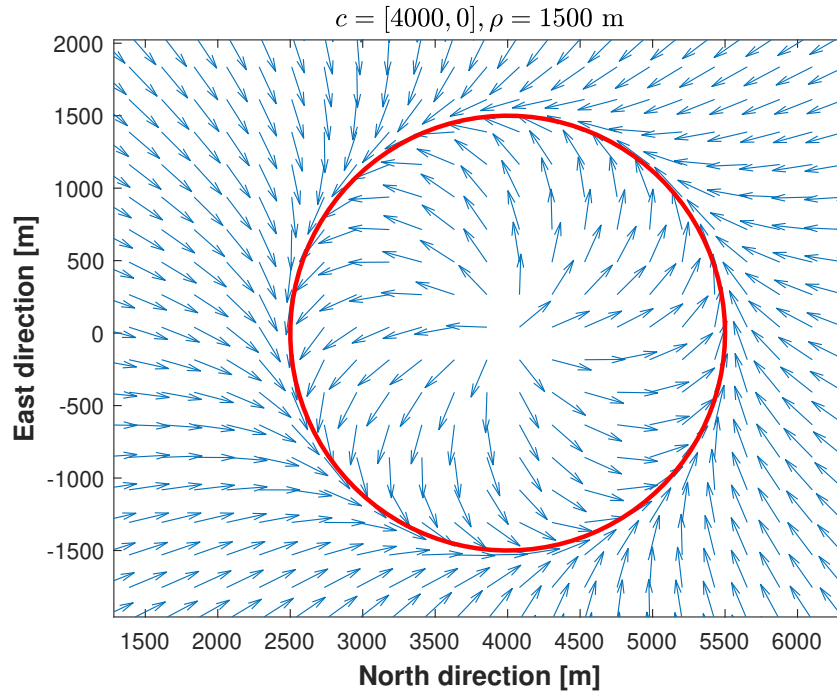


Figure 3.9: Vector field for circular trajectory tracking.

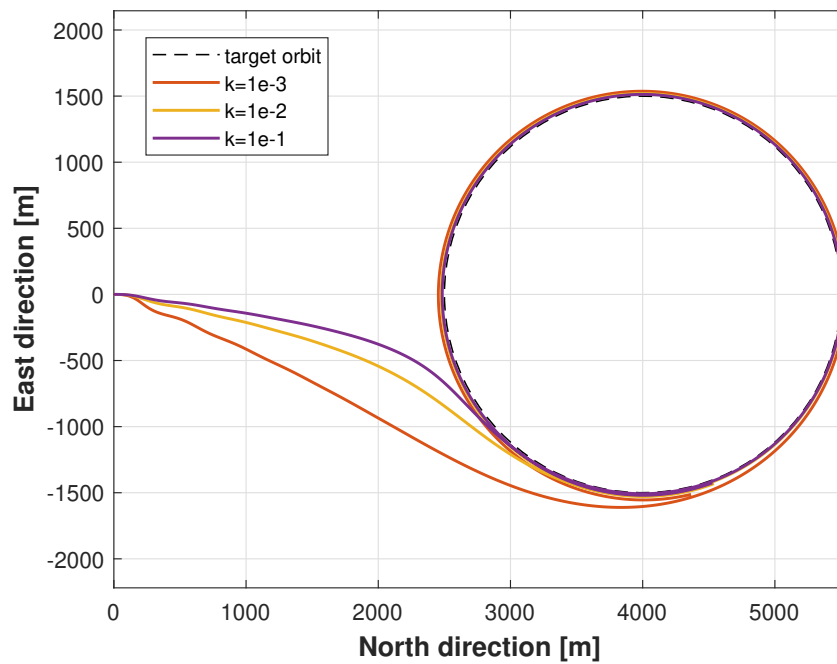


Figure 3.10: Effect of k_0 parameter on orbit transition rate.

3.3. Rendezvous Guidance

The rendezvous problem is now addressed to encompass the scenario of a real-world mission, considering the potential for swarm assembly during flight. This scenario contemplates an initial condition where multiple aircraft approach the rendezvous point from different directions.

There are mainly two possible techniques for achieving an in-flight rendezvous. Let's briefly discuss them.

Linear rendezvous. In the linear rendezvous technique, multiple aircraft converge on a common point along a straight line. This approach is characterized by its simplicity and is suitable for scenarios where vehicles need to assemble quickly. Among the advantages:

- **Simplicity:** straight paths are easier to plan and execute.
- **Flexibility:** can easily incorporate changes in formation size or order.
- **Efficiency:** a straight path allows for direct travel, reducing overall travel time (true with a wide velocity range available).

Meanwhile, the main related challenges are:

- **Vulnerability:** predictable trajectory may make UAVs more susceptible to attacks or disruptive maneuvers.
- **Spatial limitations:** the requirement to follow a straight path may limit flexibility.
- **Wind sensitivity:** wind effects can lead to drift or dispersion among approaching aircraft.

Circular rendezvous. This technique involves aircraft converging on a central point along the circumference of a circle. It comes with its own set of advantages, such as:

- **Redundancy:** circular formation assembly offers redundancy in communication and sensing capabilities as UAVs maintain a continuous line of sight with multiple neighbors.
- **Enhanced situational awareness:** 360-degree coverage allows for improved surveillance and monitoring capabilities.
- **No spatial restriction:** It is possible to safely assemble the formation without the risk of encroachment into hostile territory or collisions due to orographic constraints.

On the other hand, the procedure entails:

- **Increased complexity:** Planning and executing a circular rendezvous requires more advanced navigation algorithms and coordination.
- **Longer duration:** circular rendezvous can take more time to complete compared to linear rendezvous.

Given the aircraft in question, its installed power restricts the attainable range of velocities within the established flight envelope. This constraint may present challenges when contemplating a linear rendezvous scenario, particularly when the aircraft are approaching from considerable distances. Consequently, a preference emerges for the adoption of a circular rendezvous procedure. In this approach, a leader positions itself on a stable circular trajectory and awaits the incoming followers. The followers can perform simple coordination maneuvers to enter the circular path and chase the leader. Additionally, phasing techniques can be employed to expedite the process: these involve tightening the circular trajectory to reduce the phase angle separating the leader from the followers.

The proposed procedure is a fusion of two distinct guidance techniques: the first is based on circular trajectory tracking using the vector field approach discussed in Section 3.2. Aircraft incoming from various directions converge onto a stable circular trajectory. Subsequently, the phasing procedure introduced by [29] for leader chasing comes into play.

3.3.1. Circling Over a Fixed Target

The proposed approach is, in turn, an extension of the author's previous work in which a gradual convergence of the aircraft around a fixed point, the center of the circular path, is ensured, regardless of the initial point and direction [30]. This accomplishment is achieved by imposing an additional component of lateral acceleration beyond that needed for flying steadily on the circumference, proportional to the side-bearing angle η (Figure 3.11), effectively steering the UAV along the intended circular trajectory:

$$a_n = \frac{V^2}{R_{ref}}(1 + K_\eta \sin \eta) . \quad (3.21)$$

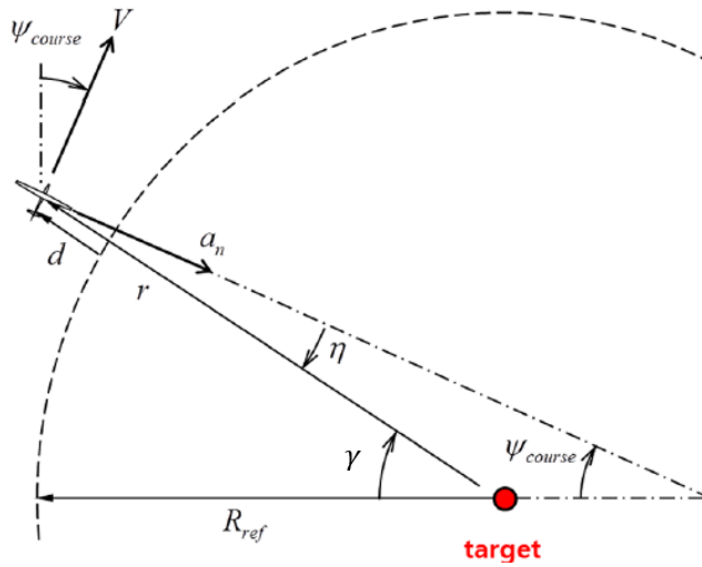


Figure 3.11: Side-bearing angle definition [30].

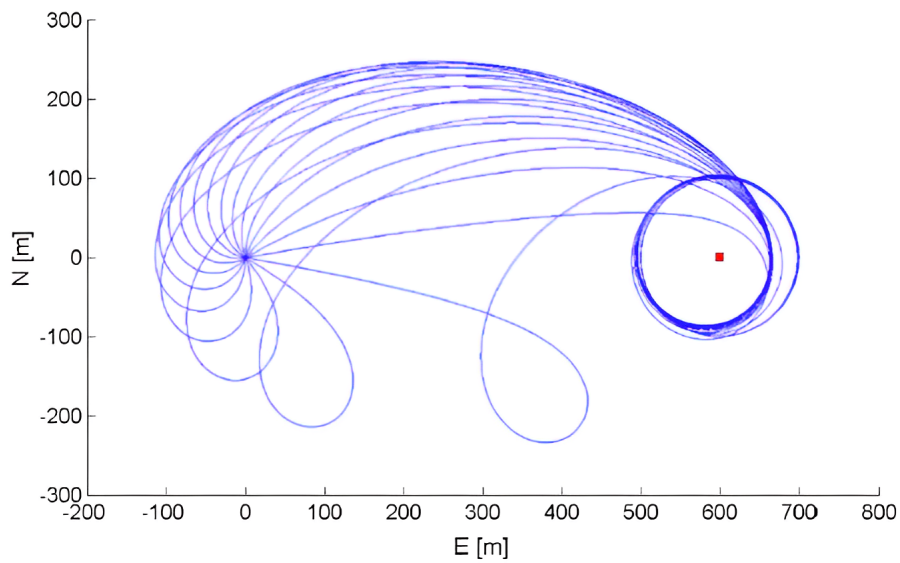


Figure 3.12: Circular trajectory attraction with different initial conditions [30].

A procedure for side-bearing computation using GPS position and velocity is here outlined, referring to Figure 3.13.

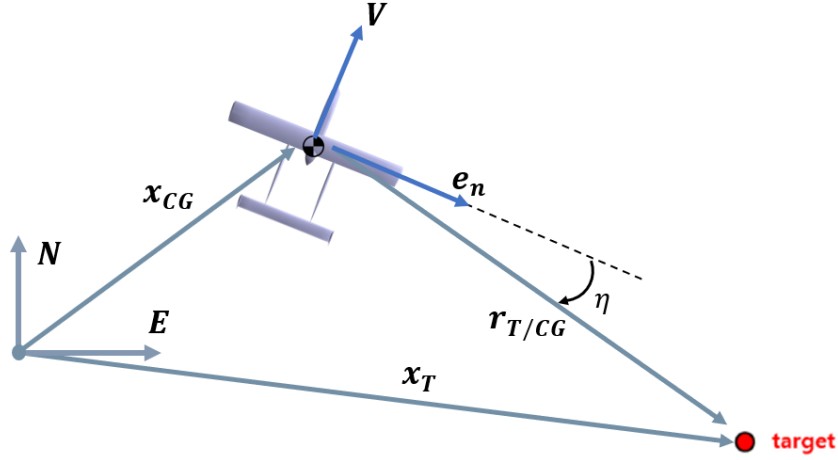


Figure 3.13: GPS-based computation scheme for side-bearing angle.

Let's define the relative position $\mathbf{r}_{T/CG}$ as the vector pointing from aircraft CG toward the orbit center (target): $\mathbf{r}_{T/CG} = \mathbf{x}_T - \mathbf{x}_{CG} = [r_{T/CG}^N, r_{T/CG}^E]^T$. By targeting the inertial velocity components as $[V_N, V_E]^T$, the unit vector normal to the velocity direction is given by:

$$\mathbf{e}_n = \frac{1}{V} \begin{bmatrix} 0 & -1 \\ 1 & 0 \end{bmatrix} \begin{bmatrix} V_N \\ V_E \end{bmatrix}. \quad (3.22)$$

Subsequently, applying the cross product property for the sine of the included angle between \mathbf{e}_n and $\mathbf{r}_{T/CG}$ results in:

$$\mathbf{e}_n \times \mathbf{r}_{T/CG} = |\mathbf{e}_n| |\mathbf{r}_{T/CG}| \sin \eta \mathbf{e}_d = |\mathbf{r}_{T/CG}| \sin \eta \mathbf{e}_d. \quad (3.23)$$

The equation is then solved for $\sin \eta$:

$$\sin(\eta) = \frac{e_n^N \cdot r_{T/CG}^E - e_n^E \cdot r_{T/CG}^N}{\sqrt{(r_{T/CG}^N)^2 + (r_{T/CG}^E)^2}}. \quad (3.24)$$

This guidance procedure, on its own, serves as an alternative to the previously discussed technique for circular trajectory tracking by vector field method. However, the latter is favored because it ensures a swifter entry into the circular path, relying on a more direct and accessible measure over longer distances, which is the course angle χ .

Once the leader has positioned itself within the rendezvous orbit, the followers, as they approach the perimeter, are guided by the phasing procedure specifically designed for leader chasing. At this stage, it is advantageous to rely on lateral acceleration as the control driver to generate small trajectory adjustments that lead the followers to assemble

the formation within the circular path.

3.3.2. Leader Chasing

Motivated by the guidance law in Equation (3.21), a modification is made for the purpose of rendezvous with a reference point (the designated leader) that moves along the circular path. Figure 3.14 shows the geometric scheme that will help to carry out the proposed guidance law. It is assumed that follower's airspeed is set to be equal to the leader's airspeed: $V = V_T$.

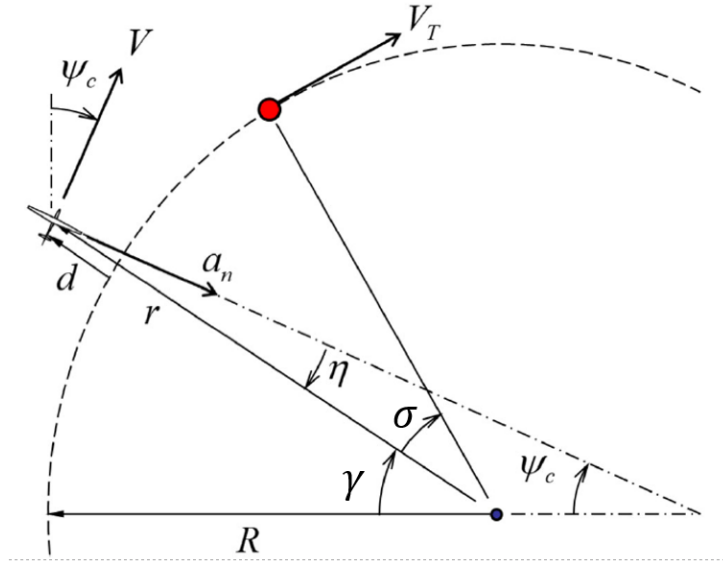


Figure 3.14: Geometric scheme for leader chasing.[29].

The control system then applies a normal acceleration, which is determined by the following expression:

$$a_n = \frac{V^2}{R_{ref}} (1 + K_\eta \sin \eta + K_\sigma \sigma) , \quad (3.25)$$

where $\sigma = \gamma_L - \gamma_F$ is the phase difference between leader and follower, and K_η, K_σ are the design parameters. Hence, in cases where the UAV falls behind the reference point, this modification enables the vehicle to adopt a tighter circular trajectory, facilitating its catch-up with the moving target. It is important to design the radius R to be significantly larger than the UAV's maneuvering limit. This ensures that the control system retains some regulatory control authority in addition to the consistent centripetal acceleration $\frac{V^2}{R}$. Furthermore, this design choice accounts for potential windy conditions where a higher acceleration might be necessary, particularly when circling under a tail-wind condition.

After defining the normal acceleration, it must be converted into a side acceleration, accounting for wind correction. The two accelerations align in still air.

$$a_s = \frac{a_n}{\cos(\chi - \psi)} . \quad (3.26)$$

Finally, a roll angle is directly commanded using the coordinated turn kinematics as follows:

$$\phi_{cmd} = \tan^{-1} \frac{a_s}{g} , \quad (3.27)$$

ϕ_{cmd} is the set point targeted by aileron deflection given by:

$$\delta_a^{Pilot} = k_p^{e_\phi} e_\phi . \quad (3.28)$$

Equation (3.28) represent an alternative feedback control branch for lateral guidance, specifically tailored for rendezvous procedure.

In addition, for faster convergence, it is possible to command an airspeed set point that accounts for phase shift σ by generating adequate thrust settling through the airspeed tracking control loop.

$$V_{cmd} = V_T (1 + k_\sigma^v \sigma) , \quad (3.29)$$

The interaction with the overall guidance control system is ruled through a switching block. Depending on the cross-track error \hat{d} from the orbit perimeter as defined by Equation (3.18), the switch regulates which feedback branch takes priority. If the aircraft is farther away, the guidance priority lies with the course angle tracking (Vector Field-based guidance) and airspeed hold that bring the aircraft close to the rendezvous orbit. Conversely, if the cross-track error is below a defined threshold, the priority shifts to the roll angle and V^* tracking (lateral acceleration guidance), which align the follower phase angle with the leader. A block diagram representing the switch logic between control laws is reported in Figure 3.15. The condition that must be satisfied for the lateral acceleration guidance (lower branch) to take priority is $\hat{d} \leq \hat{d}^*$ where \hat{d}^* is defined as the cross-track error threshold.

For the rest, the control loops outlined for beam tracking (Figure 3.7) still serve their purpose, comprising altitude hold loop and turn coordination loop.

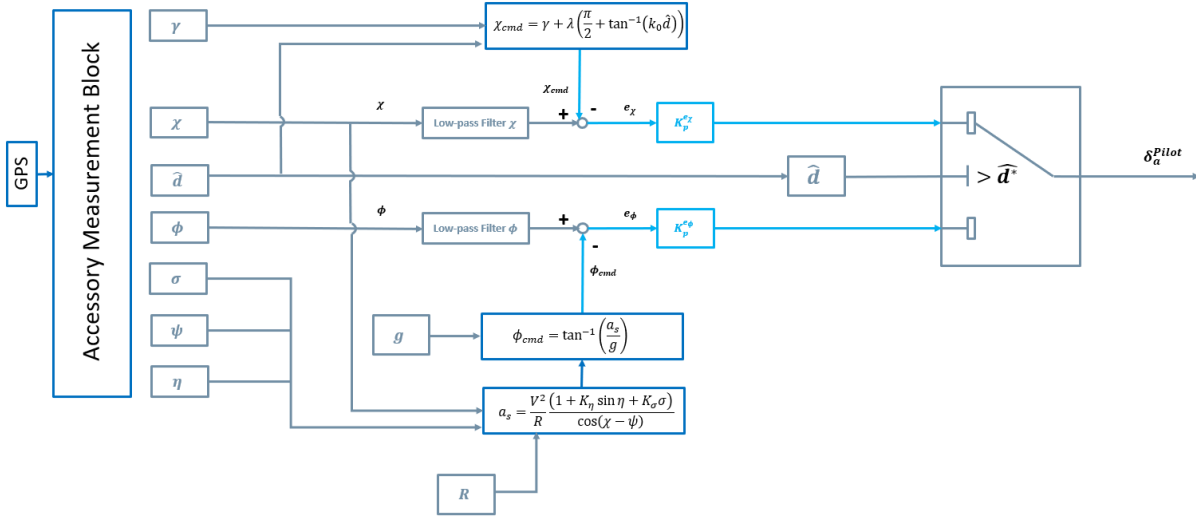


Figure 3.15: Lateral guidance law switch for rendezvous procedure.

3.4. Simulations and Results

In this section, the presented guidance methods are tested by assembling a set of simulations that accurately represent the control system's behavior in realistic scenarios. The simulation results are the outcome of the complex interplay between several design parameters. Therefore, no predefined procedure was employed for gains tuning. Control parameters selection is the result of an iterative process aimed at ensuring satisfactory performance without claiming optimality. A careful analysis of aircraft states time evolution served to eliminate combinations of values that resulted in response divergence, high-frequency oscillations, and undesired couplings while keeping the control inputs away from saturation limits and retaining aircraft states within operational limits. The set of parameters chosen for the testing phase is split into Table 3.1, for beam tracking guidance, Table 3.2 for trajectory blending, and Table 3.3 for circular trajectory tracking, and rendezvous guidance procedure.

Beam Tracking						
Longitudinal						
$k_p^{e_s}$	$k_p^{e_V^{disp}}$	$k_p^{e_V^{vel}}$	$v_V^{*,top}$	$v_V^{*,bot}$	$e_V^{disp,top}$	$e_V^{disp,bot}$
$-3 \cdot 10^{-1}$	$8 \cdot 10^{-3}$	$2 \cdot 10^{-2}$	+3 m/s	-3 m/s	+30 m	30 m
Lateral-directional						
$k_p^{e_\beta}$	$k_p^{e_L^{disp}}$	$k_p^{e_L^{vel}}$	$v_L^{*,top}$	$v_L^{*,bot}$	$e_L^{disp,top}$	$e_L^{disp,bot}$
$-1 \cdot 10^{-1}$	$4 \cdot 10^{-4}$	$6 \cdot 10^{-3}$	+1 m/s	-1 m/s	+10 m	-10 m

Table 3.1: Beam tracking design parameters.

Trajectory Blending				
p_1	p_2	ε_1	ε_2	R_p
$8 \cdot 10^{-2}$	$5 \cdot 10^{-5}$	250 m	700 m	340 m

Table 3.2: Trajectory blending design parameters.

Circular Trajectory / Rendezvous					
$k_p^{e_x}$	k_0	$k_p^{e_\phi}$	K_η	K_σ	k_σ^v
$6 \cdot 10^{-2}$	$3 \cdot 10^{-3}$	$4 \cdot 10^{-1}$	2	$3 \cdot 10^{-1}$	$5 \cdot 10^{-2}$

Table 3.3: Circular trajectory tracking/ Rendezvous guidance design parameters.

3.4.1. Beam Tracking Testing

Three testing scenarios are initially carried out in still air conditions. The first involves a single-leg ascending trajectory with an initial misalignment (Figure 3.16). The second explores a hexagonal path tracking with 60-degree angles between legs and a side length of 2000 m (Figure 3.20). The third envisioned scenario is designed to test the guidance system's ability to handle a quadrangular path with 90-degree heading changes at each checkpoint. Lastly, at the end of this subsection, the hexagonal path will be employed as a testbench for the guidance system's performance assessment under the influence of constant wind. For all forthcoming simulations, the aircraft is initially positioned at the starting checkpoint in a trimmed horizontal flight condition, and the target travel speed for each leg is set at 130 km/h (i.e. 35.9 m/s).

Ascending Track with Initial Misalignment

An ascending track is defined, with a required altitude change of 200 meters over a 2000-meter-long climb path, featuring a 5.7-degree elevation angle. To assess the effectiveness of both longitudinal and lateral-directional tracking, an initial misalignment $\Delta\psi = 40$ deg is introduced. The starting trim condition refers to an altitude of 0 m and a ground speed equal to the defined set point (35.9 m/s). The resulting trajectory is shown in Figure 3.16. For enhanced visualization, the aircraft's representation is included in the plot by sampling its inertial position and attitude every 30-time steps with a 60x scaling factor.

At the starting point, the abrupt altitude change request triggers the longitudinal control, immediately deflecting the elevator to bring the aircraft onto the climb path. Due to the loss of speed, the airspeed hold loop engages, commanding a significant increase in thrust setting until the set point is restored (see Figure 3.16 bottom-right for controls time

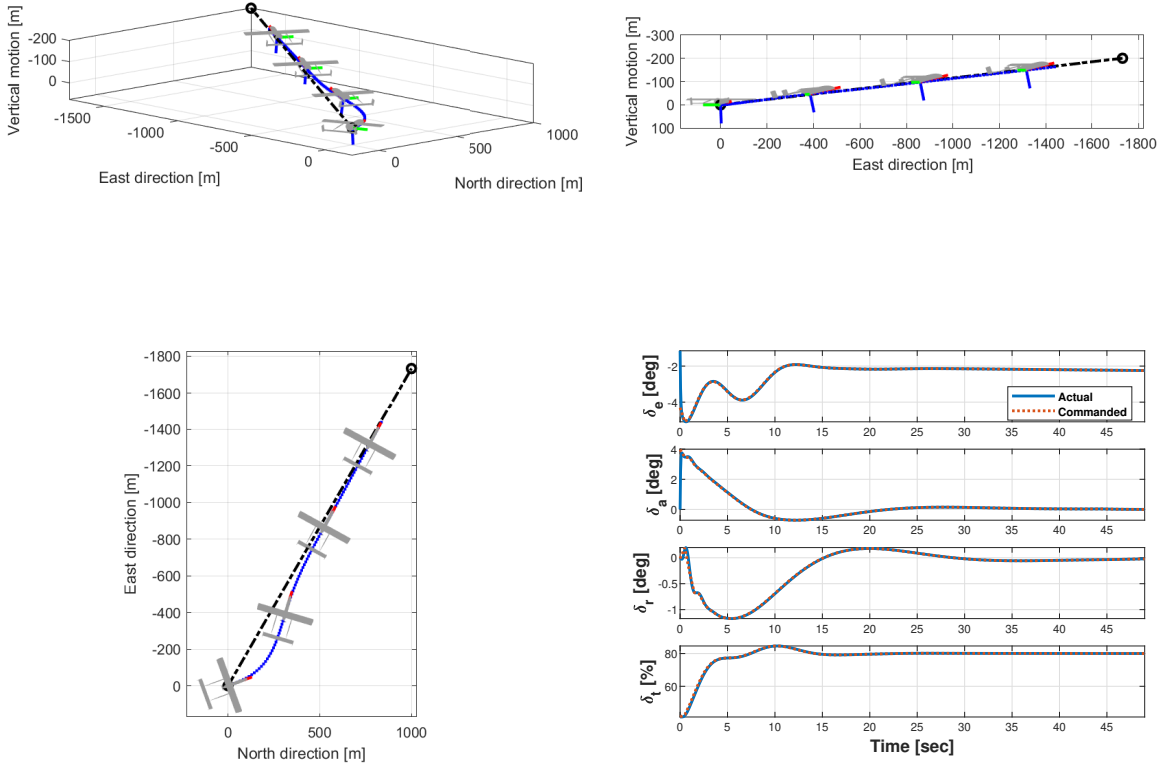


Figure 3.16: Trajectory and control behavior for ascending track with initial $\Delta\psi = 40$ deg misalignment. (**Top-left**) 3D view. (**Top-right**) lateral view. (**Bottom-left**) top view. (**Bottom-right**) controls time histories

histories). Moreover, the initial misalignment causes the aircraft to deviate more than 100 m off course in just a few seconds. The controller takes action by promptly initiating a left turn through coordinated adjustments of the ailerons and rudder, steering the aircraft back to the designated course.

A more comprehensive evaluation of the controller's performance is provided by examining the error profiles reported in Figure 3.17. This analysis also sheds light on how the gains allocated to the control laws for δ_e^{Pilot} , δ_a^{Pilot} and δ_t^{Pilot} impact the system.

By employing higher gains for longitudinal tracking, a swift compensation of vertical velocity and position errors is observed (Figure 3.17a), effectively realigning the aircraft with the desired climb path. However, a residual static error persists, attributed to the interplay between the longitudinal dynamics states and the gain settings for δ_e^{Pilot} and δ_t^{Pilot} . The stronger weighting of the airspeed hold loop imparts a high level of responsiveness to the aircraft concerning the prescribed airspeed setpoint. This, in turn,

hampers the effort to establish a pitch rate sufficient to curve the trajectory for a complete vertical position recovery. Nevertheless, this condition results in a static vertical position error of less than 2 m, a value deemed acceptable in practice.

In order to avoid the onset of oscillations during lateral tracking, it was necessary to assign a higher gain to the lateral velocity error over the position error. Consequently, the controller responds more swiftly to deviations in the lateral rate setpoint than in the actual lateral positioning. This leads to an initial sharp turn followed by a gradual realignment, which occurs only after e_L^{vel} has been canceled.

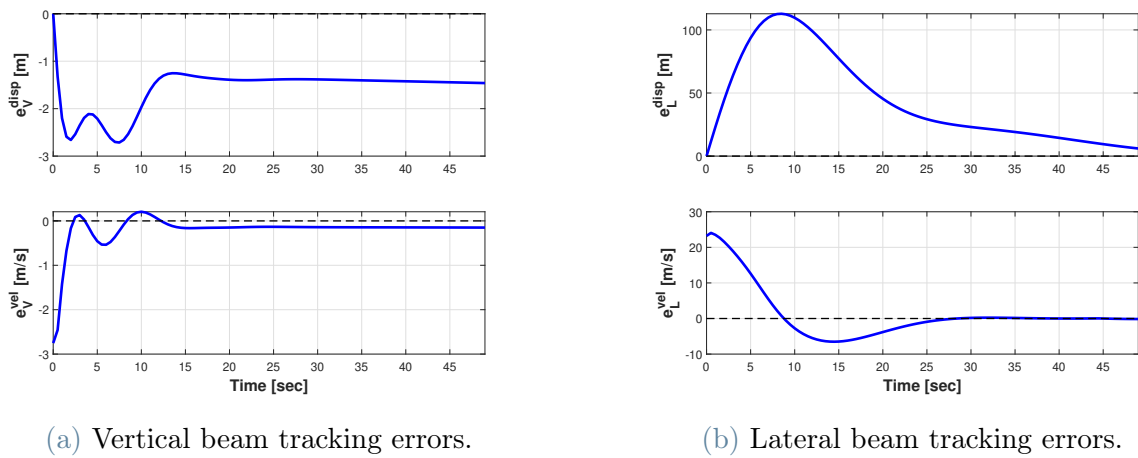


Figure 3.17: Beam tracking errors for ascending track with initial misalignment.

A quick examination of the time evolution of the states in Figure 3.18 reveals how the guidance system successfully trims the aircraft for the desired condition.

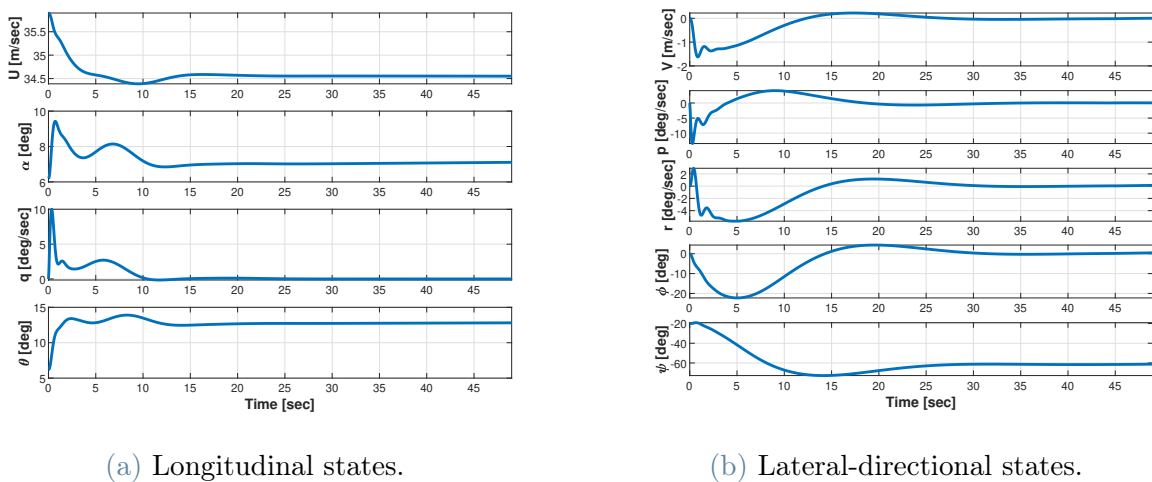


Figure 3.18: Aircraft states evolution for ascending track with initial $\Delta\psi = 40$ deg misalignment.

Hexagonal Path

A hexagonal target pattern with multiple staggered checkpoints at different altitudes is here assigned. The starting point is located at zero coordinates in the following trajectory plots. The mission profile involves five altitude changes between 80 m and 20 m above ground level and six 60-degree heading changes at each checkpoint location. This approach allows us to test the effect of the additional control branch for trajectory blending. A schematic representation of K^{blend} and K^{beam} transition is shown in Figure 3.19, over the actual distance covered from the starting checkpoint (not inertial coordinates North/East). For this representation, two consecutive legs arranged on the same vertical plane were considered, as if the heading change were zero between one leg and the next. Given the regularity of the assigned path, the transition between the two gains repeats in the same way for each pair of consecutive legs.

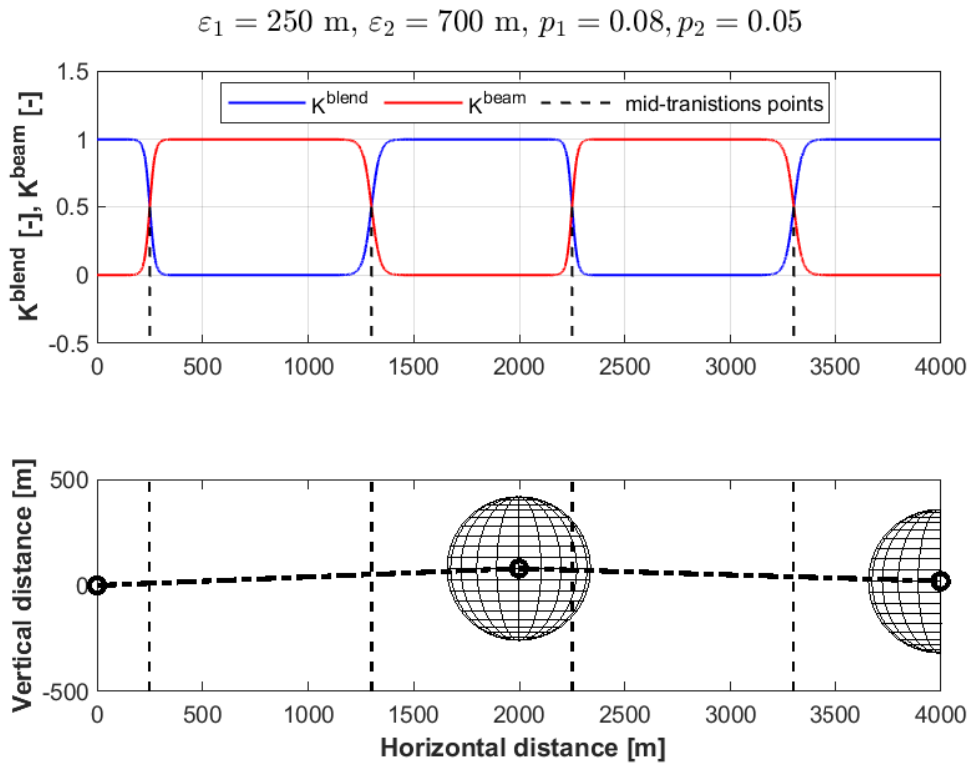


Figure 3.19: K^{blend} and K^{beam} transition over horizontal distance traveled from starting checkpoint.

The trajectory blending control assumes authority well in advance of the turning maneuver's start and hands over control to beam tracking shortly after passing the checkpoint. This allows the aircraft to minimize alignment errors as much as possible before the next

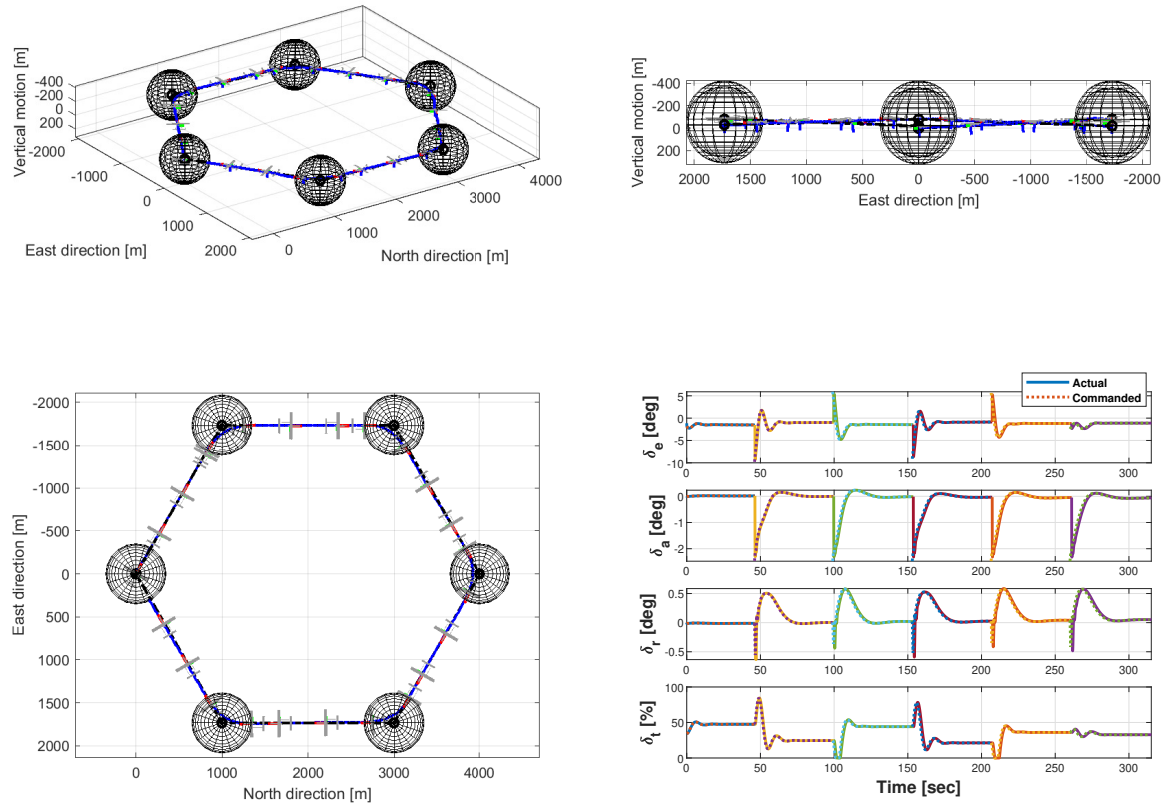


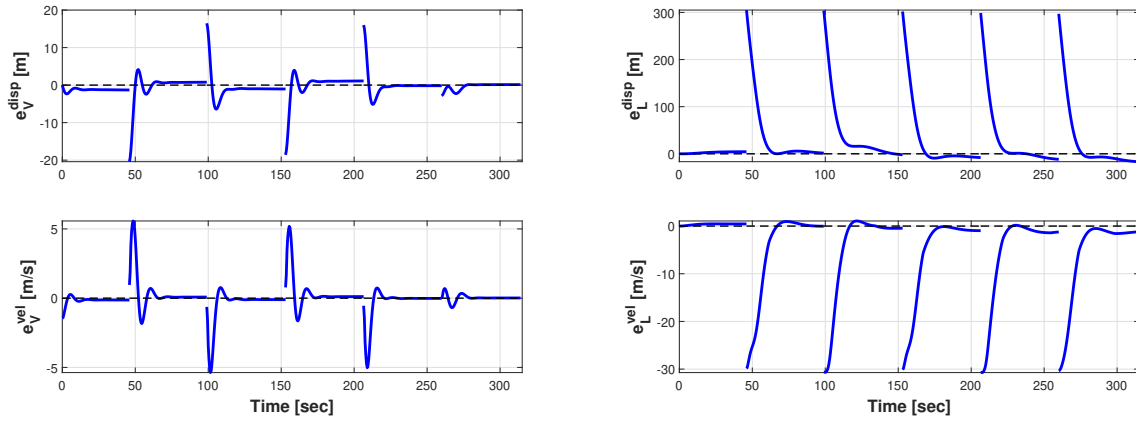
Figure 3.20: Trajectory and control behavior for the hexagonal path. (Top-left) 3D view. (Top-right) lateral view. (Bottom-left) top view. (Bottom-right) controls time histories

heading change.

The control system ensures excellent path tracking without trajectory overshooting at the direction changes. The specific choice for lateral guidance gains allows for a smooth transition between turns and subsequent re-alignment with the next beam, avoiding oscillations. This smooth handling is prominently illustrated in Figure 3.20 (bottom-right). Since the aircraft executes turns with ample lead time before reaching the checkpoint, these are achieved with only a minimal aileron deflection (less than 3 deg) and maintaining roll angles below 20 deg (Figure 3.21). The rudder control is used solely for stabilization and turn coordination.

Observing Figure 3.21, which presents the corresponding errors for vertical and lateral beam tracking, as well as Figure 3.22, depicting the time histories of the states, it is evident that the controller effectively compensates for the cross-track error, rapidly bringing

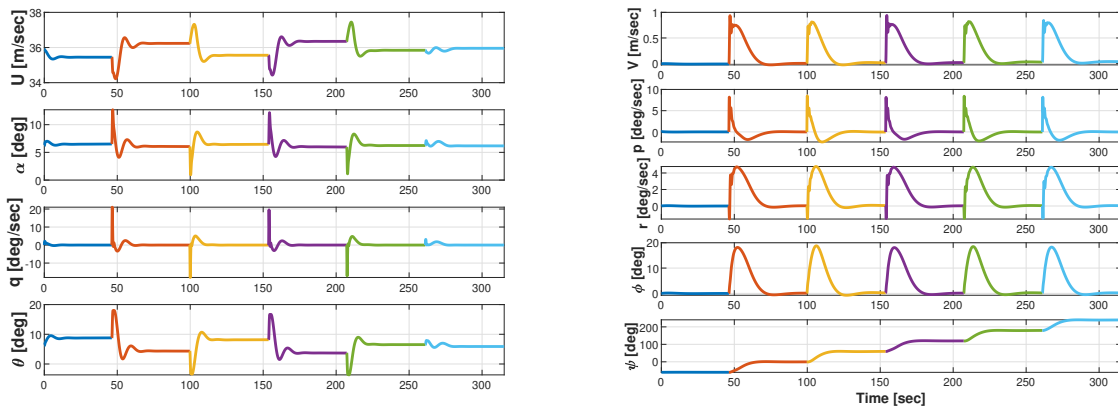
the aircraft toward trimmed condition on each path segment. This behavior proves to be particularly effective in facilitating the coordination of a swarm following a leader based solely on local measurements, without awareness of the planned path and without the ability to implement proactive correction maneuvers.



(a) Vertical beam tracking errors.

(b) Lateral beam tracking errors.

Figure 3.21: Beam tracking errors for the hexagonal path.



(a) Longitudinal states.

(b) Lateral-directional states.

Figure 3.22: Aircraft state evolution for the hexagonal path.

Quadrangular Path

The quadrangular path involves tighter right turns compared to the previous scenario. The maneuver required for path following causes the trajectory blending control branch to complete the turn before achieving the correct lateral positioning. Consequently, the intervention of the beam tracking control becomes evident at the end of the turn when it needs to correct the position error more aggressively than in the previous case, resulting in mild trajectory oscillations that do not completely dampen within the distance of a single leg (Figure 3.23 bottom-right). Nevertheless, these oscillations feature low amplitude and occur over a 30-second duration, making them entirely manageable within the context of swarm coordination.

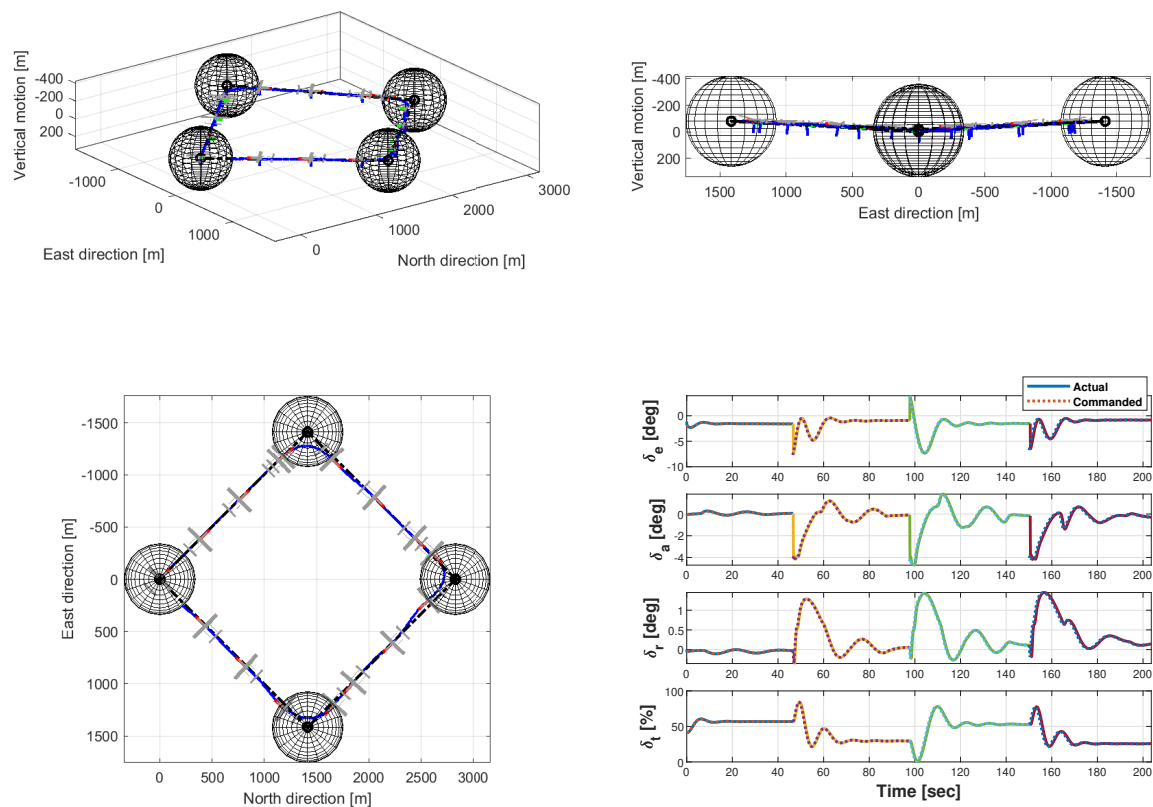
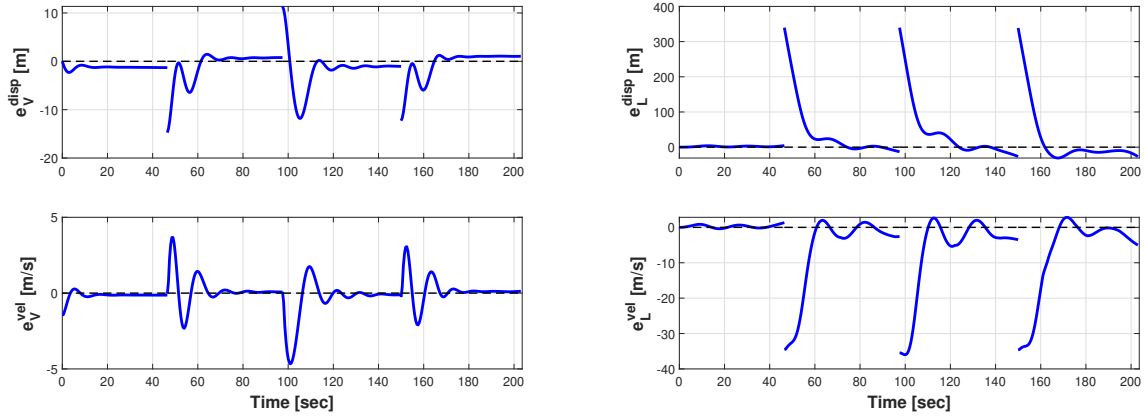


Figure 3.23: Trajectory and control behavior for the quadrangular path. (Top-left) 3D view. (Top-right) lateral view. (Bottom-left) top view. (Bottom-right) controls time histories

In this case as well, the errors related to beam tracking, as shown in Figure 3.24 consistently stay within a narrow range around zero. This provides assurance of the reliability

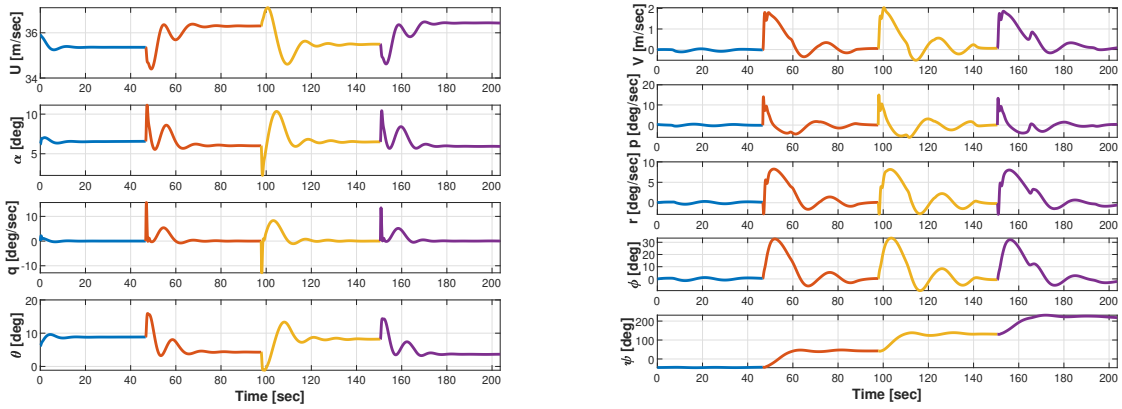
of the guidance system even in this scenario. To complete the analysis, the temporal evolution of the states is presented in Figure 3.25.



(a) vertical beam tracking errors.

(b) Lateral beam tracking errors.

Figure 3.24: Beam tracking errors for the quadrangular path.



(a) vertical beam tracking errors.

(b) Lateral beam tracking errors.

Figure 3.25: Aircraft states for the quadrangular path.

Hexagonal Path with Constant Wind

Extensive testing has been conducted, considering windy conditions that have been easily incorporated into the SILCROAD environment, which supports both stochastic and deterministic wind modeling. Sample result under the influence of a constant 5 m/s, 30 deg heading wind is herein presented. The presence of a constant moderate-intensity wind

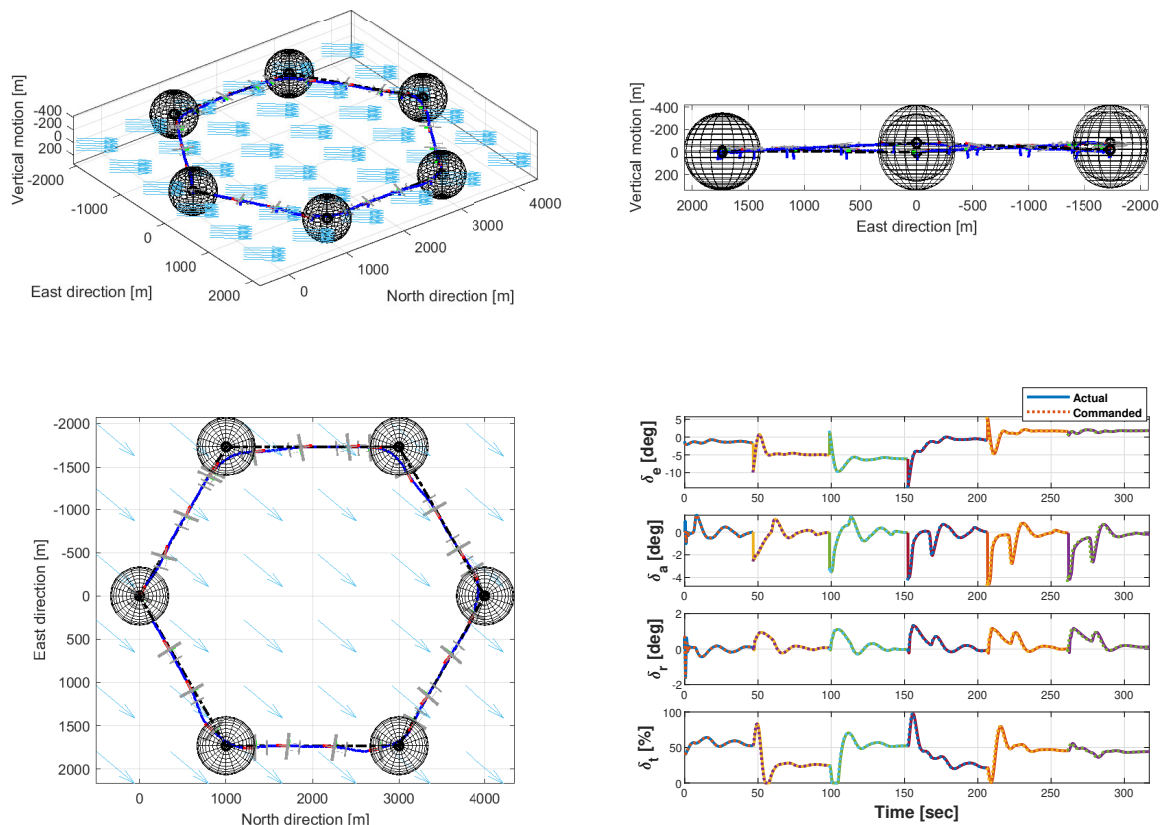


Figure 3.26: Trajectory and control behavior for hexagonal path with 5 m/s constant wind. (Top-left) 3D view. (Top-right) lateral view. (Bottom-left) top view. (Bottom-right) controls time histories

does not significantly impact the effectiveness of the guidance system, which maintains the aircraft on the designated path quite satisfactorily. However, there is a noticeable increased fluctuation in the control inputs (see Figure 3.26 bottom-right) with respect to the previous case, especially on the lateral-directional controls, which must coordinate and manage both the reduction of the wind-induced sideslip angle and the lateral beam tracking.

The effect of wind is also noticeable in vertical tracking. Examining the errors in Fig-

ure 3.27, it's apparent that in path segments where the wind is nearly aligned with the aircraft's travel direction, the control system struggles to maintain correct positioning. Specifically, in legs 2 and 3, the significant tailwind component results in an airspeed reduction, concurrently causing a decrease in altitude. This triggers the swift response of the autothrottle control loop, making the aircraft stiffen around the pitch axis. The opposite effect is observed in path segments 5 and 6, where most of the wind velocity is head-on to the aircraft.

The aircraft states time evolution is reported in Figure 3.28.

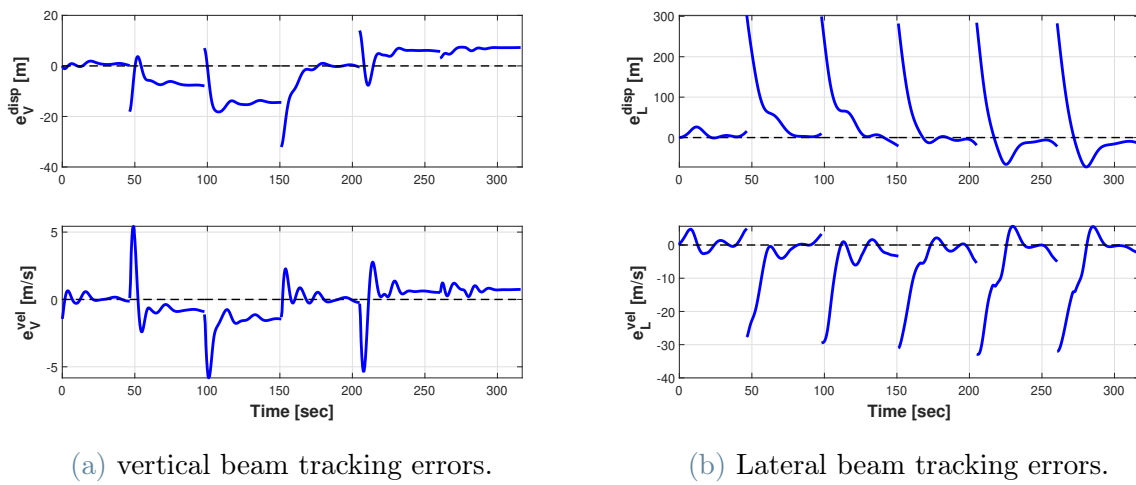


Figure 3.27: Beam tracking errors for hexagonal path with 5 m/s constant wind.

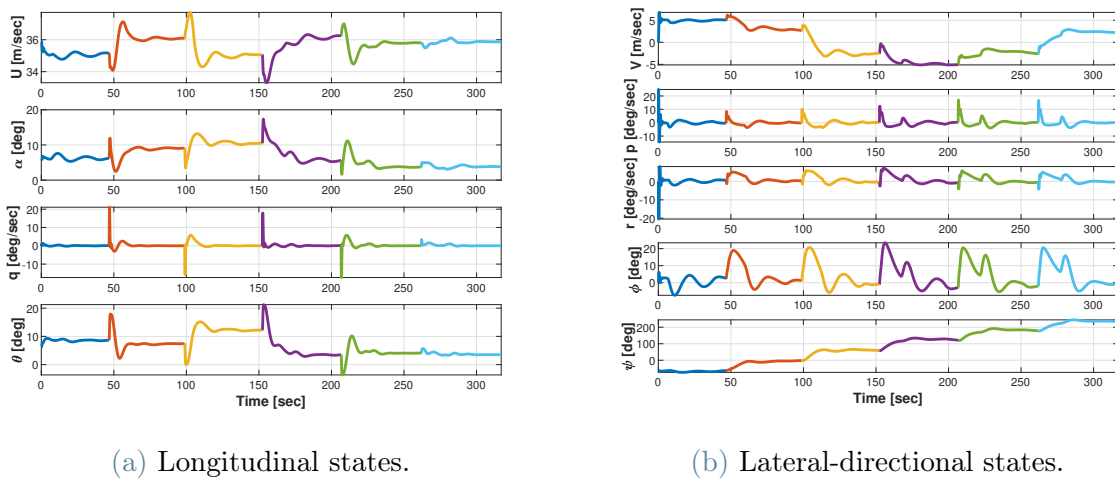


Figure 3.28: Aircraft states for hexagonal path with 5 m/s constant wind.

3.4.2. Circular Trajectory Tracking Testing

For the guidance method under evaluation, an orbit with a radius of 2000 m and center coordinates at $c=[4000,0]$ is assigned. The orbit is set at a constant altitude, to be traveled at 130 km/h ground speed. The resulting trajectory and controls behavior from the simulation are shown in Figure 3.29. The trajectory output is also depicted in the

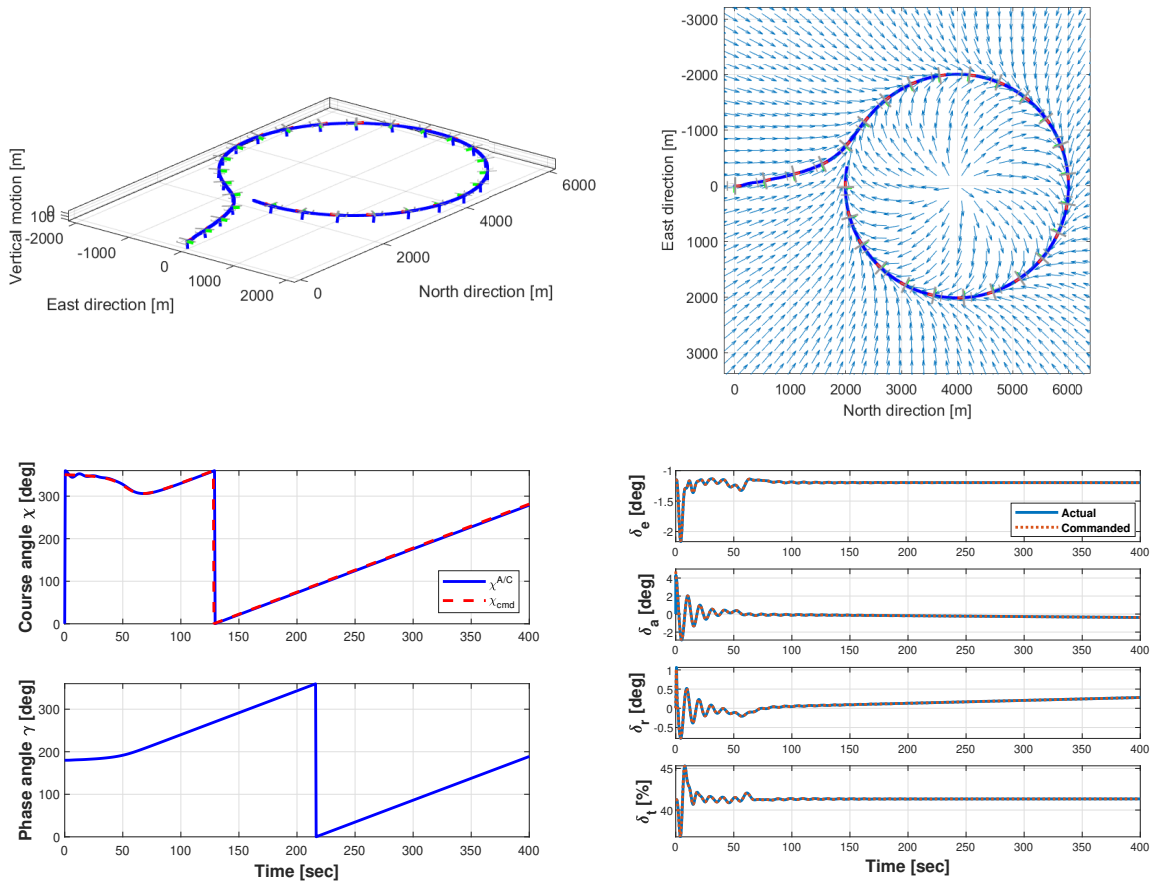


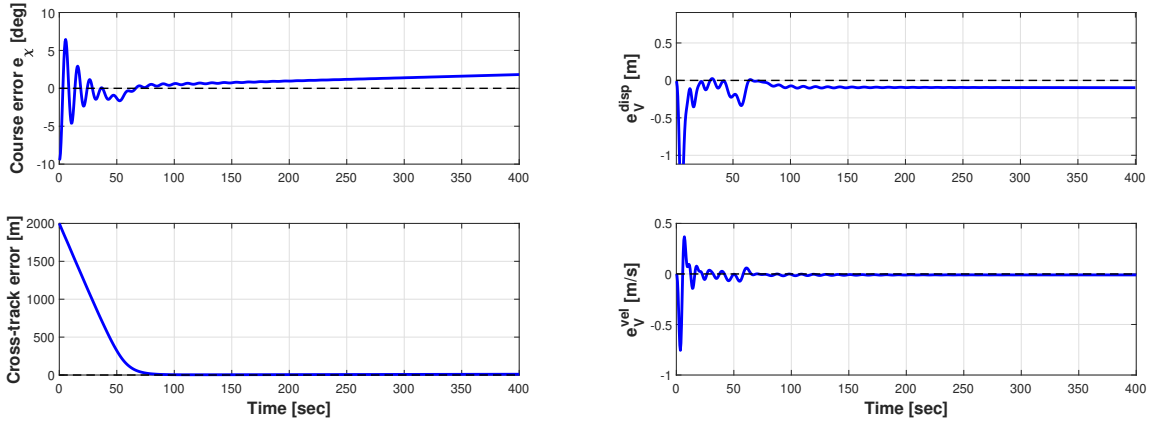
Figure 3.29: Trajectory and control behavior for circular path with $R = 2000$ m and center coordinates $\mathbf{c} = [4000, 0]$. (**Top-left**) 3D view. (**Top-right**) top view with vector field. (**Bottom-left**) trajectory angles. (**Bottom-right**) controls time histories

bottom-left subfigure, showing the sequence of course angles set by the vector field and the phase angles as they are swept while proceeding along the circuit in a clockwise direction. According to the driving logic and as confirmed by the graph, a phase quadrature is observed between these two trajectory parameters.

With reference to Figure 3.29 bottom-right, it's noticeable that at the initial instant, the elevator and throttle promptly adapt to the new required airspeed and altitude conditions. The aileron and rudder exhibit an initial oscillatory behavior due to the instantaneous

demand to align the aircraft with the route established by the vector field. Given the wide radius of the orbit, the controller enacts minimal aileron and rudder deflections that are coordinated to initiate an initial left turn to enter the orbit and subsequently establish an almost flat continuous right turn to keep the aircraft on the circuit.

In Figure 3.30, the errors for lateral tracking, including course error and cross-track error, as well as vertical tracking errors, are depicted. It's observed that despite a slight divergence in the course error (the issue might find a solution by introducing a specifically customized course-hold control loop with adaptive modification, as elucidated in [3], it remains below 5 degrees throughout the orbit's travel, ensuring an effective reduction of the cross-track error to zero. As an indicator for vertical tracking, the same errors as in the vertical beam tracking case are used since the same control loop is involved.



(a) Course and cross-track errors.

(b) Vertical position and velocity error.

Figure 3.30: Circular trajectory tracking errors.

When reducing the orbit radius, oscillations in the trajectory become apparent, necessitating a revision of the guidance gains. A brief insight is presented below with the assignment of an orbit with a radius of $R = 300$ m (Figure 3.31). Lowering the gains results in a slight performance degradation with a static error of approximately 5 degrees on course error and 40 m on the cross-track error (Figure 3.32b).

Nevertheless, it is possible in this way to ensure stable trajectory tracking avoiding prominent oscillations, which is an essential condition for the safe handling of formation flight. This is achieved despite a cross-track position offset that can be resolved through the implementation of an integral contribution in the feedback loop or through the adaptive modification earlier mentioned.

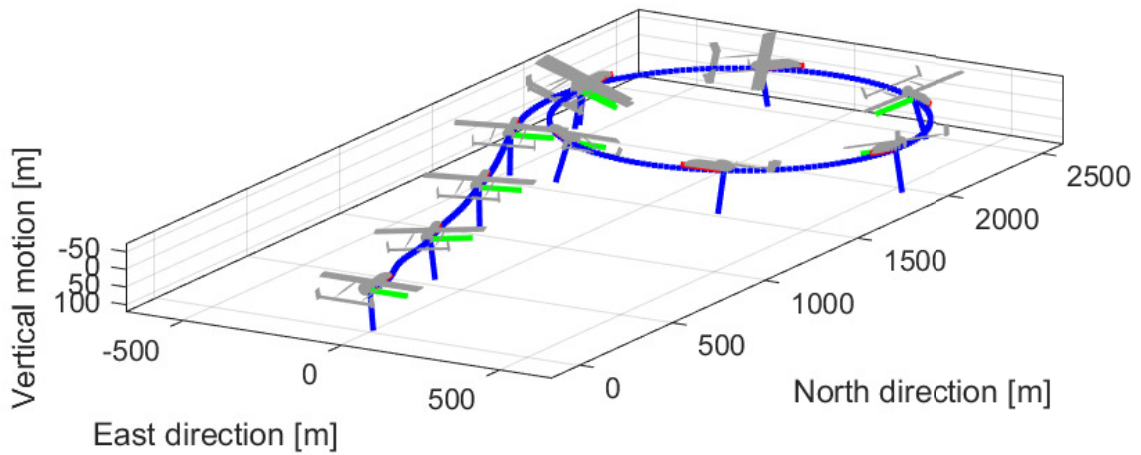
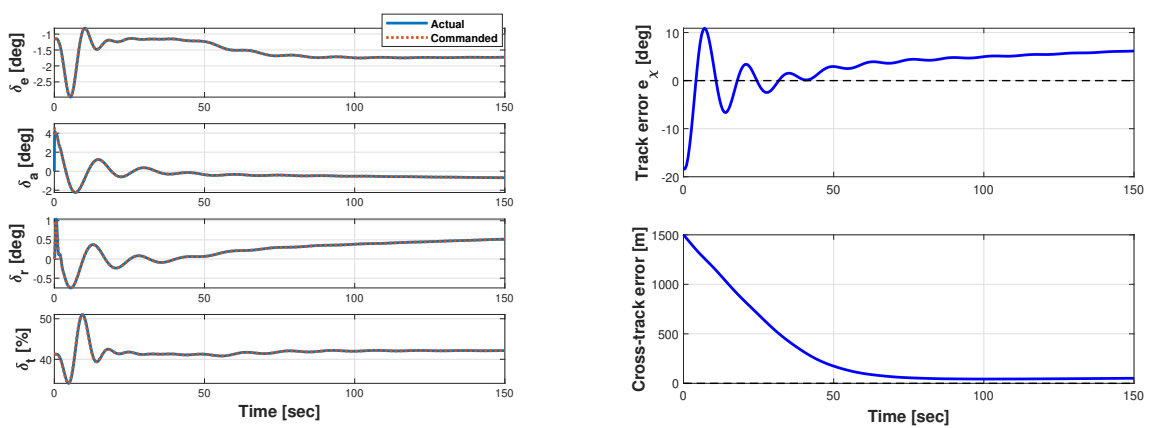


Figure 3.31: 3D trajectory view for circular path with $R = 300$ m and center coordinates $\mathbf{c} = [1800, 0]$.



(a) Controls time histories.

(b) Tracking errors.

Figure 3.32: Control time histories and trajectory tracking errors for circular path with $R = 300$ m and center coordinates $\mathbf{c} = [1800, 0]$.

3.4.3. Rendezvous Testing

Rendezvous guidance without velocity control

In this section, the proposed procedure for formation rendezvous is tested. This marks the first introduction of a scenario involving multiple aircraft, whose trajectories are co-simulated within the SILCROAD environment. At this stage, they are non-cooperative entities: one aircraft is designated as the leader (in blue) and is placed on the assigned rendezvous orbit with a radius of $R=1200$ m and center coordinates at $\mathbf{c} = [2500, 0]$. Two followers (in red) approach the orbit from different directions: one from the west and the other from the southwest. As they near entry into the circuit, the rendezvous procedure is engaged, guiding the followers onto a tighter circular path until they completely recover the phase shift with the leader. An event function is employed to halt the simulation once both followers are within 50 m of the leader.

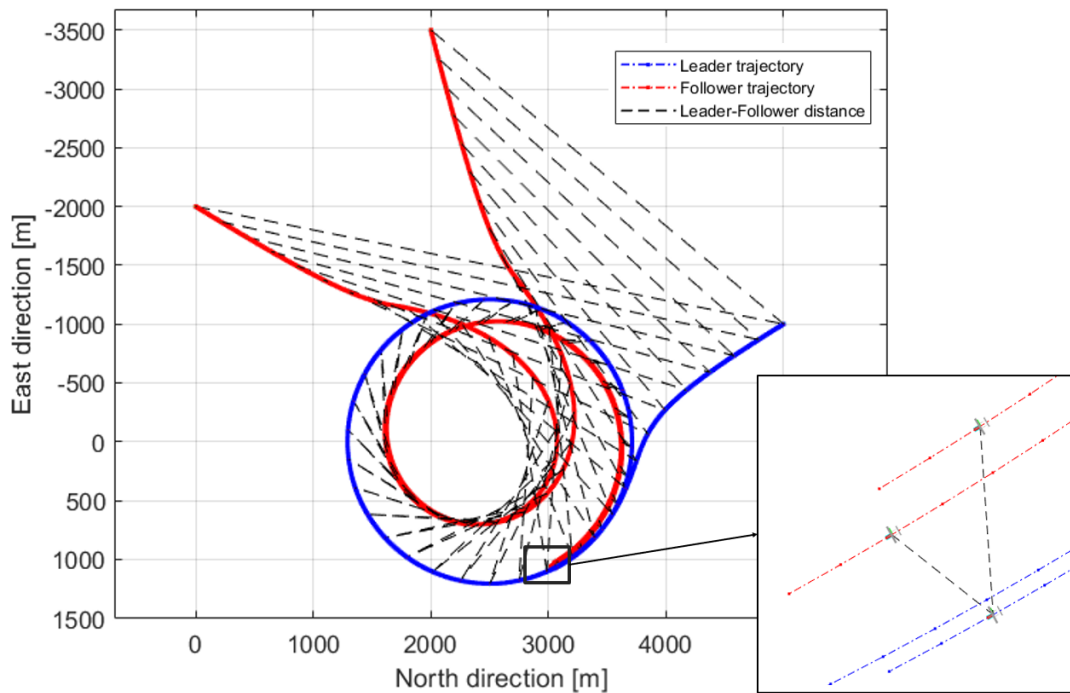
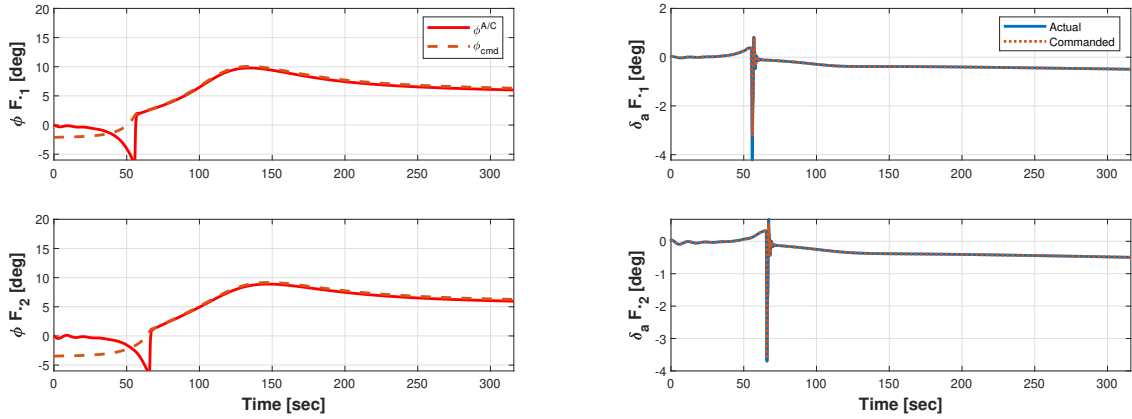


Figure 3.33: Leader and followers trajectories during rendezvous procedure.

The control authority over the rendezvous procedure is outlined in Figure 3.34. In the left subplot, the roll angles swept during the maneuver are compared to the commanded set points for both followers. Contextually, the right subplot illustrates the respective aileron control inputs for each follower. Initially, within the first 50-second time frame, the guidance system operates in course angle tracking mode (vector field-based), rendering the roll angle completely independent of the set point. After crossing the proximity threshold

distance from the target orbit, which was fixed in this case at $\hat{d} = 250$ m, the engagement of the roll angle control loop triggers an aileron impulse, initiating set-point tracking.



(a) Aircraft roll angle vs commanded set point.

(b) Aileron control inputs.

Figure 3.34: Control authority over roll angle set point tracking and corresponding aileron time history for both followers.

The prescribed maneuvering procedure guarantees the gradual approach of the followers to the leader, reducing the phase angle and stabilizing on the target orbit once the appropriate positioning for formation assembling is attained, as shown in Figure 3.35. In order, the following is reported: phase angle γ for leader and followers, phase shift σ on the leader, side bearing angle η as an indicator of target orbit capture, and the progressive reduction of relative leader-follower distance.

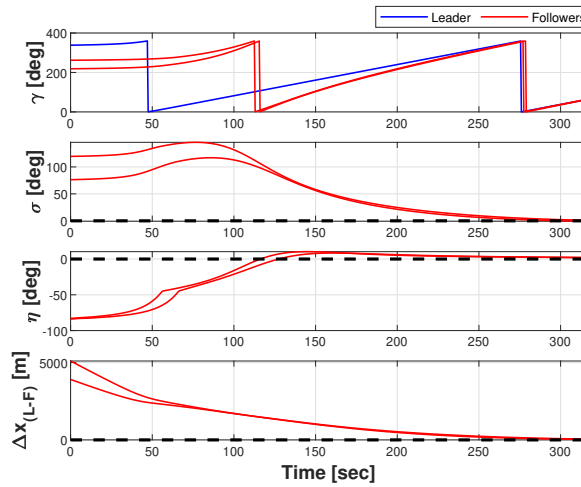


Figure 3.35: Rendezvous indicator parameters: phase angle γ , phase shift σ , side-bearing angle η , and relative leader-follower distance Δx_{GND} .

Rendezvous guidance with velocity control

A second test was conducted to assess the guidance system with the addition of velocity control to reduce convergence times (Equation (3.29)). The simulation result is shown in Figure 3.36, where it immediately becomes apparent that, under the same initial conditions, the matching point is significantly anticipated, as expected.

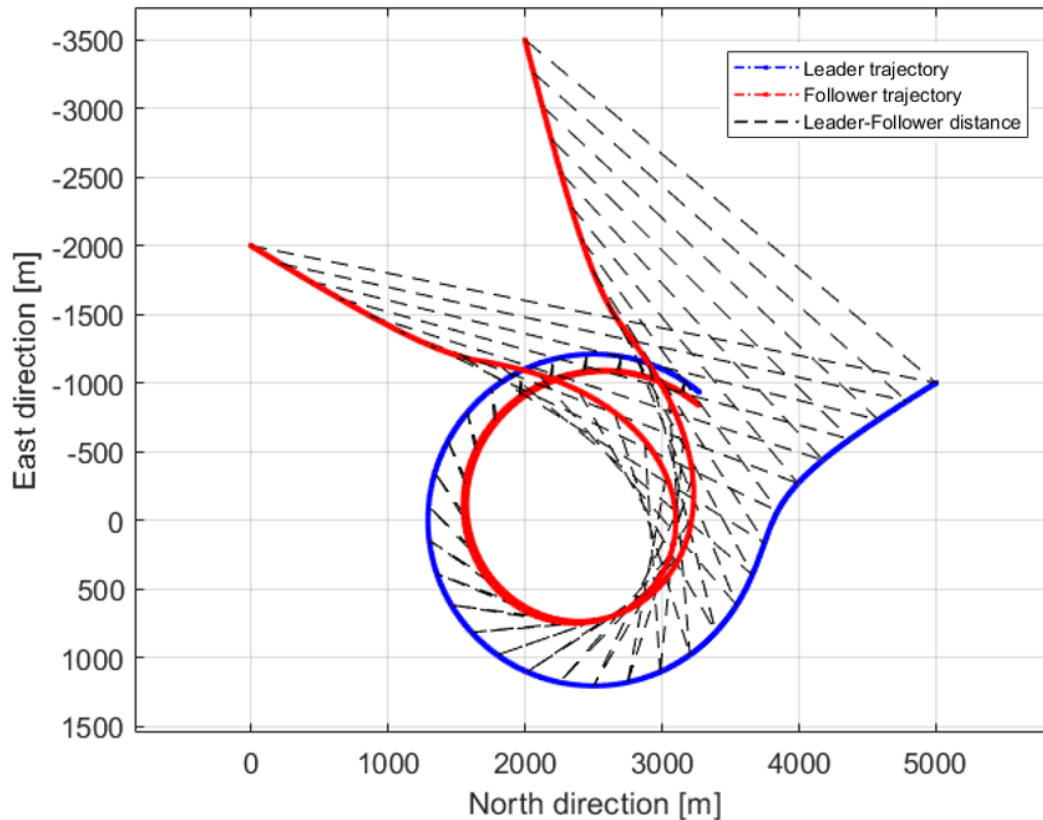
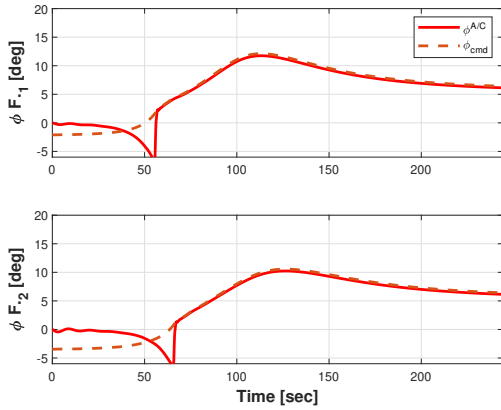


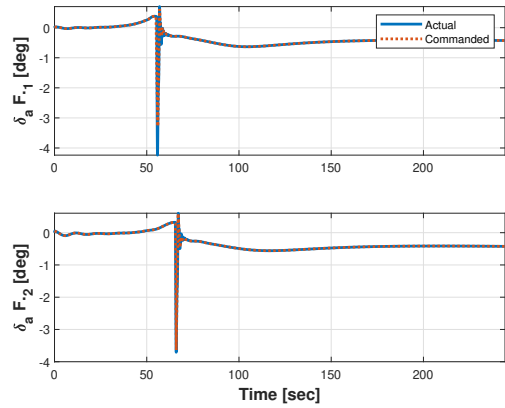
Figure 3.36: Leader and followers trajectories during rendezvous procedure with additional velocity control.

In this case, the graphs related to the roll angles swept compared to the set point and their associated aileron inputs are shown as before in Figure 3.37a. Additionally, for this case, graphs related to the velocity set point tracking and their respective throttle inputs are included (Figure 3.37c). The control authority for roll angle tracking is perfectly comparable to the previous case. Concerning the velocity control modification, the guidance modes switch also affects the autothrottle, which sets an impulse that reaches saturation for a few seconds at the beginning of the set point tracking.

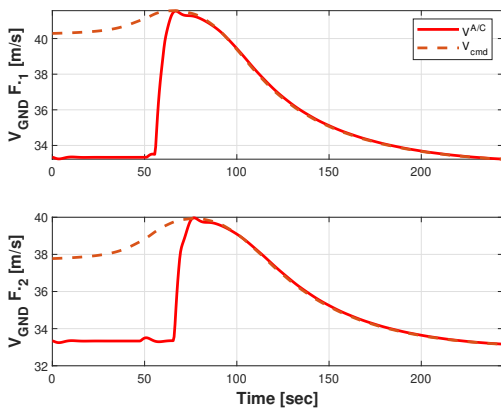
In conclusion, the set of parameters that collectively describe the follower-leader approaching maneuver is shown in Figure 3.37e.



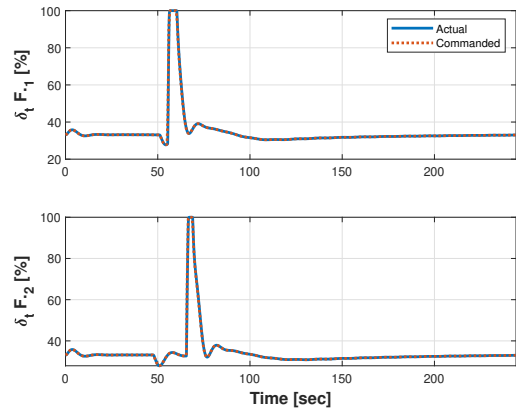
(a) Aircraft roll angle vs commanded set point.



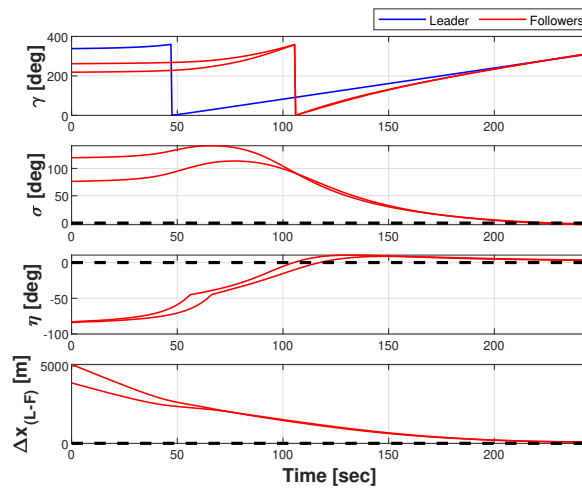
(b) Aileron control inputs.



(c) Aircraft velocity vs commanded set point.



(d) Throttle control inputs.



(e) Rendezvous indicator parameters: phase angle γ , phase shift σ , side-bearing angle η , and relative leader-follower distance Δx_{GND} .

Figure 3.37: Control authority over roll-angle and velocity set points and overall rendezvous indicator parameters.

4 | Formation Modeling and Control

This section delves into the modeling and control aspects of formation flight coordination. The modeling segment primarily involves investigating the effects of wake interaction between adjacent aircraft. The sideward and vertical stagger between two aircraft in the formation significantly influence the aerodynamic forces at play, and consequently, the aircraft's dynamic behavior. This underscores the need to develop a comprehensive database encompassing alterations in aerodynamic coefficients for the trailing aircraft concerning the leading one. Such a database can be employed to enhance the fidelity of the simulation environment through interpolation techniques.

From the perspective of swarm coordination, a distributed control strategy is proposed, entailing several advantages:

- **Enhanced Resilience and Fault Tolerance:** Each aircraft can continue operating autonomously, even if other aircraft in the formation become unavailable. This ensures a higher level of resilience and fault tolerance.
- **Reduced Computational Complexity:** Each aircraft processes only local information and interacts with neighboring aircraft, reducing computational complexity compared to a centralized approach.
- **Increased Scalability:** Aircraft can be added to or removed from the formation without the need to reconfigure the entire control system.

It is recalled that each aircraft within the formation is equipped with an AFCS capable of managing both a Guidance Mode (**GM**) for tracking a predefined path and a Formation Control Mode (**FCM**). The latter is responsible for the formation keeping and coordination and will be herein the object of discussion.

Lastly, two techniques for wind disturbance rejection are discussed. One of these involves synthesizing a supervisory control that can modulate the two coexisting modes of the AFCS to separate and reform the formation as needed, depending on the disturbance intensity and mission phase.

4.1. Wake Interference Modeling

Aerodynamic wake interference plays a critical role in swarm architecture design, when it comes to defining a 3D structure of the formation, and cannot be disregarded. The vortex flow field generated by the wingtips of a leading aircraft affects the trailing aircraft by subjecting them to a non-uniform induced velocity field. This field features an upwind region on the outer portion of the wake and a downwind region on the inner portion (see Figure 4.1). The induced velocity effect results in either a positive or negative change in the angle of attack of the trailing aircraft, depending on its sideward displacement relative to the leading one.

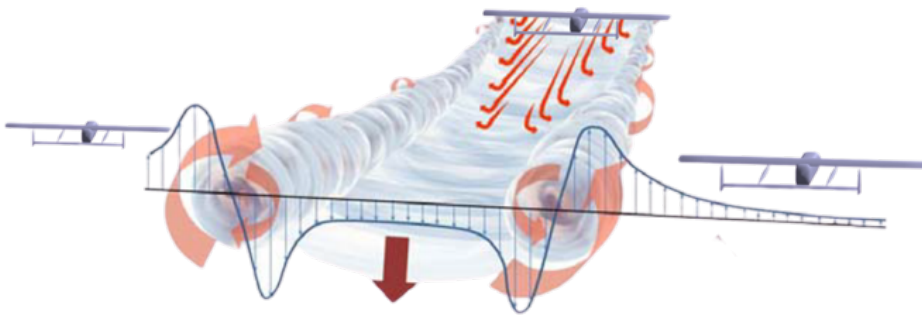


Figure 4.1: Vortex flow field behind a leading aircraft, investing trailing units in the formation.

As shown in Figure 4.2, in the upwind region, the increase in induced angle of attack causes the resultant aerodynamic forces to tilt forward. Consequently, the aircraft experiences an increase in lift, accompanied by a reduction in drag. Conversely, in the downwind region, the opposite effect occurs. The decreased angle of attack leads to a reduction in lift and an increase in drag, which results in higher fuel consumption and degraded flight performance [31, 32].

An investigation in this regard is not only valuable for improving the accuracy of the dynamic model but also justifies the selection of a specific formation geometry. The intent is to allow each aircraft to fly in what is commonly referred to as the "sweet spot," which is the outer region near the wingtip of the leading aircraft. This region enables the trailing aircraft to take advantage of the upwash region, resulting in reduced induced drag and, consequently, lower fuel consumption [33].

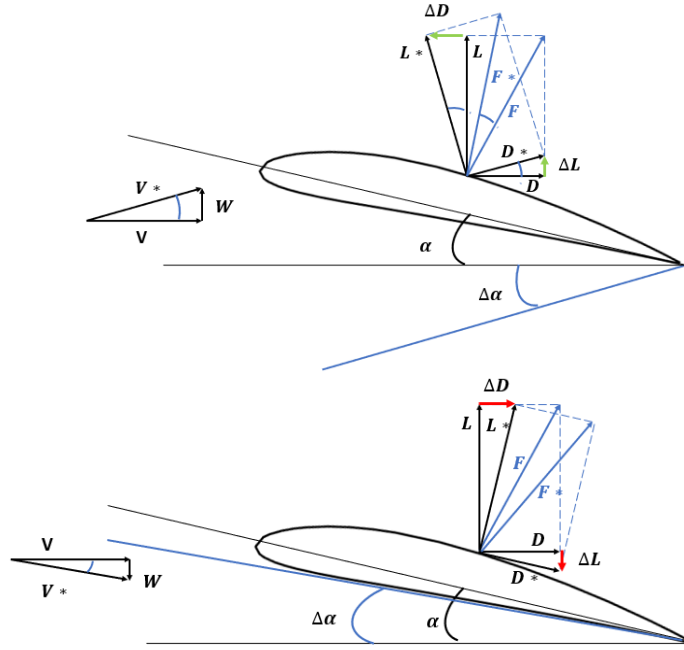


Figure 4.2: Upwind (top) and downwind (bottom) effects on lift coefficient (C_L) and drag coefficient (C_D).

To investigate the wake effects, a mid-fidelity approach based on the vortex lattice method (VLM) is employed [34], with a leading and a trailing lifting surfaces. Although the VLM provides a simplified representation of flow physics, it is widely accepted and adopted for studying and analyzing aircraft aerodynamics in formation flight.

Such a technique allows us to estimate variations of aerodynamic coefficients with respect to isolated flight [35] for each aircraft within the formation.

Formally, assuming the concentrated parameter aerodynamic model described in Section 1.3.2, we have:

$$C_L(\dots, \Delta \mathbf{s}) = C_{L_0} + C_{L_\alpha} \alpha + C_{L_{\hat{\alpha}}} \hat{\alpha} + C_{L_{\hat{q}}} \hat{q} + C_{L_{\delta_e}} \delta_e + \Delta C_L(\Delta \mathbf{s})$$

$$C_D(\dots, \Delta \mathbf{s}) = C_{D_0} + C_{D_\alpha} \alpha + C_{D_{\hat{\alpha}}} \hat{\alpha} + C_{D_{\hat{q}}} \hat{q} + C_{D_{\delta_e}} \delta_e + \Delta C_D(\Delta \mathbf{s})$$

$$C_M(\dots, \Delta \mathbf{s}) = C_{M_0} + C_{M_\alpha} \alpha + C_{M_{\hat{\alpha}}} \hat{\alpha} + C_{M_{\hat{q}}} \hat{q} + C_{M_{\delta_e}} \delta_e + \Delta C_M(\Delta \mathbf{s})$$

$$C_Y(\dots, \Delta \mathbf{s}) = C_{Y_0} + C_{Y_\beta} \beta + C_{Y_{\hat{\beta}}} \hat{\beta} + C_{Y_{\hat{p}}} \hat{p} + C_{Y_{\hat{r}}} \hat{r} + C_{Y_{\delta_a}} \delta_a + C_{Y_{\delta_r}} \delta_r + \Delta C_Y(\Delta \mathbf{s})$$

$$C_L(\dots, \Delta \mathbf{s}) = C_{L_0} + C_{L_\beta} \beta + C_{L_{\hat{\beta}}} \hat{\beta} + C_{L_{\hat{p}}} \hat{p} + C_{L_{\hat{r}}} \hat{r} + C_{L_{\delta_a}} \delta_a + C_{L_{\delta_r}} \delta_r + \Delta C_L(\Delta \mathbf{s})$$

$$C_N(\dots, \Delta \mathbf{s}) = C_{N_0} + C_{N_\beta} \beta + C_{N_{\hat{\beta}}} \hat{\beta} + C_{N_{\hat{p}}} \hat{p} + C_{N_{\hat{r}}} \hat{r} + C_{N_{\delta_a}} \delta_a + C_{N_{\delta_r}} \delta_r + \Delta C_N(\Delta \mathbf{s}) .$$

This aerodynamic model differs from the isolated flight case model by including an additional contribution resulting from the wake interaction with the preceding aircraft, which

depends on the separation vector $\Delta \mathbf{s}$ encompassing its three components (longitudinal ($\Delta \mathbf{x}$), lateral ($\Delta \mathbf{y}$), and vertical ($\Delta \mathbf{z}$)).

4.1.1. Vortex Lattice Method

The Vortex Lattice Method is a computational technique widely employed in aerodynamics for analyzing and predicting the lift and induced drag characteristics of aerodynamic surfaces. This method breaks down the wing or lifting surface into a series of discrete vortex elements, often represented as horseshoe-shaped vortices. By calculating the induced velocities and vortices, the method provides insights into the overall flow field and aerodynamic forces acting on the surface.

The VLM relies on specific flow conditions: incompressibility, inviscidness, and irrotationality. These conditions lead to a velocity field described by a conservative vector field. The velocity field is represented using a scalar velocity potential, denoted as ϕ , which combines with the free stream velocity V_∞ as shown in Equation (4.1):

$$V = V_\infty + \nabla \phi . \quad (4.1)$$

In order to satisfy incompressibility, the velocity field must obey the continuity equation, expressed in Equation (4.2):

$$\nabla \cdot V = 0 . \quad (4.2)$$

The conservative vector field, represented by the scalar potential ϕ , satisfies Laplace's equation, as described in Equation (4.3):

$$\nabla^2 \phi = 0 . \quad (4.3)$$

Laplace's equation implies that linear combinations of potential solutions are also valid solutions. This forms the foundation of potential flow theory, where solutions are combined to represent lifting surfaces. In VLM, a single elementary potential solution is used to create a vortex sheet, representing the lifting surface.

The geometry is simplified by removing the thickness, and the planform is discretized into quadrilateral panels. The number of discretizations in chord and span is chosen proportionally to the desired level of accuracy. The vector n , defined for each panel, determines its orientation.

For each panel, a vortex sheet is assigned, positioned at 1/4 chord (c). The collocation points, which define the position of each panel and where the normal vector n is defined, are located at 1/2 b and 3/4 c , with b representing the span of a single panel. The perturbation potential for an individual panel is calculated as a function of the vortex strength (Γ_j) and the influence coefficient (a_{ij}), which represents the induced flow on panel i due to the vortex on panel j :

$$\nabla\phi_i = \sum_{j=1}^N a_{ij} \cdot \Gamma_j . \quad (4.4)$$

A physical boundary condition is enforced to ensure that there is no normal flow component across each panel of the lifting surface. This boundary condition is mathematically expressed as follows at the collocation points:

$$V_i \cdot n_i = \left(V_\infty + \sum_{j=i}^N a_{ij} \Gamma_j \right) \cdot n_i , \quad (4.5)$$

where V_i is the i -th panel velocity. For a stationary panel with respect to its normal direction, the equation reduces to :

$$\sum_{j=1}^N A_{ij} \cdot \Gamma_j = b_i , \quad (4.6)$$

where $A_{ij} = a_{ij} \cdot n_i$ and the right-hand side of the equation consists of the component in the normal direction to the panel of the freestream velocity, which is defined in terms of the aerodynamic angles α and β . It can be expressed as:

$$b_i = -V_\infty \left[\cos \alpha \cos \beta, \quad -\sin \beta, \quad \sin \alpha \cos \beta \right] \cdot n_i . \quad (4.7)$$

Computationally, the problem then reduces to calculating the vortex strength, which is the solution of the linear system in Equation (4.6). All the vortices generate a downwash V_{ind} on each panel of the lifting surface, which can be computed by means of Biot-Savart law:

$$\mathbf{V}_{ind} = \frac{1}{4\pi} \int \frac{(\mathbf{dl} \times (\mathbf{r} - \mathbf{r}'))}{|\mathbf{r} - \mathbf{r}'|^3} dV . \quad (4.8)$$

In this equation: \mathbf{V}_{ind} represents the induced velocity at point \mathbf{r} due to the infinitesimal element \mathbf{dl} , located at \mathbf{r}' .

The force acting on the panel, denoted as F_i , is calculated using the Kutta–Jukovski

theorem and is given by:

$$\mathbf{F}_i = \rho \cdot \Gamma_i \cdot (V_\infty + V_{ind}) \times l_i , \quad (4.9)$$

where: F_i is the force contribution from the i -th panel, ρ is the air density, V_{ind} is the induced velocity and l_i is the vortex transverse segment vector of the i -th panel.

4.1.2. Tandem Wing Analysis

The VLM code used for the analysis is based on Tornado [36] solver implemented in Matlab. The underlying concept is to generate a tandem wing configuration with rearward, sideward, and vertical stagger, aiming to simulate the relative positioning between two adjacent aircraft within the formation (Figure 4.3).

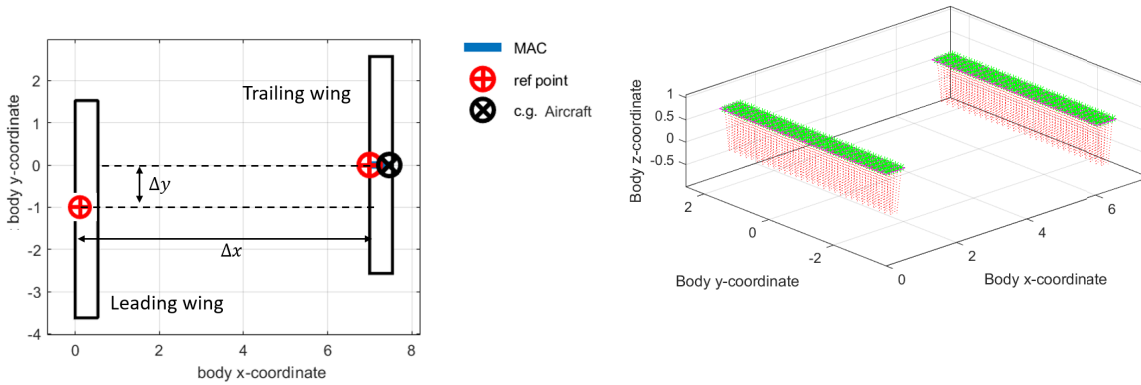


Figure 4.3: Tandem wing geometry layout (**left**) and VLM set-up with panels collocation points and normals (**right**).

Firstly, a symmetrical wing geometry, fixing the wing reference point (located at the midpoint of the leading edge) at coordinates (7,0), is created. This geometry represents the lifting surface of the trailing aircraft. An initial analysis is carried out to determine the aerodynamic coefficients for isolated flight condition. The flight state setup is defined at a fixed angle of attack ($\alpha = 6$ deg) and sideslip angle ($\beta = 0$ deg) at an airspeed of 36.11 m/s, representing a flight condition that is very close to the condition of maximum efficiency (see Appendix D). Subsequently, another identical wing geometry is placed in front. The position of this second wing is varied both horizontally and vertically, creating a matrix of values. The rows of this matrix represent the lateral separation between the two wings, measured between the two reference points (Δy), while the columns represent

the vertical distance (Δz). The position along the stream-wise direction (Δx) is initially kept constant.

The program provides the aerodynamic coefficients divided per single lifting surface. To determine the variation in these coefficients due to wake interaction, it is sufficient to subtract the coefficients obtained for the isolated wing from those obtained for the trailing wing in tandem configuration.

This approach allows us to assess the impact of lateral and vertical separation between the wings on the overall aerodynamic performance of the trailing wing, providing crucial insights for the design and optimization of formation flight.

Figure 4.4 and 4.5 introduce the analysis outcomes, illustrating the variations in forces and moments coefficients across a range of lateral and vertical separations spanning from -20 m to 20 m. The stream-wise direction distance is set to 7 m.

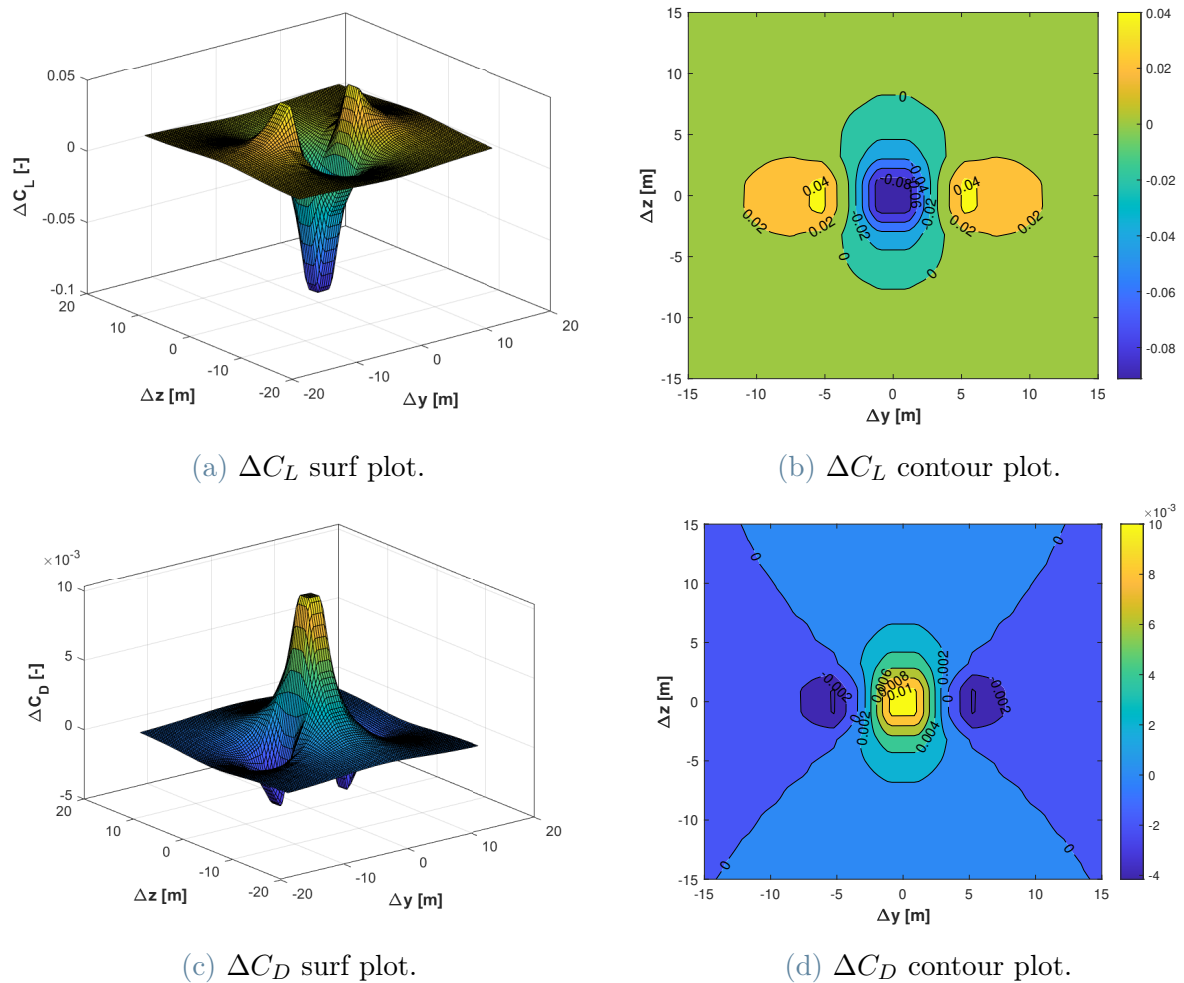
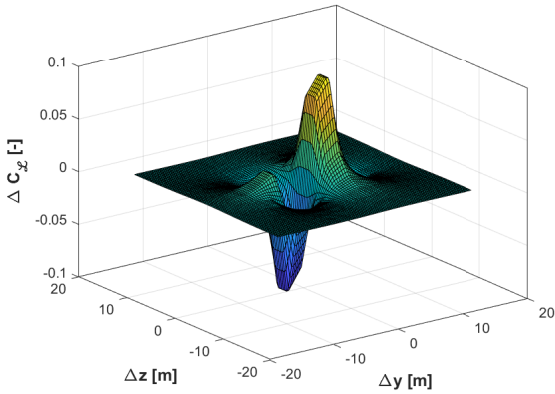
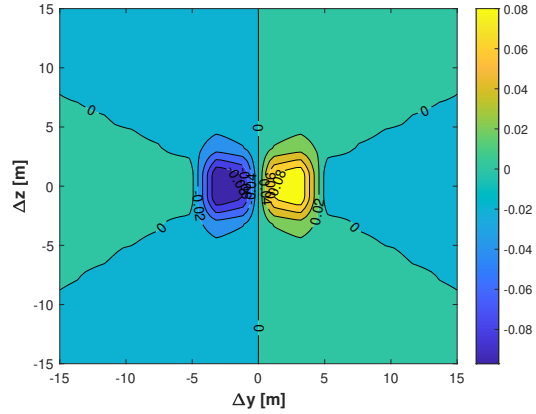


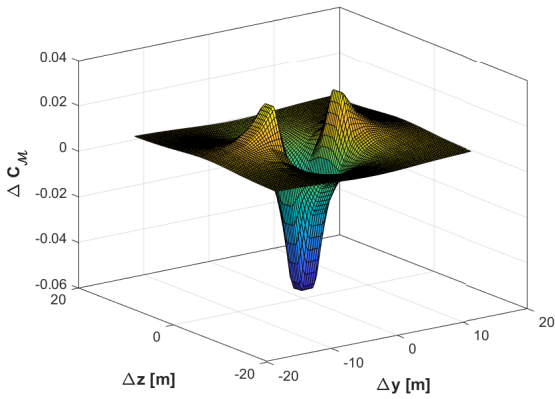
Figure 4.4: Wake-induced aerodynamic forces coefficients variations.



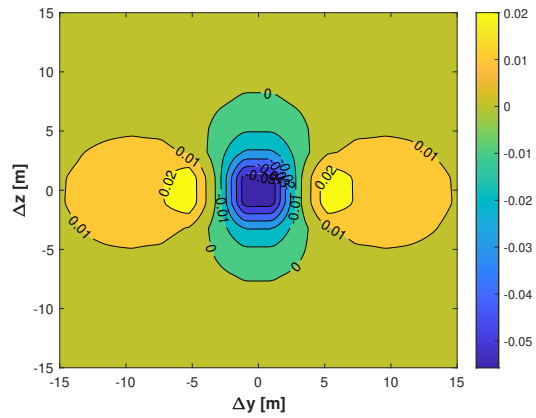
(a) ΔC_L surf plot.



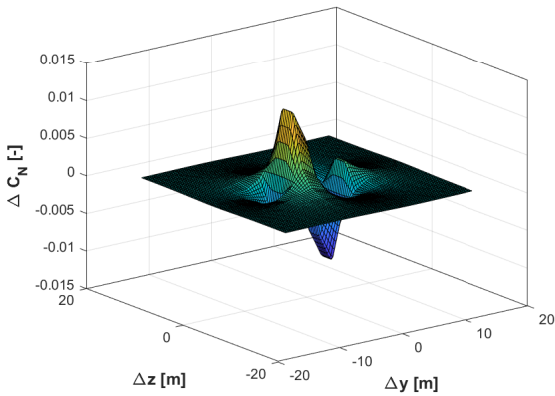
(b) ΔC_L contour plot.



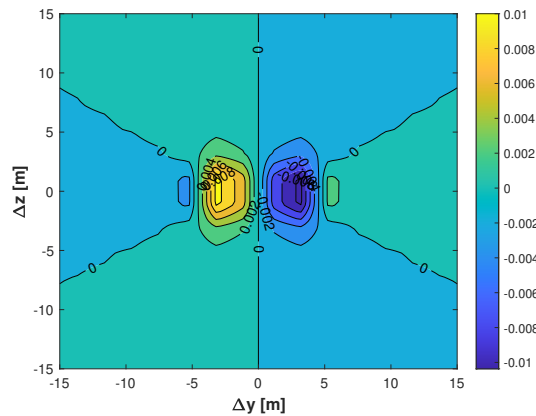
(c) ΔC_M surf plot.



(d) ΔC_M contour plot.



(e) ΔC_N surf plot.



(f) ΔC_N contour plot.

Figure 4.5: Wake-induced aerodynamic moments coefficients variations.

Some essential observations are as follows: due to the simplification of the problem at hand, considering only the horizontal lifting surfaces, the effects on the aerodynamic side force coefficient ΔC_Y cannot be determined. The regions where peaks in lift coefficient

change (ΔC_L) and valleys in drag coefficient change (ΔC_D) are observed (Figure 4.4) corresponds to the sweet spot earlier mentioned. This region is found when the two lifting surfaces have no vertical stagger and a lateral separation of just over 5 m (approximately 5.15 m), which corresponds to the length of a wingspan. Assuming lateral separation as the distance measured between the wing reference points (see Figure 4.3), the sweet spot for the trailing aircraft corresponds to having its wingtip aligned with the wingtip of the leading aircraft in stream-wise direction. This configuration allows the trailing aircraft to benefit from the upwash region generated in the outer portion of the leading aircraft's wing. In contrast, with the two wings completely overlapped ($\Delta y = \Delta z = 0$), a sharp reduction in C_L occurs with a simultaneous increase in induced drag.

A parallel trend to that obtained for ΔC_L is observed for ΔC_M . Where the trailing aircraft experiences an increase in ΔC_L , the contribution of wake-induced ΔC_M with respect to CG, rises positively. Conversely, in points where the trailing aircraft records a reduction in ΔC_L , a corresponding negative contribution in ΔC_M is observed.

The variations in the moment coefficients ΔC_L and ΔC_N are attributed to the breaking of the symmetry in lift and induced drag distribution along the wingspan, depending on the relative lateral positioning between the lifting surfaces. These distributions are depicted in Figure 4.6 for various lateral separation values ranging from -20 m to -1 m, with fixed longitudinal and vertical stagger.

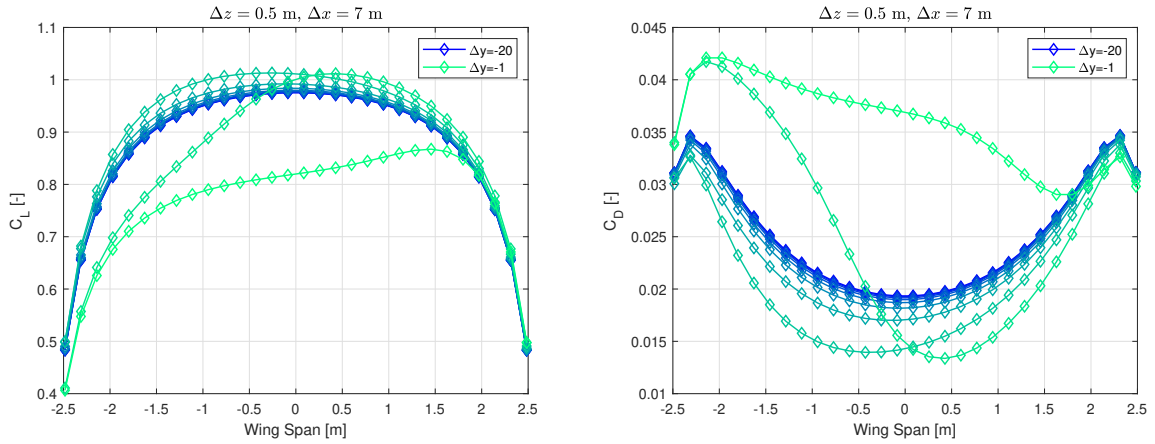


Figure 4.6: Lift and induced drag distribution over trailing aircraft wing span, for several value of lateral stagger.

As the two wings approach each other, the effect of the upwash region becomes evident with a slight increase in lift and a reduction in induced drag. For lateral separation values smaller in magnitude than 5.15 m (b), the two wings begin to overlap, resulting in an asymmetric lift and induced drag distribution on the trailing wing, that leads to the

generation of induced roll and yaw moments. In particular, when the left half-wing of the trailing aircraft overlaps with the right half-wing of the leading one ($-b < \Delta y < 0$), a decrease in lift and an increase in induced drag occur. These changes result in negative roll and yaw moments, following the convention of body axes.

To assess the effect of longitudinal spacing, the trends in peak and valley values for each aerodynamic coefficient are compared for increasing values of Δx . From Figure 4.7, it is evident that at a 40 m separation in the stream-wise direction between the two aircraft, the peaks and valleys coincide at 0, indicating the cancellation of wake effects.

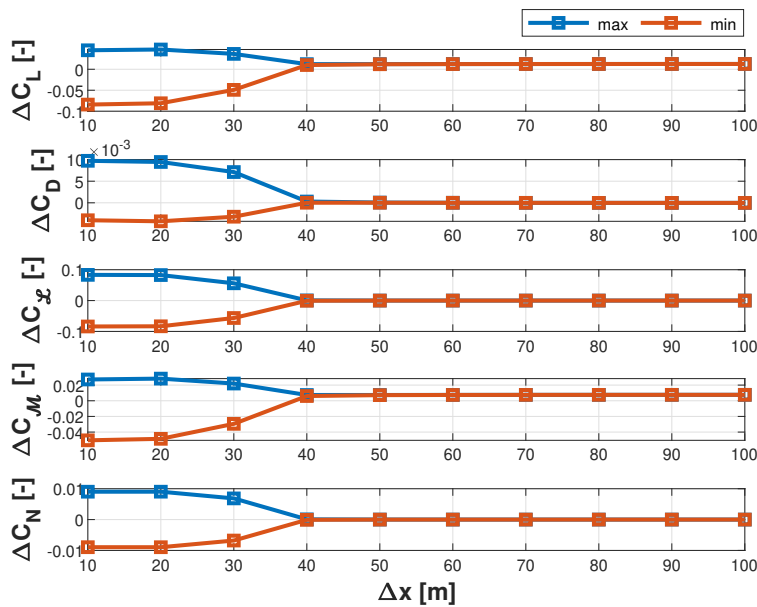


Figure 4.7: Wake-induced effect over longitudinal stagger.

The analysis was then replicated for various angles of attack to cover a broader range of scenarios within the simulation environment. The data were subsequently collected in dedicated look-up tables to interpolate the variations in aerodynamic coefficients based on the relative separation between the leading and trailing aircraft. Another significant outcome of the analysis was the identification of the "sweet spot," which defines the optimal spacing between aircraft for enhanced aerodynamic efficiency. This finding strongly advocates the utilization of a V-formation geometry, with aircraft separated by approximately one wingspan, to be exploited mainly during navigation/cruise phases.

4.2. Formation Control Mode Synthesis

As stated in the chapter introduction, the present work aims at achieving mutual independence of the units in a swarm, to the extent required to avoid loss of control of the swarm in case of disturbance or loss of a leading unit. This feature is especially interesting for the leg in the swarm mission where precision with respect to the track is of primary relevance, typically when flying over a target (for a photographic or cargo-dropping run). However, classical formation flight, implementing a basic leader-follower philosophy, remains of interest for those parts of the mission where mutual separation in a compact formation is needed [37], keeping each unit in an aerodynamically advantageous position, i.e. typically in cruise, or prior to approaching the over-target phase of the mission.

To achieve formation flight, the relationship between a leader and a follower aircraft is considered and studied. In that scenario, the control logic of the follower aircraft is rather straightforward, and it involves maintaining a fixed relative position with respect to the leader, determined in the leader's body components based on its center of gravity position. The primary objective of the controller is to minimize the distance between the follower and the specified target position, by defining three position errors that correspond to the projections of this distance in a reference frame aligned with the leader's body frame, and with the origin located at the target position. An explanatory sketch of these three position errors is depicted in Figure 4.8.

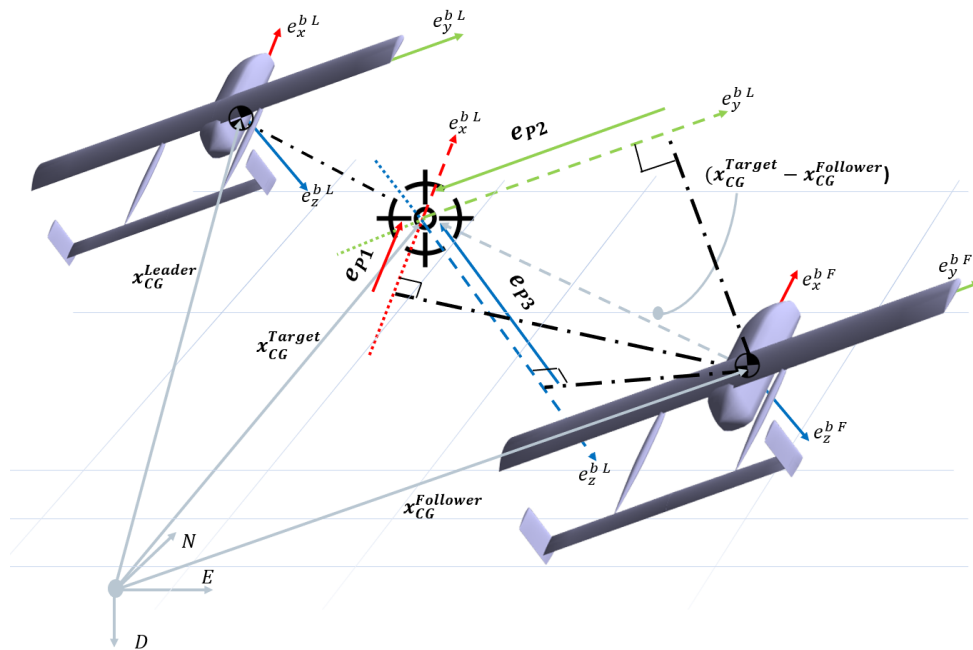


Figure 4.8: Formation control: definition of target point for the follower, and of the follower position errors e_{P1} , e_{P2} and e_{P3} .

Mathematically, the definition of position errors for the follower can be expressed as the rotation of the distance vector's inertial coordinates between the target position and the follower's center of gravity (CG) into the Leader's body frame. This transformation is accomplished using a rotation matrix defined with respect to the Leader's attitudes. $\mathcal{R}_{\mathcal{I}}^{\mathcal{B}^L}(\phi^L, \theta^L, \psi^L)$.

$$\begin{bmatrix} \mathbf{e}_{P1} \\ \mathbf{e}_{P2} \\ \mathbf{e}_{P3} \end{bmatrix} = \mathcal{R}_{\mathcal{I}}^{\mathcal{B}^L}(\phi^L, \theta^L, \psi^L) \begin{bmatrix} x_N^T - x_N^F \\ x_E^T - x_E^F \\ x_D^T - x_D^F \end{bmatrix}. \quad (4.10)$$

The superscript $(.)^L$ stands for Leader's measured states as well as $(.)^F$ stands for follower's ones. x^T denotes the target position vector expressed in inertial coordinates.

In this autonomous flight mode, coordination control is carried out using feedback variables made available through the onboard GPS system. The relative positions are elaborated by the follower, knowing the global coordinates of its own position and the target position. However, it would be impractical to execute the leader-follower coordination using only position errors as control variables. Therefore, the control system is provided with information about the direction of motion and evolution of attitude of the leader, so that a related control action adjusting the control inputs of the follower both in the longitudinal and lateral-directional body plane is enabled. Altogether, in the proposed control design, the control inputs for the follower are generated combining three factors:

1. a **position error** (as previously described),
2. a **path error** (measured with respect to the course angle χ and climb angle γ of the leader, respectively),
3. an **attitude error** (measured with respect to the roll angle ϕ and pitch angle θ of the leader respectively).

Path and attitude feedback errors provide stability and stiffness to the formation during maneuvering phases, as if the followers, to some extent, anticipate the upcoming maneuver rather than waiting to correct only their position error.

In addition, by combining them, the follower's control system can achieve accurate and stable tracking of the target position, maintaining a good sensitivity to the unfolding of the leader's dynamics. This approach enables for a precise and smooth control action of the ailerons and elevator, in turn ensuring accurate aircraft mutual positioning. The longitudinal position control is primarily handled by the throttle, which operates through

a control law based on position and velocity errors along the leader's longitudinal (i.e. e_x^b) body axis. A proportional control law is employed to mitigate the side-slip angle through rudder deflection, ensuring turn coordination. The set of control inputs provided by the FCM is listed below:

$$\delta_e^{pilot} = k_p^{eP3} \cdot e_{P3} + k_p^{e\gamma} \cdot e_\gamma + k_p^{e\theta} \cdot e_\theta, \quad (4.11a)$$

$$\delta_a^{pilot} = k_p^{eP2} \cdot e_{P2} + k_p^{e\chi} \cdot e_\chi + k_p^{e\phi} \cdot e_\phi, \quad (4.11b)$$

$$\delta_r^{pilot} = k_p^\beta \cdot \beta, \quad (4.11c)$$

$$\delta_t^{pilot} = k_p^{eP1} \cdot e_{P1} + k_p^{eV_{P1}^{vel}} \cdot e_{V_{P1}^{vel}}. \quad (4.11d)$$

A detailed diagram illustrating the control logic for formation control in cruise mode is shown in Figure 4.9.

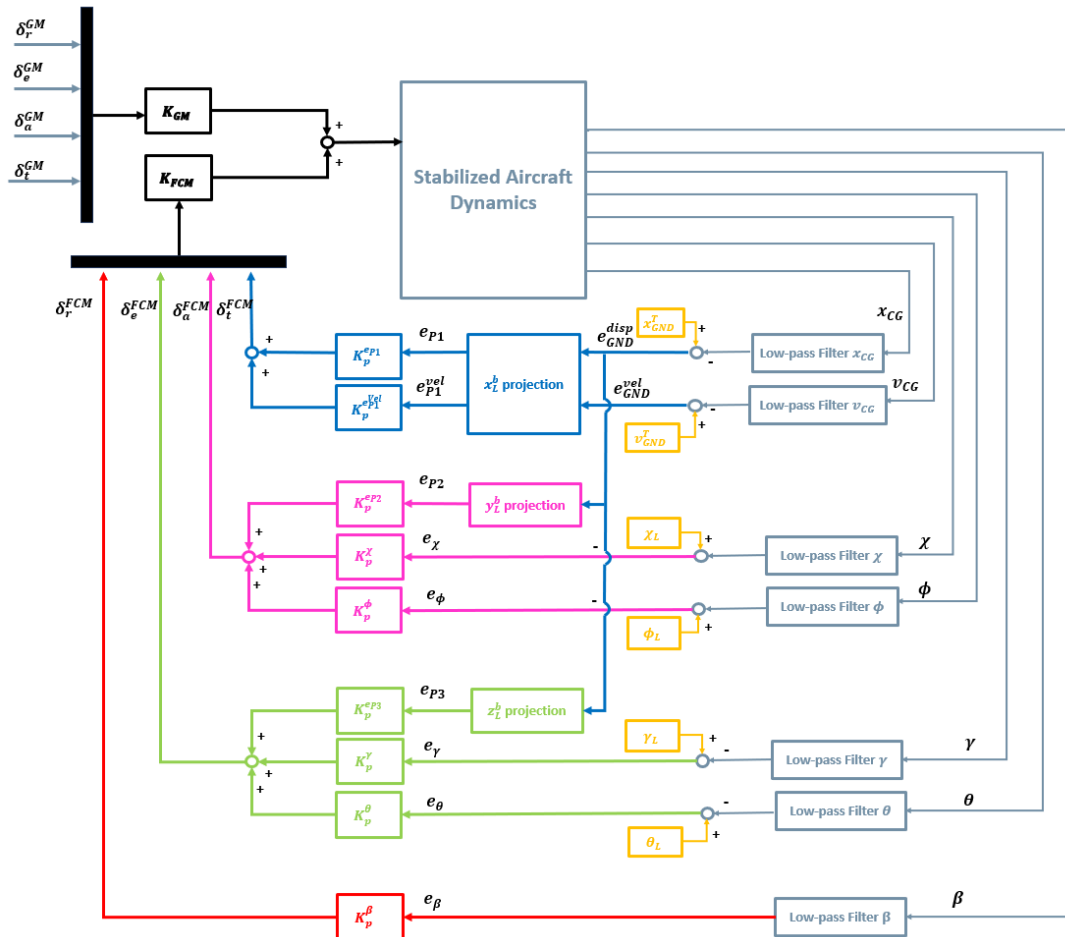


Figure 4.9: Control scheme for follower aircraft in formation flight (cruise mode). Blue: autothrottle loop. Pink: aileron control loop. Green: elevator control loop. Red: rudder control loop.

4.2.1. Flying Over Target: GM vs FCM

The **AFCS** has been designed to manage both formation control in a leader-follower logic (see Section 4.2), and guidance, with the control logics described in Chapter 3. As said, this dual functionality of the autopilot has been devised to serve the various purposes of a typical reconnaissance mission. During the navigation phase, the main objective is to maintain tight formation around the leader, leveraging the relative positioning of the swarm elements to exploit an aerodynamically advantageous position, the sweet spot (see Section 4.1). During the on-target phase instead, the primary goal is to accurately survey/overfly the area below, while mitigating potential disturbances such as wind or signal loss from the leading unit (in particular, due to hits in a hostile scenario). In this situation, each unit within the formation is capable of fulfilling the mission task by adhering to a designated path, according to the guidance mode introduced in Chapter 3. Accordingly, the two autopilot modes are regulated by two respective gains (K_{GM} and K_{FCM}), modulated via a supervisory multiplier ranging from 0 to 1, which can be adjusted based on a certain error parameter (e.g. the leader's cross-track error). As the leader's cross-track error increases, for instance due to wind disturbance, the weighting of the navigation (i.e. on-target) mode is increased compared to the formation control (i.e. cruise) mode. Alternatively, the control laws can be implemented so as to work in a mutually exclusive fashion, allowing the former or the latter to take priority.

4.3. Simulations and Results

In order to illustrate the functions of the proposed control suite, some examples will be shown in the following subsections. The model is fully non-linear in terms of mechanics and aerodynamics. In particular, the changes in the aerodynamic coefficients resulting from the wake interaction effects are accounted for in formation flight. Furthermore, all aircraft are always artificially stabilized by means of the stability augmentation systems described previously (Chapter 2). The gains assigned to the control laws in Equation (4.11) are listed in Table 4.1. These gains are generally chosen to be higher than those used for guidance control, ensuring enhanced system responsiveness to leader state changes while maintaining overall system stability.

Formation Control Mode								
k_p^{eP1}	k_p^{eP2}	k_p^{eP3}	$k_p^{e\chi}$	$k_p^{e\gamma}$	$k_p^{e\phi}$	$k_p^{e\theta}$	k_p^β	$k_p^{eV_{P1}^{vel}}$
$1 \cdot 10^{-1}$	$-9 \cdot 10^{-3}$	$7 \cdot 10^{-2}$	$-2 \cdot 10^0$	$-1.5 \cdot 10^0$	$-2 \cdot 10^0$	$-1 \cdot 10^0$	$-1 \cdot 10^{-1}$	$1.5 \cdot 10^{-1}$

Table 4.1: FCM design parameters.

4.3.1. Two-aircraft Formation: Single Leg Trajectory Path

A preliminary testing phase is conducted considering two aircraft, assigning a single straight and climbing flight path to the leader, while the follower is instructed to maintain a 6 m distance from leader along all three reference axes, starting from a non-zero (i.e. perturbed) positional error. In addition, an initial misalignment of 10 degrees from the desired course is imposed, to test formation control systems capability to counteract a sudden change in climb path and lateral course deviation. The trajectories plot is shown in Figure 4.10.

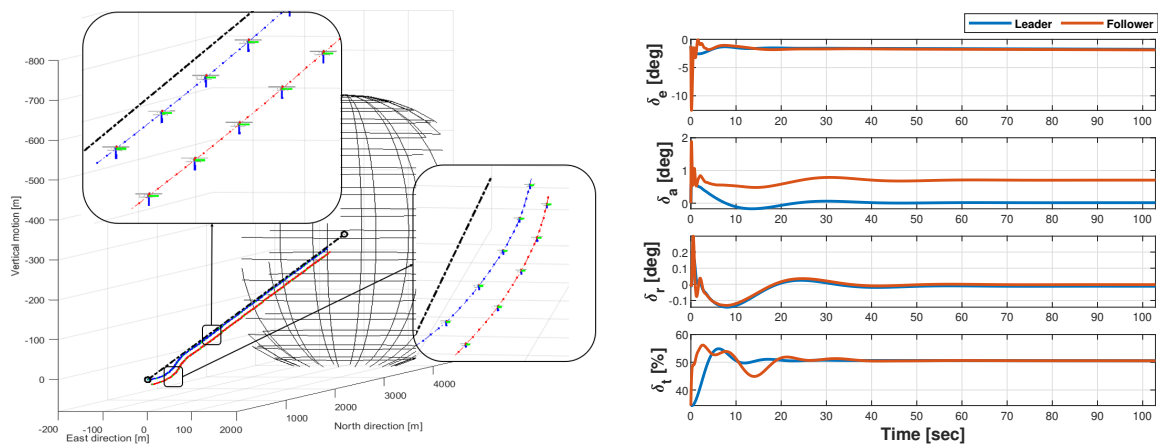


Figure 4.10: Straight climbing path with initial 10 deg misalignment. Two-aircraft formation. Left plot. Visualization of trajectories. Blue: leader. Red: follower. Right plot. Controls time histories for leader and follower.

Looking at Figure 4.10, right plot, the follower responds to the initial disturbance in a more abrupt manner, aiming to quickly catch up not only with the target position but also with the leader's attitude. However, none of the four control commands reaches saturation, thereby ensuring a wide maneuvering margin for the follower aircraft. It is noteworthy that while the elevator, rudder, and throttle tend to converge to the leader's values after the realignment maneuver, the aileron retains a residual value different from zero. This is expected, since the aileron compensates for the rolling moment induced by the wake interference.

The overall assessment of formation performance can be carried out evaluating the three characteristic errors, reported in Figure 4.11, targeted by the formation control system in cruise mode (e_{P1} , e_{P2} and e_{P3}).

The formation control system demonstrates a satisfactory performance, reducing both vertical and longitudinal position errors to zero in physically acceptable time windows.

The persistent lateral error e_{P2} can be attributed to the equilibrium condition established by the aircraft to compensate for the wake-induced rolling moment. All positional errors converge to a constant value within a tolerance band of ± 2 m

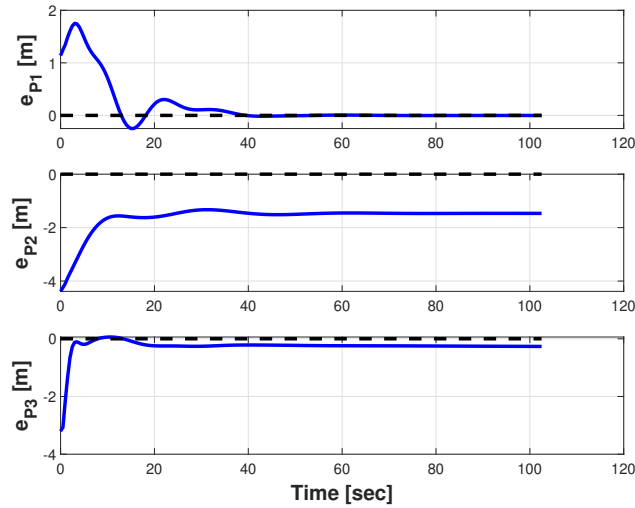


Figure 4.11: Target position errors for formation control.

From Figure 4.12, which depicts the time evolution of the states of leader and follower, it is evident how the follower effectively adapts to the new flight condition imposed by the leading unit, generating an almost identical response for both longitudinal and lateral-directional dynamics.

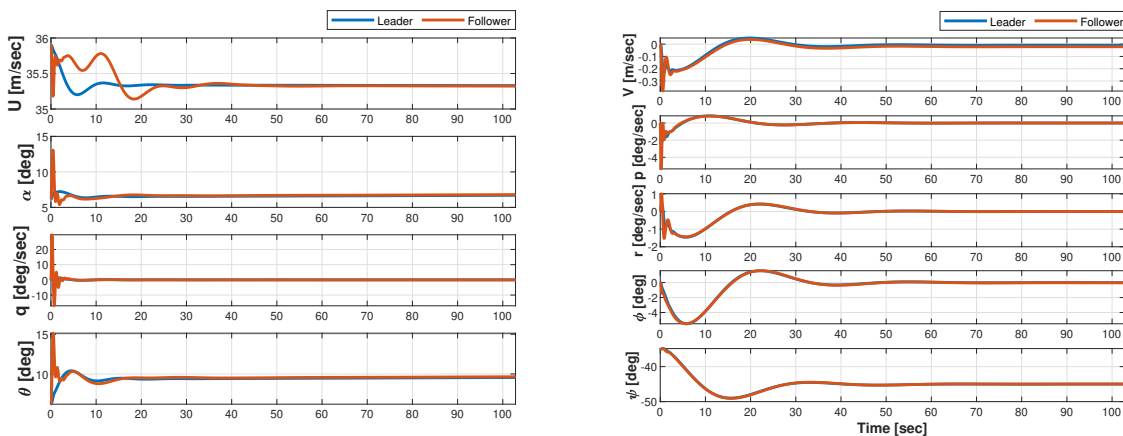


Figure 4.12: Two-aircraft formation. States time evolution.

4.3.2. Three-aircraft Formation: Hexagonal Pattern

Without any special arrangement or modification to the control architecture, a third aircraft can be added to the swarm. The latter aircraft is assigned a target position to the left of the leader, symmetrically with respect to the position of the right-hand-side follower, thus generating a V-shaped formation. Here, a hexagonal path is assigned, alternating climbs to a 100 m altitude and descents to 0 m, on the first four legs of the circuit.

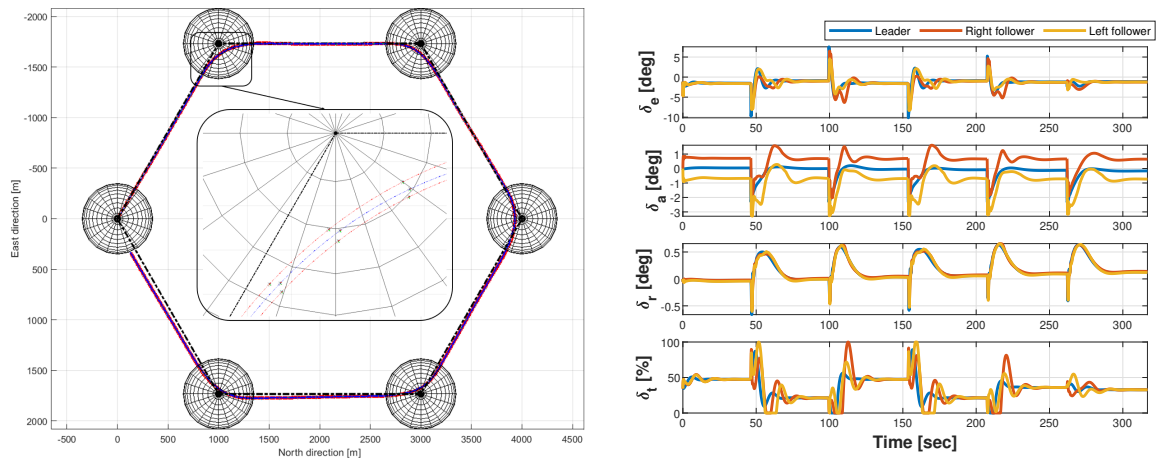


Figure 4.13: Hexagonal path with 4 alternating altitude changes. Three-aircraft formation. Left plot. Visualization of trajectories. Blue: leader. Red: followers. Right plot. Controls time histories for leader and followers.

The position errors of both followers (Figure 4.14) remain bounded within a tolerance of ± 5 m for e_{P_1} , and ± 2 m for e_{P_3} respectively, with peaks occurring only at the turning points. It can be noticed that the lateral position error is mirror-symmetric between the right and left followers, given the symmetry of the formation.

Similar to the two-unit formation flight in previous section, also in this case, the formation controller does not reduce the error e_{P_2} to zero. However, overall, this offset proves beneficial as it ensures an adequate lateral separation margin to avoid dangerous trajectory crossings during turning maneuvers.

In this case as well, for the sake of completeness, the temporal evolution of the states for each of the three aircraft in the formation is presented in Figure 4.15.

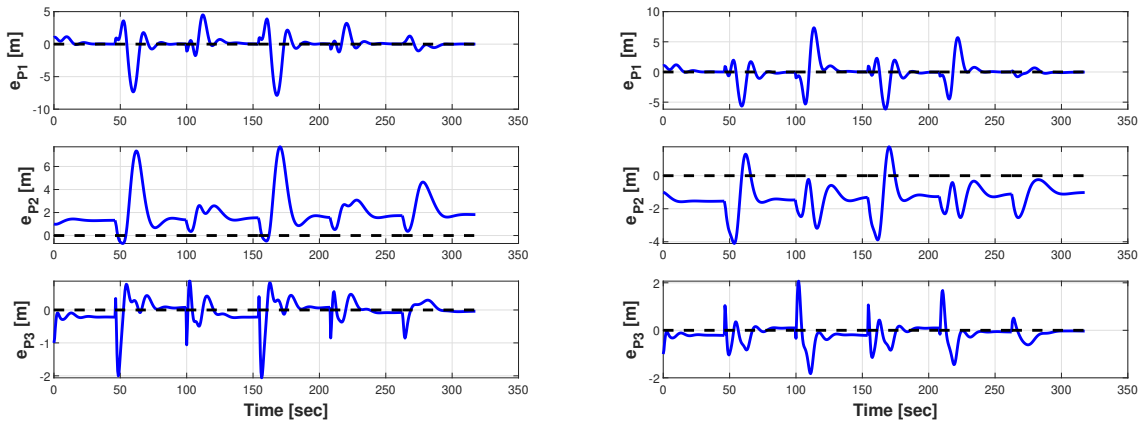


Figure 4.14: Time histories of errors for followers unit formation flight along a hexagonal pattern. Left: left-hand side follower position errors. Right: right-hand side follower position errors.

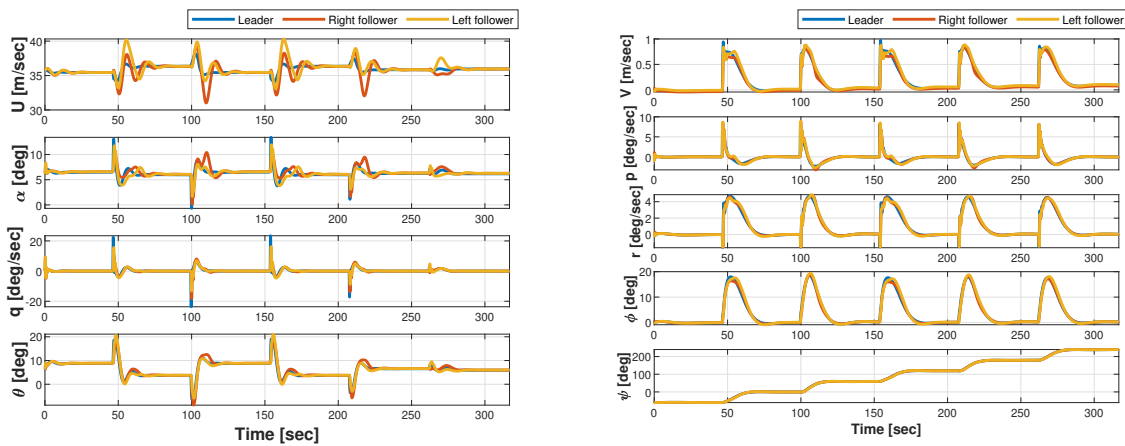


Figure 4.15: Three-aircraft formation along a hexagonal pattern. States time evolution.

4.3.3. Three Aircraft Formation: Triangular Path

In this scenario, the formation is tested on a triangular circuit with 60-degree angles at the vertices. The aim is to assess the formation's stability at the turning points and observe how the formation is recovered once the leader has realigned itself with the next leg. Trajectories and control time histories are reported in Figure 4.16.

Overall, the control system ensures a satisfactory formation recovery, with the followers reaching and maintaining their assigned target positions beyond the turning points (see Figure 4.17).

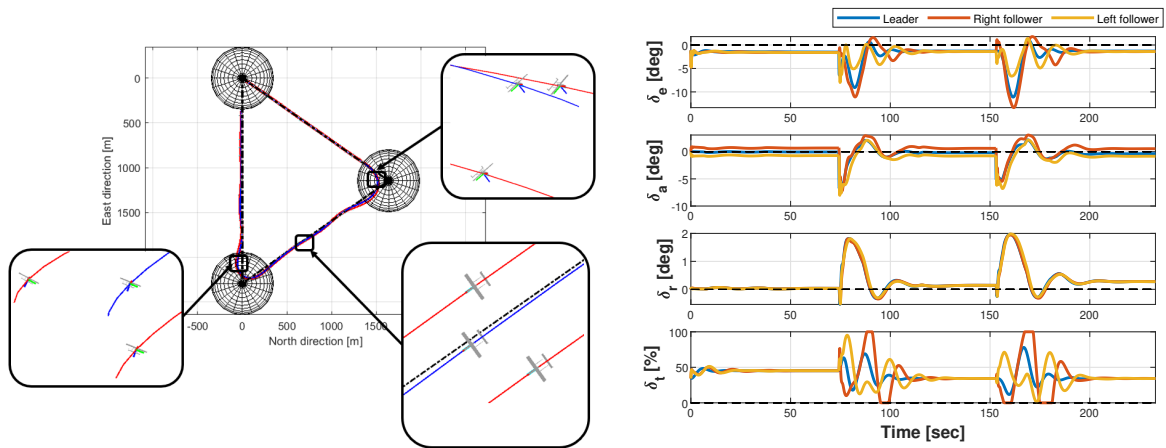


Figure 4.16: Triangular path. Three-aircraft formation. Left plot. Visualization of trajectories. Blue: leader. Red: followers. Right plot. Controls time histories for leader and followers.

The turn rate required for heading changes creates some challenges in maintaining the formation's geometry. In particular, the left follower (on the outer side of the turns) struggles to maintain the correct lateral position, while the right follower (on the inner side of the turns) makes substantial effort to maintain the correct longitudinal position, as observed in the corresponding throttle's time history.

Longitudinal and lateral-directional states are presented in Figure 4.18.

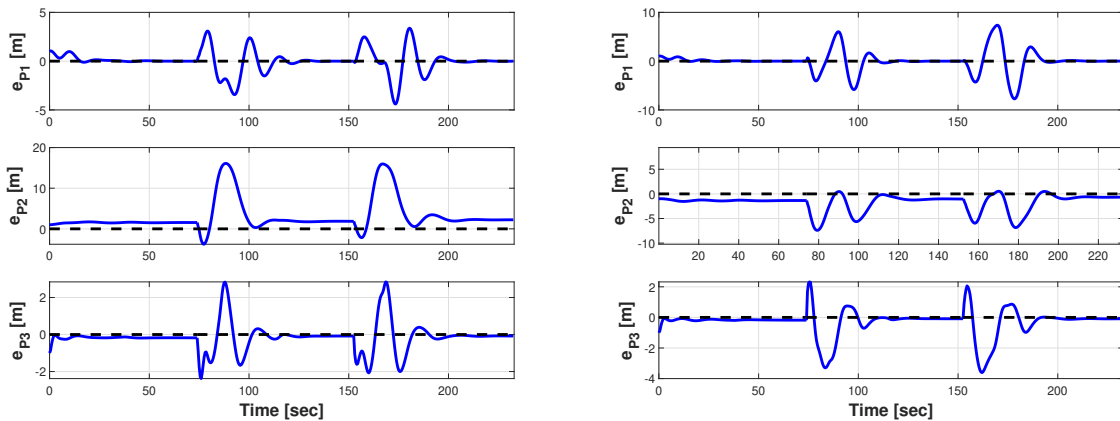


Figure 4.17: Time histories of errors for followers unit formation flight along a triangular pattern. Left: left-hand side follower position errors. Right: right-hand side follower position errors.

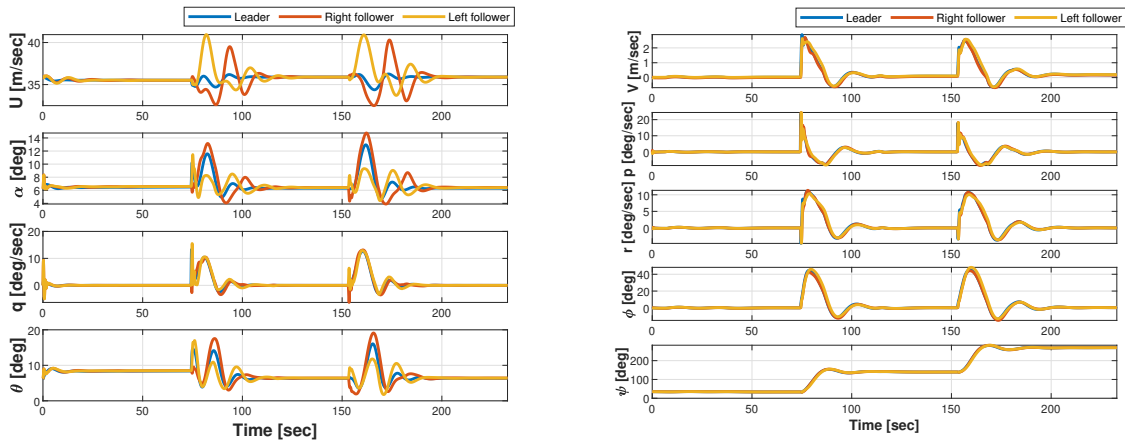


Figure 4.18: Three-aircraft formation along a triangular pattern. States time evolution.

4.3.4. Formation Testing in windy condition

An interesting scenario involves the swarm flying in a spread-out formation, maintaining a vertical separation of 20 m between leader and followers and a lateral and longitudinal separation of 10 m (no wake effects). The swarm is then subjected to a wind-stream tube featuring altitude bounds, in such a way that only the leader experiences an airspeed variation, whereas the followers do not enter the tube. This allows evaluating two possible formation behaviors:

1. when encountering a disturbance that deviates the leader from the route, the guidance mode takes priority, steering the followers back onto the established path and waiting for the disturbance to subside. Formation is momentarily lost, but most of the swarm keeps on accurately tracking the intended path.
2. In a complete leader-follower subordination logic, the followers chase the leader's trajectory, disregarding any information on the intended track. The leader's reaction to the disturbance causes the entire formation to experience an increase in cross-track error. However, mutual distances are kept within the formation.

Consider a setting where the formation is flying along a leg in a northerly direction and encounters a moderate-intensity (8 m/s, 90 deg direction) wind disturbance, that extends over a 1000 m path. It is interesting to analyze the two possible scenarios just introduced.

Formation Splitting

In the first case (Figure 4.19), which could be associated with an on-target phase of a reconnaissance mission, any disturbances encountered along the path are rejected without compromising the mission task. In this context, as soon as the leader enters the wind-stream tube, an increase in cross-track error triggers the disengagement of the formation control (cruise mode) of the autopilot, and the take over of the guidance mode (beam-tracking), which keeps the rest of the formation on the intended flight path. The formation is then reestablished by switching back to the cruise formation control mode once the disturbance has ceased.

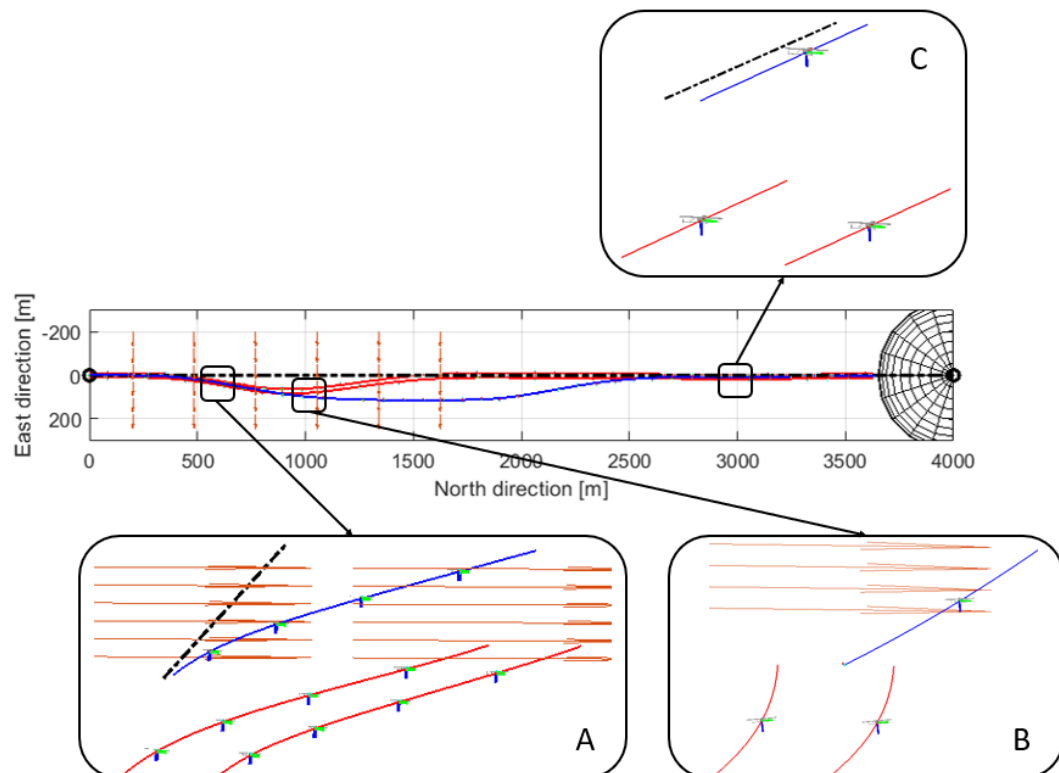


Figure 4.19: Leader flying through constant wind disturbance tube (A). Followers with on-target guidance mode engaged (B). Final formation rejoining (C).

The transition between the two control laws follows a logic reminiscent of that introduced for trajectory blending, as discussed in Section 3.1.3. However, in this case, a linear function is adopted (Figure 4.20), which prioritizes one over the other AFCS mode based on a signal indicative of the disturbance in progress, precisely, the cross-track error.

The choice of the threshold value on the cross-track error, as well as the slope coefficients governing the transition between the two autopilot modes, both upon entering and exiting

the disturbance, are user-adjustable parameters. In this case, a threshold value of 20 m was chosen, beyond which the linear transition occurs over time with angular coefficient $m_1 = 1/5$. when re-entering the tolerance band ± 20 m, the angular coefficient $m_2 = 1/20$ governs the reverse transition, aiming to reassemble the original formation.

The transition is faster at the beginning of the disturbance because switching from **FCM** to **GM** involves a shift to control laws tuned with lower gains. As a result, the return of the followers to the correct route is rather gradual, avoiding abrupt correction maneuvers (At the limit, it's possible to increase the coefficient m_1 to achieve an on-off type switch). On the other hand, the reverse transition prompts a noticeable response from the aircraft right from the beginning. Therefore, prolonging the transition times allows the followers to rejoin the formation in a smoother manner.

The implemented algorithm for AFCS modes transition is provided in Appendix C.

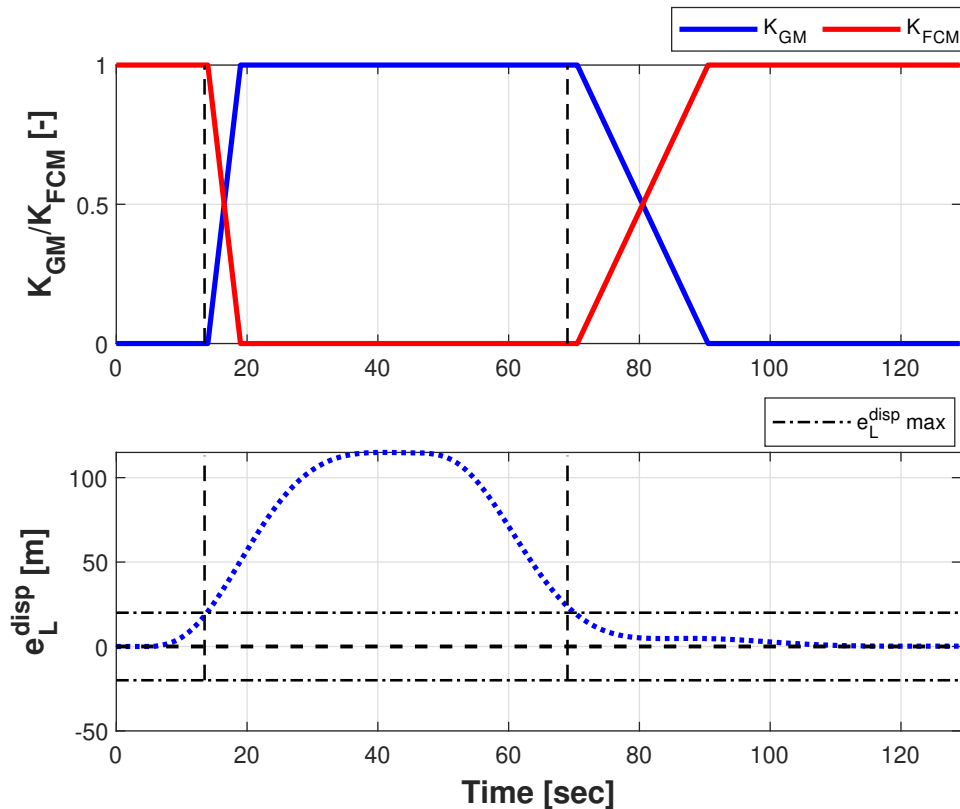


Figure 4.20: AFCS modes transition

An issue arises when the disturbance causes the leader to deviate significantly, by several tens of meters. In such cases, followers struggle to regain their longitudinal positions once the leader gets back on track. This happens because the disturbance slows down

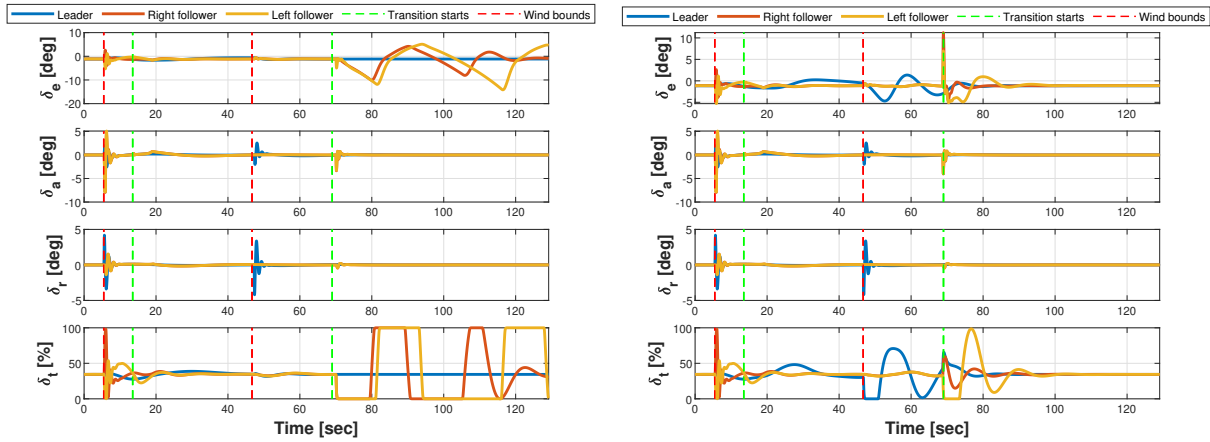
the leader, while the followers continue to fly at ground speed set point according to the guidance mode on the designated route. When the leader returns to its correct position, the separation accumulated by the followers becomes substantial.

Upon engagement of the **FCM**, the system commands, to followers aircraft, significant throttle changes, which can lead to longitudinal position errors either diverging or gradually recovering after substantial oscillations and over an extended time window. This is what is depicted in the left column of Figure 4.21, where the following is shown: in 4.21a, the command histories for the three components of the formation. In fig. 4.21c, the followers position errors.

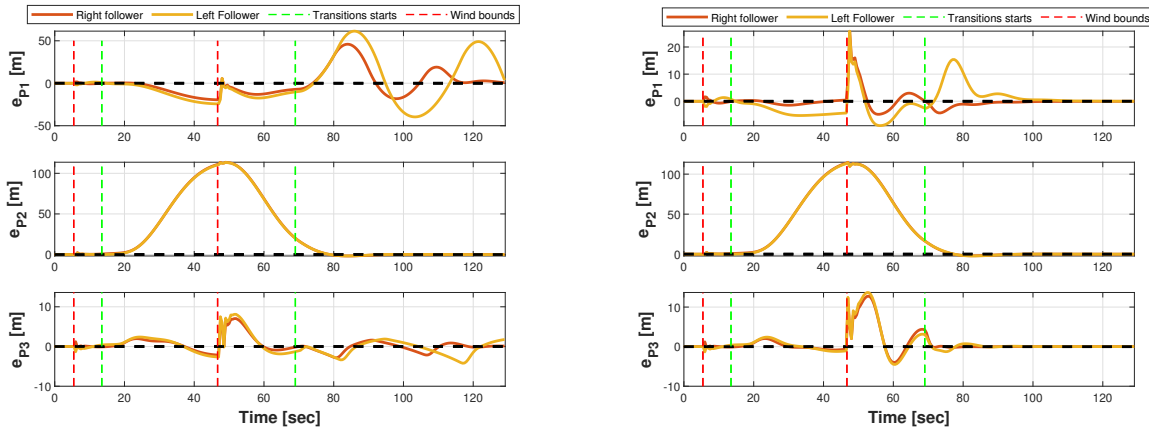
One possible solution is to provide the leader with a set point for both position and velocity, which are also calculated based on the longitudinal position error e_{P1} and velocity error e_{P1}^{Vel} . This calculation would be similar to what occurs in the autothrottle branch of the **FCM** for the followers, but with the gains sign inverted. This way, when e_{P1} and e_{P1}^{Vel} are positive (followers behind the target position or straying away from it), the followers accelerate, and the leader decelerates. Conversely, when e_{P1} or $e_{P1}^{Vel} < 0$ (followers ahead of the target position or approaching it), the leader accelerates, and the followers decelerate. This approach aims to quickly and smoothly compensate for the correct longitudinal position for the formation members without causing command saturations. This second scenario is depicted through the temporal controls histories and followers position errors in the right-hand column of Figure 4.21.

The figure, also includes a timeline, indicated by the red dashed lines, corresponding to the leader's wind stream crossing, while the green dashed lines represent the interval between time instants at which the transition between AFCS modes is engaged.

This "track precision" mode, facilitated by a supervisory control system, can prove beneficial not only for scenarios involving medium to high-intensity wind disturbances affecting only the leader but also in cases where the mission task is compromised by potential malfunctions in the leading unit, such as complete signal loss.



(a) controls time histories with non-cooperating leader. (b) controls time histories with cooperating leader.



(c) Followers position errors with non-cooperating leader. (d) Followers position errors with cooperating leader.

Figure 4.21: Formation disturbance management with separation and rejoining. Comparison between the non-cooperating leader ((a) and (c)), and cooperating leader ((b) and (d)).

Leader's Rudder correction

In the second scenario, a simple but effective solution, without requiring significant computational resources, involves correcting the formation drift through a rudder maneuver performed by the leader. In this approach, when the leader enters the wind stream, gets into skidding trim with a coordinated rudder input (based on lateral beam-tracking indicators) and aileron counter-command (crabbing maneuver, Figure 4.23), effectively reducing the cross-track error (Figure 4.24 left). The followers, controlled solely via **FCM**, then track the leader's velocity vector. This results in a more compact formation with

a significantly lower average cross-track error compared to the scenario without leader's correction, avoiding the need to split the formation.

The resulting trajectories are depicted in Figure 4.22.

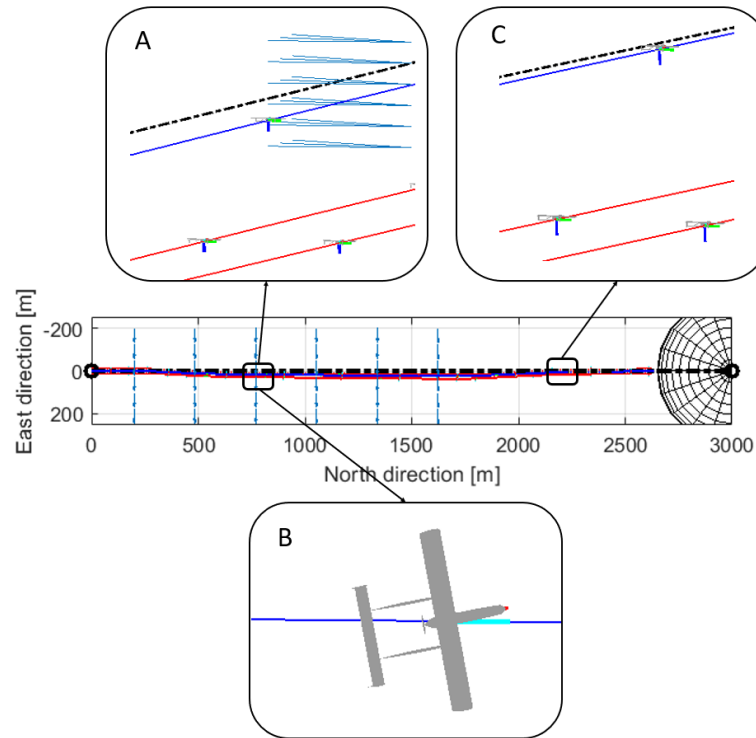


Figure 4.22: Leader flying through constant wind disturbance tube (A). Followers with on-target guidance mode engaged (B). Final formation rejoining (C).

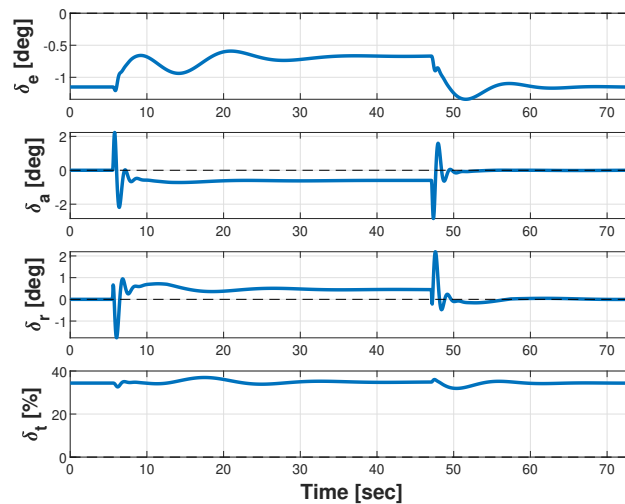


Figure 4.23: Leader's controls time histories for crabbing maneuver

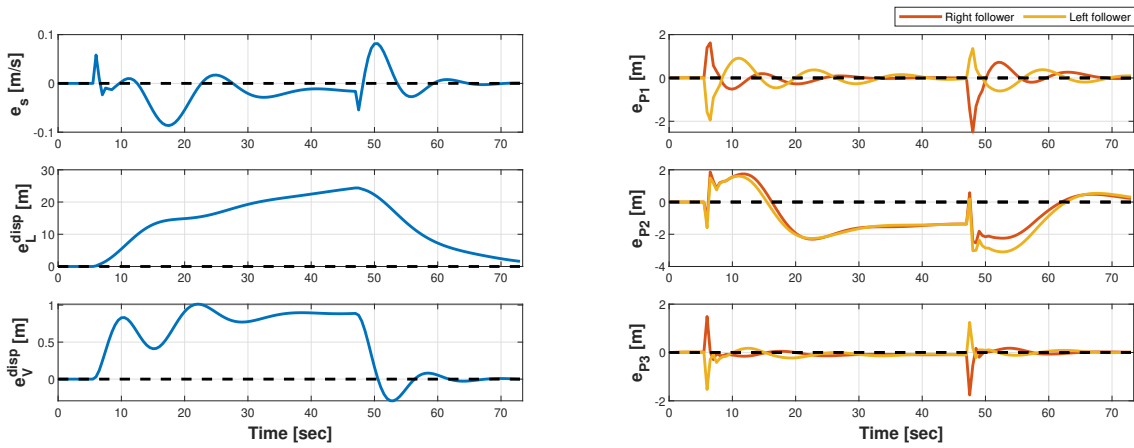


Figure 4.24: Target errors for leader's beam-tracking (left) and followers position tracking (right).

In conclusion, both of the proposed solutions are valid approaches for a wind disturbance rejection that primarily affects the leading unit. These methods can be applied to tackle a broad spectrum of challenging operational conditions: to ensure minimal average cross-track error in the presence of crosswinds, the second solution is undoubtedly the most effective. However, in the event of a major failure in the leader's **GM** control, which causes it to deviate from the planned route, or a complete loss of signal, the engagement of the first solution becomes desirable to prevent mission failure.

5 | Mission Simulation

In recent years, Unmanned Aerial Vehicles (UAVs) have emerged as a vital tool in disaster response and environmental monitoring. Their ability to efficiently survey large areas while minimizing human exposure to hazardous environments has positioned them at the forefront of crisis management operations. One such critical scenario was the Fukushima Daiichi nuclear disaster in 2011, triggered by a catastrophic earthquake and tsunami off the coast of Fukushima, Japan. This unparalleled incident necessitated extensive data collection, risk assessment, and decision-making within highly contaminated and challenging conditions.

This chapter comprehensively explores the utilization of fixed-wing UAV swarms in the Fukushima 2011 disaster context. We delve into the design, planning, and execution of a simulated mission in the Fukushima region, emphasizing the adaptable and collaborative nature of UAV swarms to address the evolving needs of disaster response.

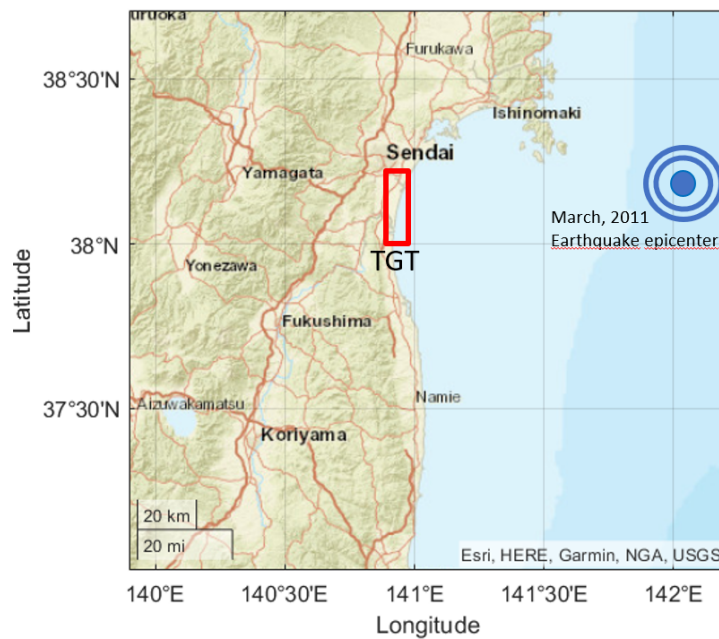


Figure 5.1: The earthquake-affected area, Japan, March 2011. Identification of the epicenter and coastal reconnaissance target area.

The mission is carried out using nine aircraft organized into three clusters. The mission's objective is to fly over a stretch of coastline damaged by the tsunami and loiter around the small town of Yamamoto, acquiring photographic material needed by ground units to coordinate rescue efforts. In the preliminary phase, one unit is designated as the leader for each cluster, responsible for guiding the three-aircraft formation to the rendezvous area and overseeing the formation rejoining process. The rendezvous area is situated near the coast, in close proximity to the town of Kakuda-shi. Cluster 1 is scheduled to depart from Yamagata Airport, located to the northwest of the target area. Cluster 2's departure is planned from Fukushima Airport, positioned to the south of the designated zone. Meanwhile, the third cluster is already airborne, heading from the west towards the rendezvous point, as shown on the map in Figure 5.2.

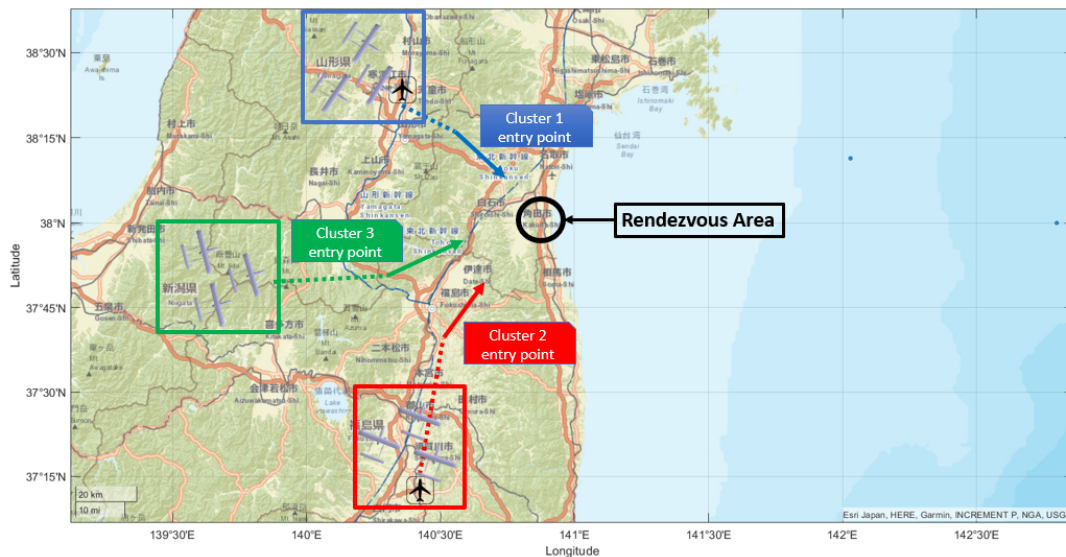


Figure 5.2: Clusters departure points and rendezvous designated area.

The target area is situated between a mountain range with medium-low relief (summit point at 690 m) and the coastline, necessitating some precautions. To reach the rendezvous point, it is necessary to fly over the mountain range with a safety margin of at least 200 m above the summit. The rendezvous is, therefore, conducted at an altitude of 900 m above ground level (3000 ft). Additionally, due to the topographical layout, the area is prone to moderate-intensity winds, both near the terrain's relief and along the coastal stretch.

A detailed mission schedule is provided in Table 5.1, while the main navigation information are reported in Figure 5.3.

Rendezvous				
Orbit center	Orbit radius	Altitude	Velocity	additional notes
38° 01' N, 140° 53' E	1200 m	900 m	120 km/h	Wind. $\psi_w = 135$, int. 4 m/s
Waypoints navigation				
Leg	Length	ΔH	Velocity	additional notes
O-A, $\psi = 60$	2400 m	-200 m	130 km/h	Formation geom. switch- V.
A-B, $\psi = 90$	1500 m	-100 m	130 km/h	-
B-C, $\psi = 180$	3100 m	-100 m	130 km/h	Wind. $\psi_w = 270$, int. 8 m/s
C-D, $\psi = 240$	2000 m	+100 m	130 km/h	Formation geom. switch- D.
D-E, $\psi = 200$	2000 m	+0 m	130 km/h	-
Loiter				
Orbit center	Orbit radius	Altitude	Velocity	additional notes
37° 57' N, 140° 53' E	1000 m	400 m	120 km/h	-
Waypoints navigation				
Leg	Length	ΔH	Velocity	additional notes
E-F, $\psi = 240$	2000 m	+200 m	130 km/h	Formation geom. switch -V.
F-G, $\psi = 270$	2600 m	+200 m	130 km/h	-

Table 5.1: Mission schedule.

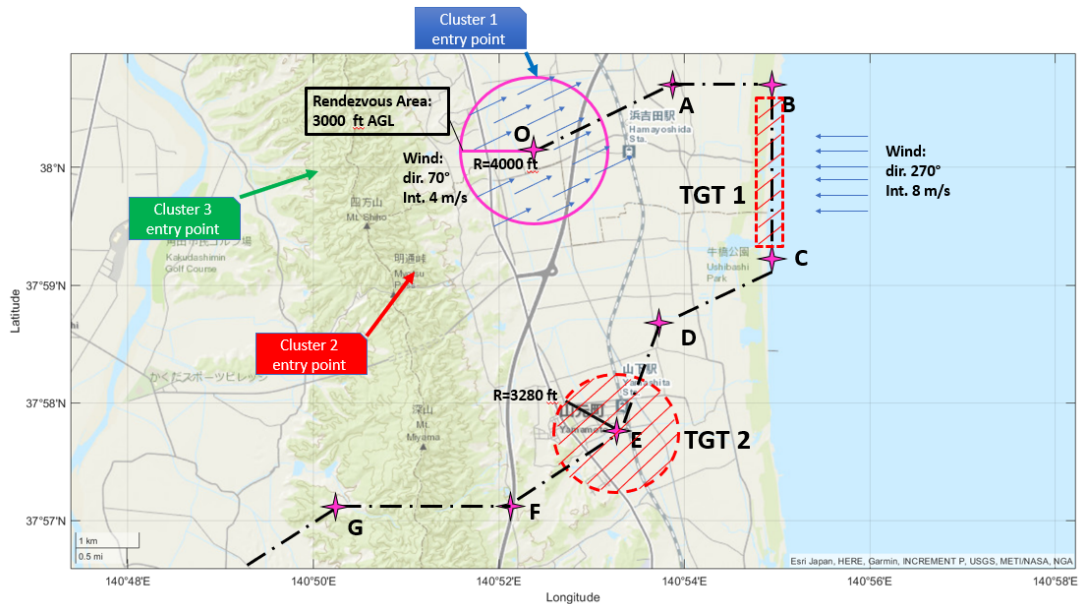


Figure 5.3: Navigation information. Waypoints and targets collocation.

Among various potential solutions, two formation geometries have been selected for this mission type. The first is a V-shaped formation, with swarm’s units arranged as shown in Figure 5.4 , for navigation phases, while the second is a diamond-shaped formation for target overflights (Figure 5.5). The interchangeability between these two geometries can

be controlled based on either time or inertial coordinates.

Once the formation geometries are defined, a choice must be made. Either each follower is linked to a unique leading unit, or positions are linked in a chain so that each aircraft is the direct follower for the preceding unit. The first solution was pursued primarily because this approach provides rigidity to the formation (in the second case, any positioning errors of more advanced followers propagate throughout the swarm). Secondly, in the event of the leading unit's loss, it would be compensated for by the track precision mode procedure discussed in Section 4.3.4.

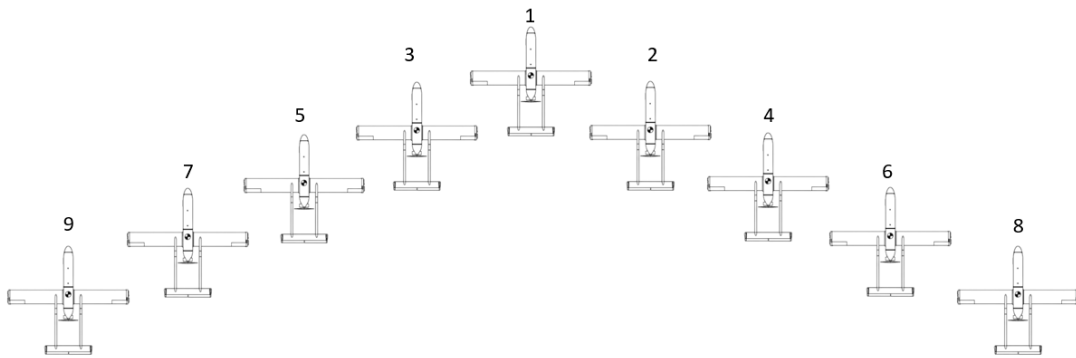


Figure 5.4: V-shape formation for navigation phases.

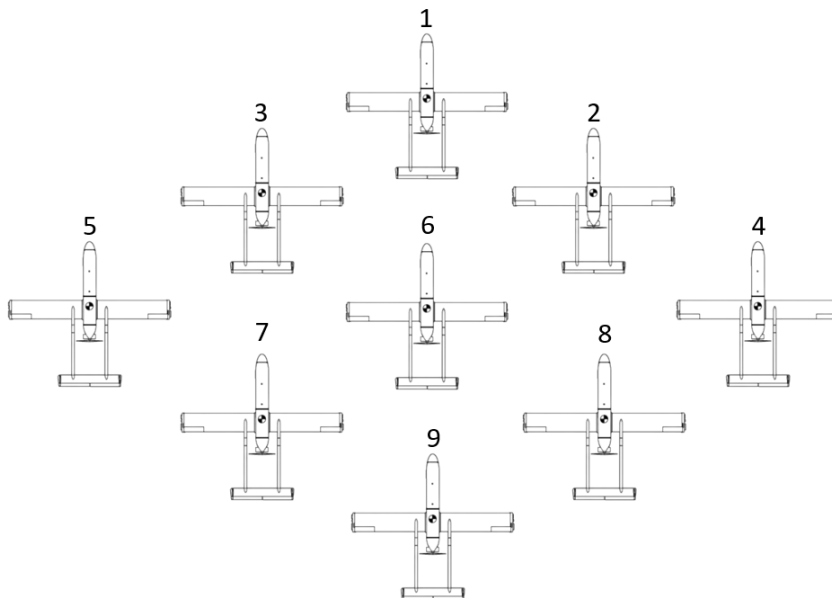


Figure 5.5: Diamond-shape formation for targets overflight.

5.1. Phase 1: Rendezvous

The rendezvous procedure follows the control logic discussed in Section 3.3, placing Aircraft 1, the designated swarm leader and leading unit of Cluster 1, on a circular orbit with a radius of $R = 1200$ m at an altitude of 900 m. Aircraft 6 and 9, leaders of Clusters 2 and 3, respectively, gradually integrate into the approach trajectory, chasing Aircraft 1. The three clusters fly with a vertical separation of 30 meters to prevent mid-air collisions during the formation rejoining. When they are within 40 m of relative distance from the formation leader, the Flight Control Mode (**FCM**) is engaged for all followers, bringing them to acquire their target positions relative to Aircraft 1. The relative position between the leader and followers 1 and 2 is marked with a black dashed line to visualize the formation's vertex once reassembled without cluttering the plot.

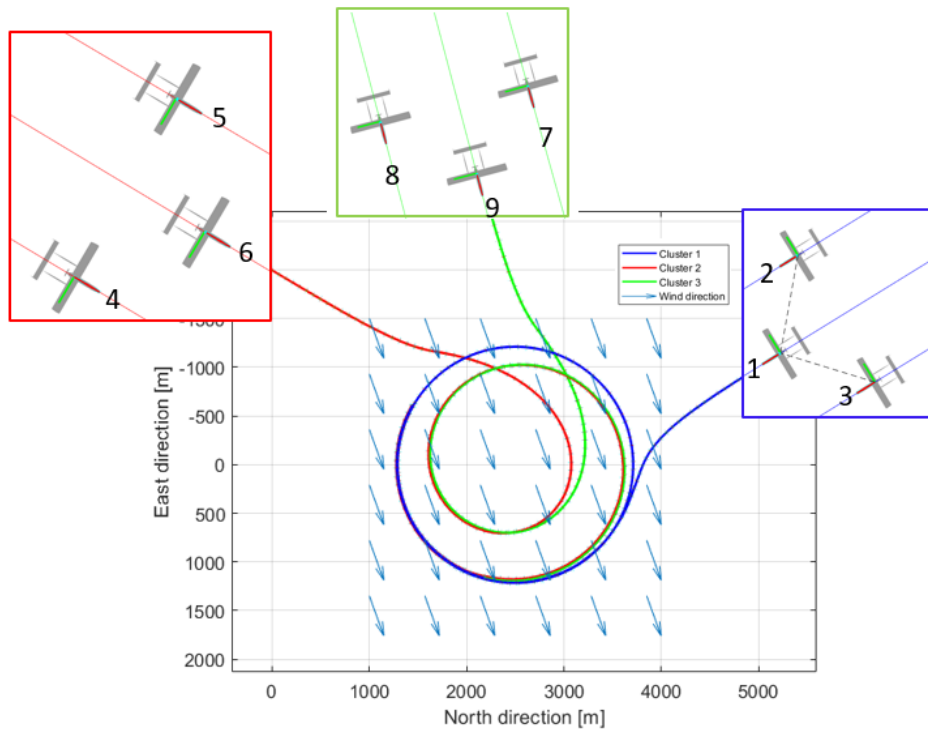


Figure 5.6: Rendezvous for formation assembly with 4 m/s crosswind heading $\psi_w = 70$ deg.

The procedure is executed without speed control, so in general, the approach of the clusters occurs rather gradually. This is done to ensure that the phase difference with Cluster 1 is not eliminated too quickly. In such a case, the followers would be at the same phase angle as the leader but at a relatively large distance to engage **FCM** without incurring abrupt repositioning maneuvers.

As shown in Figure 5.7 displaying the control parameters for the rendezvous procedure, the approach proceeds appropriately despite the presence of crosswind. The phase shift recovery is achieved within 270 seconds from entering the rendezvous area. In the subsequent time window, the clusters gradually reduce their relative distances until they achieve the complete formation rejoining in a diamond shape, as depicted in Figure 5.8.

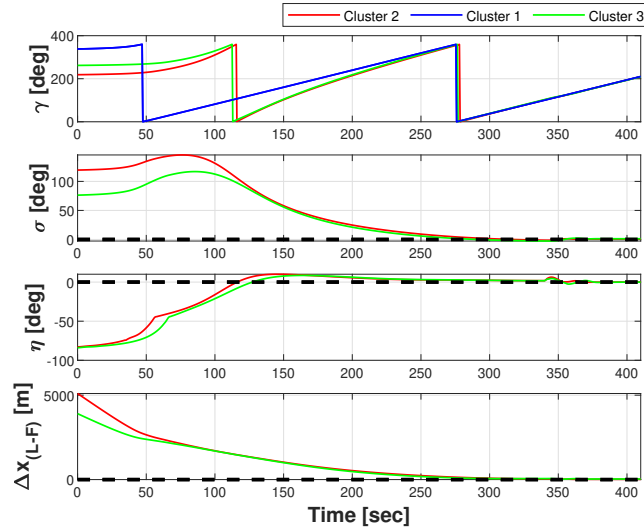


Figure 5.7: Rendezvous indicator parameters: phase angle γ , phase shift σ , side-bearing angle η , and relative leader-follower distance Δx_{GND} .

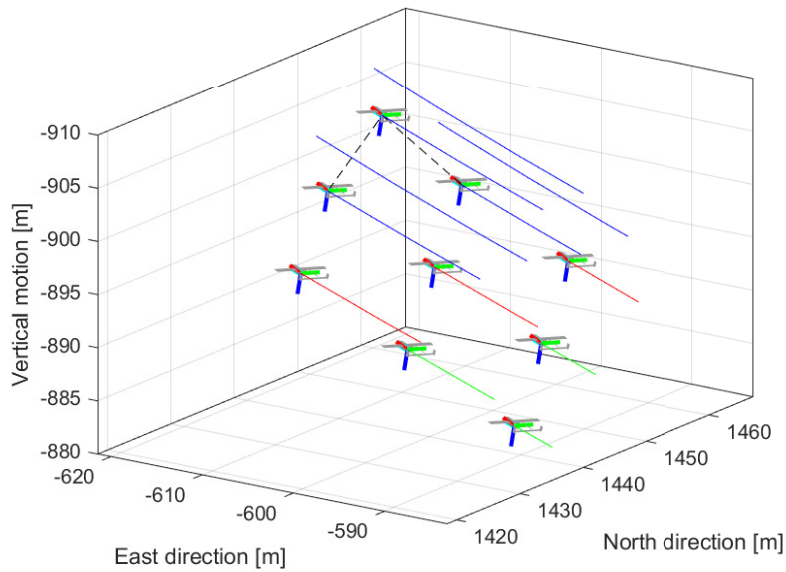


Figure 5.8: Rendezvous procedure completed ($T = 410$ s). Formation assembled in diamond shape.

A quick glance at Figure 5.9 reveals how the rendezvous phase is managed in terms of control. The rapid control oscillations between 50 and 70 seconds represent the intervention of the guidance and stabilization systems upon entering the wind-disturbed area. Importantly, this disturbance does not significantly impact the execution of the procedure, as indicated by the relatively smooth control inputs until the **FCM** engagement for clusters 2 and 3 at around 340 seconds. It is evident that the **FCM** switch on, at this point, results in a sharp throttle response to adapt the followers to the leader's longitudinal position and velocity. Nevertheless, the repositioning is completed without significant issues. One potential solution could involve managing the final phase of the approach by imposing a velocity correction on the leader as well, in order to accommodate the formation repositioning.

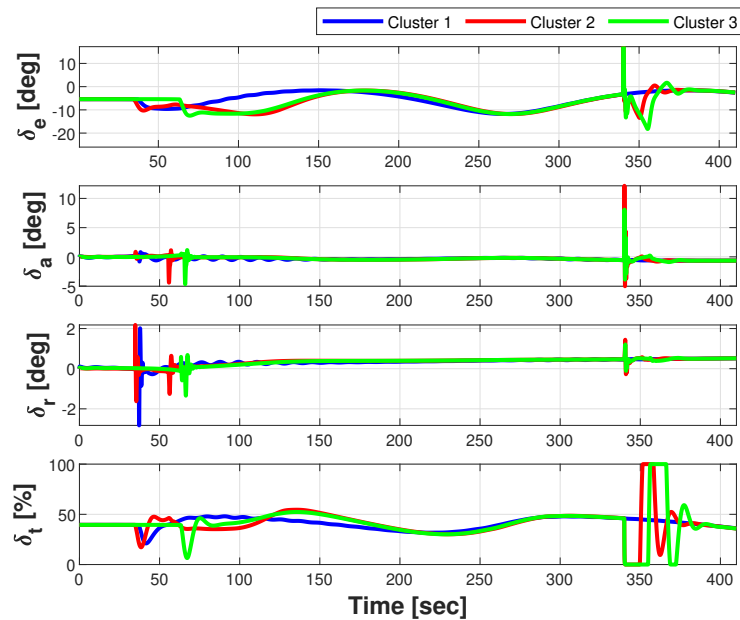


Figure 5.9: Aircraft 1,6,9 controls time histories for rendezvous procedure with crosswind.

5.2. Phase 2: Waypoint Navigation

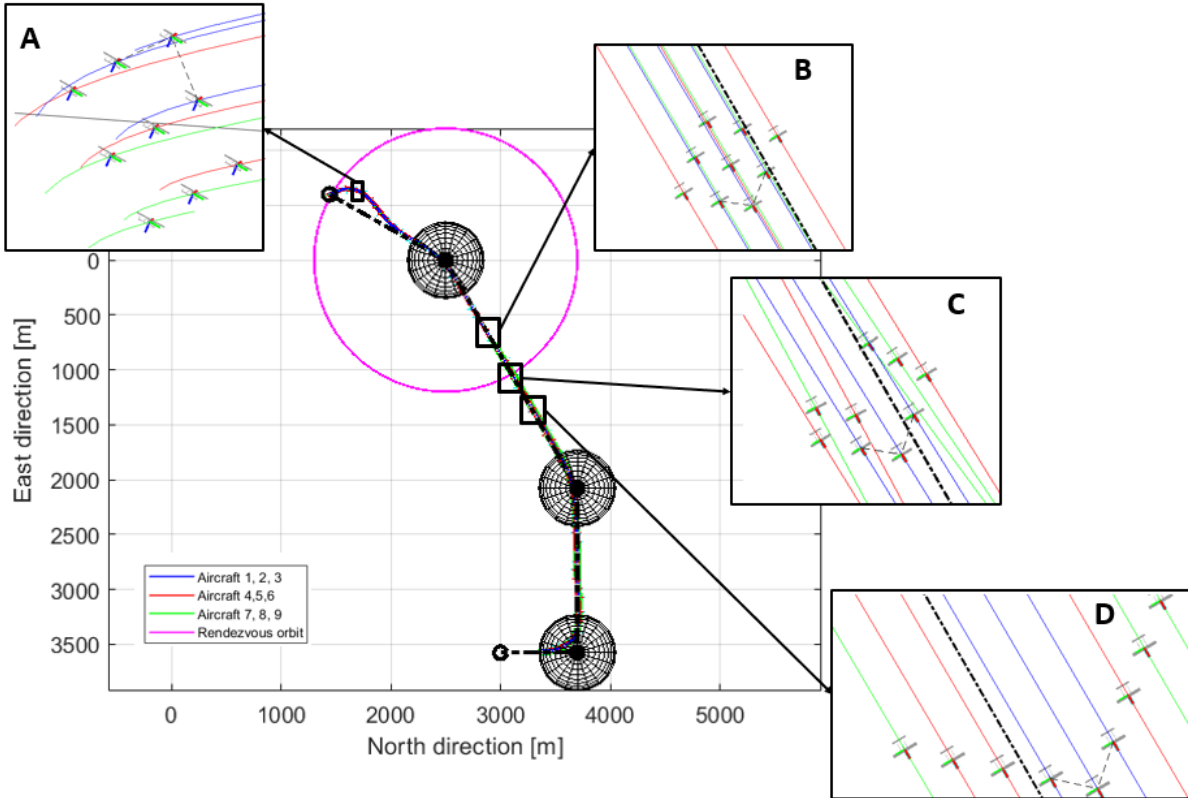


Figure 5.10: Navigation Phase. Box A: turning maneuver for route alignment. Box B: diamond-shaped formation. Box C: reconfiguration. Box D: V-shaped formation.

The navigation phase involves the swarm departing from the rendezvous orbit to head towards the first waypoint at the orbit's center. While traveling along the second leg, a reconfiguration of the formation into a V-shape is commanded, as depicted in Figure 5.10. The formation remains compact behind the leader even during more pronounced maneuvers, such as the turn towards the first waypoint.

The beam tracking errors targeted by the leader are shown in Figure 5.11. But what is more interesting to test is the formation's ability to reconfigure itself. Figure 5.12 display the position errors and the corresponding command time histories for aircraft 6, 7, 8, and 9, which undergo a positional change. In particular, aircraft 6, positioned centrally in the diamond-shaped formation, assumes the role of the third right follower in the V-shaped configuration, 7, 8, and 9, representing the rear vertices of the diamond-shaped formation, respectively take positions as the third left follower, fourth right follower, and fourth left follower at the edges of the V.

Despite the initial struggle to maintain position due to the abrupt course realignment maneuver, positioning errors are effectively reduced following the reconfiguration request.

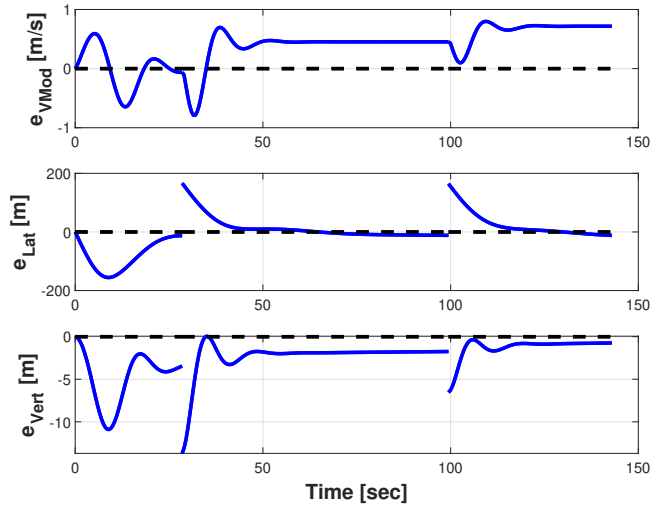


Figure 5.11: Target errors for beam tracking guidance during navigation phase.

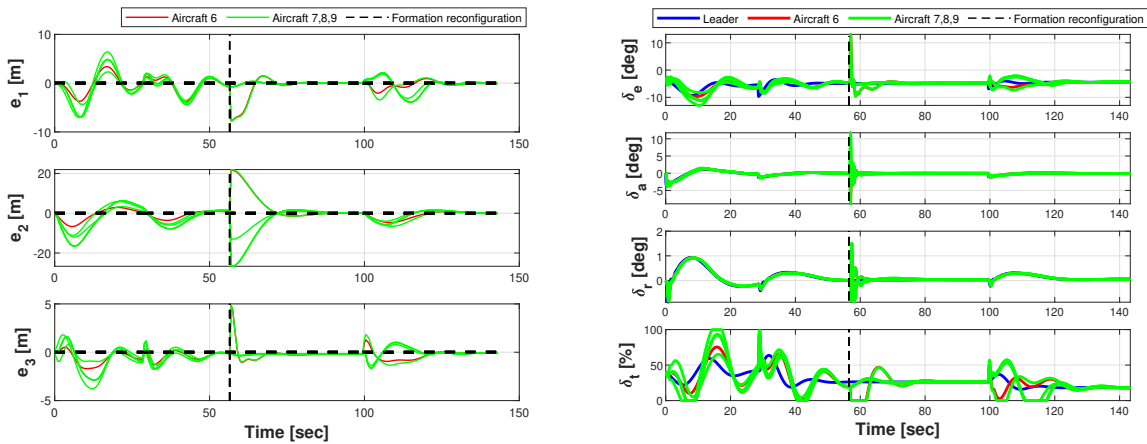


Figure 5.12: Position errors and controls time histories for Aircraft 6,7,8,9 during formation reconfiguration.

5.3. Phase 3: Target 1 Overflight

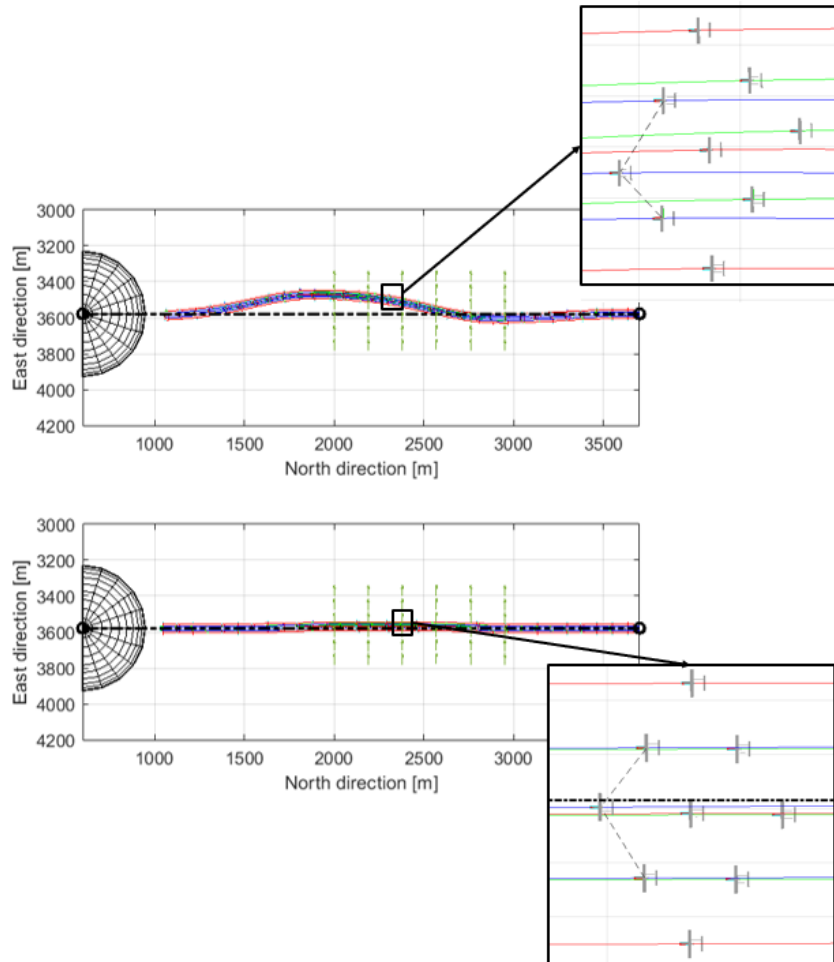


Figure 5.13: Target overflight with 8 m/s crosswind. Comparison between trajectories with and without rudder compensation.

During the target overflight, the formation, which has been spread out to provide wider ground coverage, is subjected to a medium to high-intensity crosswind.

In Figure 5.13, the comparison between trajectories obtained without any compensation and with the crabbing maneuver by the leader is shown, along with controls time history highlighting crabbing maneuver coordination in Figure 5.15.

In both cases, the formation remains relatively compact, with position errors effectively reduced to zero, despite visible perturbations during entry into and exit from the disturbance zone (Figure 5.16).

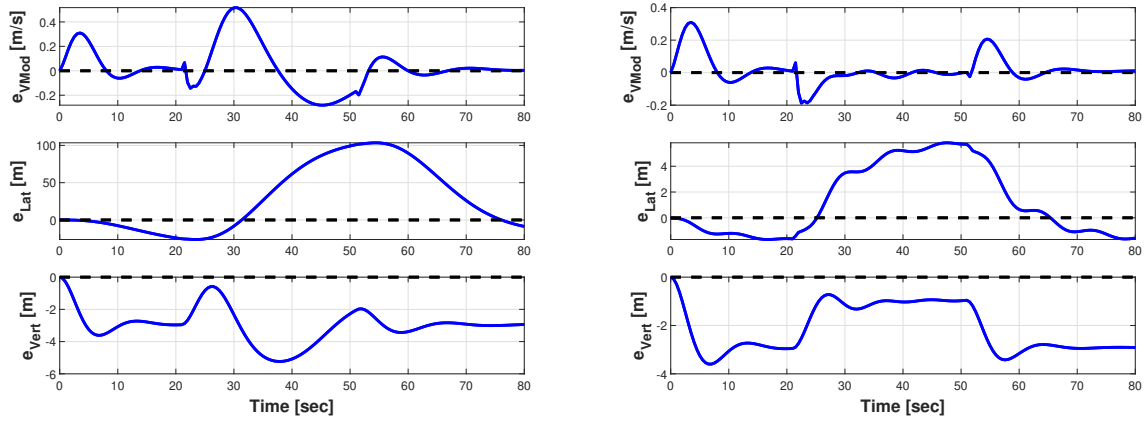


Figure 5.14: Beam tracking errors targeted by the leader. Comparison between errors resulting from no compensation (left) and crabbing maneuver (right).

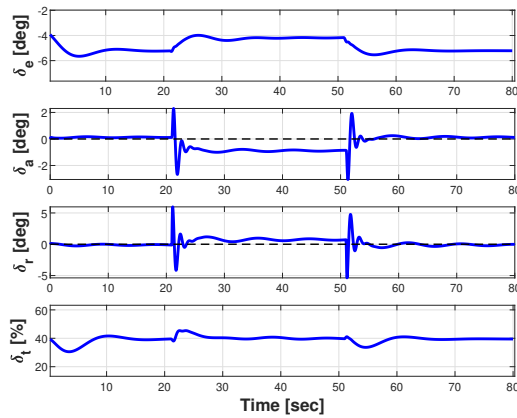


Figure 5.15: Leader's crabbing maneuver coordination.

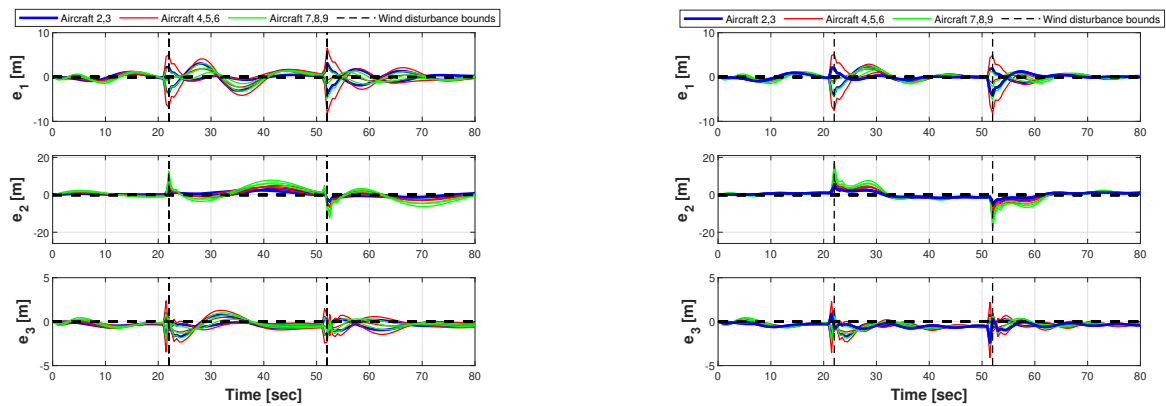


Figure 5.16: Formation position errors. Comparison between errors resulting from no compensation (left) and crabbing maneuver (right).

5.3.1. Alternative Scenario: Leader's GM Failure Over Target

A parallel scenario is envisaged. In this case, a failure in the leader's guidance system is simulated, such that the aileron and rudder commands do not intervene to compensate for the increase in cross-track error induced by the wind. The failure is extended for 25 seconds (from $t = 35$ s to $t = 60$ s), after which the guidance system regains authority, bringing the leader back on the beam (Figure 5.17).

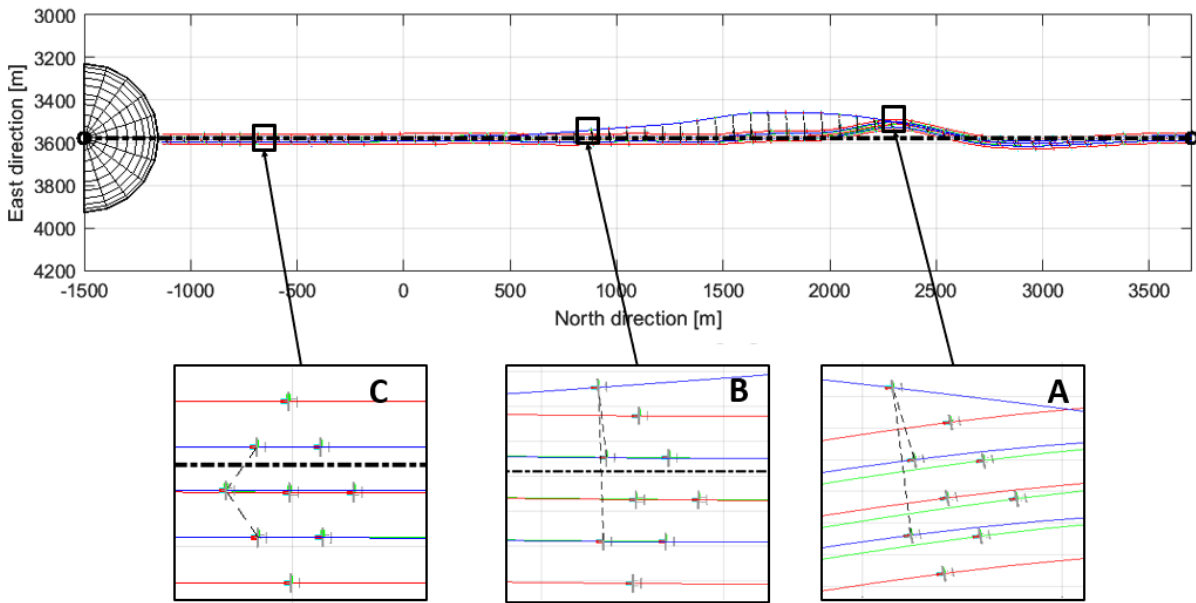


Figure 5.17: Leader's **GM** failure over target. Precision track mode sequence: Box A: formation split. Box B: Leader's rejoining. Box C: complete formation.

Beyond the 20 m threshold on cross-track error, the supervisory control system detaches the rest of the formation from the leader and returns them to their designated route.

Upon the leader's repositioning, the supervisory system instructs the followers to reacquire their respective positions within the formation.

To facilitate the followers position recovery, it is necessary to extend the leg beyond the planned waypoint and reduce the gains in the throttle control branch of the **FCM**.

The set of position errors and their respective control histories for all the followers are depicted in Figure 5.18. It distinctly shows the phase of formation detachment and the re-engagement of the **FCM** occurring at $t = 91$ s.

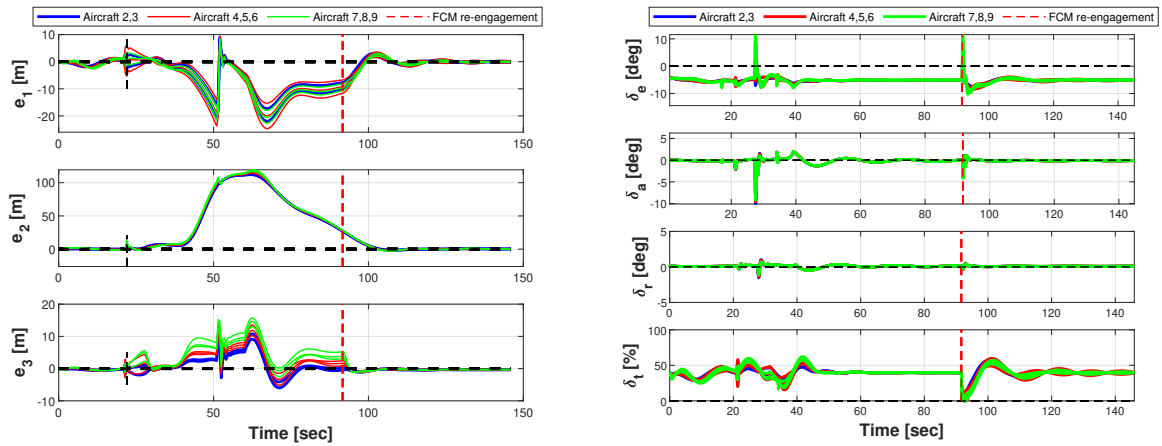


Figure 5.18: Followers position errors and control time histories during leader's failure on target.

5.4. Phase 4: Target 2 Overflight

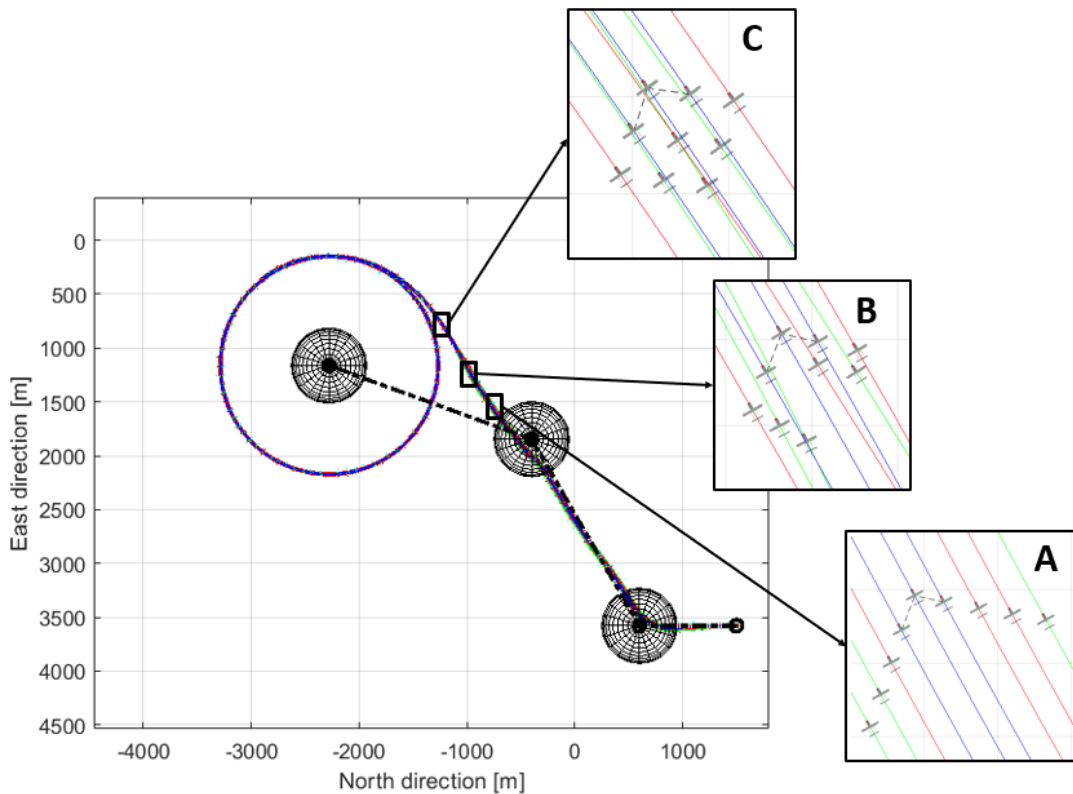


Figure 5.19: Target 2 Overflight: Circular orbit insertion and traveling. Geometry recon-figuration sequence: Box A: V-shape. Box B: transition. Box C: diamond shape.

The formation, after completing the overflight of the first target in the V configuration, reverts to the navigation route to reach the second target. At the end of the second leg of the path, the guidance system initiates tracking the vector field of course angles to enter the orbit with a rather relaxed transition rate. Before entering, a new configuration change is commanded: from V to diamond shape.

No significant issues are observed for guidance system tracking performance, and the error trends are depicted in Figure 5.20. It's worth noting that the lateral cross-track error, at the end of the second leg, is now referenced to the orbit circumference instead of the beam.

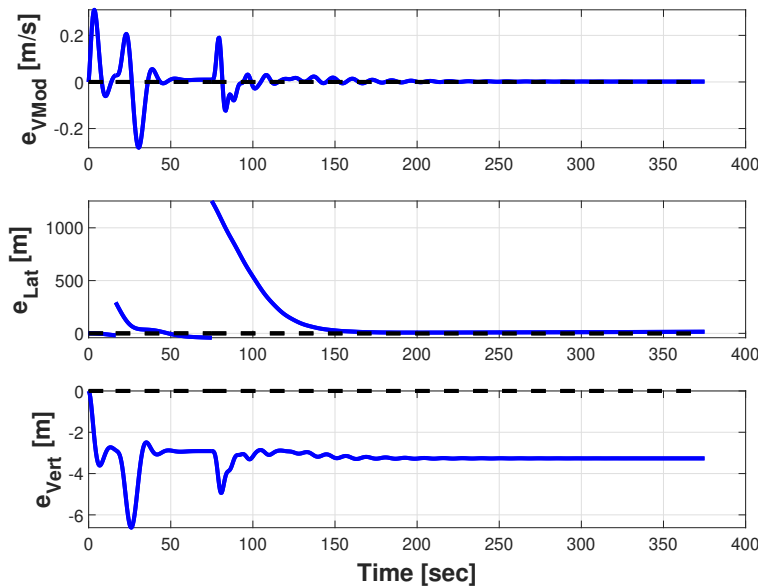


Figure 5.20: Guidance errors during target 2 overflight.

Regarding the rest of the formation, there is a slight issue during the transition to the vector field-based guidance mode. If the aircraft are not well-aligned with the field's direction at the moment of transition, the guidance system generates a strong response to align the leader with the commanded route. This leads to a series of oscillations in the follower aircraft's position tracking, which can be particularly challenging for the trailing aircraft, experiencing wider oscillations (Figure 5.21).

Beyond this, the reconfiguration of the formation's geometry occurs adequately, and afterward, the position error of the followers remains nearly constant at zero for the remainder of the target overflight.

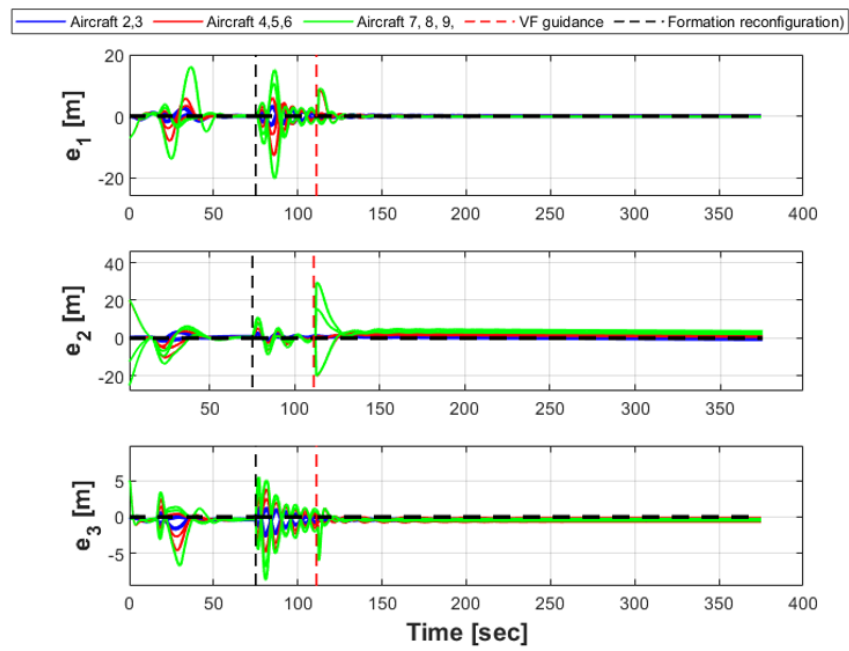


Figure 5.21: Formation position errors during target 2 overflight.

5.5. Phase 5: Disengagement and Formation Splitting

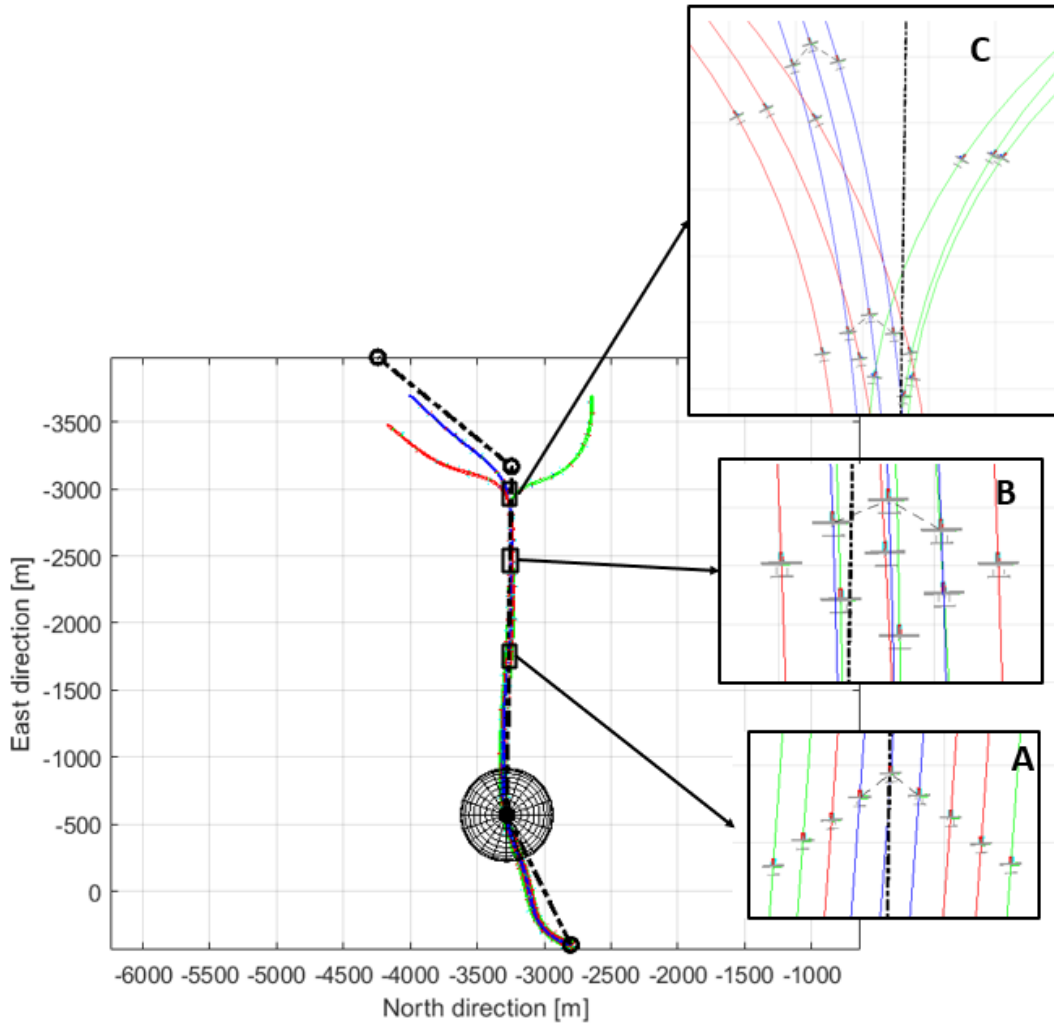


Figure 5.22: Disengagement and formation splitting sequence: Box A: V-shaped formation. Box B: diamond-shaped formation. Box C: split formation.

The final phase of the mission involves the disengagement of the formation from the operational area. The formation is directed onto an exit trajectory that includes traversing a turbulent zone along the path of the second leg. Within the simulation, turbulence is modeled using a random signal, with specified lower and upper bounds. In this instance, the deterministic wind component is fixed at 4 m/s, with turbulence occurring between ± 1 m/s. The effect of turbulence is clearly visible in Figure 5.23, where the lateral-directional states for aircraft 2, 6, and 9 are shown as examples, representing the behavior

of the entire formation.

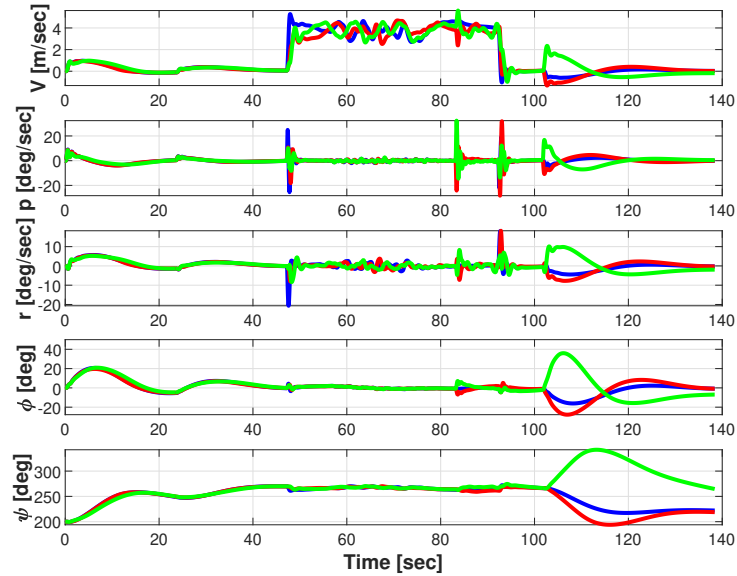


Figure 5.23: Turbulence effect on lateral-directional states of Aircraft 2,6,9.

Despite this, the formation retains compactness without the development of dangerous instabilities. The only issue, in this case as well, is that the outermost members of the formation struggle to maintain the correct longitudinal position (see Figure 5.24) during sharp turns (first maneuver when exiting the circular orbit).

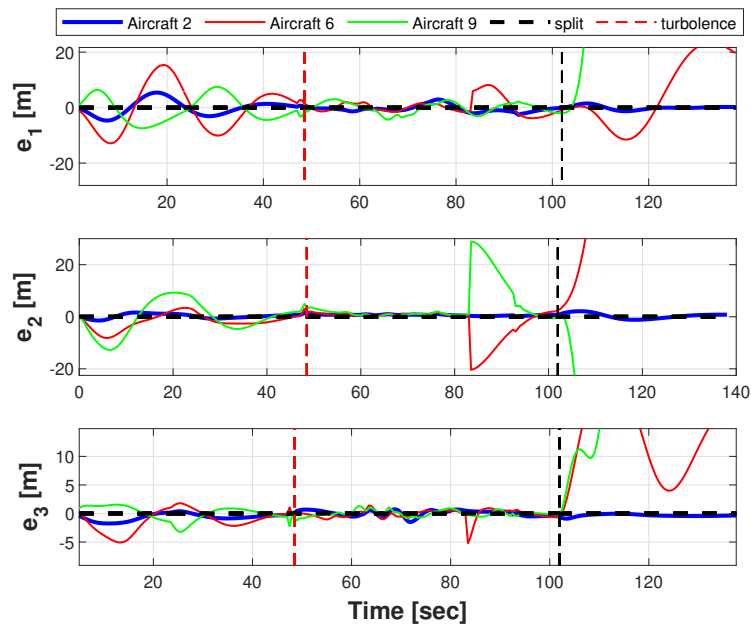


Figure 5.24: Aircraft 2,6,9 position errors during disengagement in turbulent air.

Shortly before splitting, the formation re-configures into a diamond shape, bringing the aircraft belonging to the same cluster closer together. Afterward, aircraft 9 and 6 are designated as leaders of their respective clusters, while the others acquire their target positions relative to the cluster leader. The separation occurs smoothly.

6 | Conclusions and Outlook

Various aspects of formation flight have been investigated within this thesis work. The intention of this work is not to replace the existing documentation on the control and coordination of a fixed-wing multi-unit UAV system, but rather to propose a viable alternative for a more in-depth modeling of the problem from the perspective of flight dynamics, rather than pure control architecture. The dynamic modeling in a fully non-linear environment has allowed the highlighting of specific aspects of the problem at hand, such as the stability of individual aircraft subjected to state disturbances, the challenges of interfacing with nonideal actuation systems subjected to bandwidth limitation and signal saturation, the effects induced by aerodynamic interaction, the criticality of maneuvering at angles of attack close to stall, while avoiding exceeding the constraints on minimum sustaining airspeed, as well as managing a limited available engine power, resulting in a constrained flight envelope.

The problem of stabilization was addressed by employing a stability augmentation system (SAS), designed following a model-based approach and tuned according to an LQR (Linear Quadratic Regulator) procedure. This approach resulted in a satisfactory three-axe stabilization, ensuring the required flying qualities for the specific aircraft class, and leaving sufficient bandwidth for the higher layers of the controller, responsible for guidance.

A guidance system was studied to ensure the swarm's capability to follow a path with multiple checkpoints in 3D space, adjusting the aircraft heading and altitude to accommodate realistic navigation requirements. The chosen control logic and tuning ensure adequate guidance system performance, tested on several polygonal patterns, where the cross-track error is effectively reduced to zero for each leg. Additionally, the system is able to avoid trajectory overshoots thanks to the blending technique employed.

The vector field-based guidance procedure provides an effective solution for executing loiter maneuvers and facilitating formation regrouping within confined spaces. In this regard, its integration with a specific rendezvous guidance protocol based on followers

re-phasing, by means of a lateral acceleration set point, expedites formation rejoining times and mitigates the issue of limited available speed range, which is crucial for linear rendezvous execution.

For the formation coordination, a control architecture based on the leader-follower hierarchy was employed. A decentralized control approach was adopted, where each aircraft (follower) is assigned a target position to chase, relative to the preceding aircraft (leader). This is achieved by comparing position, attitude, and trajectory information exchanged between the two involved formation elements. This communication mode ensures a limited amount of exchanged data, thereby reducing computational complexity, and required communication bandwidth, and consequently ensuring swarm scalability. The outcome of the performed testing reported an effective and promising formation coordination. The follower aircraft were able to maintain a stable (within proper tolerances) and aligned position relative to the leader aircraft, responding appropriately to variations in the leader's position and trajectory. Additional tests were performed to prove the formation behavior in the presence of a constant wind disturbance, ensuring both tight formation through relative position tracking within the swarm, or triggering formation reconfiguration, with followers flying along a designated route when properly switching their autopilot mode.

A realistic scenario has been envisaged in order to test the synthesized controllers dropped into an operational context typical of a ground reconnaissance mission.

The objective was to test the feasibility and reliability of a swarm with a scaled number of units and complexity, placed within a realistic operational context. The ensemble of control algorithms proved capable of conducting all distinct phases of the mission without significant issues. Required variations in altitude and speed conditions did not pose problems for the stabilization system, enabling individual aircraft to operate even in the presence of induced disturbances. The guidance procedures facilitated the seamless execution of different mission phases, while the formation control system demonstrated its suitability for coordinating the formation, adapting effectively to substantial trajectory changes by the leader and responding to formation reconfiguration requests.

In summary, this investigation has provided a thorough and realistic exploration of each operational phase within an unmanned multi-element formation flight mission. This underscores the presence of a sophisticated analytical tool, offering the capacity to conduct comprehensive assessments of missions of this nature with a high degree of fidelity and realism

Future Perspectives

There are several perspectives for further development of this work currently under consideration:

- firstly, the possibility of significantly increasing the number of aircraft units within the swarm while establishing a proper hierarchy to ensure stability and robustness.
- Secondly, an analysis of potential swarm reconfiguration strategies in case of signal loss. For future research, an exploration of coordination logic based on local distance measurements using laser distance measurement, as opposed to relying solely on GPS data, could be pursued. This approach not only mitigates the risk of signal interception but also holds promise for enhanced operational security in military contexts.
- The potential implementation of additional control techniques for collision avoidance, both among swarm units and with environmental obstacles, can represent a significant contribution to this research domain. It aims to refine automation and enhance system reliability in increasingly complex scenarios.
- Lastly, an optimal tuning of the control systems can be pursued to enhance performance across a wide range of deployment scenarios. This could involve conducting extensive simulations to identify the optimal control settings and refine the control algorithms with the aim of maximizing the effectiveness, efficiency, and adaptability of the control systems in different mission scenarios.

Bibliography

- [1] C. E. D. Riboldi and A. Rolando, “Layout analysis and optimization of airships with thrust-based stability augmentation,” *Aerospace*, vol. 9, p. 393, 2022.
- [2] C. E. D. Riboldi, A. Rolando, and D. Galbersanini, “Retrofitting of an ultralight aircraft for unmanned flight and parachute cargo drops,” *Journal of Aerospace Engineering*, vol. 36, no. 4, p. 04023029, 2023.
- [3] S. Farì, “Guidance and control for a fixed-wing uav,” Master’s thesis, Politecnico di Milano, 7 2016.
- [4] R. W. Beard and T. W. McLain, *Small Unmanned Aircraft: Theory and Practice*. Princeton University Press, 2012.
- [5] A. Israr, E. H. Alkhamash, and M. Hadjouni, “Guidance, navigation, and control for fixed-wing uav,” *Mathematical Problems in Engineering*, vol. 2021, 2021.
- [6] N. T. Dat, T. N. Son, and D. A. Tra, “Development of a flight dynamics model for fixed wing aircraft,” pp. 202–205, Association for Computing Machinery, 1 2018.
- [7] E. N. Mobarez, A. Sarhan, and M. M. Ashry, “Modeling of fixed wing UAV and design of multivariable flight controller using PID tuned by local optimal control,” in *18th International Conference on Aerospace Sciences & Aviation Technology, Cairo, Egypt, 9-11 April, 2019*.
- [8] V. Parunak, M. Purcell, and R. O’Connell, “Digital pheromones for autonomous coordination of swarming uav’s,” 05 2002.
- [9] C. E. D. Riboldi, L. Trainelli, C. Capocchiano, and S. Cacciola, “A model-based design framework for rotorcraft trim control laws,” in *43rd European Rotorcraft Forum, ERF 2017, Milan, Italy, 12-15 September, 2017*.
- [10] Z. Liu, X. Wang, L. Shen, S. Zhao, Y. Cong, J. Li, D. Yin, S. Jia, and X. Xiang, “Mission oriented miniature fixed-wing uav swarms: A multi-layered and distributed architecture,” 12 2019.

- [11] H. Chen, X. Wang, L. Shen, and Y. Cong, “Formation flight of fixed-wing uav swarms: A group-based hierarchical approach,” *Chinese Journal of Aeronautics*, vol. 34, pp. 504–515, 2 2021.
- [12] W. Suo, M. Wang, D. Zhang, Z. Qu, and L. Yu, “Formation control technology of fixed-wing uav swarm based on distributed ad hoc network,” *Applied Sciences (Switzerland)*, vol. 12, 1 2022.
- [13] P. K. C. Wang, “Navigation strategies for multiple autonomous mobile robots moving in formation.”
- [14] H. G. de Marina, Y. A. Kapitanyuk, M. Bronz, G. Hattenberger, and M. Cao, “Guidance algorithm for smooth trajectory tracking of a fixed wing uav flying in wind flows,” in *IEEE International Conference on Robotics and Automation (ICRA)*, 2017.
- [15] Z. Chao, S. L. Zhou, L. Ming, and W. G. Zhang, “Uav formation flight based on non-linear model predictive control,” *Mathematical Problems in Engineering*, vol. 2012, 2012.
- [16] A. Mottin, V. Onorato, and A. Rolando, “Design, simulation and manufacturing of dr-one, a formation flight-dedicated unmanned aerial vehicle,” 2014.
- [17] F. Giuliotti, L. Pollini, and M. Innocenti, “Autonomous formation flight,” *IEEE Control Systems*, vol. 20, pp. 34–44, 2000.
- [18] M. Innocenti, G. Mancino, M. Garofoli, and M. Napolitano, “Preliminary analysis of formation flight management,” pp. 258–268, American Institute of Aeronautics and Astronautics Inc, AIAA, 1999.
- [19] R. M. Bray, “A wind tunnel study of the pioneer remotely piloted vehicle,” 6 1991.
- [20] J. Roskam, *Airplane Flight Dynamics and Automatic Flight Controls*. DARcorporation, 2001.
- [21] M. H. Sadraey, “Aircraft design: a systems engineering approach,” 2013.
- [22] B. N. Pamadi, *Performance, stability, dynamics, and control of airplanes*. AIAA Education Series, American Institute of Aeronautics and Astronautics, Inc., 2004.
- [23] D. D. Moerder and A. J. Calise, “Convergence of a numerical algorithm for calculating optimal output feedback gains,” 1985.
- [24] E. N. J. Brian L. Stevens, Frank L. Lewis, *Aircraft Control and Simulation*. Wiley, 2016.

- [25] C. E. Riboldi and A. Rolando, “Thrust-based stabilization and guidance for airships without thrust-vectoring,” *Aerospace*, vol. 10, 4 2023.
- [26] C. E. Riboldi and M. Tomasoni, “Dynamic simulation, flight control and guidance synthesis for fixed-wing uav swarms,” 2023.
- [27] J. H. Blakelock, *Automatic control of Aircraft and Missiles*. John Wiley and Sons, Inc., 2 ed., 1991.
- [28] S. R. Griffiths, “Vector field approach for curved path following for miniature aerial vehicles,” 2006.
- [29] S. Park, “Rendezvous guidance on circular path for fixed-wing uav,” *International Journal of Aeronautical and Space Sciences*, vol. 22, pp. 129–139, 2 2021.
- [30] S. Park, “Circling over a target with relative side bearing,” *Journal of Guidance, Control, and Dynamics*, vol. 39, pp. 1450–1456, 2016.
- [31] Z. A. Bangash, R. P. Sanchez, A. Ahmed, and M. J. Khan, “Aerodynamics of formation flight,” *Journal of Aircraft*, vol. 43, pp. 907–912, 2006.
- [32] G. Larson, B. P. Works, and G. Schkolnik, “Autonomous formation flight mit course 16.886, spring 2004 air transportation systems architecting.”
- [33] J. S. Dennis Vechtel, Dietrich Fischenberg, “Flight dynamics simulation of formation flight for energy saving using les-generated wake flow fields.”
- [34] D. Singh, A. F. Antoniadis, P. Tsoutsanis, H. S. Shin, A. Tsourdos, S. Mathekga, and K. W. Jenkins, “A multi-fidelity approach for aerodynamic performance computations of formation flight,” *Aerospace*, vol. 5, 6 2018.
- [35] F. Giuliotti, M. Innocenti, M. Napolitano, and L. Pollini, “Dynamic and control issues of formation flight,” *Aerospace Science and Technology*, vol. 9, pp. 65–71, 2005.
- [36] T. Melin, *Tornado 1.0 User’s guide. Reference manual*. Institutionen för flygteknik Teknikringen, 12 2000.
- [37] A. W. Proud, “Close formation flight control,” 5 1999.

A | Appendix A

Here is a summary diagram of how the simulation is executed. The input file contains information about the number of aircraft, filter and actuator characteristics, navigation data, and formation geometry. This file is then passed to the main program for simulation initialization. In the main program, the swarm is assembled by arranging different Airplane.Obj objects along with their respective Filters.Obj and Actuators.Obj. Navigation information is loaded through the guidance set-up, and the trim condition at the selected airspeed and altitude at the first waypoint on the map is calculated. Initial conditions are assembled into a $No.A/C \cdot 27$ vector for the simulation (27 is the single aircraft state vector encompassing 9 canonical states, 3 inertial positions, 11 filters states, 4 actuators states).

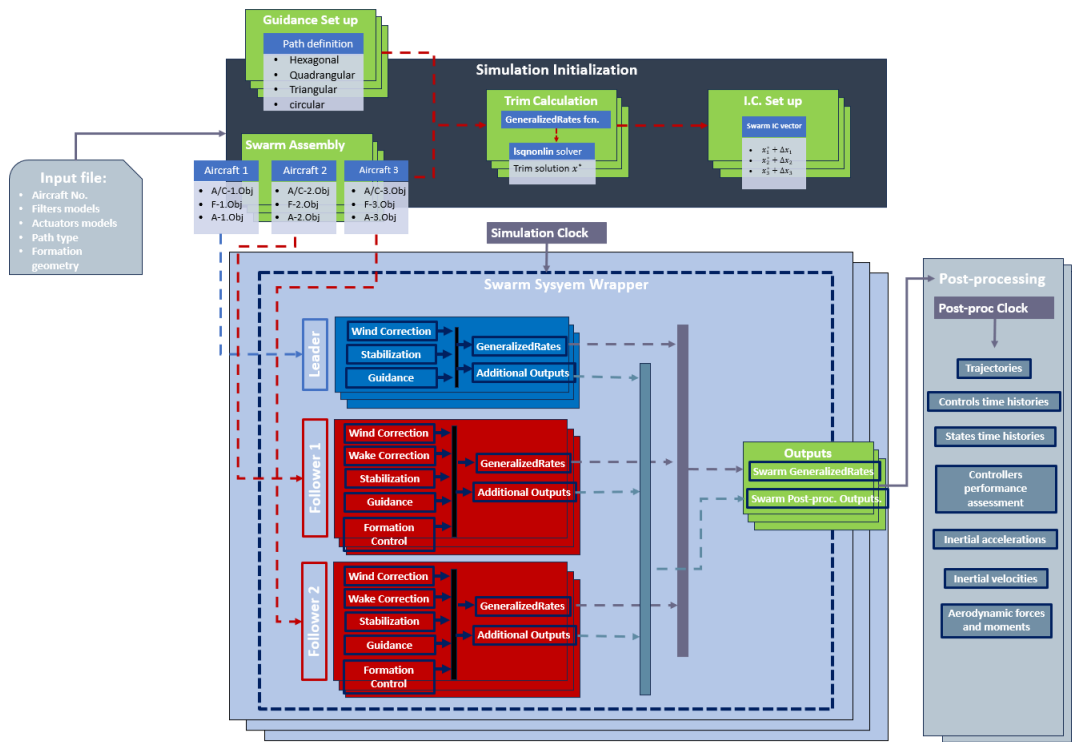


Figure A.1: Simulation scheme.

The data is then passed into the `SwarmSystemWrapper` function, which is the function provided to the `ode45` solver. Within this function, subfunctions are defined for both leaders and followers. These subfunctions, encapsulate all the subroutines for calculating control inputs computation, based on the designated role and the type of controller in use. The combination of control inputs then determines the forcing term of aerodynamic and propulsive forces and moments used to calculate the rates of the generalized balance equation. For each aircraft, these derivatives are grouped into a single vector in the `SwarmSystemWrapper` function for `ode45` integration. A series of additional outputs are collected for the post-processing phase.

B | Appendix B

The algorithm for K_{LQR} computation with output feedback is herein outlined:

Algorithm B.1 Optimal Output Feedback Solution Algorithm

1: Initialize:

Set $k = 0$.

Determine a gain K_0 so that $A - BK_0C$ is asymptotically stable.

2: k^{th} iteration:

Set $A_k = A - BK_kC$

Solve for P_k and S_k in

$$0 = A_k^T P_k + P_k A_k + C^T K_k^T R K_k C + Q$$

$$0 = A_k S_k + S_k A_k^T + X$$

Set $J_k = \frac{1}{2} \text{tr}(P_k X)$

Evaluate the gain update direction

$$\Delta K = R^{-1} B^T P S C^T (C S C^T)^{-1} - K_k$$

Update the gain by

$$K_{k+1} = K_k + \alpha \Delta K$$

where α is chosen so that

$A - BK_{k+1}C$ is asymptotically stable

$$J_{k+1} = \frac{1}{2} \text{tr}(P_{k+1} X) \leq J_k$$

If $J_{k+1} - J_k < \text{tol}$, \rightarrow go to 3

Else, set $k = k + 1 \rightarrow$ go to 2

3: Terminate:

Set $K = K_{k+1}$, $J = J_{k+1}$

End.

C | Appendix C

Algorithm C.1 Gains Blending Algorithm

```

1: Input:  $m1, m2, Time, eTLat_{max}, eTLat$ 
2: Output:  $KK = [K1_{fun}, K2_{fun}]$ 
3: Initialize variables:
    $slope1 \leftarrow m1, slope2 \leftarrow m2$ 
    $K1_{fun} \leftarrow 0$ 
    $startTime \leftarrow \text{uninitialized}$ 
    $endTime \leftarrow \text{uninitialized}$ 
4: if  $\|eTLat\| < 1$  then
5:    $startTime \leftarrow -1$  {Invalid initial value}
6:    $endTime \leftarrow -1$  {Invalid initial value}
7: end if
8: if  $\|eTLat\| \geq eTLat_{max}$  and  $startTime < 0$  then
9:    $startTime \leftarrow Time$  {Store time when  $eTLat$  exceeds threshold}
10: end if
11: if  $\|eTLat\| < eTLat_{max}$  and  $endTime < 0$  and  $startTime > 0$  then
12:    $endTime \leftarrow Time$  {Store time when  $eTLat$  falls below threshold}
13: end if
14: if  $startTime \geq 0$  then
15:    $elapsedTime \leftarrow Time - startTime$ 
16:    $K1_{fun} \leftarrow elapsedTime \cdot slope1$ 
17:    $K1_{fun} \leftarrow \max(0, \min(1, K1_{fun}))$ 
18:   if  $\|eTLat\| < eTLat_{max}$  and  $endTime > 0$  then
19:      $elapsedTime \leftarrow Time - endTime$ 
20:      $K1_{fun} \leftarrow 1 - elapsedTime \cdot slope2$ 
21:      $K1_{fun} \leftarrow \max(0, \min(1, K1_{fun}))$ 
22:   end if
23: else
24:    $K1_{fun} \leftarrow 0$ 
25: end if
26:  $KK \leftarrow [K1_{fun}, 1 - K1_{fun}]$ 

```

D | Appendix D

Below are the graphs related to the performance characterization of the RQ-2 Pioneer aircraft based on the data from [19].

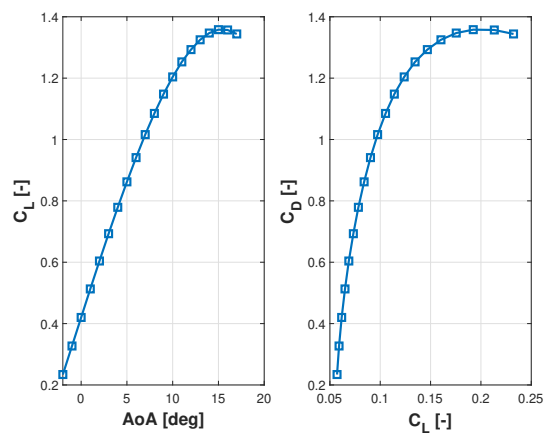


Figure D.1: Trimmed C_L curve (left) and trimmed polar curve (right)

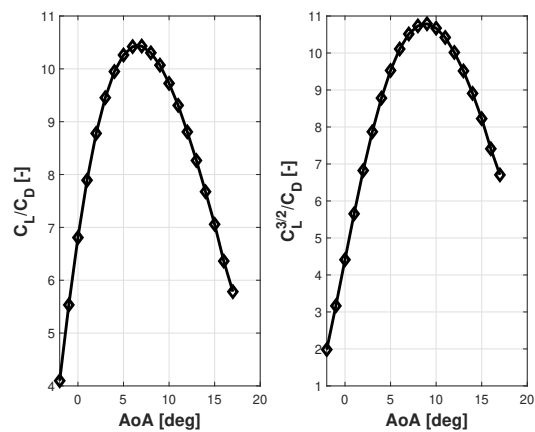


Figure D.2: Lift to Drag ratio (left) and $C_L^{3/2}/C_D$ curve (right). Max Range at 6 AoA, max endurance at 8 AoA.

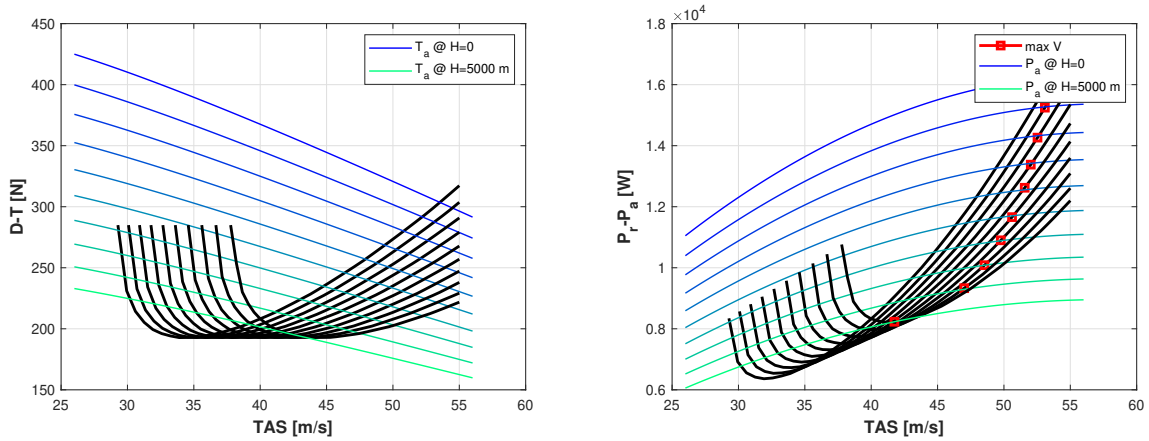


Figure D.3: Penaud diagrams: Drag-thrust over TAS (left), Power required-Power Available over TAS (right)

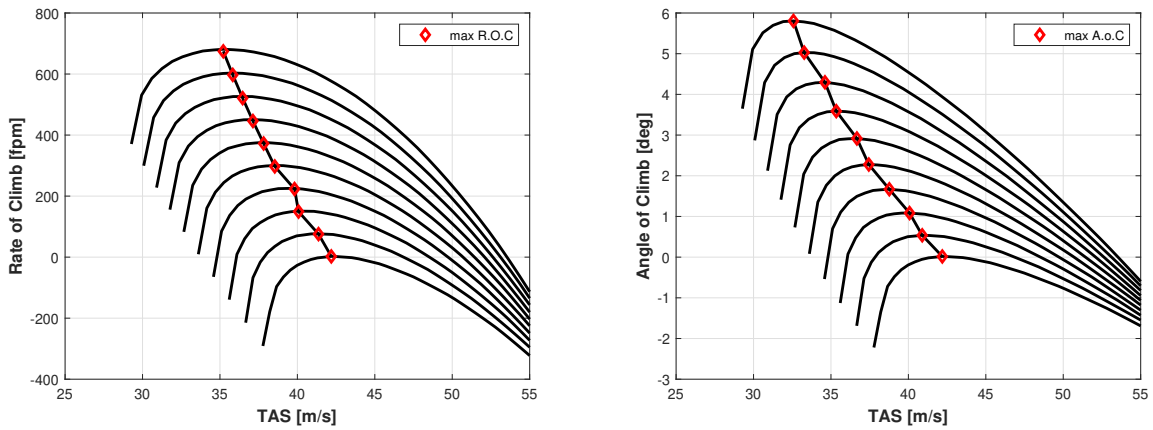


Figure D.4: Rate of climb (left) and angle of climb between $H = 0$ m to $H = 5000$ m.

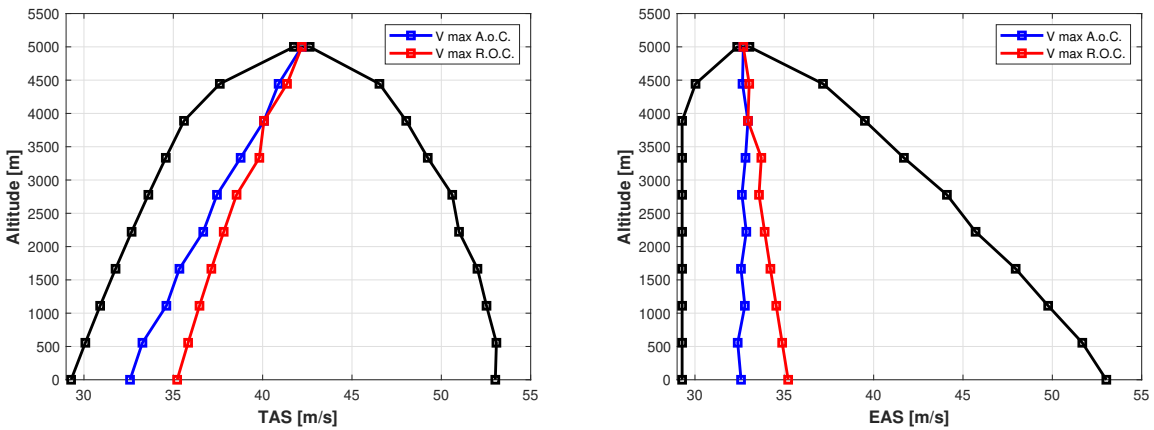


Figure D.5: TAS flight envelope (left), and EAS flight envelope (right).

List of Figures

1	fixed-wing UAVs swarm for military surveillance.	2
2	Group-based hierarchical model proposed by [11].	5
3	Airplane Object definition.	9
1.1	Rotation about \mathbf{k} (\mathbf{k} axis point outwards).	14
1.2	The LocalHorizon Frame $\mathcal{F}^{\mathcal{H}}$	15
1.3	α and β definition on body-frame $\mathcal{F}^{\mathcal{B}}$	18
1.4	Representation of stability and wind frame, $\mathcal{F}^{\mathcal{S}}$ and $\mathcal{F}^{\mathcal{W}}$	19
1.5	Sequential rotation from $\mathcal{F}^{\mathcal{I}}$ to $\mathcal{F}^{\mathcal{B}}$	21
1.6	The wind triangle	23
1.7	Body-axes components of translational and angular velocities.	24
1.8	Aerodynamic control surfaces deflections.	28
1.9	Lift and drag forces direction for a positive α	30
1.10	AAI RQ-2 Pioneer 2D views.	34
2.1	Complete system eigenvalues map. Blue: longitudinal eigenvalues. Red: lateral-directional eigenvalues.	47
2.2	Complete system eigenvalues map. Origin close-up	47
2.3	Longitudinal modes certification requirements in terms of pole distribution	49
2.4	Lateral-directional modes certification requirements in terms of pole distri- bution	50
2.5	Complete system root locus for increasing altitude.	51
2.6	Complete system root locus for decreasing airspeed.	51
2.7	Proposed stabilization control. Green: Longitudinal dynamics. Yellow: Lateral-directional dynamics. Cyan: Low-pass filters.	58
2.8	Complete system poles distribution. Comparison between open-loop and closed-loop system.	59
2.9	Longitudinal states evolution around trim condition 1. Open-loop (left) vs. closed-loop (right). Linear (dotted) vs. non-linear model.	61

2.10	Lateral-directional states evolution around trim condition 1. Open-loop (left) vs. closed-loop (right). Linear (dotted) vs. non-linear model.	61
2.11	SAS control inputs for stabilization around trim condition 1.	62
2.12	Longitudinal states evolution around trim condition 2. Open-loop (left) vs. closed-loop (right). Linear (dotted) vs. non-linear model.	63
2.13	Lateral-directional states evolution around trim condition 2. Open-loop (left) vs. closed-loop (right). Linear (dotted) vs. non-linear model.	63
2.14	SAS control inputs for stabilization around trim condition 2.	64
2.15	Longitudinal states evolution for assigned autopilot inputs. Open-loop (left) vs. closed-loop (right). Linear (dotted) vs. non-linear model.	65
2.16	Lateral-directional states evolution for assigned autopilot inputs. Open-loop (left) vs. closed-loop (right). Linear (dotted) vs. non-linear model. . .	65
2.17	Commanded control inputs with SAS enabled.	66
3.1	Sketch of beam tracking measurement in the longitudinal plane. Definition of e_V^{disp} . Illustration inspired by [25].	69
3.2	Sketch of beam tracking measurement in the longitudinal plane. Definition of $\mathbf{d}_V \cdot \mathbf{v}_{CG}$. Illustration inspired by [25].	70
3.3	Sketch of beam tracking measurement in the beam horizontal plane. Definition of e_L^{disp} . Illustration inspired by [25].	72
3.4	Sketch of beam tracking measurement in the beam horizontal plane. Definition of $\mathbf{d}_L \cdot \mathbf{v}_{CG}$. Illustration inspired by [25].	72
3.5	Hexagonal pattern target trajectory. Leg length: 2000 m.	73
3.6	K^{blend} behavior for different values of parameter $p = p_1 = p_2$	75
3.7	Proposed beam tracking control scheme. Red: airspeed tracking. Green: longitudinal beam tracking. Cyan: lateral guidance. Black: turn coordination.	76
3.8	Representative sketch for orbit path measurements.	78
3.9	Vector field for circular trajectory tracking.	79
3.10	Effect of k_0 parameter on orbit transition rate.	79
3.11	Side-bearing angle definition [30].	82
3.12	Circular trajectory attraction with different initial conditions [30].	82
3.13	GPS-based computation scheme for side-bearing angle.	83
3.14	Geometric scheme for leader chasing.[29].	84
3.15	Lateral guidance law switch for rendezvous procedure.	86

3.16	Trajectory and control behavior for ascending track with initial $\Delta\psi = 40$ deg misalignment. (Top-left) 3D view. (Top-right) lateral view. (Bottom-left) top view. (Bottom-right) controls time histories	88
3.17	Beam tracking errors for ascending track with initial misalignment.	89
3.18	Aircraft states evolution for ascending track with initial $\Delta\psi = 40$ deg misalignment.	89
3.19	K^{blend} and K^{beam} transition over horizontal distance traveled from starting checkpoint.	90
3.20	Trajectory and control behavior for the hexagonal path. (Top-left) 3D view. (Top-right) lateral view. (Bottom-left) top view. (Bottom-right) controls time histories	91
3.21	Beam tracking errors for the hexagonal path.	92
3.22	Aircraft state evolution for the hexagonal path.	92
3.23	Trajectory and control behavior for the quadrangular path. (Top-left) 3D view. (Top-right) lateral view. (Bottom-left) top view. (Bottom-right) controls time histories	93
3.24	Beam tracking errors for the quadrangular path.	94
3.25	Aircraft states for the quadrangular path.	94
3.26	Trajectory and control behavior for hexagonal path with 5 m/s constant wind. (Top-left) 3D view. (Top-right) lateral view. (Bottom-left) top view. (Bottom-right) controls time histories	95
3.27	Beam tracking errors for hexagonal path with 5 m/s constant wind.	96
3.28	Aircraft states for hexagonal path with 5 m/s constant wind.	96
3.29	Trajectory and control behavior for circular path with $R = 2000$ m and center coordinates $\mathbf{c} = [4000, 0]$. (Top-left) 3D view. (Top-right) top view with vector field. (Bottom-left) trajectory angles. (Bottom-right) controls time histories	97
3.30	Circular trajectory tracking errors.	98
3.31	3D trajectory view for circular path with $R = 300$ m and center coordinates $\mathbf{c} = [1800, 0]$	99
3.32	Control time histories and trajectory tracking errors for circular path with $R = 300$ m and center coordinates $\mathbf{c} = [1800, 0]$	99
3.33	Leader and followers trajectories during rendezvous procedure.	100
3.34	Control authority over roll angle set point tracking and corresponding aileron time history for both followers.	101
3.35	Rendezvous indicator parameters: phase angle γ , phase shift σ , side-bearing angle η , and relative leader-follower distance Δx_{GND}	101

3.36	Leader and followers trajectories during rendezvous procedure with additional velocity control.	102
3.37	Control authority over roll-angle and velocity set points and overall rendezvous indicator parameters.	103
4.1	Vortex flow field behind a leading aircraft, investing trailing units in the formation.	106
4.2	Upwind (top) and downwind (bottom) effects on lift coefficient (C_L) and drag coefficient (C_D).	107
4.3	Tandem wing geometry layout (left) and VLM set-up with panels collocation points and normals (right).	110
4.4	Wake-induced aerodynamic forces coefficients variations.	111
4.5	Wake-induced aerodynamic moments coefficients variations.	112
4.6	Lift and induced drag distribution over trailing aircraft wing span, for several value of lateral stagger.	113
4.7	Wake-induced effect over longitudinal stagger.	114
4.8	Formation control: definition of target point for the follower, and of the follower position errors e_{P1} , e_{P2} and e_{P3}	115
4.9	Control scheme for follower aircraft in formation flight (cruise mode). Blue: autothrottle loop. Pink: aileron control loop. Green: elevator control loop. Red: rudder control loop.	117
4.10	Straight climbing path with initial 10 deg misalignment. Two-aircraft formation. Left plot. Visualization of trajectories. Blue: leader. Red: follower. Right plot. Controls time histories for leader and follower.	119
4.11	Target position errors for formation control.	120
4.12	Two-aircraft formation. States time evolution.	120
4.13	Hexagonal path with 4 alternating altitude changes. Three-aircraft formation. Left plot. Visualization of trajectories. Blue: leader. Red: followers. Right plot. Controls time histories for leader and followers.	121
4.14	Time histories of errors for followers unit formation flight along a hexagonal pattern. Left: left-hand side follower position errors. Right: right-hand side follower position errors.	122
4.15	Three-aircraft formation along a hexagonal pattern. States time evolution.	122
4.16	Triangular path. Three-aircraft formation. Left plot. Visualization of trajectories. Blue: leader. Red: followers. Right plot. Controls time histories for leader and followers.	123

4.17	Time histories of errors for followers unit formation flight along a triangular pattern. Left: left-hand side follower position errors. Right: right-hand side follower position errors.	123
4.18	Three-aircraft formation along a triangular pattern. States time evolution.	124
4.19	Leader flying through constant wind disturbance tube (A). Followers with on-target guidance mode engaged (B). Final formation rejoining (C). . . .	125
4.20	AFCS modes transition	126
4.21	Formation disturbance management with separation and rejoining. Comparison between the non-co-operating leader ((a) and (c)), and co-operating leader ((b) and (d)).	128
4.22	Leader flying through constant wind disturbance tube (A). Followers with on-target guidance mode engaged (B). Final formation rejoining (C). . . .	129
4.23	Leader's controls time histories for crabbing maneuver	129
4.24	Target errors for leader's beam-tracking (left) and followers position tracking (right).	130
5.1	The earthquake-affected area, Japan, March 2011. Identification of the epicenter and coastal reconnaissance target area.	131
5.2	Clusters departure points and rendezvous designated area.	132
5.3	Navigation information. Waypoints and targets collocation.	133
5.4	V-shape formation for navigation phases.	134
5.5	Diamond-shape formation for targets overflight.	134
5.6	Rendezvous for formation assembly with 4 m/s crosswind heading $\psi_w = 70$ deg.	135
5.7	Rendezvous indicator parameters: phase angle γ , phase shift σ , side-bearing angle η , and relative leader-follower distance Δx_{GND}	136
5.8	Rendezvous procedure completed ($T = 410$ s). Formation assembled in diamond shape.	136
5.9	Aircraft 1,6,9 controls time histories for rendezvous procedure with crosswind.	137
5.10	Navigation Phase. Box A: turning maneuver for route alignment. Box B: diamond-shaped formation. Box C: reconfiguration. Box D: V-shaped formation.	138
5.11	Target errors for beam tracking guidance during navigation phase.	139
5.12	Position errors and controls time histories for Aircraft 6,7,8,9 during formation reconfiguration.	139
5.13	Target overflight with 8 m/s crosswind. Comparison between trajectories with and without rudder compensation.	140

5.14	Beam tracking errors targeted by the leader. Comparison between errors resulting from no compensation (left) and crabbing maneuver (right). . . .	141
5.15	Leader's crabbing maneuver coordination.	141
5.16	Formation position errors. Comparison between errors resulting from no compensation (left) and crabbing maneuver (right).	141
5.17	Leader's GM failure over target. Precision track mode sequence: Box A: formation split. Box B: Leader's rejoining. Box C: complete formation. . .	142
5.18	Followers position errors and control time histories during leader's failure on target.	143
5.19	Target 2 Overflight: Circular orbit insertion and traveling. Geometry re-configuration sequence: Box A: V-shape. Box B: transition. Box C: diamond shape.	143
5.20	Guidance errors during target 2 overflight.	144
5.21	Formation position errors during target 2 overflight.	145
5.22	Disengagement and formation splitting sequence: Box A: V-shaped formation. Box B: diamond-shaped formation. Box C: split formation.	146
5.23	Turbulence effect on lateral-directional states of Aircraft 2,6,9.	147
5.24	Aircraft 2,6,9 position errors during disengagement in turbulent air. . . .	147
A.1	Simulation scheme.	157
D.1	Trimmed C_L curve (left) and trimmed polar curve (right)	163
D.2	Lift to Drag ratio (left) and $C_L^{3/2}/C_D$ curve (right). Max Range at 6 AoA, max endurance at 8 AoA.	163
D.3	Penaud diagrams: Drag-thrust over TAS (left), Power required-Power Available over TAS (right)	164
D.4	Rate of climb (left) and angle of climb between $H = 0$ m to $H = 5000$ m. . .	164
D.5	TAS flight envelope (left), and EAS flight envelope (right).	164

List of Tables

1	<i>Craft</i> superclass properties.	7
2	<i>Craft</i> superclass methods.	8
1.1	General Characteristics of the AAI RQ-2 Pioneer UAV.	35
1.2	AAI RQ-2 Pioneer Inertial and geometric specifics.	36
1.3	Stability and control derivatives	37
1.4	Actuators dynamics models	38
2.1	Trim output at $V = 140$ km/h, $H = 300$ m.	46
2.2	Longitudinal modes characteristics	48
2.3	Lateral-directional modes characteristics	48
2.4	AAI RQ-2 Pioneer flying qualities classification	48
2.5	MIL-F-87-85C requirements for <i>Class I</i> aircraft, <i>Category A</i> flight phase, <i>Level I</i> adequacy.	49
2.6	Trim output at $V = 120$ km/h, $H = 2300$ m.	62
2.7	Trim output at $V = 180$ km/h, $H = 300$ m.	64
3.1	Beam tracking design parameters.	86
3.2	Trajectory blending design parameters.	87
3.3	Circular trajectory tracking/ Rendezvous guidance design parameters.	87
4.1	FCM design parameters.	118
5.1	Mission schedule.	133

List of Symbols

Variable	Description	SI unit
α	Angle of attack	rad
$\dot{\alpha}$	Incidence rate	rad/s
β	Sideslip angle	rad
$\dot{\beta}$	Sideslip angle rate	rad/s
γ	Orbit phase angle	rad
δ_a	Aileron deflection	rad
δ_e	Elevator deflection	rad
δ_r	Rudder deflection	rad
δ_t	Throttle setting	-
η	Side bearing angle	rad
ϕ, θ, ψ	Euler angles	rad
λ	Orbit travel direction flag	-
ρ	Air density	kg/m ³
σ	Phase shift (L-F)	rad
τ	Time constant	s
χ	Course angle	rad
ψ	Heading angle	rad
ω	Angular velocity	rad/s

Variable	Description	SI unit
$\mathbf{a}_x, \mathbf{a}_y, \mathbf{a}_z$	linear acceleration in body axes	m/s ²
b	Wing span	m
c	mean chord	m
$C_{(.)}$	Generic aerodynamic coefficient	-
$C_{(.)_{(.)}}$	Generic aerodynamic coefficient derivative	-
C_{D_0}	Aircraft parasite drag coefficient	-
C_{D_i}	Aircraft induced drag coefficient	-
C_L	Aircraft lift coefficient	-
$C_{\mathcal{L}}$	Rolling coefficient	-
$C_{\mathcal{M}}$	Pitching moment coefficient	-
$C_{\mathcal{N}}$	Yawing moment coefficient	-
\hat{d}	cross-track error	m
D	drag force	N
$\mathbf{e}_x^{(.)}, \mathbf{e}_y^{(.)}, \mathbf{e}_z^{(.)}$	Generic reference system's triad	-
e_L^{disp}	Lateral error on position (guidance)	m
e_L^{vel}	Lateral error on lateral rate set point (guidance)	m/s
e_V^{disp}	Vertical error on position (guidance)	m
e_V^{vel}	Vertical error on vertical rate set point (guidance)	m/s
e_{P1}, e_{P2}, e_{P3}	Follower position errors	m
g	gravitational acceleration	m/s ²
$k_p^{(.)}$	Generic proportional gain	-
L	lift force	N
$\mathbf{p}, \mathbf{q}, \mathbf{r}$	Body angular rates	rad/s
R	Circular orbit radius	m
t	time	s
T	Thrust force	N
u	Non-dimensional airspeed	-
\mathbf{v}_{CG}	inertial velocity vector	m/s
V_G	Ground speed	m/s
U, V, W	Airspeed components in body frame	m/s
\mathbf{x}_{CG}	inertial position vector	m
$\mathbf{X}, \mathbf{Y}, \mathbf{Z}$	Aerodynamic forces in body frame	N
Δy	Lifting surf. lateral stagger	m
Δz	Lifting surf. vertical stagger	m

Subscript and Superscript

Symbol	Description
$(\cdot)^{\mathcal{B}}$	Representation in body components
$(\cdot)^{bm\mathcal{I}}$	Representation in inertial components
$(\cdot)^{\mathcal{S}}$	Representation in stability frame components
$(\cdot)^{\mathcal{W}}$	Representation in wind frame components
$(\cdot)_{bf}$	Bandwidth filtered
$(\cdot)^{Pilot}$	Autopilot control input
$(\cdot)_{ref}$	Reference condition

List of Acronyms

Symbol	Description
<i>AFCS</i>	Automatic flight control system
<i>CG</i>	Center of gravity
<i>FCM</i>	AFormation control mode
<i>GM</i>	Guidance mode
<i>LQR</i>	Linear quadratic regulator
<i>VLM</i>	Vortex lattice method

Acknowledgements

Giunto alla conclusione di questo percorso desidero in primo luogo ringraziare sentitamente il Prof. Riboldi per l'instancabile supporto e la pronta disponibilità nell'accogliere e discutere di ogni mia perplessità, per le conoscenze che mi ha trasmesso, e per aver alimentato questa mia inesauribile passione per il volo.

Una menzione d'onore spetta ai miei carissimi colleghi del 104: Jaco, Stoff, Sulia, Stabbus, Andre, Luke, Ale (GDM), Rick, Massi, e infine Corl e Osc con i quali ho condiviso la preparazione della quasi totalità degli esami, e che a modo loro mi hanno sempre ascoltato e aiutato ad affrontare questo percorso fino alla fine.

Grazie anche a voi, storici amici del MNG: Looce, Linda, Checco e Benny, che nonostante le diverse strade intraprese avete sempre dimostrato la vostra vicinanza.

Un ringraziamento d'obbligo va anche a Letizia e Mattia, alla loro allegria e originalità, e alla loro capacità di trasformare anche i giorni più grigi in occasioni per ridere insieme.

Infine desidero ringraziare Vale, la persona che più di tutti in questi anni è cresciuta insieme a me e mi ha sostenuto ogni singolo giorno. Mai avrei pensato di trovare una persona a suo modo così speciale.

Alla mia famiglia, nonni ,zio, e soprattutto mamma e papà, dedico a voi questo lavoro perchè è ciò che voi, con il vostro inesauribile supporto, avete reso possibile giorno dopo giorno. Mi avete dato tutto senza chiedere nulla in cambio, e per questo non potrò che esservi per sempre grato.

